Role of Tumor Acidosis and Hypoxia in Immune Escape by IFN-γ-induced Transcriptional Induction of PD-L1 via the eIF4F Axis on Cancer Cells

Dissertation

der Mathematisch-Naturwissenschaftlichen Fakultät
der Eberhard Karls Universität Tübingen
zur Erlangung des Grades eines
Doktors der Naturwissenschaften
(Dr. rer. nat.)

vorgelegt von
Philipp Knopf
aus Biberach an der Riß

Tübingen
2021

Gedruckt mit Genehmigung der Mathematisch-Naturwissenschaftlichen Fakultät der Eberhard Karls Universität Tübingen.

Tag der mündlichen Qualifikation:	14.01.2022
Dekan:	Prof. Dr. Thilo Stehle
1. Berichterstatter/-in:	Prof. Dr. Bernd J. Pichler
2. Berichterstatter/-in:	Prof. Dr. Hans-Georg Rammensee

FOR MY **F**AMILY

Table of Contents

List of Abbreviations

αSMA	alpha smooth muscle actin
acidoCEST	acido chemical exchange saturation transfer
ADCC	antibody-dependent cell-mediated cytotoxicity
ADP	adenosine diphosphate
argonaute 2	AGO2
ANOVA	analysis of variance
AP-1	activator protein 1
APC	adenomatous polyposis coli
APC	antigen presenting cell
AMP	adenosine monophosphate
ATP	adenosine triphosphate
BBI	broad band inverse
BCA	bicinchoninic acid
BLI	bioluminescence imaging
BM-MDSCs	bone marrow myeloid-derived suppressor cells
BSA	bovine serum albumin
BTLA	B and T cell lymphocyte attenuator
B7-H3	B7 homolog 3 protein
CA	carbonic anhydrase
CAF	cancer-associated fibroblast
cAMP	cyclic AMP
CAR	chimeric antigen receptor
Cas	CRISPR-associated
CCD	charge-coupled device
CCL2	C-C motif chemokine 2
CDK	cyclin-dependent kinase
cDNA	complementary DNA
CDS	coding sequence
CD274	cluster of differentiation 274
ChK	choline kinase
cHL	classical Hodgkin lymphoma
COX-2	cyclooxygenase 2

CP	MR-compatible cell perfusion system
cpm	counts per million
CRISPR	clustered regularly interspaced short palindromic repeats
CSC	cancer stem-like cell
CSF1	colony- stimulating factor 1
CT	computed tomography
CTLA-4	cytotoxic T-lymphocyte-associated protein 4
CXCL1	C-X-C motif chemokine ligand 1
D_2O	deuterated water
DAPI	4′,6-Diamidin-2-phenylindol
DC	dendritic cell
DHA	docosahexaenoic acid
DI	degradation index
DMEM	Dulbecco's Modified Eagle's Medium
dMMR	mismatch repair deficient
DMSO	dimethyl sulfoxide
DNA	deoxyribonucleic acid
dNTP	deoxynucleotide
Dox	doxycycline hyclate
DOT	diffuse optical tomography
DPBS	Dulbecco's Phosphate-Buffered Saline
DTT	dithiothreitol
DW	diffusion weighted
ECM	extracellular matrix
EBV	Epstein-Barr virus
EGF	epidermal growth factor
EGFR	epidermal growth factor receptor
eIF4F	eukaryotic initiation factor 4F
EMT	epithelial-mesenchymal transition
ESD	Extreme Studentized Deviate
ERK	extracellular signal-regulated kinase
FA	fatty acid
FAP	fibroblast activation protein
[^{18}F]FAZA	[^{18}F]fluoroazomycinarabinoside

FBS	fetal bovine serum
FDA	U.S. Food & Drug Administration
[^{18}F]FDG	[^{18}F]2-fluor-2-desoxy-D-glucose
FGF	fibroblast growth factors
FID	free induction decay
FISP	fast imaging with steady-state precession
[^{18}F]FMISO	[^{18}F]fluoromisonidazole
FOV	field of view
FOXP3	forkhead box P3
FPKM	Fragments Per Kilobase of exon per Million reads
GAPDH	glyceraldehyde 3-phosphate dehydrogenase
GAS	IFN-γ activation site
GDC	Genomic Data Commons
GFP	green fluorescent protein
Gln	glutamine
GLUT1	glucose transporter 1
GM-CSF	granulocyte–macrophage colony-stimulating factor
G-MDSC	granulocytic myeloid-derived suppressor
GPC	sn-Glycero-3-phosphocholine
GPCR	G-protein coupled receptor
GPR81	G protein-coupled receptor 81
gRNA	guide RNA
GSH	glutathione
GSSG	glutathione disulfide
HBSS	hank's balanced salt solution
HEPES	4-(2-hydroxyethyl)-1-piperazineethanesulfonic acid
HIF-1α	hypoxia-inducible factor 1 α
HMGA	high mobility group A
HRE	hypoxia-response element
HRP	horseradish peroxidase
HSA	human serum albumin
H&E	hematoxylin and eosin
Iba1	ionized calcium binding adaptor molecule 1
i.c.	intracutaneous

ICH	immunohistochemistry
ICG	indocyanine green
ICOS	inducible T cell co-stimulator
ID	injected dose
IDO	indoleamine 2,3-dioxygenase
IFN-γ	interferon-gamma
IFNGR	interferon-gamma receptor
IHC	immunohistochemistry
IL-4/-6/-8/-13	interleukin-4/-6/-8/-13
ILC	innate lymphoid cell
iNOS	inducible nitric oxide synthase
IRF1	interferon regulatory factor 1
ISRE	interferon-sensitive response element
ISYNA1	inositol 3-phosphate synthase
IVIS	*in vivo* imaging system
JAK	Janus kinase
LAG-3	lymphocyte activation gene-3
LAK	lymphokine-activated killer cells
LDH-A	lactate dehydrogenase-A
LLC	lewis lung carcinoma
LN	lymph node
lpl	lysophospholipase
LPS	lipopolysaccharide
LSD	Least Significant Difference
luc	luciferase
mAb	monoclonal antibody
MAPK	mitogen-activated protein kinase
MCT1/4	monocarboxylate transporter 1/4
MDSC	myeloid-derived suppressor cell
MEK	mitogen-activated protein kinase kinase
MEM	minimum essential medium
MFI	mean fluorescence intensity
MHC	major histocompatibility complex
miRNA	microRNA

M-MDSC	monocytic myeloid-derived suppressor cell
MMP-2/-3/-9	matrix metalloproteinase-2/-3/-9
MRI	Magnetic Resonance Imaging
MRS	Magnetic Resonance Spectroscopy
MSI-H	microsatellite instability-high
MTA	S-methyl-5´-thioadenosine
MTBE	methyl tert-butyl ether
mTOR	mammalian target of rapamycin
mTORC1	mammalian target of rapamycin complex 1
NAD^+	nicotinamide adenine dinucleotide
NADP	nicotinamide adenine dinucleotide phosphate
NAMP	nicotinamide phosphoribosyltransferase
NBC	Na^+/HCO_3^- co-transporter
NCBI	National Center for Biotechnology Information
NEA	non-essential amino acids
NF-κB	nuclear factor kappa-light-chain-enhancer of activated B cells
NHE	Na^+/H^+ exchanger
NIR	near-infrared
NK cell	natural killer cell
NLS	nuclear localization signal
NMR	Nuclear Magnetic Resonance
NSCLC	non-small-cell lung cancer
NTDLN	non-tumor-draining lymph nodes
OCC	oral cavity squamous cell carcinoma
ODD	oxygen-dependent degradation domain
OI	Optical Imaging
ORR	overall response rate
OS	overall survival
OXPHOS	oxidative phosphorylation
PAMPs	pathogen-associated molecular patterns
PBS	phosphate-Buffered Saline
PBS-T	0.5% Tween in PBS
PC	O-phosphocholine
PCr	creatine phosphate

PD-1	programmed death-1
pde	glycerophosphocholine phosphodiesterase
PD-L1	programmed death ligand-1
PDGF	platelet-derived growth factor
PE	phosphatidylethanolamine
PEG	poly(ethylene glycol)
PET	Positron Emission Tomography
PFC	perfluorocarbon
pH_e	extracellular pH
pH_i	intracellular pH
plA/C/D	phospholipase A/C/D
PKA	protein kinase A
PLA2R	phospholipase A2 receptor
PMBC	peripheral blood mononuclear cells
pRb	retinoblastoma protein
PtCho	phosphatidylcholine
PTEN	phosphatase and tensin homolog
PVDF	polyvinylidene difluoride
MLBCL	mediastinal large B-cell lymphoma
RAG2	recombinant activating gene 2
RF	radiofrequency
RIPA	radioimmunoprecipitation assay
RISC	RNA interference – induced silencing complex
RNA	ribonucleic acid
RNA-seq	RNA sequencing
ROI	region of interest
ROS	reactive oxygen species
RPMI-1640	Roswell Park Memorial Institute 1640
RT	reverse transcriptase
SAβGAL	senescence-associated β-galactosidase
SASP	senescence associated secretory phenotype
s.c.	subcutaneous
SCLC	small-cell lung cancer
SDS-PAGE	sodium dodecyl sulfate polyacrylamide gel electrophoresis

SEM	standard error of the mean
SHP2	Src homology region 2 domain-containing phosphatase-2
shRNA	short hairpin RNA
siRNA	short-interfering RNA
SM	sphingomyelin
SMARCD1	SWI/SNF-related matrix-associated actin-dependent regulator of chromatin subfamily D member 1
SPECT	single photon emission computed tomography
STAT1/2	signal transducer and activator of transcription 1/2
TAM	tumor-associated macrophage
TAN	tumor-associated neutrophil
TCA	tricarboxylic acid
TCGA	The Cancer Genome Atlas
TCR	T cell receptor
TDLN	tumor-draining lymph nodes
TGF-α/-β	transforming growth factor-α/-β
T_h1	T-helper 1
TIGIT	T cell immunoglobulin and ITIM domain
TIL	tumor infiltrating T lymphocyte
TIM-3	T cell immunoglobulin and mucin-domain containing-3
TIME	tumor immune microenvironment
TIS	therapy-induced senescence
T_m	melting temperature
TMS	tetramethylsilane
TNF	tumor necrosis factor
TSP	3-(trimethylsilyl) propionic 2,2,3,3-d4 acid sodium salt
TTP	tristetraprolin
UTR	untranslated regions
VEGF	vascular endothelial growth factor
VISTA	V-domain Ig suppressor of T cell activation
VOI	volume of interest
VSVG	vesicular stomatitis virus G
WB	western blotting

List of Figures

List of Tables

Acknowledgement

First and foremost, I would like to thank Prof. Dr. Bernd Pichler, for giving me the opportunity to prepare my PhD thesis at the Werner Siemens Imaging Center in Tübingen. Furthermore, I want to say many thanks for supporting this dissertation scientifically and providing me the opportunity to stay abroad for several month and performing parts of my PhD project at the Johns Hopkins University. In addition, Prof. Dr. Bernd Pichler gave me the opportunity to attend national as well as international conferences. I am deeply grateful for these opportunities of scientific exchange.

Moreover, I want to thank Dr. Manfred Kneilling who supervised and scientifically supported this PhD thesis and used his network to push the project forward. Furthermore, I enjoyed the scientific discussions as well as the leisure activities.

My thanks further go to Prof. Dr. Hans-Georg Rammensee for agreeing to take on the second opinion for this thesis.

Furthermore, I want to thank Prof. Dr. Zaver Bhujwalla and her team, namely Dr. Balaji Krishnamachary, Dr. Jesus Pacheco Torres, Yelena Mironchik, Flonne Wildes and Noriko Mori, for the various scientific discussions and making my stay in Baltimore an unforgettable experience.

My thanks also go to my collaboration partners and colleagues, Prof. Dr. Kamran Ghoreschi, Dr. Andreas Maurer, Dr. Marieke F. Fransen, Dr. Sabrina Hoffmann, Dr. Daniela Kramer, Prof. Dr. Mark D. Pagel, Dr. Sanhita Sinharay, Valentina Bucher, Birgit Fehrenbacher, Dr. Irene Gonzalez-Menendez, Prof. Dr. Leticia Quintanilla-Fend, Dr. Christoph Trautwein and Dr. Omelyan Trompak.

I would like to thank Natalie Herrmann, Dennis Haupt, Maren Harant, Sandro Aidone und Linda Schramm for their excellent technical support.

Most importantly, I want to thank my girlfriend Mojgan, my mum Beate, my dad Siegfried and my sisters Sina and Alica who surrounded me with love through the last five years and my entire life. Without their support, empathic and well-balanced advice as well as their patience, I would not have been able to manage this step of my life.

1 Introduction

1.1 Malignant tumors and the tumor microenvironment

1.1.1 Malignant tumor biology

Malignant neoplasms also named malignant tumors are the second leading cause of death after heart diseases in the US according to the U.S. Department of Health and Human Services [1]. Despite tremendous research efforts in the last decades and 16 out of 59 U.S. Food & Drug Administration (FDA) approved drugs in the field of oncology in 2018 [2], cancer remains a widespread and often deadly disease.

Cancer is a complex and dynamic disease with several mutual influencing processes and various cell types that interact with each other. A holistic picture of the disease itself, risk factors, underlying molecular processes involved in carcinogenesis and tumor progression, diagnostics, response biomarkers, drugs with high treatment efficacy as well as longitudinal therapy monitoring, and readjustment remain elusive.

The initial question that arises in this regard is how a normal, healthy mammalian cell transforms into a malignant cancer cell and how this transformation over time results in a solid malignant tumor. Vogelstein and Kinzler described it as a multistep process from the acquisition of several mutations via the succession of clonal expansion to the gradual increase in tumor mass [3, 4]. Hanahan and Weinberg comprehensively described the underlying processes and summarized the hallmarks of cancer in 2000, which were updated more than a decade later [4, 5]. In their first review, the authors described 6 main characteristics and capabilities that most cancers have in common. Amongst those alterations that characterize malignant cancers are self-sufficiency in growth signals, insensitivity to growth-inhibitory signals, programmed cell death evasion, limitless replicative potential, sustained angiogenesis and tissue invasion and metastasis [5]. While normal mammalian cells depend on mitogenic growth signals, malignant cancer cells proliferate independent of these signals due to acquired mutations in oncogenes that are involved in growth factor signaling like the GTPase Ras (H-Ras, N-Ras, K-Ras) [6] or the kinase epidermal growth factor receptor (EGFR) [7]. Furthermore, overexpression of the oncogene Myc (c-Myc, N-Myc, and L-Myc) [8, 9] or mutations in tumor suppressor genes like p53 [10] result in sustained cancer cell

proliferation. In addition, cancer cells produce growth factors like platelet-derived growth factor (PDGF) or transforming growth factor-α (TGF-α) themselves to sustain cell growth [5, 11, 12]. Cancer cells are also characterized by an evasion of apoptosis via altered pro-apoptotic proteins like Bax, Bak, Bid and Bim or anti-apoptotic proteins including Bcl-2, Bcl-XL or Bcl-W [5]. In contrast to healthy mammalian cells characterized by a finite replicative potential and the subsequent induction of a process named senescence, cancer cells circumvent the limited replication by mutated tumor suppressor proteins like retinoblastoma protein (pRb) and p53 [4, 5, 13]. These characteristics lead to an accumulation of cancer cells, clonal expansion, and ultimately an increase in tumor mass. Although being independent of external growth stimuli, proliferation and replication, cancer cells depend on adequate nutrient and oxygen supply. Sufficient vascularization of the tumor mass requires sustained angiogenesis mediated by vascular endothelial growth factor (VEGF) and fibroblast growth factors (FGF1/2) signaling [4, 5, 14, 15]. With tumor mass expansion, cancer cells furthermore invade surrounding tissue, ultimately leading to cell liberalization, migration and distal metastasis [4, 5].

Due to a remarkable progress in the first decade of this century, Hanahan and Weinberg amended the hallmarks of cancer in 2011 to deregulating cellular energetics, genome instability and mutation as well as most noteworthy escaping immune destruction and tumor-promoting inflammation [4]. Cancer cells are characterized by a high energy demand and undergo several metabolic changes. In contrast to normal mammalian cells which oxidize glucose to CO_2 during oxidative phosphorylation in the mitochondria, cancer cells favor limiting their energy metabolism to glycolysis even in the presence of oxygen. This effect was first discovered by Otto Warburg [16, 17]. Accordingly cancer cells are characterized by an enhanced glucose demand, which is covered by elevated glucose uptake via upregulation of glucose transporter 1 (GLUT1) expression [4]. This characteristic of cancer cells has been exploited for non-invasive *in vivo* identification of tumor lesions via positron emission tomography (PET) by detection of enhanced radioactive glucose analog [^{18}F] 2-fluor-2-desoxy-D-glucose ([^{18}F]FDG) uptake. In recent years it became more evident that genomic instability and an increased mutational rate in cancer cells are key characteristics and drivers of carcinogenesis [4, 18, 19]. Genomic instability can result in the expression of

unique ‘non-self’ peptides so called neoantigens, which make a tumor recognizable by the immune system and improve checkpoint inhibitor therapies [4, 20, 21]. In this context, the two emerging hallmarks immune destruction and tumor-promoting inflammation point out the role of the lymphoid system as well as the tumor immune microenvironment (TIME) in tumor development, progression, and metastasis. Furthermore, these two hallmarks paved the way for recent progresses in immunotherapies, including immune checkpoint inhibitor and chimeric antigen receptor (CAR) T cell therapies. Malignant tumors consist of not only cancer cells, but also infiltrated immune cells (T cells, macrophages, neutrophils), which shape the TIME and are either tumor-antagonizing or tumor promoting [4]. Further cancer cells express checkpoint inhibitor proteins that mediate immune evasion and allow carcinogenesis in the first place.

1.1.2 Tumor immunology

Human beings encounter many different pathogens every day, from which some can be harmful. Respectively, the immune system developed different mechanisms of response, which can be grouped into three major phases. The first line of defense includes the anatomic barriers of human beings like skin or mucosa, with antimicrobial peptides and enzymes as well as the complement system that targets pathogens for lysis and phagocytosis by innate immune cells like macrophages. The second line of defense, the innate immune system specifically recognizes pathogen-associated molecular patterns (PAMPs), which are exclusive for pathogens and not shared by host cells. In the third phase of defense, the so-called adaptive immune response, long-term immunity is obtained by the transport of antigens to the lymph nodes (LNs), T and B cell recognition, clonal expansion and differentiation into effector cells [22].

In contrast to external pathogens with antigens being clearly distinguishable from the host cells, malignant tumors consist of cancer cells that arose from normal, healthy cells and therefore they share most of the antigens which are recognized as self by the host immune system. Nevertheless, malignant tumors express tumor-specific antigens that can be recognized by T cells, finally resulting in the elimination of cancer cells by the host immune system. This principle was termed ‘immune surveillance’ by Frank MacFarlane Burnet and Lewis Thomas in the 1950s [22]. Although, the immune system can detect cancer cells by antigen recognition, transformation of normal cells to cancer cells does not necessarily

result in the presentation of neoantigens on the cancer cell surface. The host immune system also imposes a selection pressure on cancer cells promoting the generation of different cancer cell variants with different mutations conferring survival and growth advantages, a process termed cancer immunoediting [23]. The malignant tumor mass that escaped immune control, consists of cancer cells bearing various mutations as well as regulatory and immunosuppressive characteristics [22]. Experiments with immune compromised and syngeneic immune competent mice outline the importance of the host immune system for carcinogenesis and cancer progression.

Noteworthy amongst these immune cells are macrophages, which are large, mononuclear phagocytic cells. These cells secrete pro-inflammatory cytokines, present antigens and are involved in the innate as well as humoral and cell-mediated immunity [22]. Tumor-associated macrophages (TAMs) are key players in all stages of cancer development and furthermore mediate chronic cancer-associated inflammation [24]. Macrophages are classified into pro-inflammatory, lipopolysaccharide (LPS) and interferon-γ (IFN-γ) driven M1 as well as anti-inflammatory, interleukin-4 (IL-4) or IL-13 driven M2 macrophages [24]. Therefore, M1 macrophages play a prominent role during immune surveillance. In contrast, M2 macrophages have an important impact on tumor progression by promotion of angiogenesis, metastasis or suppression of the anti-tumor immune response [24, 25]. Similarly, phagocytic neutrophils play an important role during inflammation and can either be pro-tumorigenic or anti-tumorigenic [22, 26]. Depending on the type of cancer, neutrophils are present in the TME and secrete various cytokines, including pro-tumor TGF-β [24, 26]. In some type of cancers, the activated neutrophils exert myeloid-derived suppressor cell (MDSC) activities and can suppress T cell proliferation [27, 28]. Natural killer (NK) cells, which eliminate virus infected as well as some cancer cells represent another cell type of the TME. In addition, NK cells play a key role in innate immunity and antibody-dependent cell-mediated cytotoxicity (ADCC) [22]. NK cells exhibit their anti-tumor effect by presenting stimulatory cell surface receptors leading to release of perforin and granzyme [24]. Furthermore, NK cells produce tumor necrosis factor (TNF) and trigger apoptotic pathways in cancer cells [24]. In contrast, conventional dendritic cells (DCs) present tumor antigens to T cells in the tumor-draining lymph node (TDLN) and thereby induce anti-tumor immune response [22]. These antigen-

presenting cells (APCs) therefore represent the connection between innate and adaptive immunity and enable a tumor neoantigen specific T cell mediated response. T cells are antigen-specific lymphocytes and convey the cell-mediated adaptive immune response [22]. Specific antigens presented by major histocompatibility complexes (MHC) on the cell surface of APCs are recognized by the T cell receptor (TCR) of T cells. Based on highly variable TCRs two main T cell lineages are discriminated, namely α:β T cells and γ:δ T cells. In anti-tumor response, γ:δ tumor-infiltrating T lymphocytes (TIL) are the main source of IFN-γ, which mediates cancer cell elimination [22, 29]. T cells are grouped into $CD4^+$ T cells and cytotoxic $CD8^+$ T cells. Several subsets of $CD4^+$ T cells, including T helper cells (T_h cells) and regulatory T cells (T_{reg} cells) that assist or inhibit other immune cells are described and discriminated based on their cytokine signature. T_h1 cells are characterized by the production and secretion of IFN-γ, whereas T_h2 cells secrete IL-4, IL-5 and IL-13 [22]. Thereby, T_h1 cells for example activate macrophages. In contrast, $CD8^+$ T cells engage with neoantigen-presenting MHC class I complexes and release perforin as well as granzyme to induce apoptosis in target cells. Furthermore, $CD8^+$ T cells also secrete IFN-γ and TNF shaping the TME by e.g. the induction of programmed death ligand-1 (PD-L1) expression, a molecule also known as cluster of differentiation 274 (CD274) [22, 30, 31]. The second type of antigen-specific lymphocytes are B cells. Activation of naïve B cells requires an antigen as well as T_h cells and results in the differentiation of B cells into antibody producing plasma and memory B cells. Therefore, B cells are essential for the humoral part of the adaptive immune response and convey long-term memory [22].

Although human beings possess a complex and tightly regulated immune system, malignant tumors exhibit several immune evasion mechanisms. An anti-tumor immune response fails when malignant cells do not express neoantigens or in the absence of cellular adhesion or co-stimulatory molecules. Even if the host immune system develops cancer neoantigen-specific antibodies those antigens can be removed by endocytosis and degradation or changes of the antigens, termed antigenic modulation. Furthermore, cancer cells secrete cytokines like TGF-β, IL-10 or indoleamine 2,3-dioxygenase (IDO), which inhibit $CD8^+$ T cells and T_h1 cells directly or via the action of T_{reg} cells. Furthermore, expression of immune checkpoint proteins like PD-L1 prevents elimination of the tumor by the immune

system. Beside this tumor-induced immune suppression, tumors build up and maintain a privileged site with collagen creating a physical barrier preventing the infiltration of immune cells. Other factors including tumor acidosis or hypoxia contribute to the tumor immune cell exclusion (**Figure 1**) [22].

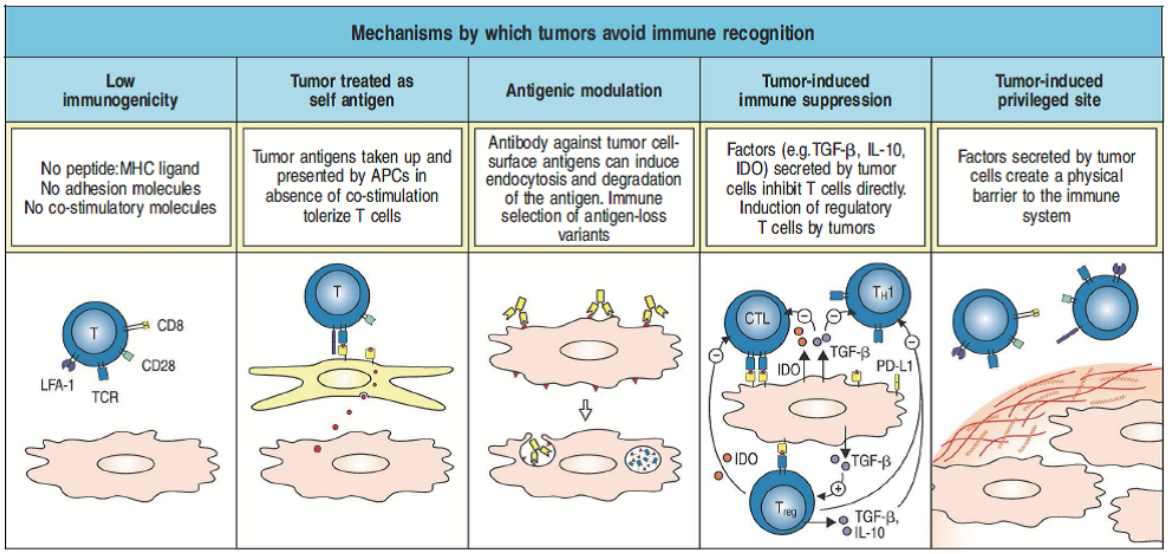

Figure 1: Malignant tumors evade immune recognition by various mechanisms.
These immune evasion mechanisms include low tumor immunogenicity, tumors treated as self-antigens, antigenic modulation, and tumor-induced immune suppression as well as tumor-induced privileged sites. Tumor-induced immune suppression can be induced by immune-modulatory molecules such as TGF-β, IL-10, IDO and PD-L1 [22]. Figure adapted from [22].

When tumors reach a volume, which is detectable by [^{18}F]FDG-PET/magnetic resonance imaging (MRI) they already escaped immune recognition, via the various mechanisms described. Nevertheless, the immune system can be re-activated by blockage of immune checkpoint proteins like PD-L1. Therefore, the interplay of tumors and the immune system is essential for anti-cancer therapies.

1.1.3 Composition of the tumor microenvironment

Malignant tumors consist of cancer cells, various stromal cells, extracellular material and immune modulatory factors like cytokines and chemokines that shape the TIME. These individual components of the TME interact, influence each other's function, and often mutually depend on each other (**Figure 2**). The malignant as well as non-malignant cellular components of the TME feature key functions during cancer development, progression, invasion, metastasis, immune suppression, and

immune escape, representing promising targets for therapeutic intervention.

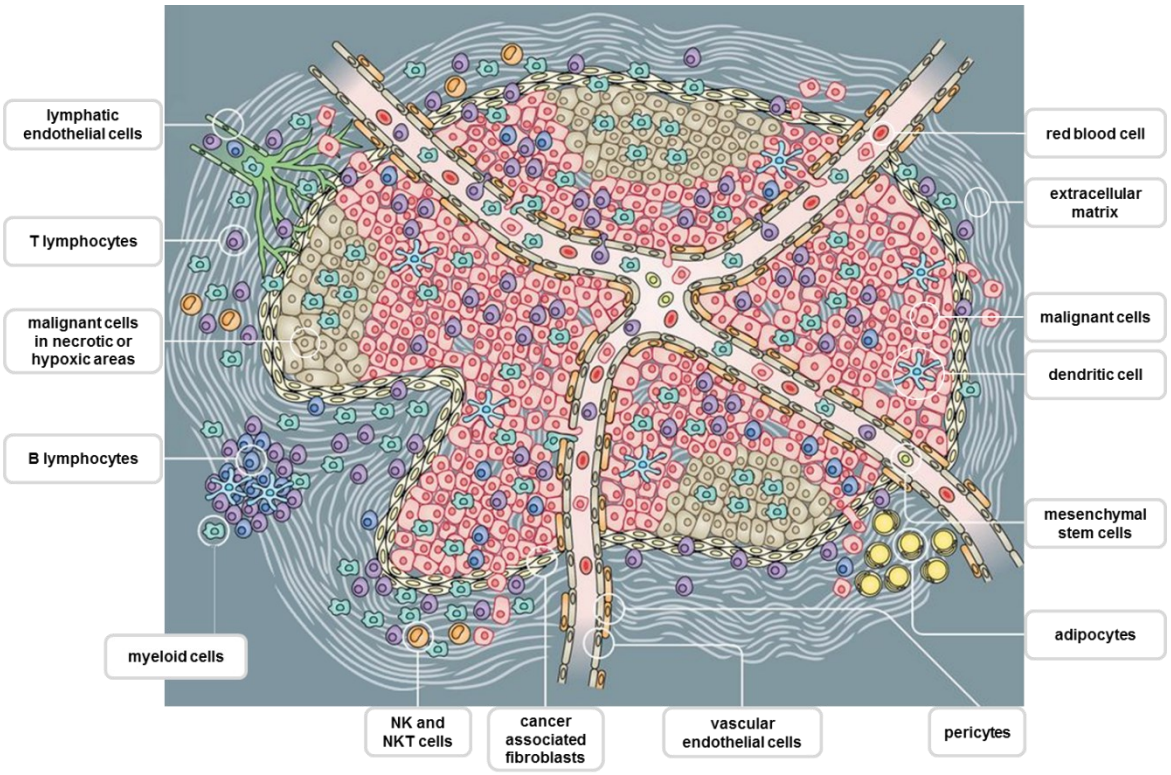

Figure 2: Cellular composition of the TME.

The TME is complex and heterogeneous in terms of its cellular composition. It consists of malignant cancer cells with different characteristics depending on the location within the tumor. Malignant cancer cells in necrotic or hypoxic regions differ substantially from malignant cells in well perfused tumor regions or at the invasive front of a tumor. Furthermore, several cell types and cytokines within the TME together with mutational evolution trigger clonal heterogeneity within the tumor. Neoangiogenesis ensures sufficient nutrient and oxygen supply of the tumor, with blood vessels consisting of endothelial cells and pericytes. Growth factors like VEGFC and VEGFD produced by cancer cells promote lymphangiogenesis pioneering LN metastasis. Cancer-associated fibroblasts (CAFs) are present in various cancers and promote cancer invasion as well as interfere with immune cells. The immune cell populations within tumors include T cells, B cells, NK and NKT cells as well as myeloid cells like TAMs, MDSCs, TANs and terminally differentiated myeloid DCs [4, 32-35]. Figure adopted from [32].

Tumors consist of malignant cells that constitute a heterogeneous population. Depending on the mutational evolution of cancer cells influenced by immune mediated clonal selection, distinct cancer cell clones evolve in certain tumor regions resulting in genetically diverse cancer cell subpopulations across the entire tumor [33, 36]. At the invasive front of tumors, cancer cells undergo a process termed epithelial-mesenchymal transition (EMT) and acquire a fibroblast-like

morphology resulting in cancer cell migration and metastasis [37]. Cancer stem-like cells (CSCs) represent a small population within the malignant tumor mass and are closely related to EMT. CSCs have self-renewal abilities that lead to tumor relapse [38], as they are considered to be a distinct cancer cell population. Beside cancer cell heterogeneity within a primary or metastatic tumor, the TME also consists of non-transformed cells like angiogenic vascular endothelial cells. Malignant tumor expansion is accompanied by induction of angiogenesis via VEGFA secreted by hypoxic cancer cells [39], FGFs and PDGFs [32, 40]. Angiogenic vasculature comprises endothelial cells and pericytes that form blood vessels and ensure sufficient oxygenation and nutrient supply of the malignant tumor [33]. Besides neoangiogenesis, cancer cells together with other cells in the TME trigger the formation of new lymphatic vessels by the secretion of VEGFC and VEGFD and thus enable metastasis towards the lymphatic system [41]. Another prevailing cell population within the TME represents cancer-associated fibroblasts (CAFs), which are the activated fibroblasts. The majority of CAFs express alpha smooth muscle actin (αSMA) or fibroblast activation protein (FAP) [34]. In contrast to quiescent fibroblasts, CAFs contribute to build-up non-cellular components of the TME including collagen, fibrin and other extracellular matrix (ECM) components [34]. The ECM is a physical scaffold that determines tumor stiffness, contains growth and angiogenic factors and is subject to remodeling by matrix metalloproteinases (MMPs) secreted by cancer cells, TAMs and CAFs [32]. Furthermore, CAFs directly or indirectly modulate the recruitment and mediate suppression of immune cells, which represent another non-transformed cellular component of the TME [34, 35]. Besides promoting cancer cell proliferation and angiogenesis, CAF derived IL-6 contributes to immune suppression by restricting DC maturation and promoting monocyte differentiation into macrophages [34]. Interestingly, CAFs express PD-L1 as well as PD-L2 and therefore may contribute to immune suppression of T cells [42]. The presence of immune cells within malignant tumors often determines response to a cancer immunotherapy. The TME comprises T cells, B cells, NK and NKT cells as well as myeloid cells like TAMs, MDSCs, tumor-associated neutrophils (TANs) and terminally differentiated myeloid DCs. The presence of these immune cells can either be tumor-promoting or tumor-suppressive. Whereas cytotoxic $CD8^+$ T cells, NK cells and M1 macrophages [4, 43] contribute to cancer immune control, M2 macrophages, mast

cells, neutrophils and T_{reg} cells might rather promote malignant tumor progression [4, 24, 25, 32].

The TME along with the TIME are subject to temporal and spatial dynamics in terms of their cellular as well as non-cellular composition that contributes to the hallmarks of cancer [4, 33]. Therefore, beside cancer cells, different components of the TME are considered as promising targets for therapeutic intervention. In recent years, tyrosine kinase inhibitors targeting VEGF signaling, the VEGF-neutralizing monoclonal antibody (mAb) bevacizumab as well as multiple immune checkpoint inhibitor therapies including anti-CTLA-4, anti-PD-1 and anti-PD-L1 mAb have therefore been developed, FDA approved and are nowadays in clinical use for various cancers types [40, 44, 45].

1.1.4 Malignant tumor metabolism, acidosis, and hypoxia in immune suppression

Cancer cells are characterized by a high metabolic turnover due to their enhanced proliferation rate. Rapid tumor progression results in inadequate vascularization, limited oxygen diffusion and poor perfusion in the context of high oxygen demand. Tumor hypoxia is defined by a partial oxygen pressure below 10 mm Hg O_2 [46-48]. Within the tumor mass, the degree of hypoxia and subsequently acidification of the TME varies. In response to hypoxia, the transcription factor hypoxia-inducible factor 1 alpha (HIF-1α) induces the expression of a set of genes that contribute to malignant tumor progression [49-51] such as GLUT1 [52], the lactate dehydrogenase-A (LDH-A) [53] and the monocarboxylate transporter 4 (MCT4), which is a lactate/H^+ symporter [54]. These hypoxia-inducible gene expression patterns increase the glycolytic flux and lead to an enhanced adenosine triphosphate (ATP) production and lactate export into the extracellular space. ATPase and kinase activity results in the production of H^+ ions, acidifying the TME [55]. Under deep hypoxia ATP hydrolysis mainly contributes to H^+ production, whereas lactate and H^+ are produced independently [46]. Accumulation of H^+ ions in the TME results in an extracellular pH (pH_e) between 6.5 to 7.0 whereas the intracellular pH (pH_i) slightly increases in cancer cells [56, 57]. In tumor regions of moderate hypoxia, glutamine (Gln), fatty acids (FA) and lactate feed the tricarboxylic acid (TCA) cycle and energy is generated by oxidative phosphorylation (OXPHOS) resulting in CO_2 production. The hypoxia induced carbonic anhydrase IX (CAIX) and carbonic anhydrase XII (CAXII) convert CO_2 in the presence of H_2O into HCO_3^- and H^+ and therefore contribute to the pH_e

acidification in tumor regions of moderate hypoxia [46, 58]. In well vascularized, well perfused, and therefore sufficiently oxygenated tumor regions, cancer cells generate ATP either by the Warburg effect or via full glycolysis followed by the TCA cycle and OXPHOS. In well vascularized tumor regions, H^+ ions are not trapped in the TME, but removed by blood vessels and therefore acidification of the TME is prevented (**Figure 3**) [46].

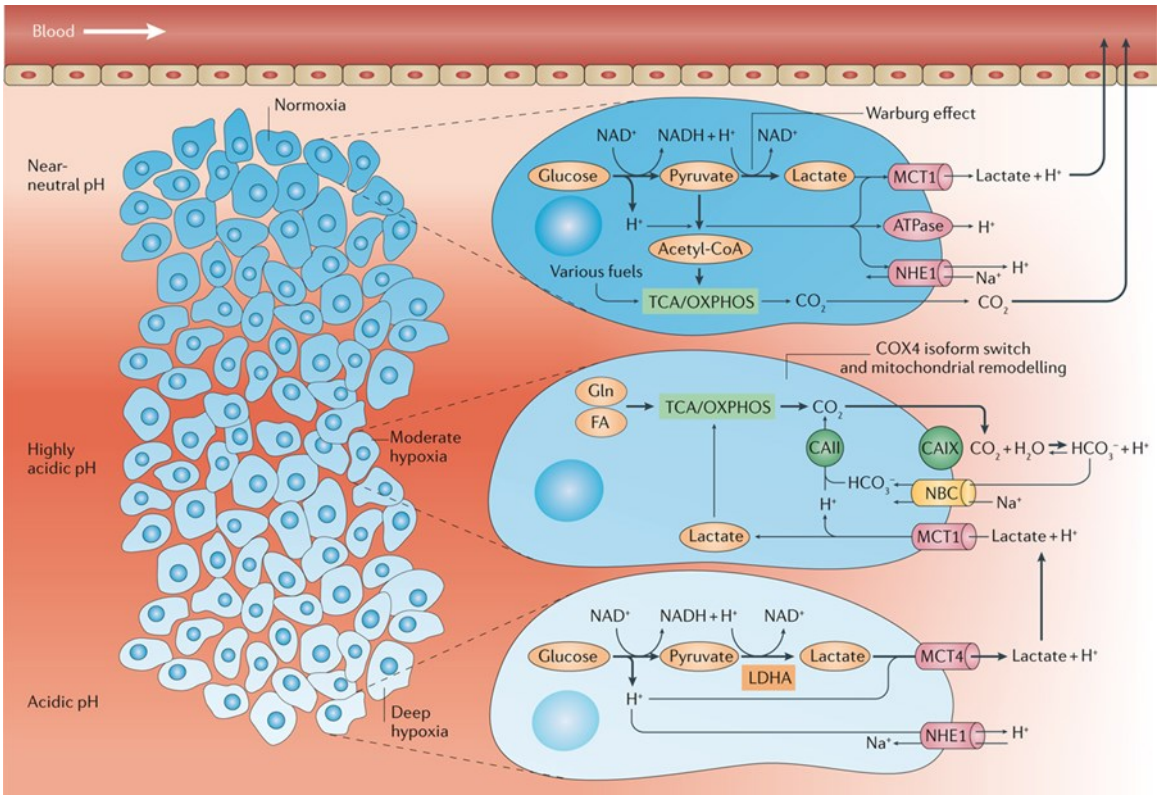

Figure 3: Relationship between tumor hypoxia and tumor acidosis development.
In well-perfused and vascularized normoxic tumor regions, glycolysis takes place and at the same time lactate as well as H^+ are generated and exported by cancer cells via MCT1 symporters. Furthermore, the H^+-ATPase and the Na^+/H^+ exchanger 1 (NHE1), a membrane-bound antiporter, largely discharge H^+ into the bloodstream resulting in near-neutral pH_e in these tumor areas. In regions more distant from blood vessels, characterized by moderate hypoxia Gln, FAs and lactate fuel the TCA cycle resulting in CO_2 generation by OXPHOS. Membrane diffused CO_2 is converted to H^+ and HCO_3^- via carbonic anhydrase IX (CAIX) leading to acidification of the tumor pH_e. The Na^+/HCO_3^- co-transporter NBC fuels intracellular HCO_3^- which is then converted into CO_2 by carbonic anhydrase II (CAII). Furthermore, MCT1 fuels intracellular lactate resulting in CO_2 generation via the TCA cycle and OXPHOS. Tumor regions of deep hypoxia are characterized by an acidic pH_e facilitated by the dependency on glycolysis and lactate as well as H^+ production and export into the extracellular space via MCT4. Furthermore, H^+ exported by NHE1 contributes to acidification of the TME [46]. Figure adapted from [46].

Accumulation of H^+ ions and subsequent acidification of the TME represents one of the main causes for cancer progression, invasion and metastatic spread, why substantial efforts are undertaken to counteract this phenomenon [46, 57, 59-62]. Genes induced by hypoxia or proteins involved in acidification of the TME are therefore studied as potential therapeutic targets. Amongst those, carbonic anhydrase inhibitors like imatinib (Gleevec®) [63] and nilotinib (Tasigna®) [64, 65] are in clinical use, whereas ATPase and MCT inhibitors like omeprazole (clinically approved for treatment of gastric ulcer gastritis) [66, 67] and AZD3965 [68-70] are currently applied in clinical oncology studies. Na^+/H^+ exchangers (NHEs) contribute to pH_e acidification by the export of ions. The drug amiloride which blocks the antiporter NHE1 is currently in experimental pre-clinical studies [71-73]. Another strategy to counteract acidification of the TME in moderate hypoxic tumor regions is to inhibit the Na^+/HCO_3^- co-transporter (NBC) and therefore prevent HCO_3^- titration of H^+ by the intracellular carbonic anhydrase II (CAII) [74, 75]. Treatment with sodium bicarbonate has been evaluated pre-clinically [76-78] as well as in a clinical phase 0/1 study [79, 80]. In pre-clinical tumor models, oral administration of sodium bicarbonate raised pH_e by increasing the buffer capacity of the tumor interstitial fluid and reversed the plasmalemmal pH gradient [81, 82]. Furthermore, sodium bicarbonate-treatment of mice resulted in an enhanced immune cell activity and reduced tumor volumes in selected tumor models [77, 83]. In contrast, oral or *i.v.* administration of sodium bicarbonate in humans slightly increased the blood pH_e, whereas the tissue pH_e remained unchanged [84].

Independent of the therapeutic strategy to counteract tumor acidosis, the role of immune cell recruitment, immune cell activation and/or polarization is essential for an efficient antitumor response. Pharmacological inhibition of MCT1 caused intracellular lactate accumulation and increased tumor immune cell infiltration [85]. Furthermore, sodium bicarbonate-treatment increased T cell activity [77]. Both studies are targeting tumor acidosis and thus highlight the interplay between tumor pH_e and the immune system [86]. Preventing acidification of the TME furthermore enhances the efficacy of immune checkpoint inhibitor therapies including anti-CTLA-4 and anti-PD-1 [77]. The effect of lactate and acidosis on immune cells ranges from immune cell inhibition to a pro-tumor polarization, depending on the immune cell population. Tumor acidosis results in a pro-tumoral phenotype of IL-4-driven M2 macrophages characterized by an increased expression of the

mannose receptor (CD206), arginase 1 and Reltna. Interestingly, buffering of the tumor pH_e *in vivo* by sodium bicarbonate-treatment resulted in a pro-inflammatory M1 phenotype of TAMs [83]. Apart from acidosis, lactate secreted by cancer cells induces differentiation of macrophages into a M2 phenotype [87, 88]. NK cell function, survival and cytotoxic anti-tumor activity are impaired by increased lactate levels and tumor acidosis, both lowering the expression of granzyme, perforin and Nkp46 [89, 90]. Inhibition of the IFN-γ secretion by NK cells because of an acidic and lactate rich environment can be restored in a neutral micromilieu [91]. In contrast, the inhibition of the cytotoxicity of NK cells is permanent and irreversible [91, 92]. Another immune cell population of interest are DCs, which present tumor antigens to T cells. Acidosis activates immature DCs, enhances the presentation of MHC class I-restricted antigens and thereby induces a $CD8^+$ T cell and B cell response [93]. Low pH_e furthermore enhances the differentiation of monocytes into DCs, which is driven by a reduction of mammalian target of rapamycin complex 1 (mTORC1) activity thereby contributing to an inflammatory reaction [94, 95]. In addition, T cell-mediated tumor immunity is significantly impaired at low pH_e. Elevated amounts of extracellular lactic acid impair T cell function and increase apoptosis via blocking MCT1-mediated lactate and ^+H export by cytotoxic $CD8^+$ T cells [96]. An acidic TME with elevated lactate levels further inhibits IL-2, TNF, IFN-γ, granzyme B and perforin secretion of immune cells and therefore attenuates T cell proliferation and cytotoxicity [86, 96, 97]. Acidosis-induced inhibition of IFN-γ production of T cells takes place at a post-transcriptional level and is reversible [77, 86].

In summary, tumor acidosis as well as lactate secretion by cancer cells significantly impair anti-tumor immune cell function and can even lead to a more pro-tumoral phenotype. Nevertheless, the effects of tumor acidosis on immune cells are mostly reversible and immune cell functions can be restored by buffering the pH_e and thus increases the efficacy of immune checkpoint inhibitor therapies.

1.2 Immune checkpoint inhibitors

1.2.1 Types and mechanisms of immune checkpoint inhibitors

The human immune system consists of several cell types that recognize and eliminate virally infected as well as neoplastic cells with abnormal cell growth. This process is commonly termed immune surveillance. Like checks and balances, a

principle of constitutional, tripartite governments, so called immune checkpoints keep the immune response against neoplastic cells under control. This mechanism is important to maintain self-tolerance as well as to fine tune and prevent excessive, life-threatening immune responses. Immune checkpoint proteins are generally grouped into co-stimulatory or inhibitory membrane-bound receptors or ligands as well as inhibitory metabolic enzymes [98]. The membrane bound immune checkpoints can either be targeted by agonistic or antagonistic antibodies. Activated T cells express OX40 (CD134), which transfers a co-stimulatory signal, resulting in an enhanced T cell division, survival and expansion of effector and memory subsets [99]. Amongst the most widely known inhibitory immune checkpoints are the cell surface proteins cytotoxic T-lymphocyte-associated protein 4 (CTLA-4, CD152), programmed death-1 (PD-1, CD279) and PD-L1 (CD274). The immune checkpoint CTLA-4 discovered by Allison and Bluestone [100-102] is exclusively expressed on T cells and regulates the early stages of activation, via outcompeting the T cell co-stimulatory receptor CD28 by binding to CD80 and CD86 [98, 103-105]. It unfolds its effect by down-regulating the T_h cell activity and mediates the development of forkhead box P3 (FOXP3) expressing T_{reg} cells [98, 106-108]. In contrast, PD-1 is expressed upon T cell activation and confers an inhibitory signal dampening T cell activity in peripheral tissue [98, 109]. Upon engagement of PD-1 with the ligands PD-L1 or PD-L2, it regulates effector T cell activity within the tumor by inhibition of kinases involved in T cell activation [98]. Upon continuous antigen exposure, like in tumors, membranous T cell PD-1 expression is induced, results in T cell exhaustion upon PD-1/PD-L1 interaction and finally leads to immune tolerance and tumor immune escape [98]. Ahmadzadeh *et al.* and others have shown that $CD8^+$ TILs with elevated PD-1 expression exhibit an exhausted and anergic phenotype with decreased cytokine production and poor clinical outcome [110, 111]. Similarly, PD-L1 expression is subject to intrinsic characteristics of cancer cells as well as various factors in the TME like hypoxia or IFN-γ. Beside cell surface immune checkpoints, metabolic enzymes also confer immune suppression. IDO expressed by cancer cells and tumor infiltrating myeloid cells catabolizes the essential amino acid tryptophan and thereby inhibit T cell proliferation and effector functions [112, 113]. Similarly, the inhibitory metabolic enzyme arginase suppresses T cell function via local depletion of the essential amino acid arginine [98, 114]. Beside the well described immune

checkpoint proteins, several others have been discovered in recent years including lymphocyte activation gene-3 (LAG-3, CD223), T cell immunoglobulin and mucin-domain containing-3 (TIM-3, CD366), T cell immunoglobulin and ITIM domain (TIGIT), V-domain Ig suppressor of T cell activation (VISTA), B7 homolog 3 protein (B7-H3) as well as B and T cell lymphocyte attenuator (BTLA).

Based on these basic research and pre-clinical studies, several mAb therapies have been developed and clinically tested in recent years. In 2011 the first candidate of immune checkpoint targeting drugs, ipilimumab a fully human anti-CTLA-4 mAb was FDA approved for the treatment of advanced malignant melanoma [115]. In the following years several drugs targeting the immune checkpoints CTLA-4, PD-1 and PD-1 received FDA approval [116] or are subject of clinical trials [117] for several tumor entities. Notably, in humans anti-CTLA-4 mAb therapies feature more severe immune toxicity including colitis, diarrhea, adrenal insufficiency, thyroiditis, and pneumonitis [45, 118] compared to anti-PD-1 or anti-PD-L1 mAb therapies [98, 119]. These side effects were anticipated by pre-clinical studies in CTLA-4 knockout mice experiencing massive lymphoproliferation and lethal systemic immune hyperactivation [120, 121]. In contrast, PD-L1 knockout mice are viable and exhibit comparable numbers of various immune cells in wild type and knockout mice [122]. Similarly, PD-1 deficient mice developed as wild type mice but exhibited an increased number of lymphoid and myeloid cells and moderate splenomegaly [123]. Although several immune checkpoint inhibitors have been approved by the FDA, clinical response rates vary depending on the tumor entity. For treatment of NSCLC patients with the PD-1 inhibiting mAb pembrolizumab, Garon *et al.* reported an objective response rate of 19.4% among all patients [124]. A phase III study in metastatic melanoma patients revealed an objective response rate of 57.6% upon combined treatment with the anti-PD-1 mAb nivolumab together with the anti-CTLA-4 mAb ipilimumab and revealed a significantly higher progression-free survival compared to ipilimumab monotherapy [125]. Limited response rates can be addressed and improved by identifying reliable biomarkers to predict response rates as well as counteracting resistance mechanisms to improve therapeutic responses. One of the biomarkers that predicts the efficacy of checkpoint inhibitor immunotherapy are immunogenic neoantigen peptides, which are generated by the tumor mutational burden [126]. In this regard Le *et al.* identified mismatch repair deficiency as a predictive

biomarker for response to an anti-PD-1 mAb therapy in solid tumors [127, 128]. In addition to cancer cell intrinsic response biomarkers, several studies focus on the composition of the TME, in terms of TILs and dynamics of immune checkpoint protein expression on the individual cell types [126]. The current FDA approved clinical diagnostic for an anti-PD-1 therapy patient stratification is the PD-L1 immunohistochemistry (IHC), although the total PD-L1 expression alone is an imperfect predictor of response [126].

The search for more predictive biomarkers highlights the role of resistance mechanisms to an immune checkpoint inhibitor therapy. Pardoll *et al.* distinguished two resistance mechanisms; the constitutive also named innate and the adaptive immune resistance. Whereas innate immune resistance occurs due to oncogenic pathways resulting in an increased immune checkpoint inhibitor expression on cancer cells, the adaptive immune resistance refers to the induction of immune checkpoint inhibitor expression in response to cytokines like IFN-γ in the TME [98]. In this regard, Havel *et al.* classified tumors into three tumor-immune phenotypes: 1) Immune-inflamed tumors are characterized by the $CD8^+$ and $CD4^+$ T cell presence and therefore exhibit a pre-existing anti-tumor immune response making them sensitive to an immune checkpoint inhibitory therapy; 2) Immune excluded tumors are characterized by the absence of T cells, which can be overcome by e.g. inhibition of transforming growth factor-β (TGF-β); 3) Immune desert tumors which completely lack T cells do not respond to an immune checkpoint inhibitor therapy [126].

This classification of the tumor immune phenotype together with the induction of immune checkpoint protein expression in particular of PD-L1 upon changes in the TME, currently represents the most promising approach to identify response biomarkers and to reveal the underlying mechanisms of acquired resistance. Therefore, a detailed understanding of the underlying mechanisms of PD-L1 expression and signaling is essential.

1.2.2 PD-L1 expression and signaling

In 1992 Tasuku Honjo discovered the checkpoint inhibitor molecule PD-1, preventing immune cell engagement and activity. For this breakthrough, he was awarded with the Nobel Prize in physiology in 2018 [129, 130]. A few years later Gordon J. Freeman and Tasuku Honjo identified the ligand of the PD-1 protein and named it PD-L1 [131-133]. Since then the research institutions and the

pharmaceutical industry have focused on the discovery and optimization of antibodies targeting these checkpoint inhibitor structures, resulting in the FDA approval of the first PD-1 inhibitor pembrolizumab (Keytruda®) in 2014 [44, 134] and the first PD-L1 inhibitor atezolizumab (Tecentriq®) in 2016 [135]. Despite the great success of immune checkpoint inhibitor therapies, the impact of PD-L1 expression and signaling for response prediction of an anti-PD-1/anti-PD-L1 mAb therapy remains vague.

Regulation of PD-L1 gene expression can be divided into cancer cell intrinsic and TME-mediated mechanisms. PD-L1 expression varies between tumor types due to their genetic and epigenetic characteristics. Amplification of the PD-L1 gene located on chromosome 9p24.1 increases PD-L1 expression in various cancers, including small-cell lung cancer (SCLC) [136] and gastric adenocarcinoma [137]. Furthermore, the extended 9p24.1 amplification region also induces the Janus kinase 2 (JAK2) loci in classical Hodgkin lymphomas (cHLs) and mediastinal large B-cell lymphoma (MLBCL) [138]. Amplification of JAK2 involved in IFN-γ-mediated PD-L1 induction enhances PD-L1 transcription [138-141]. Patients with amplification of the PD-L1 gene in NSCLC revealed a worse prognosis compared to patients without the PD-L1 amplification [139]. Epigenetically, expression of PD-L1 is inversely correlated with methylation of the PD-L1 promoter in various cancers, including advanced gastric cancer [142], malignant melanoma [143], NSCLC [144, 145] and prostate cancer [146]. Furthermore, PD-L1 expression is regulated by non-coding single-stranded microRNAs (miRNAs). Several miRNAs interfere with PD-L1 expression at different stages. For instance, the miRNA-197 represses the cyclin-dependent kinases regulatory subunit 1 (CKS1B)/ signal transducer and activator of transcription 3 (STAT3) axis, and its expression is inversely correlated with PD-L1 expression in NSCLC [147]. Further downstream, several miRNAs such as miRNA-513, miRNA-34a and miRNA-200 negatively regulate PD-L1 gene and protein expression by targeting the *Pd-l1* mRNA for degradation [148-154]. Besides genetic and epigenetic regulation, oncogenic signaling interferes with PD-L1 expression. Oncogenic Ras signaling through mitogen-activated protein kinase kinase (MEK) and the kinase MK2 leads to the phosphorylation and inhibition of the AU-rich element-binding protein tristetraprolin (TTP), a *Pd-l1* mRNA destabiliser, and subsequently increases tumor PD-L1 expression [155]. Murine lung cancers with mutant epidermal growth factor

receptor (EGFR) or mutant K-Ras demonstrated an increased activation of AKT/mammalian target of rapamycin (mTOR) and elevated PD-L1 expression [156]. Furthermore, the tumor suppressor gene phosphatase and tensin homolog (PTEN) negatively regulates PD-L1 expression and loss of PTEN results in increased PD-L1 levels [157, 158]. In summary genetic, epigenetic as well as oncogene induced perturbations of PD-L1 expression in cancer cells have been associated with fortunate as well as unfortunate prognosis [142, 146, 159].

In addition to cancer cell intrinsic factors, certain TME characteristics like hypoxia as well as several immune cells-derived cytokines regulate PD-L1 protein expression. Malignant tumors are characterized by rapid growth, insufficient vascularization and oxygen deprivation due to disturbed microcirculation and deterioration of diffusion [160]. Under low tissue oxygen levels, the transcription factor HIF-1α is stabilized and binds to the hypoxia-response element (HRE) in the PD-L1 proximal promoter region [161]. It has been shown that hypoxia controls PD-L1 expression in MDSCs, macrophages and DCs [161]. In addition, hypoxia induces PD-L1 expression in cancer cells, including B16-F10 and lewis lung carcinoma (LLC) [161, 162]. These molecular findings were further substantiated by positive correlations between HIF-1α and PD-L1 protein expression in tumors with infiltrated immune cells [163, 164]. Beside hypoxia, lactate accumulates in the TME due to the Warburg effect [16, 165]. Extracellular lactate represents a new inducer of PD-L1 expression in cancer cells, which occurs via the lactate sensing G protein-coupled receptor 81 (GPR81) [166]. In an experimental tumor model, blockage of LDH-A and thus inhibition of lactate production improved the efficacy of an anti-PD-1 mAb therapy [167]. Besides cancer cells, the TME consists of infiltrated immune cells that significantly contribute to the cytokine milieu. Amongst those, IFN-γ is probably the most prominent inducer of PD-L1 expression [30, 168] and is secreted by $CD8^+$ T cells, T_h1, NK cells and innate lymphoid cells (ILCs) [169-171]. IFN-γ is a type II interferon and binds to the interferon-gamma receptor (IFNGR) 1 and 2. Upon receptor heterodimerization, the receptor-associated JAKs get activated, which leads to tyrosine residue phosphorylation in the IFNGR cytoplasmic domain and to the recruitment and phosphorylation of STAT1 molecule. Phosphorylated STAT1 dimerizes and translocates to the nucleus, binds to its IFN-γ activation site (GAS) element in the promoter region and induces the expression of the interferon regulatory factor 1 (IRF1) [30, 170, 172-174]. Induction

of PD-L1 expression is furthermore dependent on the IFN-γ-mediated induction of STAT1 gene and protein expression. In this regard, the eukaryotic translation initiation complex (eIF4F) binds the 5' cap of *Stat1* mRNA and thereby increases the STAT1 as well as PD-L1 protein expression [30]. Induction of PD-L1 via the IFN-γ-JAK-eIF4F-STAT1-IRF1 axis is of paramount importance, as it combines several factors that contribute to immune escape. Therefore several scientists recently proposed a combined assessment of PD-L1 and TIL by IHC to account for TIME-induced PD-L1 expression [175-179]. This approach is promising, as it considers the immune cell activity in the TME. Several factors like tumor acidosis shape the composition of the TIME and interfere with T cell infiltration and activity [77, 86, 96, 180] as well as macrophage polarization [83]. In this regard, the detection of inducible PD-L1 protein expression by factors of the TME is one of the most promising approaches for an anti-PD-1/anti-PD-L1 mAb therapy response prediction.

Beside PD-L1 expression, signaling pathways upon PD-1/PD-L1 engagement are of great interest. Interaction of PD-1 with PD-L1 negatively regulates T cell activity by recruitment of the tyrosine phosphatase Src homology region 2 domain-containing phosphatase-2 (SHP2) to the intracellular domain of the PD-1 molecule [109, 132, 181, 182]. PD-1 inhibits T cell function by down-regulating intracellular TCR signaling pathways. Furthermore, it reduces activation of transcription factors responsible for T cell activation, proliferation cytokine production and survival [109]. Interruption of the PD-1 and PD-L1 interaction by blocking antibodies can successfully restore cancer cell-specific T cell cytotoxicity [183]. Expression of PD-L1 by cancer cells protects them from T cell-mediated cell death by interfering with pro-apoptotic signals or interfering with the activation of the AKT/mTOR pathway in T cells [184, 185].

1.3 Tumor models and characteristics

The interplay of the immune system with malignant cancer cells is fairly complex, bidirectional, dynamic and dependent on various cancer cell and host immune system specific factors. Amongst these factors are the cancer cell intrinsic genetic and epigenetic alterations that influence gene expression of immune checkpoint inhibitor molecules including PD-L1. Furthermore, different tumors exhibit unique metabolic characteristics that shape vascularization, hypoxia, and acidification of

the tumor. Furthermore, the immune system itself varies between humans and adds another degree of complexity towards response prediction to a checkpoint inhibitor therapy. The complex immune system and malignant tumor interplay, led to the advancement of the concept of immune surveillance towards immune editing taking into account the mutual and bidirectional interactions [186-188]. To address the complexity of tumor immune biology, several murine and human cancer cell lines with different origin as well as genetic and epigenetic characteristics were studied.

Colorectal cancer is one of the most commonly diagnosed cancers and a leading cause of cancer related death [189]. In 2020 the FDA approved the anti-PD-1 mAb pembrolizumab (Keytruda®) for first-line treatment of metastatic microsatellite instability-high (MSI-H) or mismatch repair deficient (dMMR) colorectal cancer [190]. Due to the similarity to human colorectal cancer, murine colon adenocarcinoma MC38^{wt} cells were used to study the interplay between the tumor and the immune system. Originally, MC38^{wt} cancer cells were generated in female C57BL/6 mice by *s.c.* injection of dimethylhydrazine. Then the mice developed adenocarcinomas, which were dissected and maintained as *s.c.* serial transplants. For cancer cell culture, adenocarcinomas were trypsinized and maintained in cell culture dishes [191-193]. Efremova *et at.* characterized the genome and transcriptome of MC38^{wt} cancer cells *in vitro* as well as the transcriptome and immune cell composition of solid MC38^{wt} tumors [194]. These studies revealed that MC38^{wt} tumors are a model for hypermutated/MSI colorectal cancer, resembling grade III adenocarcinomas. A genome analysis revealed in total 5931 somatic mutations, including the transversion C>A/G>T similar to human hypermutated colorectal cancer [194, 195]. Furthermore, MC38^{wt} tumors carry missense mutations in p53 and PTEN, mutations in the TGF-β pathway and in the BRAF gene [194]. The tumor model is considered to be fairly immunogenic qualifying it as an ideal responder model for anticancer immunotherapy studies [196, 197]. Nevertheless, when transplanted into immune competent wild type C57BL/6 mice, the host immune system failed to eradicate the MC38^{wt} tumor due to immunosuppressive cells which are recruited to the tumor site. MC38^{wt} tumors are characterized by infiltration of CD8$^+$ T cells, NK cells and classically activated M1 macrophages [194, 196]. Hos *et al.* reported a strong CD8$^+$ T cell response towards neoepitopes in MC38^{wt} tumors [198]. A strong CD8$^+$ T cell infiltration was

furthermore correlated with a better prognosis and a superior checkpoint inhibitor therapy outcome in hypermutated/MSI colorectal cancer, which is most likely attributed to the high number of neoantigens [199]. Efremova *et at.* also studied the impact of immune cell recruitment and infiltration on gene expression induction of selected immune checkpoint proteins. During the course of $MC38^{wt}$ tumor development and progression in immune competent mice, the expression of PD-1, CTLA-4, TIM-3 and LAG-3 was up-regulated [194]. The immune compromised, recombinant activating gene 2 (RAG2)-deficient mice, which lack mature T cells and B cells [200], exhibit only a marginal upregulation of PD-L1. In contrast to RAG2-deficient mice, $MC38^{wt}$ tumors transplanted into immune competent mice exhibit a more pronounced induction of PD-L1 gene expression [194]. This underlines the interplay between immune cell infiltration, cytokine secretion and immune checkpoint protein expression on cancer cells. $MC38^{wt}$ cancer cell exposure to IFN-γ secreted by different immune cells results in PD-L1 upregulation, which might be sufficient for tumor immune escape [30, 172, 201, 202]. These findings suggest an important role of PD-L1 induction and immune escape upon cancer-immune cell interaction. In contrast to $MC38^{wt}$ cells, $CT26^{wt}$ cancer cells are the murine counterpart of human non-hypermutated/MSI colorectal cancer [194]. $CT26^{wt}$ cells were generated by intrarectal administration of N-nitroso-N-methylurethane in BALB/c mice. Animals subsequently developed grade IV carcinomas that were maintained by serial *s.c.* transplantation [203]. The adenocarcinomas carry an oncogenic K-Ras [204] and adenomatous polyposis coli (APC) mutation [205], whereas p53 is not mutated [206]. The $CT26^{wt}$ cell line also bears somatic mutations, predominantly C>T/G>A similar to human non-hypermutated/MSI colorectal cancer and is characterized by high N-Ras, VEGF-α, p53, Myc, Mdm2 and HIF-α expression levels [207]. Interestingly, $MC38^{wt}$ and $CT26^{wt}$ cells, both generated from carcinogen induced murine colorectal carcinomas exhibited a high somatic nonsynonymous mutational burden [206]. Similar to $MC38^{wt}$, $CT26^{wt}$ cells are also commonly applied in immune checkpoint inhibitor studies, as the resulting tumors respond to a wide range of immune checkpoint inhibitor mAb therapies including anti-CTLA-4, anti-PD-1 and anti-PD-L1 [196, 206, 208].

In tumor biology, genetic modifications of cells applying the CRISP/Cas 9 technology are used to study the underlying mechanisms of immunological

surveillance and immune editing. The CRISP/Cas system was initially discovered and described as the adaptive immune system in vertebrates [209] and was awarded with the Nobel Prize in Chemistry in 2020 [210]. The technology was subsequently further refined to permanently knockout genes of interest in cancer cell lines. In this regard the CRISP/Cas 9 technology was e.g. applied by Kleinovink *et al.* to study the role of PD-L1 cancer cell expression for an anti-PD-L1 mAb therapy [196].

Amongst other human cell lines applied in this work, the human colon adenocarcinoma cell line HCA-7 colony 29 was chosen for in depth mechanistic studies, as it belongs to the identical tumor type as murine MC38^{wt} and CT26^{wt} cells. The HCA-7 cell line was established from a primary human colon adenocarcinoma of a 58-year old female [211, 212]. Colony 29 of the HCA-7 cell line is characterized by expression of the cyclooxygenase 2 (COX-2) [213] and also carries a p53 mutation [214]. Furthermore, Botti *et al.* reported a correlation between COX-2 and PD-L1 expression in human primary malignant melanomas [215]. Beside this correlation, inhibition of COX-2 reduced PD-L1 expression in melanoma cell lines [215]. Prima *et al.* proposed that inhibition of the bioactive lipid prostaglandin E_2 (PGE_2) forming enzyme COX-2 represents a promising approach to interfere with PD-L1 upregulation on macrophages and MDSCs in order to overcome immune evasion [216]. Therefore, HCA-7 colony 29 cells are an interesting human cancer cell model to study regulatory mechanisms of PD-L1 expression.

In contrast to MC38^{wt} and CT26^{wt} tumors, both responsive to anti-PD-1 and/or anti-PD-L1 mAb checkpoint inhibitor therapies [196, 206, 208, 217], B16-F10^{wt} and 4T1^{wt} tumors are classified as non-responsive or partially responsive [206, 217, 218]. B16-F10^{wt} is a murine malignant melanoma cell line derived from C57BL/6 mice harboring a BRAF mutation [219-221]. B16-F10 cells exhibit elevated levels of proteases and glycosidases compared to B16-F1 cells [222]. In contrast, the mammary carcinoma 4T1^{wt} cell line was generated from a spontaneously arising tumor in female BALB/BfC3H mice [223, 224]. 4T1^{wt} tumors are characterized by a high tumorigenicity and invasiveness [225]. Mosely *et al.* performed transcriptome analysis of tumors established in syngeneic mice to elucidate the differential responsiveness to an immune checkpoint inhibitor therapy in the four mentioned syngeneic murine tumor models. For the anti-PD-L1 mAb therapy

responsive MC38^{wt} tumor model, the authors reported low expression of genes involved in the MHC II pathway and a considerable tumor immune cell infiltrate consisting mainly of monocytic MDSCs (M-MDSCs), but also NK cells, NKT cells, macrophages and T cells [206]. CT26^{wt} tumors were characterized by elevated numbers of NK cells, granzyme B^{+} NK cells and T cells. The relative number of T cells in CT26^{wt} tumors was most pronounced amongst the four studied exogenous tumor models [206]. MC38^{wt} as well as CT26^{wt} tumors were also characterized by a strongly enhanced pro-inflammatory cytokine expression profile, including IL-2, IFN-γ, TNF and IL-1β [206]. In contrast to the responsive tumor models, Mosely *et al.* reported a moderate immune cell infiltration, a reduced activation of immune pathways accompanied by lower expression of MHC class I and II pathway genes for the non-responsive B16-F10^{wt} tumor model [206]. The anti-PD-L1 mAb therapy non-responsive 4T1^{wt} tumor model is characterized by a pronounced granulocytic MDSC (G-MDSC) infiltrate [206]. In addition, cytokine analysis revealed elevated levels of T_h2-associated cytokines, including IL-4 and IL-10 in B16-F10^{wt}, 4T1^{wt} and surprisingly also MC38^{wt} tumors [206]. These studies impressively illustrate the role of cancer cell intrinsic and host immune system specific characteristics. Furthermore, the authors outline the role of immune cell recruitment, infiltration, cytokine secretion and the induction of checkpoint inhibitor proteins on cancer as well as immune cells for immune evasion. According to literature, the two described murine tumor models MC38^{wt} and CT26^{wt} are therefore assigned to the anti-PD-L1 mAb therapy responsive group with strong endogenous anti-tumor immune response. In contrast, B16-F10^{wt} and 4T1^{wt} tumors were classified as non-responsive due to a weak endogenous anti-tumor immune response (**Figure 4**).

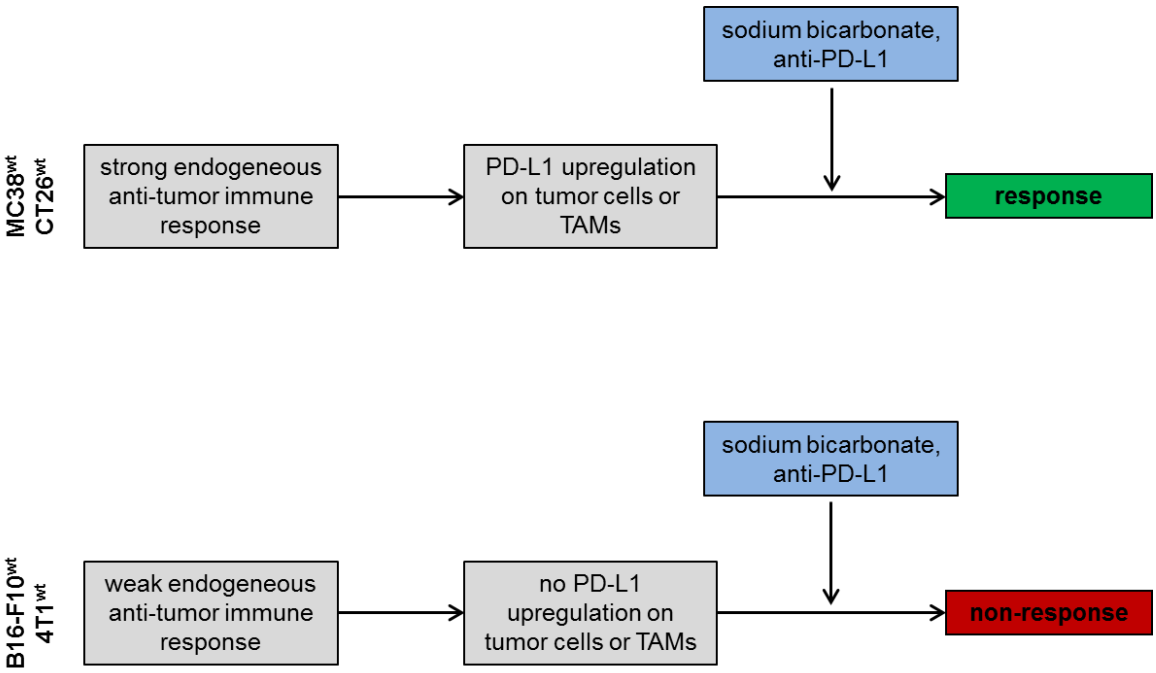

Figure 4: Implications of adaptive immune resistance on cancer immunotherapy.
Proposed impact of the endogenous anti-tumor immune response and the TME-induced PD-L1 upregulation on cancer and immune cells and the discrimination in responders and non-responders to a sodium bicarbonate or immune checkpoint inhibitor anti-PD-L1 mAb therapy in the mentioned tumor models. MC38^{wt} and CT26^{wt} are considered as anti-PD-L1 mAb therapy responder, whereas B16-F10^{wt} and 4T1^{wt} are considered as non-responder tumor models to an anti-PD-L1 mAb therapy. Schematic representation adapted from [98].

To address the complexity of the host immune system and its impact on the efficacy of immune checkpoint inhibitor therapies, different mouse strains varying in their immune cell composition and polarization were applied in this thesis. The mouse strains differ in their cytokine profiles and T_h cell polarization. *In vivo* MC38^{wt} and B16-F10^{wt} tumor studies were carried out in C57BL/6J mice, which endogenously promote a T_h1 cells polarization, characterized by elevated IFN-γ , IL-12 and TNF levels as well as low IL-4 and IL-13 production by CD4$^+$ T cells [226, 227]. *In vivo* CT26^{wt} and 4T1^{wt} tumor studies were carried out in BALB/c mice which are rather T_h2 prone and characterized by increased IL-4 cytokine expression levels [226, 228]. This allows gaining a more holistic picture on TME-induced cancer cell PD-L1 expression, independent of the applied mouse strain.

In summary, the four mentioned tumor models and the two mouse strains allow studying the conserved underlying mechanisms of PD-L1 regulation as wells as the cancer-immune cell interplay within the TME.

1.4 Cancer Senescence

Recent findings underline the importance of senescence for tumor immune control, rendering the induction of senescence a promising biomarker for response that can be detected by non-invasive *in vivo* imaging.

1.4.1 Definition of senescence

Cellular senescence is defined as a non-growing state of cells, characterized by a stable and permanent cell cycle arrest and non-response to growth and proliferation signals [229, 230]. Cellular senescence was first described by Leonard Hayflick and Paul Moorhead in 1961 and initially named replicative senescence [230-232]. Cell cycle progression is halted in senescent cells by increased expression of $p16^{INK4A}$ (hereinafter p16) and $p21^{Cip1}$ (hereinafter p21) that inhibit the tightly regulated activity of cyclin-dependent kinases (CDKs), imposing a non-growing, senescent cell state [230, 233, 234]. P53, a tumor suppressor, also plays an important role in senescence, as demonstrated by a murine liver carcinoma model with controlled p53 expression, which forces cancer cells into an irreversible senescent state upon re-activation [230, 235, 236]. Senescent cells are characterized and identified by the absence of proliferative markers, the expression of tumor suppressor proteins like p53 and cell cycle inhibitors, including p16 and p21 [230, 237]. Further, senescent cells exhibit an increased senescence-associated β-galactosidase (SA-β-GAL) activity [230, 237].

1.4.2 Types of senescence and immune control

Cellular senescence can be divided, based on their underlying induction mechanisms in: 1) replicative senescence, which is characterized by a proliferation arrest due to telomere shortening [238]; 2) stress-induced senescence upon exposure to reactive oxygen species (ROS) and subsequent DNA damage [239]; and 3) oncogene-induced senescence, like Ras [240]. Radiotherapy and chemotherapy can also induce cancer cell senescence by increasing genomic instability, inducing DNA damage, interfering with DNA synthesis or inhibiting topoisomerase I activity [241-243]. Cellular cancer immunotherapy with tumor-antigen specific T_h1 cells arrests cancer growth via induction of cancer cell senescence upon conjoint IFN-γ and TNF signaling [244]. The different types of senescence induction are commonly summarized as therapy-induced senescence and result in a tumor growth arrest [245, 246].

Senescence induction in cancer cells leads to a cell cycle arrest, limiting tumor growth and therefore representing a tumor-antagonizing effect. But beside the absence of proliferation, senescent cells also possess a specific senescence associated secretory phenotype (SASP) that shapes the local cytokine and chemokine microenvironment and triggers autocrine and paracrine signaling in adjacent cancer as well as stromal cells. In this context, senescence can also elicit a tumor-promoting effect [245]. Some examples include oncogene-induced senescent cells secreting pro-inflammatory cytokines, including IL-6 and IL-8 [247]. In human fibrosarcoma HT1080 cells these cytokines synergistically enhance cell migration [248]. Similarly, in papillary thyroid carcinoma the chemokine C-X-C motif chemokine ligand 12 (CXCL12) secreted by senescent cancer cells governs a collective invasion [249]. Furthermore, MMP-3 secreted by senescent cells exhibits a tumor-promoting effect on pre-malignant epithelial cells through paracrine signaling [246]. In contrast to tumor-promotion, the SASP also mediates senescent cancer cell clearance by macrophages, neutrophils, NK cells [250] and, in some tumor models, by $CD4^+$ T_h cells [251]. In an H-Ras driven liver carcinoma mouse model, p53 restoration induces senescence, NK cell recruitment and subsequent tumor regression, which is mediated by the secretion of chemokines such as C-C motif chemokine 2 (CCL2) [235, 250]. Other immune supportive factors of the SASP include IL-6, IL-15, CXCL1 and colony- stimulating factor 1 (CSF1) [252]. In contrast, cytokines that constitute the SASP can also exhibit immune suppressive functions by recruiting MDSCs and T_{reg} cells or by inhibition of cytotoxic $CD8^+$ T cells. These SASP related cytokines include CCL2, IL-6, granulocyte–macrophage colony-stimulating factor (GM-CSF), M-CSF or IL-10 [252].

Due to the dual role of senescence on tumors and the immune modulatory effect of the SASP, therapeutic compounds have been developed to eliminate senescent cancer cells. One of these so called senolytic drugs is navitoclax, a Bcl-2 inhibitor targeting exclusively senescent cells [253, 254]. To precisely treat patients with senolytic drugs and to avoid the negative effects of senescent cells on tumor growth and progression, non-invasive *in vivo* imaging biomarkers are needed to identify senescent cancer cells.

1.4.3 Metabolism and senescence

Although senescent cells have irreversibly lost the ability to proliferate, they remain

metabolically active [230]. Metabolic alterations of senescent cells were closely linked to the SASP. Nacarelli *et al.* reported that nicotinamide phosphoribosyltransferase (NAMPT) regulation of nicotinamide adenine dinucleotide (NAD^+) biosynthesis regulates the pro-inflammatory SASP of senescent cells, including the expression of IL-1β, IL-6 and IL-8 [255]. During senescence, high mobility group A (HMGA) proteins regulate the expression of NAMPT and the strength of the pro-inflammatory SASP is governed via the HMGA-NAMPT-NAD^+-signaling pathway. This pathway enhances glycolysis and mitochondrial respiration, which is promoting cancer progression and increasing T cell (CD3) and macrophage (F4/80) infiltration [255]. Others described metabolic alterations during senescence in human lung fibroblasts include a decreased ratio of O-phosphocholine (PC) to sn-Glycero-3-phosphocholine (GPC) [256, 257]. This is important because cancer cells often exhibit altered choline metabolism, depicting increased PC and total choline-containing phospholipid metabolites compared to GPC [258, 259]. However, the mechanisms behind these changes are very different. In cancer, these metabolic alterations are due to an increased phosphatidylcholine (PtCho) catabolism and choline uptake [260]. In senescent cells, the increased GPC levels are most likely due to the elevated breakdown of PtCho by phospholipase A_1 and/or A_2 and lysophospholipase (**Figure 5**) [256]. Decreased PC and increased GPC levels were also described in two breast cancer cell lines upon drug-induced senescence [261].

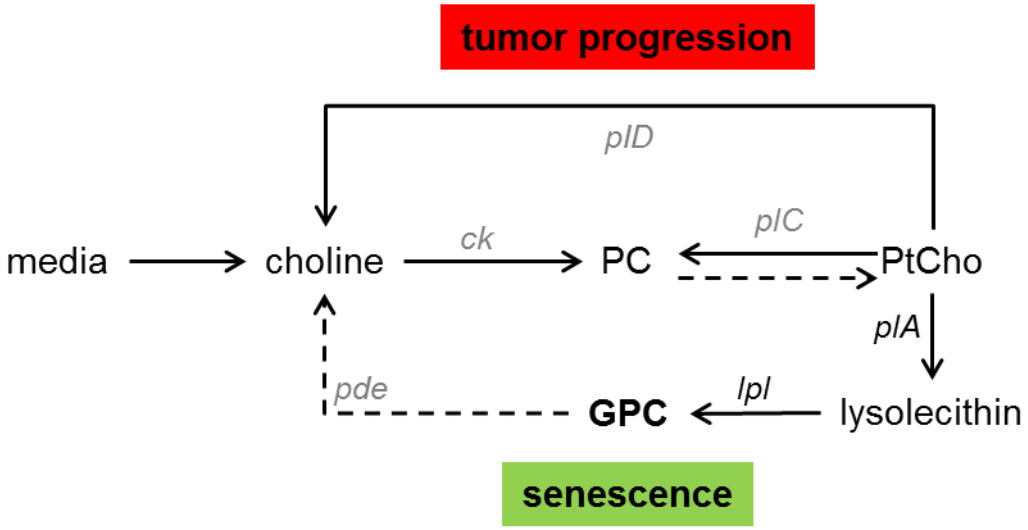

Figure 5: Schematic representation of the choline metabolism in cancer and senescent cells.

During tumor progression, proliferating cancer cells are characterized by increased O-phosphocholine (PC) and reduced sn-Glycero-3-phosphocholine (GPC) levels. Elevated PC levels are fueled by increased choline uptake from the cell culture media and conversion into PC by choline kinase (ck) as well as increased phosphatidylcholine (PtCho) catabolism catalyzed by phospholipase C (plC) and phospholipase D (plD). Senescent cells are characterized by elevated GPC levels mediated by increased activity of phospholipase A (plA) and lysosphospholipase lpl and reduced glycerophosphocholine phosphodiesterase (pde) [256, 260]. Schematic representation adapted from [256].

Beside changes in choline metabolism (**Figure 5**) senescence is also associated with major alterations in lipid metabolism. In human HepG2 cells, senescence induction was accompanied by an accumulation of lipids [262]. A lipidomic study combined with a transcriptomic analysis of proliferating and senescent fibroblasts revealed changes in lipid-regulating gene expression and abundance of certain lipid families [263].

As a result, senescent cancer cells will have a specific metabolic signature that could be used as a biomarker for identification of senescent tumor regions non-invasively *in vivo* by magnetic resonance spectroscopy (MRS).

1.5 Imaging and spectroscopy technologies

Malignant tumor progression, the heterogeneity of the TME and cancer metastasis can only be addressed and studied longitudinally by non-invasive *in vivo* imaging methods. Furthermore, spectroscopy technologies allow monitoring of metabolic alterations that are specific for certain tumor types or progression stages.

Therefore, several modalities are applied pre-clinically and clinically, including Optical Imaging (OI), Positron Emission Tomography (PET) and Nuclear Magnetic Resonance (NMR) imaging and spectroscopy.

1.5.1 Optical Imaging

Optical Imaging (OI) is a powerful technology to study dynamic cellular processes, cell-cell interactions, and dynamic changes in the TME. Macroscopic OI is characterized by an imaging depth greater than a few hundred microns up to several centimeters for near-infrared (NIR) imaging [264].

For macroscopic optical contrast three major modalities are described based on the contrast generation method: fluorescence, luminescence and photoacoustic imaging [264, 265]. Fluorescence and luminescence imaging are based on light emission, resulting from light absorbance and electron excitation or spontaneous photon emission respectively [264, 266]. For fluorescent imaging various fluorescent proteins are used pre-clinically including green fluorescent protein (GFP) and tandem dimer Tomato (tdTomato), a red shifted fluorescent protein allowing for imaging a greater depth with inducible or constitutive expression in cells of interest [266, 267]. Furthermore, small fluorophores like indocyanine green (ICG) are commonly used [268]. In fluorescent imaging, the sample is excited by an illumination light source at a wavelength close to the excitation maximum of the fluorophore absorbance spectrum [265, 266, 269]. Following an excitation/de-excitation process, photons are emitted, albeit at a higher wavelength (with a lower energy) by the fluorophore [265, 266]. The emitted photons are then collected by a cooled charge-coupled device (CCD) camera for photon counting. The use of appropriate filters is important to obtain an image with low noise and high contrast [269, 270]. Classically, *in vivo* fluorescence imaging is performed using a planar approach with either trans- or epi-illumination (such as in an IVIS®), although tomographic systems have appeared in the last decade and provided a new 3D view of the fluorophore distribution in the sample. Therefore, the volume of interest (VOI) *in vivo* is reconstructed and therefore provides spatially resolved images [271, 272]. The advantage of 3D OI is that information about the emitted photon distribution within the tissue can be obtained [272, 273]. Therefore, this approach might lead to a more quantitative OI, which was already applied in a clinical setting for human breast imaging using ICG as a contrast agent [268]. A major disadvantage of fluorescence imaging is auto- or non-specific fluorescence by

animal tissue including skin, which reduces the signal to background ratio [265]. This limitation can be overcome by multispectral imaging and dedicated analysis tools, further enabling the simultaneous use of multiple fluorophores [274]. Besides fluorescence imaging, bioluminescence imaging (BLI) is commonly applied in pre-clinical imaging to study regulation of gene expression [275, 276] or detect the activity of enzymes [277]. The principle of BLI is based on an enzymatic reaction catalyzed by a luciferase originating amongst others from the North American firefly (*Photinus pyralis*) with a size of approximately 61 kDa [265, 278, 279]. In nature, bioluminescence is used for communication and signaling in courtship of certain insects [280]. Upon cloning of the luciferase gene into vectors, it was accessible for reporter gene studies *in vitro* as well as *in vivo*. The firefly luciferase converts D-luciferin in the presence of oxygen, ATP and Mg^{2+} into oxyluciferin, adenosine monophosphate (AMP) and CO_2. In this enzymatic reaction, photons of yellow to green light (550-570 nm) are emitted, which are then detected by a CCD camera in an IVIS® system [281]. The conversion of D-luciferin to oxyluciferin by the firefly luciferase is dependent on the pH and the polarity of the solvent [265, 277]. In contrast to fluorescence imaging, BLI is commonly characterized by the absence of auto-bioluminescence, as only certain cells express the luciferase, resulting in a higher signal to background ratio [265].

Pure optical contrast imaging has several limitations including light absorbance of tissue, due to hemoglobin, melanin and fat, which strongly reduces the intensity of the emitted light in a depth-dependent manner [265, 266, 282]. Shifting fluorophore excitation and emission wavelengths to the near infra-red increases the *in vivo* imaging detection depth from a few hundred microns to several centimeters and decreases tissue absorbance [264]. Another limitation is scattering effects of photons yielding in a resolution loss [264, 266]. Together these limitations result in a low resolution and imaging depth.

The third modality, optoacoustic or photoacoustic imaging is based on light absorption and subsequent sound emission, also known as the photoacoustic effect [265]. Photoacoustic imaging overcomes the scattering effects with only a marginal loss in signal to background ratio at increased penetration depth, conserving resolution performance several centimeters deep in tissue [265]. Furthermore, photoacoustic tomography allows the reconstruction of 3D images and provides information on the distribution of the optical energy absorption within

the tissue of interest [283, 284]. Briefly, tissue is exposed to a laser pulse leading to a temperature increase and therefore thermodynamic expansion, which causes the emission of pressure waves in the MHz range. The generated ultrasound waves are then recorded by a wideband ultrasonic transducer and images are 3D reconstructed [285].

Taken together, OI is a straightforward, cost- and time-effective technology and most of the contrast and imaging agents applied exhibit no or only low systemic or local toxicity [286]. Nevertheless, on a macroscopic level, the induction of *Luciferase* gene expression upon tumor hypoxia can be longitudinally monitored by whole-body non-invasive *in vivo* OI [267, 275]. Furthermore, cell migration dynamics and the homing sites of fluorescently labeled T cells or MDSCs are studied [287, 288]. When cancer cells stably express the gene luciferase, OI can be applied for longitudinal monitoring of the tumor burden [289]. On a microscopic level, OI is applied to study tumor growth dynamics, therapy response, cell division, apoptosis, cell-cell interactions or cell invasion by intravital microscopy [290-293].

1.5.2 Positron Emission Tomography

With the development of Positron Emission Tomography (PET) systems by Michael E. Phelps, Michael Ter-Pogossian and Edward J. Hoffman [294, 295] in 1975, the field of nuclear imaging rapidly developed and found its way into the clinical diagnostic routine with [^{18}F]FDG being the most commonly applied radiotracer utilized for oncological applications. In contrast to other imaging technologies, PET is characterized by a very high detection sensitivity in the picomolar range and allows longitudinal acquisitions of high-resolution spatial and temporal *in vivo* radiotracer biodistribution in a single imaging subject [296].

The basic underlying feature of PET imaging is the decay of positron-emitting radionuclides, including ^{18}F, ^{64}Cu and ^{89}Zr [297]. The positron emitting radionuclides differ in their half-life, which determines their suitability for tracing certain biomarkers or pathways. The most commonly applied tracer [^{18}F]FDG, based on the isotope ^{18}F, has a half-life of 109.8 min [296]. [^{18}F]FDG is a glucose analog and is widely applied in oncology, as cancer cells, characterized by an enhanced glucose metabolism, exhibit elevated GLUT1 expression levels and therefore an enhanced [^{18}F]FDG uptake. The radiotracer is phosphorylated by the hexokinase and thereby trapped within cells of high energy demand, leading to an increased [^{18}F]FDG accumulation detectable by PET imaging [298]. Following the

decay of the isotope ^{18}F, a positron is emitted from the nucleus of a radionuclide and travels until it reaches an electron within the nearby tissue and undergoes an annihilation reaction, resulting in the emission of two γ-rays with an energy of 511 keV [296]. A ring of position-sensitive scintillation crystal detectors around the imaging subject subsequently registers the two γ-rays generated and released in the opposite direction at approximately 180 degree angle, which is also referred to as line of response [296, 299]. Within the scintillation detector, the γ-rays release energy under emission of visible light, which is collected by a photomultiplier tube, converted into electrons and the resulting electrical signal is amplified and processed [296]. The simultaneous detection of the two photons right opposite of each other by a detector in a ring PET scanner is also named “coincidence”. Upon reconstruction, it allows localization of the positron emitting radiotracer accumulation site within the imaging subject [299]. Since the first [^{18}F]FDG-PET studies in the early 1980s [300, 301], the interest for the development of new radionuclide tracers as well as the production of new radioisotopes has increased ever since.

When combined with MRI or X-ray computed tomography (CT) the PET image can be overlaid with the MRI or CT image to obtain additional anatomical information about the exact localization of the radiotracer uptake *in vivo*. In 2008, Judenhofer *et al.* reported the development of the first simultaneous small-animal three-dimensional PET/MRI scanner [302, 303]. Combined PET/MRI allows to obtain functional and anatomical information at the same physiological state and combines the benefits of both modalities, i.e. the high sensitivity of PET for biomarker tracking with the high soft-tissue contrast, as well as functional information provided by MRI [302]. High field MRI for pre-clinical studies is of paramount importance, as it increases spatial resolution or decreases acquisition time resulting in a higher signal to noise ratio in comparison to low-field pre-clinical MRI [304]. Combined PET/MRI measurements can be utilized to image and study tumor metabolism, heterogeneity as well as certain characteristics of the TME. In this regard, PET tracers, including [^{18}F]fluoromisonidazole ([^{18}F]FMISO) and [^{18}F]fluoroazomycinarabinoside ([^{18}F]FAZA) were applied to detect hypoxia non-invasively *in vivo* [305, 306]. In the context of immune oncology, T cell imaging with $CD4^+$ or $CD8^+$ specific antibody fragments of different size was implemented for PET imaging [307-309]. Kristensen *et al.* studied different pre-clinical tumor

models and found that PET imaging of TILs can serve as a prognostic biomarker to predict response to an anti-PD-1 mAb therapy [309]. Notably, several studies suggest a combined assessment of PD-L1 and TILs by IHC to monitor PD-L1 expression within the TIME [175, 176]. Therefore, visualization of PD-L1 together with TIL expression patterns within the tumor is considered to be a promising biomarker to forecast response to an immune checkpoint inhibitor therapy [177]. In NSCLC patients, Niemeijer *et al.* performed quantitative PD-1 and PD-L1 PET imaging focusing on the lung and reported heterogeneous radiotracer up-take signatures between patients and across tumor lesions [310]. Similarly, Stutvoet *et al.* were able to discriminate different PD-L1 expression levels in pre-clinical tumor models [311]. Therefore, combined PET/MRI or PET/CT are synergizing imaging modalities to characterize the TME in terms of hypoxia or immune cell composition as well as immune checkpoint inhibitor expression patterns non-invasively and longitudinally *in vivo*. Multimodal PET/MRI and PET/CT imaging represents a promising tool for patient stratification for immune checkpoint inhibitor therapies.

Furthermore, [^{18}F]FDG has been widely applied to detect TDLN as well as lymphogenic metastatic spread [312, 313]. In this regard, within this thesis [^{18}F]FDG-PET/MRI was applied to combine functional and anatomical TDLN imaging in an experimental MC38^{wt} murine colon adenocarcinoma model.

1.5.3 Nuclear Magnetic Resonance imaging and spectroscopy

The Nuclear Magnetic Resonance (NMR) phenomenon is a quantum mechanical resonant effect that appears when a magnetic dipole is placed in a strong static magnetic field and is perturbed by an oscillating electromagnetic field [264]. Discovered independently by Felix Bloch [314] and Edward Purcell [315] in 1946, the Nobel Prize in Physics in 1952 was awarded for this discovery [316]. NMR led to the development of MRI by Paul C. Lauterbur and Sir Peter Mansfield, who were awarded with the Nobel Prize in Physiology or Medicine in 2003 [317].

MRI is a non-invasive imaging technique, which is applied to study morphological characteristics of tissues, obtain anatomical information and measure physiological parameters like water diffusion, blood vessel perfusion or changes in blood oxygenation levels [318]. MRI presents a high tissue contrast and is a non-ionizing radiation method. MR Spectroscopy (MRS) is an analytical, non-destructive technique applied in metabolomic studies to quantify metabolite levels

in vivo even in large-scale clinical studies [319]. However, MRS presents low sensitivity, limiting its application only to metabolites within the millimolar concentration range [318]. Nevertheless, MRI and MRS found its way into the clinical routine diagnostic supporting clinical decision making.

The underlying principle of Magnetic Resonance (MR) is based on angular momentum quantum number (hereinafter referred to as spin), which depends on the ratio of protons to neutrons of the different nuclei. Only those nuclei with a non-zero spin value, as e.g. ^{1}H, ^{3}He, ^{13}C, ^{19}F, ^{23}Na or ^{31}P, will result in an MR signal [264, 320, 321]. The MR phenomenon relies on the ^{1}H nucleus, which possesses a spin of ½, as a small magnet. In the presence of a strong magnetic field (B_0), this spin will align along the magnetic field with two possible orientations, parallel (i.e., the north pole of the spin pointing in the same direction of B_0) and antiparallel. These two orientations represent different energy levels, with the parallel representing a low energy state and the antiparallel a high energy state [320]. The small magnets will experience a movement of precession around the direction of B_0 at a frequency proportional to the strength of B_0, a rate called the Larmor frequency. For a clinical magnet with a B_0 of 1.5T, the Larmor frequency is 64 MHz [321]. When the spins inside a magnet are perturbed by an oscillating magnetic field, by utilizing radiofrequency (RF) coils, with a frequency close enough to the Larmor frequency, some of the spins will change from a low to a high energy state and the spins that are processing asynchronically around B_0 will acquire phase coherence. Consequently, the macroscopic magnetization vector can be measured. When the RF pulse is switched off, the protons will return from the high to the low energy state over time and the magnetization vector will gradually increase. This process is called T_1, transversal or spin-lattice relaxation. Further, the spins will gradually lose their phase coherence due to T_1 relaxation, magnetic field inhomogeneity and subsequently the magnetization vector will decrease [321]. This process is known as T_2, transversal or spin-spin relaxation [321]. This relaxation process will create an oscillating magnetic field that will induce a voltage change detected by a receiver coil and the signal is recorded as the free induction decay (FID) [320, 321]. Several RF pulses are applied and the respective FIDs are recorded, averaged and resolved by a Fourier transformation to obtain either an image (MRI) or a frequency spectra (MRS) [320].

A promising application represents *in vivo* MR measurements of tumor pH_e values

by acido chemical exchange saturation transfer MRI (acidoCEST-MRI) [322-324]. Another application represents the MR-compatible cell perfusion system for longitudinal *in vitro* monitoring of metabolic alterations as well as ECM degradation and invasion characteristics of cells, which are cultured on microcarrier beads in a 3D-like conformation [325, 326].

2 Aims and perspectives of this work

In recent years the hallmarks of cancer have been extended to evading immune destruction and reprogramming of energy metabolism [4]. The TME is complex and consists of inflammatory immune cells, which are affected by acidification or hypoxia, but also determine the TME by secretion of mediators and can even promote tumor progression [327-331]. Cancer cells exhibit an altered metabolism characterized by an increased lactate production which affects immune cell activity and represents a mechanism of immune evasion [16, 17, 92, 165, 332]. Another mechanism of tumors to escape the immune system is the expression of immune checkpoint molecules representing a promising strategy for targeting this negative immune regulatory effect. The interplay between these metabolic changes in tumors, the temporal dynamics of tumor hypoxia and tumor acidosis as well as immune escape by PD-L1 expression of cancer and immune cells remains largely enigmatic and therefore is subject of this thesis.

Immune checkpoint inhibitor therapies rely on the activation of the immune system against the cancer, with TDLNs being critical for the effectiveness of an anti-PD-1/anti-PD-L1 therapy [208]. Therefore, within this dissertation different imaging agents and modalities have been evaluated for their suitability to detect TDLN. These results thereby provide the basis for further, more in-depth TDLN imaging studies.

Beside immune cells in TDLNs, the mechanisms of action of immune checkpoint blockade are of great interest. A recent publication suggests that that the effect of an immune checkpoint inhibitor therapy depends on the induction of senescence [333]. In addition, various therapeutics can be applied to drive cancer cells into senescence, characterized by a stable cell cycle arrest [237]. Nevertheless, these senescent cells exhibit a SASP, which can also present a mechanism of tumor evasion. Furthermore, cytokines can drive tumors into senescence and therefore contribute to cancer immune control [237, 244, 333]. Nevertheless, to date there is no robust biomarker allowing identification of senescent cells by non-invasive *in vivo* imaging, enabling monitoring of senolytic treatment approaches as well as chemotherapy or immune checkpoint inhibitor therapy-induced senescence.

Therefore, metabolic alterations of senescent cancer cells were studied in this thesis, to identify a potential biomarker for senescence.

In summary, the presented dissertation aims to answer the following questions:

I. Does tumor acidosis modulate PD-L1 expression within the TME in the context of immune cell-derived IFN-γ?
II. Does conjoint IFN-γ- and acidosis-induced membrane-bound PD-L1 expression of cancer cells represent a novel mechanism of tumor immune escape?
III. How does short-lived, acute tumor hypoxia develop, and does it affect PD-L1 expression?
IV. Are non-invasive *in vivo* OI and PET/MRI suitable to identify TDLN?
V. Do senescent cancer cells exhibit reliable metabolic biomarkers, which are qualified for specific detection and identification of senescent cancer cells?

3 Materials and Methods

The below listed Materials and Methods were used and applied in the present thesis. Parts of the experiments were performed in the laboratory of Prof. Dr. Zaver M. Bhujwalla at the Department of Radiology and Radiological Science, The Johns Hopkins University School of Medicine, Baltimore, MD, USA. Therefore, different reagents and methods were applied in the laboratory of Prof. Dr. Zaver M. Bhujwalla than in the laboratory of Prof. Dr. Bernd Pichler at the Department of Preclinical Imaging and Radiopharmacy, University of Tübingen, Germany, which is indicated at the respective position. If the location is not indicated, the experiment was performed at the University of Tübingen. This is important for *in vivo* animal studies, as different regulations might apply.

Experiments performed by technical assistants or collaboration partners are indicated in the respective Method section. Although the experiment was performed by another person, the idea and experimental design comes from me, and I interpreted the data. If no name is mentioned in a Method section, the experiment was performed by me.

3.1 Materials

3.1.1 Equipment

Equipment and devices used in this study are listed in **Table 1**

Table 1: List of equipment and devices.

equipment/ device	item number	company
iCycler real-time PCR detection system	170-8740	Bio-Rad, Hercules, CA, USA
PowerPacTM HC Power Supply	1645052	Bio-Rad
Mini Gel Holder Cassette	1703931	Bio-Rad
Mini Trans-Blot Module	1703935	Bio-Rad
Buffer Tank and Lid	1658040	Bio-Rad
Mini-PROTEAN® Tetra Electrode Assembly	1658037	Bio-Rad
SevenCompact pH meter S220	30019028	Mettler-Toledo, Columbus, OH, USA
Spacer Plates with 1.0 mm Integrated Spacers	1653311	Bio-Rad
Spacer Plates with 1.5 mm	1653312	Bio-Rad

Integrated Spacers		
Mini-PROTEAN® Short Plates	1653308	Bio-Rad
Duomax 1030 (5° Neigungswinkel) Schüttel- & Mischgeräte	543-32205-00	Heidolph Instruments, Schwabach, Germany
Thermomixer Comfort 5355 Block 24 x 1,5 ml Schüttler Mixer Shaker	2984	Eppendorf, Hamburg, Germany
Mixing Block MB-102	BYQ6008E-1884	Hangzhou Bioer Technology, Hangzhou, China
Centrifuge MiniSpin®	5452000010	Eppendorf
MIKRO 220 | 220 R	2200 | 2205	Hettich, Tuttlingen, Germany
NanoDrop™ 1000	OH524	VWR International, Radnor, PA, USA
Light Cycler® 1.5	1408154	Roche, Basel, Switzerland
Herasafe™ KS18/KS12 biologische Sicherheitswerkbänke der Klasse II	41091129/ 40451721	Thermo Fisher Scientific, Waltham, MA, USA
Heraeus Megafuge 40R Universalzentrifuge	75004518	Thermo Fisher Scientific
Julabo® water baths	Z615501	Merck, Darmstadt, Germany
CO_2-Inkubatoren mit Heißluftsterilisation und hitzesterilisierbarem CO_2-Sensor CB150	03-53643	Binder, Tuttlingen, Germany
Leica Microsystems Microscope	090-135.001	Leica Camera, Wetzlar, Germany
OdysseySA Infrared Imaging System		LI-COR Bioscience, Lincoln, NE, USA
BD LSRFortessa flow cytometer	649225	BD Bioscience, San Jose, CA, USA
Analytical Balance	ME235S	Sartorius, Göttingen, Germany

3.1.2 Biochemical assay kits

Biochemical assay kits used in this study are listed in **Table 2**.

Table 2: List of biochemical assay kits.

biochemical assay kit	item number	company
QIAshredder	79654	Qiagen, Hilden, Germany
RNeasy Mini kit	74104	Qiagen
iScript cDNA synthesis kit	1708890	Bio-Rad
peqGOLD Total RNA Kit	12-6834-02	VWR International
peqGOLD DNase I Digest Kit	12-1091-02	VWR International
Micro BCA™ Protein Assay Kit	23235	Thermo Fisher Scientific

3.1.3 Consumables

Consumables used in this study are listed in **Table 3**.

Table 3: List of consumables.

consumable	item number	company
Immobilon-FL PVDF	IPFL 00010	Merck
Whatman® cellulose chromatography papers	WHA3017915	Merck
Falcon® 6-well Clear Flat Bottom TC-treated Multiwell Cell Culture Plate	353224	Corning, NY, USA
CELLSTAR® CELL CULTURE FLASK, 250 ML, 75 CM²	658170	Greiner Bio-One, Kremsmünster, Austria
TC-Schale 100, Standard	83.3902	Sarstedt, Nümbrecht, Germany
M-NZ Disposable Hemocytometer Chips	2022.05.10	Kisker Biotech, Steinfurt, Germany
CELLSTAR®, TUBE, 50 ml	227261	Greiner Bio-One
Falcon® 5 mL Round Bottom Polystyrene Test Tube	352008	Corning
Titertube® Micro Test Tubes	2239391	Bio-Rad
Stericup Quick Release-GP Sterile Vacuum Filtration System, 0.22 µm	S2GPU05RE	Merck

3.1.4 Chemicals

Chemicals used in this study are listed in **Table 4**.

Table 4: List of chemicals.

compound, buffer	item number	company
DMEM - high glucose	D5648	Merck
DMEM	2098600	Thermo Fisher Scientific
RPMI-1640	R6504	Merck
fetal bovine serum (FBS)	BCBV3645, BCBW7154, BCCC0665	Sigma-Aldrich, St. Louis, MO, USA
penicillin streptomycin	A2212	Merck
penicillin streptomycin	30001133	Corning
HEPES	L1613	Biochrom, Berlin, Germany
sodium pyruvate	L0473	Biochrom
non-essential amino acids	K0293	Biochrom
doxycycline hyclate		BD Bioscience
PBS	2085516	Thermo Fisher Scientific
Trypsin	L2143	Biochrom
methanol	4595	Thermo Fisher Scientific
MTBE	306975	Sigma-Aldrich

3.2 *In vitro* methods

3.2.1 Cell lines and cell culture

Murine colon adenocarcinoma MC38^{wt}, MC38$^{PD\text{-}L1\text{-}/\text{-}}$, MC38$^{STAT1\text{-}/\text{-}}$ and MC38-HRE-ODD-luc cell lines as well as human MCF-7, MIA-PaCa-2, SK-MEL-28, and U87 MG were maintained in Dulbecco's modified eagle's medium (DMEM) with 3.7 g l^{-1} sodium bicarbonate supplemented with 10% fetal bovine serum (FBS), 100 U ml^{-1} penicillin-streptomycin and 10 mM 4-(2-hydroxyethyl)-1-piperazineethanesulfonic acid (HEPES). Human HCA-7 colony 29 cells were maintained in DMEM with 3.7 g l^{-1} sodium bicarbonate supplemented with 10% FBS, 100 U ml^{-1} penicillin-streptomycin and 1 mM sodium pyruvate. Murine melanoma B16-F10^{wt}, B16-F10-HRE-ODD-luc, human breast cancer MCF-7 and human glioma U87 MG cell lines were maintained in DMEM with 3.7 g l^{-1} sodium bicarbonate supplemented with 10% FBS and 1% penicillin-streptomycin. Murine CT26^{wt}, CT26$^{PD\text{-}L1\text{-}/\text{-}}$, CT26-HRE-ODD-luc, 4T1^{wt}, 4T1-HRE-ODD-luc cell lines

were maintained in Roswell Park Memorial Institute (RPMI) 1640 culture media with 2.0 g l^{-1} sodium bicarbonate supplemented with 10% FBS and 1% penicillin-streptomycin. Murine shp53;H-RasV12 hepatocellular carcinoma cells (H-Ras) were maintained in DMEM culture media containing 10% FBS, 100 U ml^{-1} penicillin-streptomycin, 1% non-essential amino acids, 1 mM sodium pyruvate and 5 µg ml^{-1} doxycycline hyclate, which was refreshed in cell culture medium every second day. Oncogene-induced senescence was triggered by doxycycline hyclate withdrawal via p53 silencing within 72 h. The cell lines used in this study, the tumor type and their origin are indicated in **Table 5**.

Table 5: List of cell lines.

cell line	tumor type	origin	reference
$MC38^{wt}$	colon adenocarcinoma	C57BL/6	gift from M. F. Fransen [196]
$MC38^{PD\text{-}L1\text{-}/\text{-}}$	colon adenocarcinoma deficient in PD-L1	C57BL/6	gift from M. F. Fransen [196]
$MC38^{STAT1\text{-}/\text{-}}$	colon adenocarcinoma deficient in STAT1	C57BL/6	generated in house
$MC38^{STAT2\text{-}/\text{-}}$	colon adenocarcinoma deficient in STAT2	C57BL/6	generated in house
$CT26^{wt}$	colon carcinoma	BALB/c	gift from M. F. Fransen [196]
$CT26^{PD\text{-}L1\text{-}/\text{-}}$	colon carcinoma deficient in PD-L1	BALB/c	gift from M. F. Fransen [196]
$B16\text{-}F10^{wt}$	melanoma	C57BL/6	ATCC (CRL-6475)
$4T1^{wt}$	breast cancer	BALB/c	gift from M. A. Neveu
H-Ras	shp53;H-RasV12 liver carcinoma	C57BL/6	gift from L. Zender
HCA-7 colony 29	colon carcinoma	human	gifted from K. Fuchs
MCF-7	breast cancer	human	gifted from C. Calaminus
U87 MG	likely glioblastoma	human	gift from S. Fulda
SK-MEL-29	malignant melanoma	human	gifted from M. Krüger
MIA-PaCa-2	pancreatic carcinoma	human	gifted from K. Fuchs

For *in vitro* acidosis experiments, a cell culture media pH_e of 6.8 was adjusted by supplementing unbuffered DMEM with 10% FBS, 100 U ml^{-1} penicillin-streptomycin and 4 mM sodium bicarbonate ($NaHCO_3$). The cell culture incubator with a 5% CO_2 atmosphere allowed adjustment to pH_e 6.8. Similarly, a pH_e of 6.8

was achieved in unbuffered RPMI-1640 media supplemented with 10% FBS, 100 U ml^{-1} penicillin-streptomycin and 1 mM $NaHCO_3$. For lactic acidic cell culture condition, media with 4 mM $NaHCO_3$ and 20 mM sodium L-lactate were prepared. For lactosis cell culture condition, media was supplemented with 44.05 mM $NaHCO_3$ and 20 mM sodium L-lactate.

3.2.2 siRNA transfections

The short-interfering RNA (siRNA) technology is used to suppress the expression of genes. Briefly, the siRNA, argonaute 2 (AGO2) and the RNA interference-induced silencing complex (RISC) assemble, recognize and cleave the target gene [334, 335]. To study the role of STAT1 and STAT2 in the IFN-γ signaling pathway siRNA-mediated knockdowns of the respective genes were performed. Therefore, murine $MC38^{wt}$ cells were seeded in a 6 well plate 24 h prior transient transfections with 50 nM siRNA against *Stat1*, *Stat2* or a non-targeting siRNA (**Table 6**). A pool of four siRNAs against the individual target gene (Dharmacon, Lafayette, CO, USA) was used to increase potency and specificity of target gene silencing and therefore reduce off-target effects [336, 337]. At the day of transfection cells were 60-70% confluent. Per well of a 6 well plate, 2 µl lipofectamine were incubated with 48 µl Opti-MEM in a reaction tube for 5 min. Next this mixture was added to a 50 µl Opti-MEM and siRNA mixture and incubated for 20 min at room temperature. During this incubation, the lipofectamine 2000-siRNA complex is formed. Culture media in the 6 well plates was changed with 900 µl fresh culture media without penicillin-streptomycin. Then the lipofectamine 2000-siRNA mixture was added slowly and dropwise to the plate. After 24 h, cells were treated with IFN-γ (10 ng ml^{-1}) and acidic media for another 24 h and then subjected either to Western Blot (WB), quantitative real-time polymerase chain reaction (qRT-PCR), or flow cytometry analysis.

Table 6: List of siRNAs.

siRNA	catalog number
murine *Stat1*	M-058881-02
murine *Stat2*	M-049890-00
human *Stat1*	M-003543-01
non-targeting siRNA	D-001206-13-20

Experiments with human HCA-7 colony 29 cells using the lipofectamine 2000

transfection protocol, revealed only moderate siRNA-mediated STAT1 knockdown efficiencies. Therefore, siRNA-mediated STAT1 knockdowns (**Table 6**) in human HCA-7 colony 29 cells were performed by electroporation using the Cell Line Nucleofector™ Kit V (Lonza, Basel, Schweiz) and the Amaxa Nucleofector™ II device (Lonza, Basel, Schweiz). Electroporation was performed according to manufacturer's instructions. First, the nucleofection solution was supplemented at room temperature and cells were harvested by trypsinization. Respective positive (pmaxGFP vector) and negative (pmaxGFP vector without electroporation) controls were performed to assess electroporation efficiency. Therefore, 100 µl cell suspensions ($1*10^6$ cells) were supplemented with 50 nM siRNA against STAT1, non-targeting siRNA or 1 µg pmaxGFP vector and exposed to electroporation using program T-020 according to the manufacturer's instructions. After electroporation, cells were immediately transferred to 6 cm TC-dishes with 3.8 ml DMEM supplemented with 10% FBS and 1 mM sodium pyruvate in the absence of penicillin-streptomycin and maintained at 37 °C and 5% CO_2. After 24 h, 90% of the HCA-7 colony 29 cells were GFP positive. Cells were treated with IFN-γ (10 ng ml^{-1}) and acidic media 48 h post electroporation for another 24 h before harvesting the cells with trypsin for protein extraction. Samples were analyzed for total protein expression by WB analysis.

3.2.3 CRISP/Cas9-mediated knockouts

A nucleic-acid-based adaptive immune system named clustered regularly interspaced short palindromic repeats (CRISPR)-associated (Cas) protects bacteria and archaea from viruses by silencing their nucleic acid [338, 339]. Based on these findings in nature, the genetic engineering CRISP/Cas9 technology was developed as a genetic tool to silence target genes permanently in cells. In this regard, CRISP/Cas9 was used to generate MC38 cells with a stable knockout of either the *Stat1* or the *Stat2*. Therefore, three guide RNAs (gRNAs) per gene were designed *in silico* by Dr. Omelyan Trompak using the online CRISPR Design Tool (www.benchling.com) [340] and are listed in **Table 7**.

Table 7: List of custom-designed gRNAs for CRISP/Cas9 genome editing.

gRNA	sequence (forward, reverse)
#1 *Stat1*	CACCGGTACTGTCTGATTTCCATG
	aaacCATGGAAATCAGACAGTACC
#2 *Stat1*	CACCGAACTGTCATCGTACAGCTGG
	aaacCCAGCTGTACGATGACAGTTC
#3 *Stat1*	CACCGGACTCCAAGTTCCTGGAGC
	aaacGCTCCAGGAACTTGGAGTCC
#1 *Stat2*	CACCGTTCCTGGACCAGTTACACC
	aaacGGTGTAACTGGTCCAGGAAC
#2 *Stat2*	CACCGGTCCAGGAACAGGCTGTCA
	aaacTGACAGCCTGTTCCTGGACC
#3 *Stat2*	CACCGCTGTCGAACGTCCATTGGC
	aaacGCCAATGGACGTTCGACAGC

The day prior transfection, 300.000 MC38 cells were seeded in a 6 well plate. The next day, cells reached a confluence between 40% and 50%. Then, 10 µg gRNA against *Stat1*, *Stat2* or the empty gRNA control vector px459.v2 were mixed with 150 µl Opti-MEM and added to a mixture of 15 µl lipofectamine 2000 in 150 µl Opti-MEM. After a five-minute incubation step at room temperature, the lipofectamine 2000-gRNA mixture was added to the MC38 cells in the 6 well plate containing fresh culture media with 10% FBS. After 24 h, culture media was changed, and cells were selected with 1 µg ml^{-1} puromycin. Another 24 h later, cells were seeded in a 96 well plate using limiting dilution to obtain a monoclonal cell population. The following weeks, individual clones were expanded and transferred into larger cell culture flasks. During the dilution cloning process, cells were maintained in cell culture media without puromycin. MC38 cells transfected with an empty gRNA control vector px459.v2 were used as a pool as well as subjected to dilution cloning. Knockouts were confirmed by WB analysis detecting the total protein expression of the respective gene. Furthermore, the individual CRISP/Cas 9 knockout clones as well as the $MC38^{control}$ pool were tested *in vivo* for their ability to engraft and form tumors as well as their growth kinetics.

3.2.4 Generation of the 5xHRE-ODD-luc cell lines

Tumor hypoxia is an important characteristic of various tumors. Therefore, hypoxia reporter genes have been developed to image tumor hypoxia non-invasively *in vivo* using OI. Tumor hypoxia leads to the formation of the heterodimer HIF which consists of the HIF-1α and HIF-1β subunits [341]. Dr. Pierre Danhier and

Dr. Balaji Krishnamachary have previously generated a reporter gene system, where a luciferase is expressed under the control of five HREs. Under hypoxia, the heterodimer HIF is formed and binds to the HRE upstream of the *Luciferase* gene. Subsequently, the luciferase gene is transcribed, and the mRNA is translated into an active luciferase enzyme, which catalyzed the reaction from D-luciferin to oxyluciferin. In this process light is emitted, which can then be detected by OI (**Figure 6**) [267, 275].

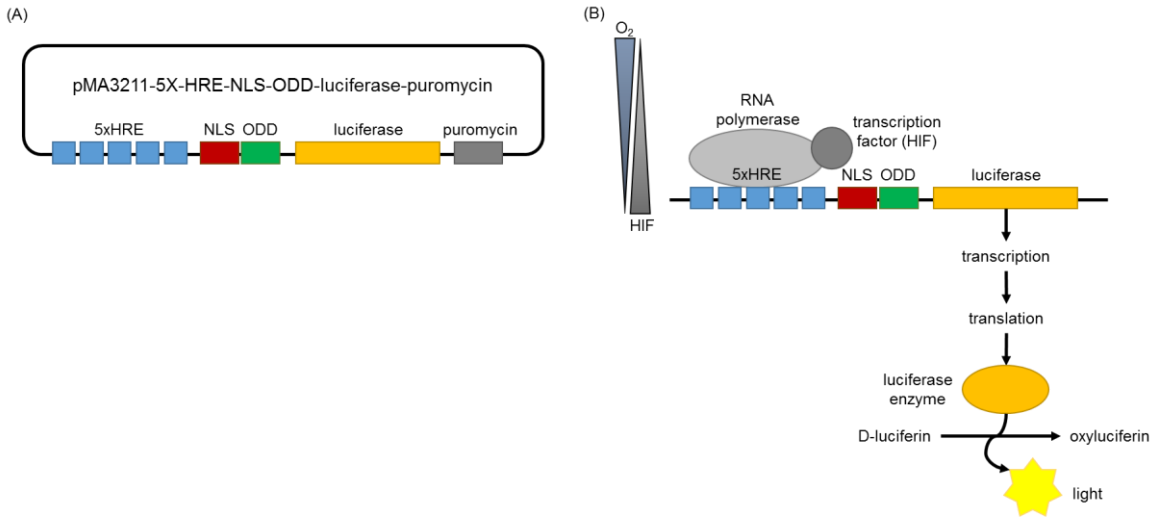

Figure 6: Schematic representation of the HRE-ODD-luc reporter gene construct and the mechanism of luciferase expression upon hypoxia.
(A) Schematic showing the hypoxia reporter pMA3211-5X-HRE-NLS-ODD-luciferase-puromycin plasmid. The plasmid contains five hypoxia response elements (HRE), a nuclear localization signal (NLS), an oxygen-dependent degradation domain (ODD), a luciferase gene and the puromycin resistance gene. (B) With increasing hypoxia characterized by low oxygen levels, the transcription factor HIF consisting of HIF-1α and HIF-1β is formed and stabilized. HIF binds to the 5xHRE region and initiates transcription and translation of the luciferase. The luciferase enzyme catalyzes the reaction from D-luciferin to oxyluciferin and light is emitted. Adapted from and modified according to [267, 275].

Murine MC38 and CT26 colon adenocarcinoma, 4T1 breast cancer and B16-F10 melanoma cells containing the hypoxia reporter 5xHRE-ODD-luc construct were generated as previously described [267, 275]. Briefly, the pMA32II-HRE-ODD-luc plasmid was co-transfected in 293T cells with vesicular stomatitis virus G (VSVG) and ΔR8.2 plasmids to produce high-titer lentiviral particles using lipofectamine 2000. For virus production 293T cells were maintained in DMEM containing 1% FBS. Virus containing supernatant was harvested and transferred

together with 8 µg ml^{-1} polybrene triple to the respective cells cultured for 48 h ($1*10^6$ cells per 100 mm cell culture dish) prior to transduction. The pMA3211-5X-HRE-NLS-ODD-luciferase-puromycin plasmid contains a puromycin resistance cassette. Cells successfully transduced with the plasmid were selected by puromycin. Selection pressure with puromycin was gradually increased, reaching concentrations of 6 µg ml^{-1} puromycin for MC38-HRE-ODD-luc, CT26-HRE-ODD-luc and 4T1-HRE-ODD-luc cells and 0.2 µg ml^{-1} puromycin for B16-F10-HRE-ODD-luc cells.

The generated hypoxia reporter cells were validated *in vitro* for luciferase expression upon hypoxia (1% O_2) on mRNA level by qRT-PCR and on a functional level using luciferase activity measurements. Furthermore, the induction of luciferase expression upon $CoCl_2$ treatment was measured by OI.

3.2.5 Quantitative real-time polymerase chain reaction

Total mRNA was isolated from cells and cDNA was synthesized following standard protocols. Gene expression was evaluated from cDNA by using gene specific primers by qRT-PCR analysis.

University of Tübingen:

Cells cultured and treated with the indicated compounds and cell culture media *in vitro* were harvested by trypsinization. Cells were lysed by addition of 400 µl RNA lysis buffer and total RNA was isolated according to manufacturer's instructions (RNA-Isolierung, Gesamt-RNA Kit, peqGOLD, VWR International) including genomic DNA digestion (DNase I Digest Kit, peqGOLD, VWR International).

The cDNA was synthesized from 1 µg total RNA. First, RNA and oligo(dT) primer (Eurofins, Ebersberg, Germany) were incubated at 65 °C for 5 min. Then, nucleoside triphosphates (20 mM dNTPs, Amersham, UK), 5x buffer with reverse transcriptase (18064-014, Invitrogen, Carlsbad, CA, USA), SuperScript II Reverse Transcriptase (Invitrogen), β-mercaptoethanol (Carl Roth, Karlsruhe, Germany) and recombinant ribonuclease inhibitor (Promega, Madison, WI, USA) were added and the mixture was incubated at 37 °C for 55 min followed by a 5 min incubation at 95 °C. The synthesized cDNA was diluted with dH_2O to a final concentration of 10 ng $µl^{-1}$.

For gene expression analysis, gene specific, custom-designed primers were used.

Primers were designed using the Primer3web version 4.1.0 tool from the Whitehead Institute for Biomedical Research (Cambridge, MA, USA) [342-344] against the coding sequence (CDS) of the respective genes that were curated by the National Center for Biotechnology Information (NCBI, U.S. National Library of Medicine, Bethesda, MD, USA). Primers were tested against mRNA from the NCBI's Reference Sequence collection using Primer-BLAST (U.S. National Library of Medicine) [345]. This allows prediction of off-target binding, self-complementary and the primer melting temperature (T_m). Custom-designed primers were synthesized and purchased from Eurofins and are listed in **Table 8**.

Table 8: Custom-designed primers for qRT-PCR - University of Tübingen.

species	primer	sequence (5'->3')
murine	*Aldolase*	TGGGCCTTGACTTTCTCCTAT
		TGTTGATGGAGCAGCCTTAGT
	β-actin	CGGATGTCAACGTCACACTT
		GGCCAGGTCATCACTATTGG
	Gapdh	ACACATTGGGGGTAGGAACA
		AACTTTGGCATTGTGGAAGG
	Pd-l1	CGCCTGCAGATAGTTCCCAA
		ATCGTGACGTTGCTGCCATA
	Stat1	TTGACGACCCTAAGCGAACT
		TCAAATTCGGGGCCCACTAT
	Stat2	TCCTGTTTGAGCTCCAGAGG
		CGCTTCCTCTATCCCCGAAT
	Mmp-2	CACACCAGGTGAAGGATGTG
		AGGGCTGCATTGCAAATATC
	Mmp-9	CGTCGTGATCCCCACTTACT
		AACACACAGGGTTTGCCTTC
human	*Aldolase*	AATGTTCTGGCCCGTTATGC
		CCAGGTAGATGTGGTGGTCA
	β-actin	ACTCTTCCAGCCTTCCTTCC
		TCTCCTTCTGCATCCTGTCG
	Gapdh	CCAGAACATCATCCCTGCCT
		CCTGCTTCACCACCTTCTTG
	Pd-l1	GTGCCGACTACAAGCGAATT
		CTTGGAATTGGTGGTGGTGG
	Stat1	GTGGTACGAACTTCAGCAGC
		CATGAAAACGGATGGTGGCA

For qRT-PCR analysis, 10 ng cDNA, 5 pmol forward primer, 5 pmol reverse primer,

5 µl SYBR® Green PCR Master Mix (Qiagen) and 3 µl PCR grade water was mixed, and gene expression of duplicates was quantified in the LightCycler Real Time PCR system (Roche) using the program indicated in **Table 9**.

Table 9: Protocol for qRT-PCR - University of Tübingen.

step	temperature	time	no. cycles
activation	95 °C	15 min	1
amplification	95 °C	15 sec	40
	60 °C	45 sec	
	72 °C	30 sec	
melting	65 °C	15 sec	1

Gene expression levels of target genes were normalized to the mean of three reference genes (*Aldolase*, *β-actin* and glyceraldehyde 3-phosphate dehydrogenase (*Gapdh*)) and analyzed using the $\Delta\Delta C_t$ method (**Equation 1**) [346].

$$2^{-\Delta\Delta C_t} = 2^{-((C_t(target) - C_t(mean\ reference)_{treated} - (C_t(target) - C_t(mean\ reference)_{untreated}))}$$

Equation 1

The mean of three reference genes was used to ensure robustness of the normalization and reduce the likelihood of genes being induced by one or the other condition in a double (acidosis and IFN-γ) or triple (acidosis, IFN-γ and silvestrol) treatment approach.

Johns Hopkins University:

For expression analysis of luciferase upon hypoxia, MC38-HRE-ODD-luc, CT26-HRE-ODD-luc, B16-F10-HRE-ODD-luc and 4T1-HRE-ODD-luc cells were grown under normoxia or hypoxia at 80-90% confluence in 100 mm cell culture dishes. Total RNA was isolated using QIAshredder and RNeasy Mini kit (Venlo, Netherlands) according to the manufacturer's protocol. The total RNA (1 µl) was transcribed into cDNA according to manufacturer's instructions using the iScript cDNA synthesis kit (Bio-Rad).

The primers used for gene expression analysis were designed by Dr. Balaji Krishnamachary using the Beacon designer software 7.8 (Premier Biosoft, Palo Alto, CA, USA) and are listed in **Table 10**.

Table 10: Custom-designed primers for qRT-PCR - Johns Hopkins University.

primer	sequence (5'->3')
Pd-l1	TTCAGATCACAGACGTCAAGCTG
	ATTCTCTGGTTGATTTTGCGGTA
Luciferase	TGGGCGCGTTATTTATCGGA
	GCTGCGAAATGCCCATACTG
18S	CGGCGACGACCCATTCGAAC
	GAATCGAACCCTGATTCCCCGTC

For gene expression quantification, qRT-PCR was performed using diluted cDNA (1:10), 10 µM gene specific primers, 5 µl iTaq™ Universal SYBR® Green Supermix (Bio-Rad) and 3 µl PCR grade water in the iCycler Real Time PCR system (Bio-Rad). The qRT-PCR analysis was performed in triplicates following the settings as indicated in **Table 11**.

Table 11: Protocol for qRT-PCR analysis - Johns Hopkins University.

step	temperature	time	no. cycles
activation	95 °C	3 min	1
amplification	95 °C	15 sec	39
	60 °C	30 sec	
	72 °C	30 sec	
melting	55 °C	5 sec	1

The expression of the luciferase or PD-L1 relative to the reference gene 18S was calculated based on the $\Delta\Delta C_t$ method (**Equation 1**).

3.2.6 SDS-PAGE and Western Blot analysis

WB analysis is an analytical tool in biochemistry to detect the total content of a certain protein of interest in cells by specific antibodies. Furthermore, WB analysis allows detection of protein modifications like phosphorylation and therefore allows differentiation between the active and the inactive form of proteins [347, 348]. First, proteins are separated according to their molecular weight by sodium dodecyl sulfate polyacrylamide gel electrophoresis (SDS-PAGE). Then they are transferred to a membrane and incubated with specific monoclonal or polyclonal primary antibodies against the protein of interest. After incubation with a secondary antibody, the total protein content can be assessed under different treatment conditions.

University of Tübingen:

To elucidate the role of acidosis in the IFN-γ-mediated PD-L1 regulation, cells were cultured *in vitro*, treated as indicated and harvested by trypsinization. The cell pellets were lysed by addition of radioimmunoprecipitation assay (RIPA) lysis buffer supplemented with protease inhibitor (cOmplete, Roche), phosphatase inhibitor cocktail 2 and 3 (Sigma-Aldrich). Importantly, protein lysates were stored on ice during the whole process. Then, protein lysates were sonicated (5 min), centrifuged (15 min) and protein concentration was measured by bicinchoninic acid (BCA) assay according to manufacturers' instructions (Micro BCA™ Protein Assay Kit, Thermo Scientific, Rockford, IL). Next, 60 µg protein lysate were separated using 10% SDS-PAGE. After semi-dry transfer on polyvinylidene difluoride (PVDF) membranes, washing with tris-buffered saline with 0.5% Tween in PBS (PBS-T) and blocking with intercept blocking buffer (927-70001, LI-COR Bioscience), membranes were incubated with primary antibodies against the respective target protein listed in **Table 12**.

Table 12: List of antibodies used for WB analysis - University of Tübingen.

antibody target	monoclonal	polyclonal	company	item no.
STAT1		X	Cell Signaling	9172
STAT1	X		Cell Signaling	14995
STAT2	X		Cell Signaling	72604
pSTAT1 (Y701)	X		Cell Signaling	9167
pSTAT1 (Y701)	X		abcam	29045
PD-L1		X	R&D Systems	AF1019
eIF4A1		X	Cell Signaling	2490
eIF4E	X		Cell Signaling	2067
β-actin	X		Cell Signaling	4970
IRDye® 680RD Donkey anti-Mouse IgG (H + L)			LI-COR Bioscience	926-68072
IRDye® 680RD Donkey anti-Rabbit IgG (H + L)			LI-COR Bioscience	926-68073
IRDye® 800CW Donkey anti-Rabbit IgG (H + L)			LI-COR Bioscience	925-32213
IRDye® 680RD Donkey anti-Goat IgG (H + L)			LI-COR Bioscience	926-68074

Following washing with PBS-T, the membranes were incubated with the respective secondary antibodies listed in **Table 12**. After washing the membranes, proteins were detected using the OdysseySA Infrared Imaging System (LI-COR Bioscience). Induction of protein expression upon the respective treatment, was semi-quantified by densitometry analysis. Therefore, regions of interest (ROIs) were drawn around the WB bands. The signals were background subtracted and quantified using the software Image Studio Light Ver 5.2 (LI-COR Bioscience). The target protein signal was divided by the reference protein (β-actin) and the treated condition was normalized to the untreated condition. The data was represented as the relative target protein density.

The SDS-PAGE, BCA-assay and WB were performed by Natalie Herrmann. The WB in **Figure 21 B,D** was performed by Valentina Bucher. Antibody selection, WB densitometry analysis and data interpretation were done by me.

For the WB in **Figure 18 A** cells were lysed with lysis buffer containing 20 mM

TRIS-HCl pH 7.5, 150 mM NaCl, 1% Triton X-100, 1 mM Na_2EDTA, 1 mM EGTA, 1 mM β-glycerophosphate, 2 M urea and 1x protease inhibitor cocktail (Roche) for 10 min on ice. Next, protein lysates were sonicated for 10 min using a bioruptor, Laemmli buffer was added and the samples were separated by SDS-PAGE and transferred to a nitrocellulose membrane.

The SDS-PAGE and BCA-assay for the WB in **Figure 18 A** was performed by Dr. Daniela Kramer.

Johns Hopkins University:

For immunoblotting, H-Ras cells were either harvested by trypsinization or direct addition of RIPA lysis buffer supplemented with protease inhibitor, phenylmethylsulfonylfluoride (PMSF), dithiothreitol (DTT), sodium fluoride (NaF) and sodium orthovanadate (Na_3VO_4). CT26-HRE-ODD-luc and 4T1-HRE-ODD-luc tumors were grinded on liquid nitrogen and prepared in RIPA lysis buffer supplemented with protease inhibitor, PMSF, DTT, NaF and sodium Na_3VO_4. Importantly, protein lysates were stored on ice during the whole process. Next, protein extracts were centrifuged, and protein concentration was determined using the Bradford Bio-Rad protein assay kit (Bio-Rad). Proteins were sepaqrated by SDS-PAGE and transferred to a nitrocellulose membrane. Blots were incubated with primary antibodies (**Table 13**) against the respective target proteins after blocking with 5% non-fat milk.

Table 13: List of antibodies used for WB analysis - Johns Hopkins University.

antibody target	monoclonal	polyclonal	company	item no.
p53	X		Cell Signaling	2524
Ki67		X	Novus Biologicals	NB500-170
PD-L1		X	R&D Systems	AF1019
GAPDH	X		Sigma-Aldrich	G8795
β-actin	X		Sigma-Aldrich	A1978
Donkey anti-Goat IgG (H+L; HRP)		X	Novus Biologicals	NB7357
Goat anti-mouse IgG (HRP)	X		Perkin Elmer, Waltham, MA	NEF822001EA

Target and reference (GAPDH, β-actin) proteins were visualized by horseradish peroxidase (HRP)-conjugated secondary antibodies (**Table 13**) using the SuperSignal West Pico Chemiluminescent substrate kit (Thermo Scientific).
SDS-PAGE, BCA-assay and WB were performed by Yelena Mironchik. Antibody selection and data interpretation were performed by me.

3.2.7 Flow cytometry analysis

Flow cytometry allows multi-parametric analysis of single cell characteristics, including e.g. size, granularity, viability as well as cell surface or intracellular protein expression levels [349]. In contrast to WB analysis where total protein levels in a cell are analyzed, flow cytometry allows detection of cell surface protein expression only. Therefore, target protein specific antibodies are labeled with a fluorochrome, which is then detected in the flow cytometry instrument.
Cells cultured and treated *in vitro* were harvested by trypsinization. The cell pellet was suspended in PBS and passed through a 40 µm cell strainer cap (Corning) to singularize cells and exclude larger cell clusters. Single cell suspensions were stained with Zombie NIR™ Fixable Viability Kit (Biolegend, San Diego, CA, USA), anti-mouse PD-L1-BV605 (clone 10F.9G2, Biolegend) or anti-human PD-L1-BV605 (clone 29E.2A3, Biolegend) for 45 min at 4 °C, washed three times with PBS supplemented with 1% FBS and analyzed using the BD LSRFortessa flow cytometer (BD Bioscience). Flow cytometry data was analyzed using the

FlowJo Flow Cytometry Analysis Software (BD Bioscience).

3.2.8 Fluorescence microscopy

Fluorescence microscopy is a powerful tool to study cell morphology and visualize the localization of individual cell populations within a tissue section. Furthermore, it allows to study the expression of certain proteins, including the immune checkpoint PD-L1 or the early activation marker CD69 expressed by T lymphocytes [350, 351] and macrophages [352]. Cellular structures are stained by fluorescent dies and proteins of interest are visualized by specific antibodies labeled with a fluorescent die [353].

University of Tübingen:

For fluorescence microscopy, $MC38^{wt}$ cells were grown and treated in chamber slides and fixed with periodate-lysine-paraformaldehyde. After permeabilization with 0.5% Triton X 100, cells were blocked with donkey serum and then incubated with the respective primary antibodies (**Table 14**).

For dual CD4 and CD69 as well as dual CD8a and CD69 staining, paraffin-embedded $MC38^{wt}$ tumor tissue sections were unmasked by citrate buffer (Thermo Scientific) at pH 6.0 in a steamer for in total 32 min. Samples were transferred into distilled water for 10 min at room temperature. For dual Iba1 and Ki67 staining, paraffin-embedded tumor tissue sections were unmasked by 1x EDTA buffer (Thermo Scientific) at pH 9.0 in a steamer for 20 min and transferred into distilled water for 10 min at room temperature. Then unmasked tumor tissue samples were washed with PBS as well as with PBS containing bovine serum albumin (BSA) and Tween. Tumor tissue samples were blocked with donkey serum and then incubated with the respective primary antibodies (**Table 14**).

Target proteins were visualized with fluorochrome-conjugated secondary antibodies binding to primary antibodies (**Table 14**). To investigate the localization of the target proteins in the cell, nuclei were stained with either 4′,6-Diamidin-2-phenylindol (DAPI) or YO-PRO®-1 iodide and F-actin was visualized using Phalloidin-Alexa 488.

Table 14: List of antibodies and dyes for fluorescence microscopy.

antibody/dye	monoclonal	polyclonal	company	item no.
PD-L1	X		Cell Signaling	13684
Ki67	X		eBioscience	14-5698
Iba1	X		abcam	ab178846
CD4	X		eBioscience	14-9766
CD8a	X		eBioscience	14-0808
CD69		X	GeneTex	GTX37447
donkey F(ab')2 anti-rabbit IgG (H+L)-Cy3		X	Dianova	711-166-152
donkey F(ab')2 anti-rat IgG (H+L)-Alexa Fluor 647		X	Dianova	712-606-153
donkey F(ab')^2 anti-goat IgG (H+L)-Alexa Fluor 488		X	Dianova	705-546-147
nucleus (DAPI)			Sigma-Aldrich	D9542
nucleus (YO-PRO®-1 iodide)			Molecular Probes	Y3603-70
F-actin (Phalloidin-Alexa 488)			Molecular Probes	A12379

Fluorescent images obtained were analyzed with a Zeiss LSM 800 confocal laser scanning microscope, software-version ZEN 2.3 (blue edition).

Furthermore, immunofluorescence of PD-L1 from MC38^{wt} tumor tissue sections was quantified. Based on morphological characteristics and the expression of the proliferation marker Ki67, regions with proliferating and therefore Ki67 positive cancer cells as well as regions rich in non-proliferating, Ki67 negative immune cells were identified within the tumor tissue sections. Three representative images per tumor slide were obtained for cancer cell as well as immune cell enriched regions and three individual paraffin-embedded tumor tissue sections per treatment condition (control and sodium bicarbonate) were analyzed. Fluorescent images were obtained at a 250x magnification and YO-PRO®-1 iodide positive nuclei were counted in cancer cell (between 44 and 325 nuclei per image) and immune cell rich (between 223 and 674 nuclei per image) tumor tissue regions. For quantification of PD-L1, the area [µm^2] of PD-L1 signal was measured and

normalized to the number of YO-PRO®-1 iodide positive nuclei within this tumor tissue region, to obtain the PD-L1 area per cancer cell [μm^2 $cell^{-1}$].

Staining, fluorescence microscopy and quantification of immunofluorescence were performed by Birgit Fehrenbacher and me.

Johns Hopkins University:

Fluorescence microscopy is also applied to visualize the expression of reporter genes like GFP. In murine shp53;H-RasV12 (H-Ras) liver carcinoma cells the expression of p53 is controlled by a small hairpin RNA (shRNA). In the presence of doxycycline hyclate (Dox) the shRNA and GFP are expressed, with the shRNA leading to p53 suppression. Under this condition, cells are proliferating (non-senescent) indicated by high Ki67 expression. Upon doxycycline hyclate withdrawal, shRNA and GFP expression are repressed and p53 expression is induced leading to senescence induction and reduced proliferation indicated by reduced Ki67 expression. As shown in **Figure 7**, the expression of the reporter gene GFP indicates the presence of the shRNA against p53, whereas the absence of GFP indicates the downregulation of the shRNA.

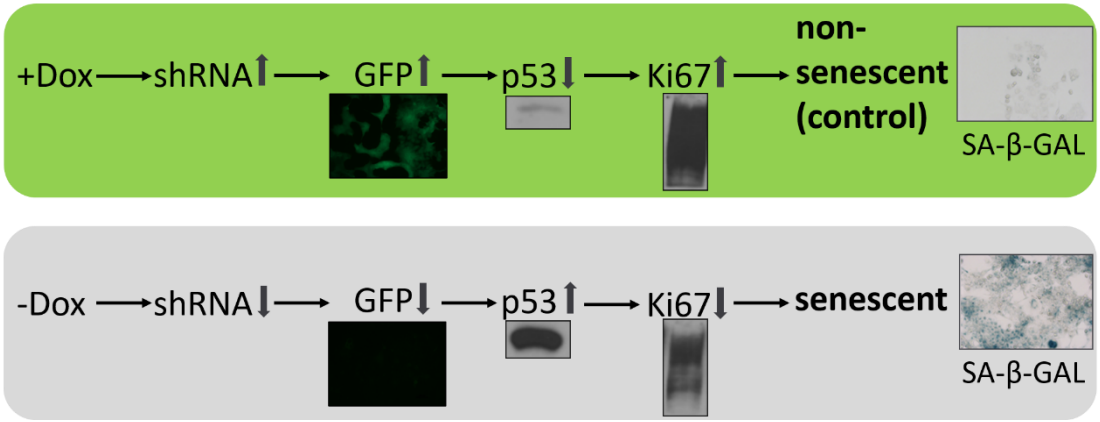

Figure 7: Schematic representation of the underlying principle of senescence induction in murine shp53;H-RasV12 (H-Ras) liver carcinoma cells.

In the presence of doxycycline hyclate (Dox) shp53;H-RasV12 (H-Ras) cells express a shRNA against p53. If the shRNA is expressed, cells also express GFP. Upon p53 repression, cells proliferate indicated by high Ki67 protein expression levels and low β-galactosidase activity. Upon doxycycline hyclate withdrawal, the expression of shRNA and GFP is repressed and p53 expression is re-activated leading to reduced Ki67 protein expression levels and senescence induction characterized by increased SA-β-GAL activity. The schematic figure is partly based on the principle of senescence induction described by Xue *et al.* [235]. The fluorescent GFP image and the p53 and Ki67 WB images of H-Ras cells were generated by me. The SA-β-GAL image of H-Ras cells was kindly provided by Benyuan Zhou.

Murine H-Ras cells were plated either in a monolayer or on microcarrier beads in 100 mm cell culture dishes. Before inducing senescence as before described, cells were photographed under bright field and fluorescence under 10x objective using a Nikon inverted microscope which was equipped with a Nikon Coolpix digital camera (Nikon Instruments, Melville, NY). Exposure times used for bright field (70 ms) and fluorescence imaging (monolayer: 20 s, microcarrier beads: 4 s) at day 3 and day 5 post doxycycline hyclate withdrawal were kept constant for capturing images at later time points.

3.2.9 Luciferase activity measurements

The degree of luciferase induction and activity in hypoxia reporter cells upon hypoxia can be measured and quantified using a multilabel plate reader.

Johns Hopkins University:

To validate the hypoxia reporter cells *in vitro*, luciferase enzyme activity upon hypoxia was measured using luciferase activity measurements. Briefly, MC38-HRE-ODD-luc, CT26-HRE-ODD-luc, B16-F10-HRE-ODD-luc and 4T1-HRE-ODD-luc cells were maintained for 48 h in a modular incubator chamber (Billups-Rothenberg, Del Mar, CA), flushed at 2 psi with a gas mixture (1% O_2/ 5% CO_2/ N_2) for 3 min. Luciferase enzyme activity under hypoxia (1% O_2) was compared to cells cultured under normoxia in a cell culture incubator with a 20% O_2/ 5% CO_2 atmosphere. Cells were grown at 90% confluence in 6-well plates, washed with cold PBS and lysed in the plate with 100 µl 1x Passive Lysis Buffer (E19A4, Promega) on ice. Then the lysate was harvested with a cell scraper and centrifuged at 12.000 g and 4 °C for 2 min. For luciferase activity measurements the Luciferase Assay System (Promega) was applied, and the measurement was performed in a black flat bottom 96 well plate (Greiner Bio-One). The assay was performed by adding 20 µl cell lysate to 50 µl Luciferase Assay Reagent (E1501, Promega) using the injector. The luciferase activity was measured by a Victor 3V plate reader (Perkin Elmer). The results are presented as fold induction of luciferase activity upon hypoxia compared to normoxia.

3.2.10 Optical Imaging

OI is a powerful method to detect fluorescence and bioluminescence of phantoms or cells *in vitro*. In this regard, phantoms with Patent Blue V bound to BSA can be

measured by fluorescence imaging. Furthermore, the luciferase activity of hypoxia reporter cells treated with $CoCL_2$, mimicking hypoxia *in vitro* was measured by BLI. The IVIS® Spectrum OI system (Perkin Elmer) was used for phantom and *in vitro* measurements and the images obtained were analyzed using Living Image Software 4 (Perkin Elmer).

University of Tübingen:

To determine the optimal excitation and emission wavelength of Patent Blue V (sodium salt) for *in vivo* experiments, fluorescent measurements with Patent Blue V bound to BSA were performed *in vitro* as previously described in a slightly modified set-up [354]. Therefore, the Patent Blue V sodium salt was diluted to a final concentration of 4 µmol l^{-1} in PBS containing 33 g l^{-1} BSA (Sigma-Aldrich). Different excitation (570 to 675 nm) and emission (620 to 780 nm) filters were selected (binning: medium, f-Stop: 2). The optimal excitation and emission wavelength were chosen based on the background signal as well as the excitation time automatically chosen by the IVIS® Spectrum OI system (Perkin Elmer).

Johns Hopkins University:

Validation and suitability of the generated hypoxia reporter cells for OI was first tested *in vitro*. OI was performed by seeding MC38-HRE-ODD-luc, CT26-HRE-ODD-luc, B16-F10-HRE-ODD-luc and 4T1-HRE-ODD-luc cells ($1x10^6$ cells) in a T175 cell culture flask. The next day one set of flasks was treated with 200 µM $CoCL_2$ for 48 h to mimic hypoxia while the other flask was not treated and served as the normoxia control. Then cells were harvested by trypsinization. Cells from both normoxic and hypoxic conditions were washed with PBS and trypsinized. The cells from the hypoxic condition were maintained with 200 µM $CoCL_2$ even during the trypsinization process and until OI was performed. Then $1.5*10^6$ cells were centrifuged, and luciferase activity of the cell pellet was measured 5 min after addition of 20 µl VivoGlo™ Luciferin P1042 (150 µg ml^{-1}, diluted in PBS, potassium salt of D-Luciferin, Promega). For *in vitro* BLI measurements, the IVIS® Spectrum OI system (Perkin Elmer) was used (F-Stop = 1, Binning = medium, exposure = 0.1 s). Images were analyzed and prepared using Living Image Software 4 (Perkin Elmer) and the photon radiance [photons/second/cm^2/sr] is shown.

3.2.11 Nuclear Magnetic Resonance spectroscopy

NMR was discovered by Felix Bloch [314] and Edward Purcell [315] and this pioneering discovery was granted the Nobel Prize in Physics in 1952 [316]. NMR is widely used in biomedical research to detect and quantify metabolic alterations in malignant cells or tissue.

Johns Hopkins University:

To study metabolic differences induced by senescence, the metabolome of control and senescent H-Ras cells was studied using high-resolution ^{1}H NMR. The water-soluble and the lipid fraction were both extracted from the H-Ras cells using a dual-phase extraction. Briefly, $0.5*10^{6}$ cells (control) or $0.25*10^{6}$ cells (senescence) were seeded in a T175 flask (Greiner Bio-One) in the presence of 5 µg ml^{-1} doxycycline hyclate (BD Bioscience). After 24 h cells were washed with PBS to remove residual doxycycline hyclate for senescence induction. For control cells media was replaced with 5 µg ml^{-1} doxycycline hyclate supplemented media 2 days after seeding (**Figure 8**).

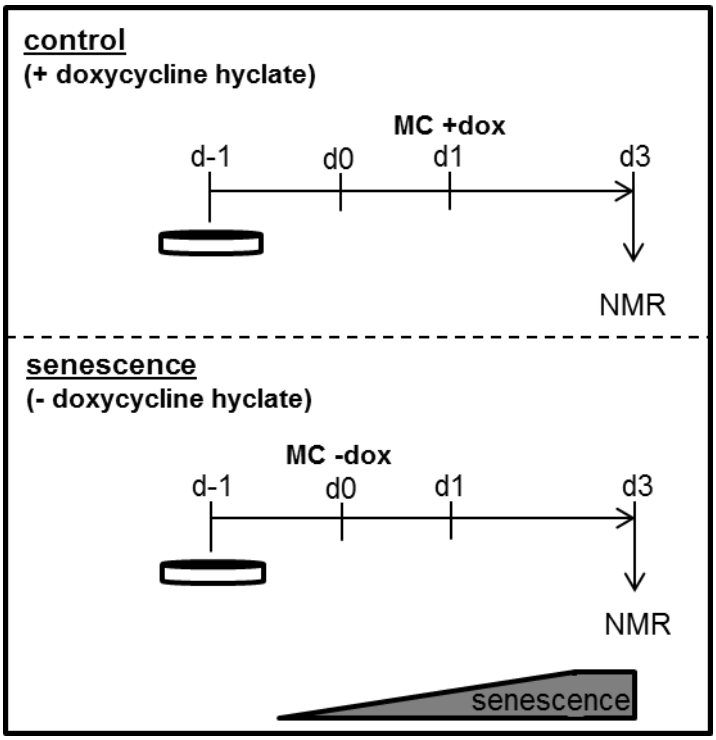

Figure 8: Schematic representation of senescence induction in H-Ras 2D monolayer cells subjected to ^{1}H NMR analysis.

Cells were seeded in a 100 mm TC-dish in the presence of 5 µg ml^{-1} doxycycline hyclate (Dox). Senescence was induced by doxycycline hyclate withdrawal by thoroughly washing the cells with

PBS at the indicated time point followed by a media change (MC). Cells were then cultured in the presence (control) or absence (senescence) of 5 µg ml^{-1} doxycycline hyclate and harvested for ^{1}H NMR analysis of cell extracts at day 3 (d3).

Cells were harvested with a cell scraper and centrifuged in ice cold PBS 4 days after seeding, which is equivalent to 3 days post senescence induction. Water-soluble and lipid fractions were extracted from the cells using a dual-phase extraction method. The pelleted cells were quenched by addition of 400 µl ice cold methanol (Thermo Scientific) and vigorously vortexed. Cells from 5 different T175 cell culture flasks were combined and stored at -80 °C until further processing. Later, 3 ml methyl tert-butyl ether (MTBE, Sigma-Aldrich) were added, and the samples were sonicated (UltraSonic Heatsystem W-385). Finally, 3 ml water was added. All these steps were performed on ice. The dual-phase separation was performed by centrifugation at 8,000 x g at 4°C for 5 min. Then the water phase with the water-soluble metabolites was collected; methanol was evaporated using nitrogen gas and the remaining water was lyophilized (SP Scientific. Warminster, PA, USA). The lyophilized aqueous phase extracts were solved in NMR buffer (0.2 M KH_2PO_4, 0.2 mM NaN_3 and 100 µM 3-(trimethylsilyl) propionic 2,2,3,3-d4 acid sodium salt (TSP) in deuterated water (D_2O); pH was adjusted to pH 7.4), centrifuged and the supernatant was used for ^{1}H NMR analysis. As an internal standard TSP was dissolved in D_2O. The lipid phase extracts were nitrogen gas dried and re-suspended in a 2:1 ratio in 0.6 mL deuterated chloroform and methanol containing tetramethylsilane (TMS) 0.05% v/v [355].

For high-resolution ^{1}H MR spectra acquisitions, a Bruker Biospin Avance-III 750 MHz NMR (Bruker Biospin Billerica, MA, USA) spectrometer was used. For spectroscopy measurements a 5-mm broad band inverse (BBI) probe head with z-gradient accessories was used. The spectrometer operates at a proton frequency of 750.21 MHz. Metabolites were quantified by determining the resonance integrals and normalizing them to the number of cells and comparing it to the TSP standard (water/aqueous phase) or TMS standard (lipid phase). Thereby relative concentrations are obtained. The NMR spectroscopy procedures are based on a protocol described in [355]. Heat maps were generated based on the normalized concentration of metabolites, mean-centered and divided by the standard deviation of each variable.

NMR measurements were performed and analyzed by Dr. Jesus Pacheco Torres.

3.2.12 MR-compatible cell perfusion system

Tumors are complex system with spatial and temporal heterogeneity in terms of extracellular pH_e, oxygenation and metabolism. Thus, assessing the interaction of cancer cells with the ECM upon environmental stimuli *in vivo* is difficult, but this information is critical to design effective treatments for cancer. Bioreactors or perfusion systems, ensuring controlled oxygenation and pH_e conditions, provide a stable environment for longitudinal investigations of cancer cells and their interaction with the ECM. Moreover, the development of MR-compatible cell perfusion systems enables continuous monitoring of cell metabolism and pH_e [326, 356, 357]. Oxygenation can also be measured using ^{19}F MR relaxometry of perfluorocarbon (PFC) added to the MR-compatible cell perfusion system [358]. Finally, adding a chamber with a particular gel mimicking the ECM will allow studies about how cells interact with the different components of the extracellular space. The set-up of the MR-compatible cell perfusion system has been extensively described [325, 326, 359], and it is schematized in **Figure 9 A**. The whole set-up consists of a warmed media bottle with a continuous flow of media into the cell perfusion tube. Media oxygenation and pH_e are controlled by flowing a gas with the desired oxygen and CO_2 concentration into a gas exchanger where it exchanges with the media. Media passed through the cell perfusion system is re-cycled into the media bottle and again enriched with oxygen. Temperature in the cell perfusion system is maintained by a continuous flow of warm water through a heat sheathing surrounding the glass tube. Cells are seeded and grown on microcarrier beads that allow the intact transfer of cells to the cell perfusion system. Additional elements of the cell perfusion system include PFC alginate beads and filters, as illustrated in **Figure 9 B**. Briefly, the cell perfusion tube is composed of a porous filter material (polyethylene; Small Parts, Miami Lakes, FL) placed at the bottom so that the media can pass through but not the cells grown on the microcarrier beads. Then, a first (bottom) layer of control or senescent H-Ras cells grown on microcarrier beads (Solohill Engineering, Ann Arbor, MI) is loaded into the cell perfusion tube, with a layer of PFC alginate beads interspersed. Then a second filter is placed into the cell perfusion tube, and above that a custom-made ECM chamber is inserted, consisting of a polycarbonate membrane (Millipore, Bedford, MA) conjoined to a Delrin ring (McMater-Carr Supply Company, Chicago, IL) filled with ECM Matrigel (Sigma-Aldrich) at a concentration of 8.8 mg ml^{-1}. On

top of the ECM chamber, a second (top) layer of H-Ras cells grown on microcarrier beads and a layer of PFC alginate beads is added. Finally, a third filter is placed on top.

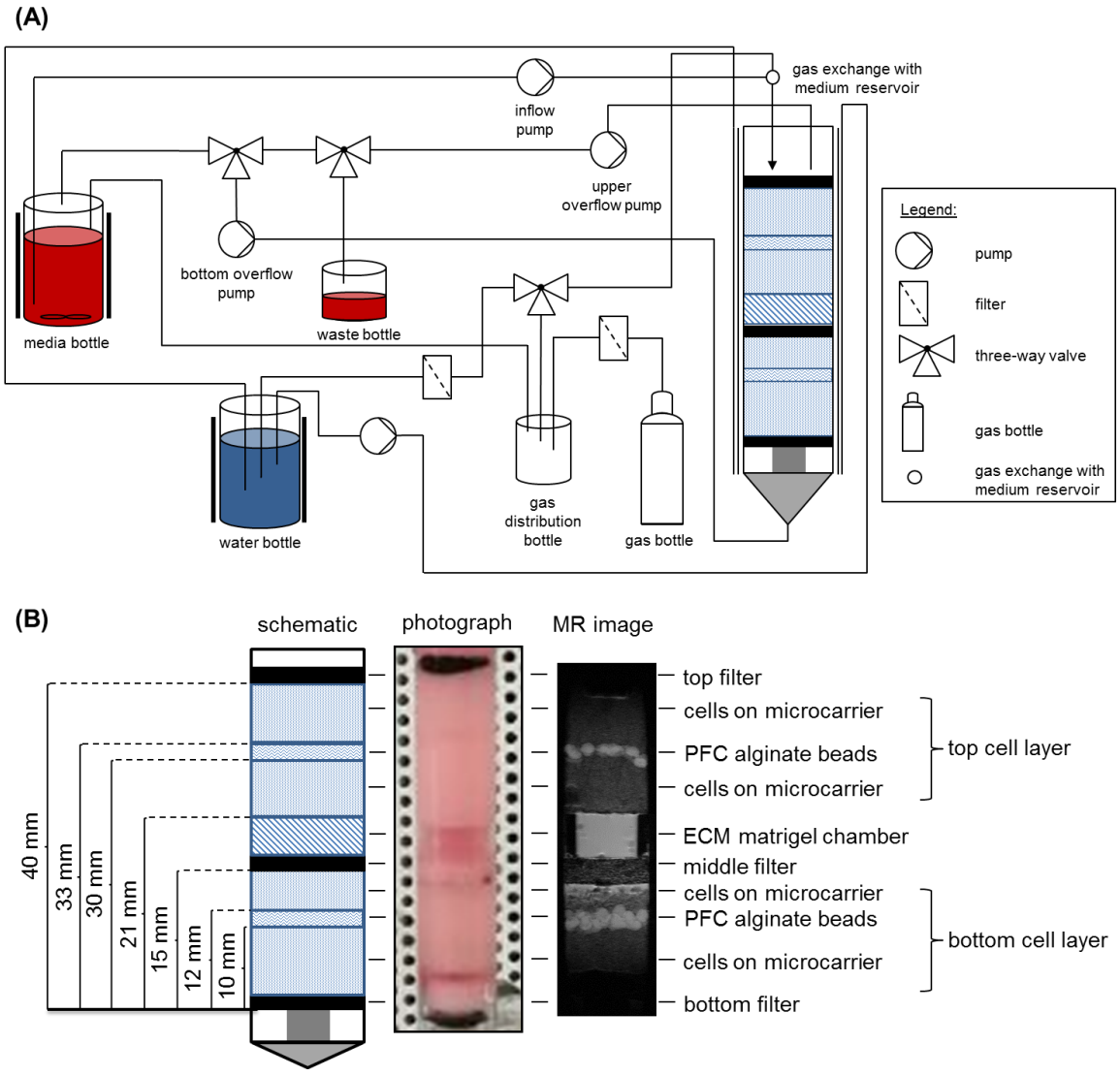

Figure 9: Schematic representation of the MR-compatible cell perfusion system set-up.
(A) Representation of the individual components of the MR-compatible cell perfusion system. The set-up consists of a **(B)** glass tube loaded with cells coated on microcarrier beads, perfluorocarbon (PFC) alginate beads and an extracellular matrix (ECM) Matrigel chamber as well as a top and bottom filter. The glass tube containing the cells on microcarrier beads is warmed and continuously perfused from top to bottom, with oxygen enriched, warm (37°C) cell culture media. The schematic representation is based on [325, 359] with minor modifications.

In the present study, metabolic changes and ECM degradation of control and senescent H-Ras cells was monitored using a MR-compatible cell perfusion system. For control experiments, 2×10^6 H-Ras cells were seeded on 0.5 ml packed

Plastic Plus microcarrier beads (Solohill Engineering) and cultured in the presence of 5 µg ml^{-1} doxycycline hyclate in petri-dishes (Labtec, Nunc, Denmark) for 4 days (**Figure 10**). For senescence experiments, 2×10^6 H-Ras cells were seeded as before on microcarrier beads at day -3, and senescence was induced by doxycycline hyclate withdrawal at day 0. Cells were maintained in senescence conditions for 3 extra days. Cells were loaded into the MR-compatible cell perfusion system 4 days (control) or 6 days (senescence) after being seeded on the microcarrier beads and were maintained in a continuous media flow with (control) or without (senescence) 5 µg ml^{-1} doxycycline hyclate for another 2 days (**Figure 10**). During the experiment, the media pH_e in the MR-compatible cell perfusion system was kept between 7.4 and 7.7 and the temperature was maintained at 37°C for all experiments. Oxygen levels were kept constant by a continuous flow of a mixture of 95% O_2 and 5% CO_2 into the system.

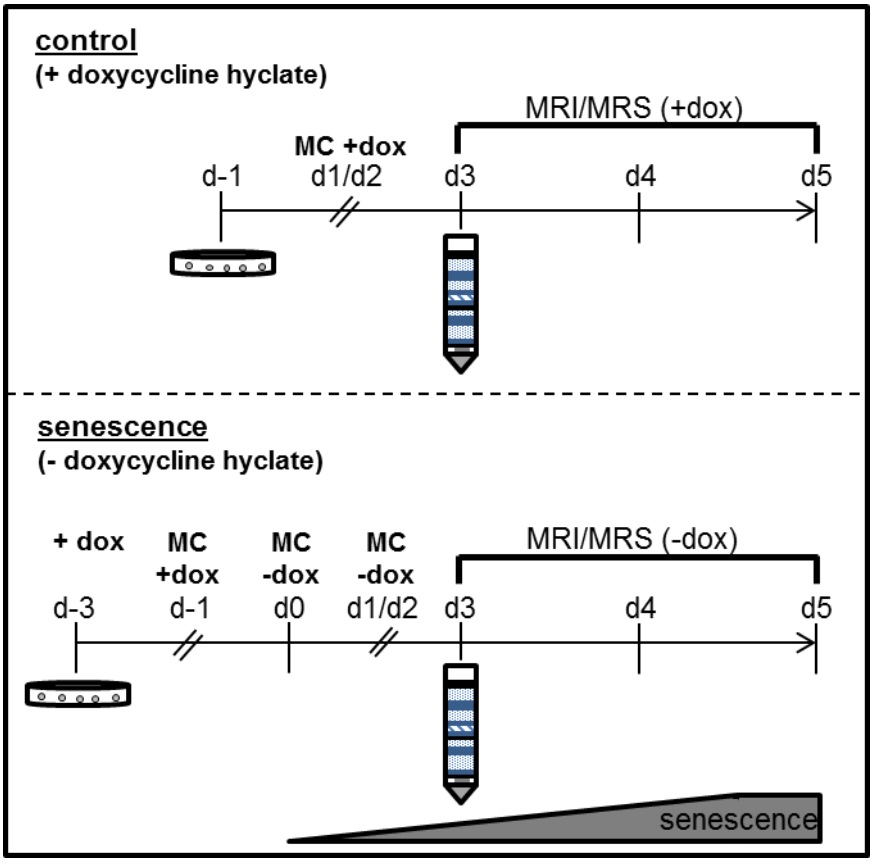

Figure 10: Schematic representation of senescence induction in H-Ras cells cultured in a 3D-like setting on microcarrier beads subjected to MRI and MRS analysis.

H-Ras cells were seeded on microcarrier beads in a 100 mm TC-dish in the presence of 5 µg ml^{-1} doxycycline hyclate (Dox). Senescence was induced by doxycycline hyclate withdrawal via thoroughly washing the cells with PBS at the indicated time point followed by a media change (MC).

Cells were then cultured in the presence (control) or absence (senescence) of 5 µg ml^{-1} doxycycline hyclate and loaded into the MR-compatible cell perfusion system at day 3 (d3) and subjected to longitudinal MRI and MRS measurements until day 5 (d5).

The MR acquisitions were obtained on a 9.4 T MR spectrometer (Bruker) every 12 h over a period of 2 days (till day 5; **Figure 10**), as also previously described [325, 360]. Proton MRI was performed to image the ECM gel geometry and to determine the degree of ECM gel degradation by control or senescent H-Ras cancer cells. For two-dimensional (2D) images from a 2 mm central slice, a spin-echo imaging sequence with a 40 mm field of view (FOV), a Repetition Time (TR) of 1 s, and an Echo Time (TE) of 30 ms were used. Degradation of ECM was determined by drawing region of interest (ROI) around the ECM gel region in the T_1-weighted images at the respective time points using ImageJ 1.4.9v software (National Institutes of Health, Bethesda, MA, USA). The degradation index (DI) was calculated based on **Equation 2**.

$$DI = -\left(\frac{ROI_{t=x} - ROI_{t=0}}{ROI_{t=0}}\right) * 10 \qquad \textbf{Equation 2}$$

Where $ROI_{t=x}$ is the ROI area at the time point x (d3, d3.5, d4, d4.5 and d5) and $ROI_{t=0}$ is the ROI area at the initial time point.

As described by Shah *et al.* intracellular total choline (tCho) , total creatine as well as lactate and lipid (Lac/lipid) levels were obtained from global, diffusion weighted (DW) ^{1}H MR spectra [360]. The represented tCho levels comprise PC, GPC and free choline, whereas the total creatine levels shown comprise the signals from creatine and phosphocreatine [360]. Similar settings for 1D ^{1}H spectra acquisitions were used as described by Shah *et al.* Briefly, for a 1D ^{1}H spectra acquisition, a DW stimulated echo pulse sequence with a CHESS water suppression with TR 2 s, 4 kHz sweep width, 2 k data points, and 128 scans that were processed with a 5 Hz line broadening was applied. DW water suppressed 1D ^{1}H MR spectra with TR 2 s, 4 kHz sweep width, 2 k data points, 256 averages, and 8 Hz line broadening were acquired using lactate editing [361] to determine changes in intracellular lactate. The H-Ras cell proliferation was indirectly measured by acquiring DW 1D ^{1}H MR spectra with eight averages and without water suppression. Subsequently, the measured metabolite signals were

normalized to the number of H-Ras cells in the MR-compatible cell perfusion system. Phosphor containing metabolites including PC and GPC were determined by performing global 1D ^{31}P MR spectra measurements [362]. The ^{31}P spectra were obtained by acquiring 4000 scans with a 45° RF pulse and TR 1 s, 10 kHz sweep width, 2 k data points, and 15 Hz line broadening. Each experiment was carried out at least 3 times. All MR data were processed using XsOs MR Software [363].

MRI and MRS measurements were performed and analyzed by me and approved by Dr. Jesus Pacheco Torres.

3.3 *In silico* analysis of The Cancer Genome Atlas dataset

Regulation of gene expression varies across different cancer types as well as between individual cancer patients and therefore represents a unique fingerprint of a malignant tumor. Transcription levels and alterations of certain key proteins like e.g., p53 or PD-L1 can contribute to cancer progression and can represent a prognostic biomarker for clinical outcome. In this regard, the *Pd-l1* expression levels across different human cancer types were evaluated and *Pd-l1* expression was assessed for being a prognostic biomarker. Furthermore, the question was raised, whether colorectal cancers high in *Ifn-γ* and *Stat1* expression also show elevated *Pd-l1* expression levels, which would be an indication for IFN-γ-induced *Pd-l1* mRNA expression. Colorectal cancer samples were used for this correlation analysis, as the studied murine MC38^{wt} and CT26^{wt} cell lines in this thesis are both colon carcinomas.

To answer the addressed questions, RNA-sequencing (RNA-seq) data of The Cancer Genome Atlas (TCGA) project (https://www.cancer.gov/tcga) of the Genomic Data Commons (GDC) curated by The Human Protein Atlas was used. The RNA-seq data set comprises of 17 major cancer types ranging from 102 patients' samples for melanoma up to 1075 patients' samples for breast cancer and allows a genome-wide transcriptional analysis. For the RNA-seq data analysis a detection threshold of 1 number Fragments Per Kilobase of exon per Million reads (FPKM) was applied and the data were analyzed in a system-level analysis as described by Uhlen *et al.* [364] to generate The Human Pathology Atlas (https://www.proteinatlas.org/humanproteome/pathology). Some major cancer types comprise of subtypes, like colorectal cancer includes colon and rectum

adenocarcinomas [205, 364]. The Human Protein Atlas provides clinical meta data including age, gender, race, or stage of cancer. Clinical outcome analysis for the expression levels of certain proteins of interest using Kaplan-Meier survival plots were performed by Uhlen *et al.* as described in [364]. For *Ifn-γ* vs. *Pd-l1* and *Stat1* vs. *Pd-l1* correlation analysis in malignant tumor tissue, the RNA-seq data for the respective protein was extracted from The Human Pathology Atlas for colorectal cancer (438 patients with colon adenocarcinoma and 159 patients with rectum adenocarcinoma). The individual tumor samples for the respective gene transcripts (*Ifn-γ*, *Stat1*, *Pd-l1*) were matched according to their TCGA sample ID. Next a nonparametric Spearman correlation was computed, and a two-tailed P value was computed (*P<0.05). In addition, a linear regression analysis was performed, and presented in the respective graph.

3.4 *In vivo* methods

3.4.1 Animal experiment licenses

Animal experiments were performed at two institutions and the local guidelines were followed for all animal handling, housing, and intervention procedures at the respective institution.

University of Tübingen:

All animal experiments conducted at the Werner Siemens Imaging Center (Tübingen, Germany) were approved by the Regierungspräsidium Tübingen (R 10/17, R 03/18, R 01/19 G, R 11/19 G) and were in concordance with German federal regulations. The veterinarians at the University of Tübingen were consulted for planning and conducting *in vivo* animal experiments.

Johns Hopkins University:

All animal experiments conducted at the Johns Hopkins School of Medicine (Baltimore, MD, USA) were in accordance with experimental protocols approved by the Institutional Animal Care and Use Committee of the Johns Hopkins University School of Medicine and conform with the Guide for the Care and Use of Laboratory Animals published by the National Institutes of Health.

3.4.2 Mouse strains, breeding and husbandry conditions, interventions

Animal experiments were performed at two institutions. Mice were purchased from local vendors and husbandry conditions vary between institutions.

University of Tübingen:

Female C57BL/6J and BALB/c mice were purchased from Charles River Laboratories (Sulzfeld, Germany) at the age of 6-7 weeks. For the studies relating to the identification of tumor-draining LNs of *s.c.* $MC38^{wt}$ colon adenocarcinomas in chapter 4.3, female as well as male C57BL/6J mice bred at the animal facility Tübingen were used. Animals were kept in type 2 long individually ventilated cages under low-germ conditions at the Werner Siemens Imaging Center. A maximum of 5 animals were kept in a cage. Animals were provided with enrichment like timber houses and cellulose. Water as well as standard rodent pellet food was provided *ad libitum*. Animals were used for experiments 2 weeks after delivery. B6.129S7-Ifngtm1Ts/J mice [365] were purchased from The Jackson Laboratory and bred in the animal facility Tübingen. For direct comparison and in consideration of the animal facility specific microbiome, C57BL/6J mice bred in the same animal facility were used for the respective experiments as control animals. Animals used for the studies were at the age of 8 to 10 weeks and maintained in individually ventilated cages at the animal facility of the Werner Siemens Imaging Center.

For experiments animals either received regular drinking water or drinking water enriched with 200 mM sodium bicarbonate (3 days prior to cancer cell inoculation) [77] *ad libitum*. Tumors were inoculated by *subcutaneous* (*s.c.*) injection of 500.000 $MC38^{wt}$, 500.000 $MC38^{PD\text{-}L1\text{-}/\text{-}}$, 500.000 $MC38^{STAT1\text{-}/\text{-}}$, 100.000 $CT26^{wt}$ or 100.000 $CT26^{PD\text{-}L1\text{-}/\text{-}}$ cells in PBS into the right shoulder. B16-$F10^{wt}$ cancer cells were inoculated by *intracutaneous* (*i.c.*) injection of 125.000 cells in PBS into the right shoulder. $4T1^{wt}$ cancer cells were inoculated by injection of 200.000 cells in PBS into the fourth mammary fat pad. Tumor outgrowth was measured in two dimensions (length and width) and tumor volume was calculated using the **Equation 3**.

$$tumor\ volume = \frac{(length * width * width)}{2} \qquad \textbf{Equation 3}$$

Tumor-bearing mice were treated *intraperitoneally* (*i.p.*) every third day with 200 µg

of a PD-L1 blocking antibody (anti-PD-L1 mAb, clone 10F.9G2, Bio X Cell, West Lebanon, NH, USA) or IgG2b isotype antibody (control, clone LTF-2, Bio X Cell) starting from day 4 ($MC38^{wt}$, $CT26^{wt}$, B16-F10) or day 5 (4T1) post cancer cell inoculation. Mice were sacrificed due to tumor burden or weight loss according to the local guidelines and regulations or at a pre-defined time point.

Johns Hopkins University:

For *in vivo* experiments, 5-7-week-old female BALB/c mice were purchased from Charles River Laboratories (Wilmington, MA, USA). Animals were kept in individually ventilated cages at the animal facility at Johns Hopkins School of Medicine.

For *in vivo* hypoxia measurements $2*10^6$ CT26-HRE-ODD-luc cells were injected *s.c.* on the right shoulder of the animal and $2*10^6$ 4T1-HRE-ODD-luc cells were injected in the second mammary fat pad. The tumor dimensions length, width and height were taken, and the tumor volume was calculated using the **Equation 4**.

$$tumor\ volume = (length * width * hight) * 0.52 \qquad \textbf{Equation 4}$$

Mice were sacrificed due to tumor burden according to the local guidelines and regulations or at a pre-defined time point.

3.4.3 Optical Imaging

OI is a non-invasive imaging technology used for *in vivo* diagnostics and therapy monitoring, both pre-clinical as well as clinical. Planar imaging, a subcategory of OI allows *in vivo* fluorescence as well as bioluminescence imaging. Fluorescence imaging can be applied to detect TDLN by either using Patent Blue V [354] or the near-infrared dye IRDye® 800CW PEG [366]. The characteristics of the applied imaging agents and their application in previous studies are listed in **Table 15**.

Table 15: Comparison of imaging agents for LN identification.

imaging agent	imaging modality	excitation/ emission wavelength	molecular weight	literature
Patent Blue V (sodium salt)	OI	675 nm / 720 nm	582.7 g mol^{-1} [367]	[354]
IRDye® 800CW PEG	OI	745 nm / 800 nm	25-60 kDa [368]	[366, 369, 370]

On the other hand, hypoxia reporter cell lines expressing the luciferase enzyme upon hypoxia exposure are one example for functional BLI [267, 275]. The enzyme luciferase oxidizes the substrate luciferin in the presence of ATP and Mg^{2+} under the emission of light at a wavelength between 530 to 640 nm [265, 371]. Therefore, OI is used to monitor tumor hypoxia longitudinally.

At both institutions, OI experiments were performed using an IVIS® Spectrum OI system (Perkin Elmer). Mice were anesthetized with 1.5% isoflurane (CP Pharma, Burgdorf, Germany) in 100% oxygen in a temperature-controlled anesthesia chamber. In the IVIS® Spectrum OI system, mice were continuously warmed. Images were analyzed using Living Image Software 4.

University of Tübingen:

For TDLN imaging using Patent Blue V (Guerbet, Roissy CdG Cedex, France) and IRDye® 800CW PEG (LI-COR Bioscience), mice were anesthetized with 1.5% isoflurane in 100% oxygen and depilated prior to OI. For TDLN imaging using FDA approved Patent Blue V, 12.5 µl of the dye (25 mg ml^{-1}) were injected *s.c.* near the $MC38^{wt}$ tumor (day 7 post cancer cell injection) on the right shoulder of the animal. Following a 5 min uptake, fluorescence imaging was performed using a 1 s exposure time, f-Stop 2, an excitation wavelength of 675 nm and an emission wavelength of 720 nm.

For near infrared fluorescence imaging of TDLN, 25 µl IRDye® 800CW PEG reconstituted in PBS (0.1 nmol) were injected *s.c.* near the $MC38^{wt}$ tumor (day 7 post cancer cell injection) on the right shoulder of the animal. Following a 30 min contrast agent uptake, fluorescence imaging was performed using auto exposure, f-Stop 2, medium binning, a FOV of 14 cm, an excitation wavelength of 745 nm and an emission wavelength of 800 nm. Twenty-five segments with a delay of 1 min were acquired. *Ex vivo* imaging of the relevant LNs was performed with the settings used for the respective contrast agent.

Johns Hopkins University:

For longitudinal *in vivo* tumor hypoxia imaging of CT26-HRE-ODD-luc tumors, 150 mg kg^{-1} VivoGlo™ Luciferin P1042 were injected *i.p.* in a volume of 100 µl PBS. Following a 15 min uptake, BLI was performed using an exposure time of 30 s, f-Stop 1, medium binning and a FOV of 12.8 cm as previously described

[267].

3.4.4 Positron Emission Tomography/Magnetic Resonance Imaging

Combined PET and MRI is a powerful method to visualize in particular deep-tissue TDLN [372]. Therefore, the PET tracer [^{18}F]FDG with a molecular weight of 181.2 g mol^{-1} can be applied [373, 374].

For [^{18}F]FDG-PET measurements, a small-animal Inveon microPET scanner (Siemens Healthineers, Knoxville, TN) was applied. For anatomical information, [^{18}F]FDG-PET images were merged with MR images acquired at a small-animal 7T MRI system (Bruker) using a 3D T2-TurboRARE (TE 4,763 ms, TR 1800 ms, matrix 256x256x64, FOV 76.8x34.8x22.8 mm³, resolution 0.3x0.3x0.3 µm³, total acquisition time 9 min 7 s 200 ms) without a breathing trigger. At day 7 post MC38^{wt} cancer cell injection, mice were anesthetized 5 min to 10 min prior [^{18}F]FDG tracer injection with 1.5% isoflurane in 100% oxygen in a temperature-controlled anesthesia chamber. Blood glucose concentration was measured prior PET tracer injection and ranged from 126-161 mg dl^{-1}. Mice were *s.c.* injected 3.3 – 4.0 MBq [^{18}F]FDG in proximity to the MC38^{wt} tumor on the right shoulder of the mouse. Dynamic PET scans were acquired 2 min post tracer injection for 60 min with 13 frames and an image size of 128. Images were reconstructed using OSEM 3D without maps and the last frame between 50 min and 60 min is shown. PET images were processed and smoothed using a Gaussian filter with the Inveon Research Workplace (Siemens Healthineers). For *ex vivo* biodistribution analysis TDLN and NTDLN were exposed to γ-counting analysis. Counts were radioactive decay corrected and represented as % injected dose (ID). Furthermore, autoradiography of the respective TDLN and NTDLN was performed.

3.4.5 acido Chemical Exchange Saturation Transfer-MRI

In recent years, acido chemical exchange saturation transfer MRI (acidoCEST-MRI) measurements were developed and continuously improved to non-invasively measure tumor pH_e in the range of 6.2 to 7.4 *in vivo* [322-324]. Therefore, the FDA-approved CT contrast agent iopamidol (Isovue®, Bracco Diagnostics, Milan, Italy) is commonly applied. This external contrast agent consists of three labile amide protons, whose exchange rate with water is markedly pH_e dependent. These amid protons generate two CEST signals after saturation at 4.2 and 5.6 ppm. Upon selective irradiation of the two resonances, saturation transfer effects are induced

and compared to determine the tumor pH_e [375-378].

In vivo MR imaging was performed on a pre-clinical 7 T BioSpec 70/30 MR scanner with a ^1H volume coil (inner diameter: 86 mm; Bruker). Experimental animals were anesthetized with 1.5% isoflurane in compressed air as carrier gas (flow rate: 0.8 L min^{-1}). For contrast agent infusion, a catheter was placed into a lateral tail vein. Correct positioning of the animals was achieved with the aid of a short T_1-weighted FLASH sequence (**Table 16**). $MC38^{wt}$ tumors on the right shoulder were localized using a standard axial 2D T_2-weighted TurboRARE protocol (**Table 16**). Body temperature was monitored with a rectal probe and maintained between 35.0-37.8 °C with water-heating systems (Medres, Cologne, Germany). While respiration was monitored and breathing rate was kept between 30-50 breaths per minute, respiratory gating was not performed. Single-slide acidoCEST-MRI was performed using a previously established protocol combining saturation pulses with a fast imaging with steady-state precession (FISP) acquisition [322, 323], cestFISP sequence details are given in **Table 16**.

Resulting spectra were fit in MATLAB (MATLAB R2017b, MathWorks, Inc., Natick, MA) with a previously described Bloch fitting analysis method to generate pH_e maps [324, 375, 376]. Briefly, the pre-injection and post-injections images, respectively, were averaged at each saturation frequency and smoothed with a Gaussian spatial smoothing algorithm. The resulting averaged and smoothed pre-injection image was subtracted from the post-injection image at each saturation frequency to correct for endogenous CEST signals. CEST spectra for each pixel were fitted with the Bloch-McConnell equations for the CEST effects from iopamidol at 4.2 and 5.6 ppm as well as the water peak; pixels with insufficient contrast (defined as std_noise*2√2/mean_signal) were excluded. Additionally, pixels with pH_e values below pH 6.2 and above pH 7.4 were excluded from the analysis. The calculated pH_e map was overlaid on the anatomical reference and data is given as average pH_e value derived from the sum of individual pixels.

Table 16: Acquisition parameters for MR imaging.

	T1 FLASH	T2 TurboRARE	cestFISP
TE	2.670 ms	33.580 ms	1.435
TR	100 ms	5551.773 ms	2.870
Flip Angle	30.0°	-	30.0°
Spatial Resolution	0.43x0.43	0.3x0.3 mm²	0.6x0.6 mm²
Matrix Size	256x256	128x128	64x64
FOV	110x100 mm²	38.4x38.4 mm²	38.4x38.4 mm²
Slice thickness	1 mm	1 mm	1 mm
Number of averages	1	1	
Number of repetitions	1	1	
Number of CEST spectra	-	-	4 pre-injection, 6 post-injection
Saturation power	-	-	3 µT
Saturation pulses (pulse duration)	-	-	60 (100 ms)
Number of saturation frequencies	-	-	40
Saturation frequency range (increments), Hz	-	-	-30000 -4500 to -3600 (900) -3600 to 0 (600) 0 to 2100 (75) 2100 to 2700 (600) 2700 to 4500 (900)
Total acquisition time	12 s 800 ms	1 min 28 s 828 ms	44 min 22 s

AcidoCEST-MR measurements were performed by Dr. Sabrina Hoffmann and analyzed by Dr. Sanhita Sinharay and Prof. Dr. Mark D. Pagel.

3.4.6 Histology and Immunohistochemistry

Histology is a widely applied method to assess the composition, structure, and characteristics of healthy and pathologic tissue to provide diagnostic information and allow physicians to make adequate treatment decisions. Therefore, tissue is formalin-fixed, and paraffin-embedded before staining with e.g., hematoxylin and eosin (H&E). Nucleic acids and nuclei are stained blue by hematoxylin, whereas eosin non-specifically stains proteins pink and therefore visualizes the ECM and the cytoplasm of cells [379]. Therefore, tumor tissue stained with H&E allows the identification of necrotic tumor tissue. To study the expression of certain markers

on different cellular subsets within the tumor, immunohistochemistry (IHC) is a powerful tool. In this regard IHC is applied to stain for tumor tissue PD-L1 expression and therefore select patients based on the expression of this predictive biomarker of response to a PD-1 inhibitor therapy with pembrolizumab. Expression analysis of PD-L1 by IHC allows the identification of NSCLC patients with an increased response prognosis to pembrolizumab [380]. Furthermore, IHC is applied to quantify and visualize the distribution of tumor infiltrating immune cells like T cells (CD3) or macrophages (Iba1) and therefore allows the characterization of the TME cellular composition [381]. Taken together, histology and IHC was applied to detect tumor necrosis, characterize the immune cell composition, and determine PD-L1 expression in murine tumor tissue samples.

Tumors extracted from mice were halved and fixed in 4.5% neutral buffered formalin (SAV Liquid Production, Flintsbach am Inn, Germany) for at least 24 h. Next, tumor tissue was dehydrated using a Leica TP1020 dehydrator (Leica Biosystems, Nussloch, Germany). First the tissue was fixed twice for 1 h in 4.5% formalin followed by increasing ethanol (SAV Liquid Production) concentrations (70% ethanol for 45 min, twice 96% ethanol for 45 min each, three times in 99% ethanol for 45 min and 1 h). Then the tumor tissue was transferred in xylol (45 min and 1 h, Thermo Scientific) followed by two steps in paraffin (1.5 h and 2 h, Leica Biosystems). Tumor tissue was embedded in paraffin using the Leica EG1150C (Leica Biosystems) embedding machine. The morphological and immunohistochemical features were analyzed on formalin-fixed and paraffin-embedded tissue sections. For histology 3-5 µm-thick sections were cut and stained with H&E.

Necrosis was evaluated and measured in H&E-stained tumor tissue sections. The entire tumor area was photographed at 12.5x magnification. The images were acquired with an Axioskop 2 plus Zeiss microscope equipped with a Jenoptik (Laser Optik System, Jena, Germany) ProgRes C10 plus camera and the respective software. The total area of the tumor and necrosis has been measured with the IMS Client Software. The areas are given as mm^2 and necrosis with an area smaller than 0.01 mm^2 were not considered.

IHC was performed on an automated immunostainer (Ventana Medical Systems, Inc., Oro Valley, AZ) according to the manufacturer's instructions for open procedures with slight modifications [382]. The antibody panel used included CD3

(1:50, clone SP7), PD-L1 (1:50), Iba1 (1:3000) and HIF-1α (1:12000, clone ESEE 122). Detailed information is provided in **Table 17**. Appropriate positive and negative controls (without primary antibody) were used to confirm the adequacy of the staining. For validation of CD3 and Iba1 staining, splenic tissue served as a positive control. Brain infarct tissue was used for validation of HIF-1α staining. Splenic tissue as well as $MC38^{PD\text{-}L1\text{-}/\text{-}}$ and $CT26^{PD\text{-}/\text{-}}$ tumor tissue with no PD-L1 expression on cancer cells, but PD-L1 expression on macrophages served as a positive control for PD-L1 staining.

Table 17: List of antibodies used for IHC analysis.

antibody	monoclonal	polyclonal	company	item no.
CD3	X		DCS Innovative Diagnostik-Systeme	C1597C01
PD-L1	X		Cell Signaling	13684
Iba1	X		abcam	ab178846
HIF-1α	X		abcam	ab8366

Tumor tissue samples for histology and IHC were prepared by me. Histology and IHC were performed, and tumor tissue slides were assessed by Dr. Irene Gonzalez-Menendez and Prof. Dr. Leticia Quintanilla-Martinez. The reported results were interpreted by me, Dr. Irene Gonzalez-Menendez, Prof. Dr. Leticia Quintanilla-Martinez, and Dr. Manfred Kneilling.

3.5 Statistical analyses

Graphs were generated and the respective statistical analysis was performed using the software GraphPad Prism (Version 7.03, GraphPad Software, Inc., USA). If not indicated differently, the mean was calculated and presented with the standard error of the mean (SEM). The number of independent experiments as well as the total number of replicates (n) is indicated in the respective figure legend. Statistical significance was either determined by Tukey`s multiple comparison, Sidak`s multiple comparison or Mann Whitney test (one-tailed or two-tailed) with a confidence level of 95%. Statistical difference of tumor pH_e determined by acidoCEST-MRI between the sodium bicarbonate-treated $neutral^{IFN\text{-}\gamma}$ and the untreated $acidosis^{IFN\text{-}\gamma}$ group was determined by a one-tailed Mann Whitney test, as only the increase of tumor pH_e upon sodium bicarbonate treatment was tested

for statistical significance. For correlation analysis between two parameters, nonparametric Spearman correlations were computed. The statistical test applied is indicated in the respective figure legend.

To identify outliers within a dataset, a two-sided Grubbs' test was performed. Hierarchical clustering heatmaps of metabolomics data were generated with MetaboAnalyst 4.0 (http://metaboanalyst.ca) [383]. The concentrations of individual metabolites were mean-centered and divided by the standard deviation of each variable for representation. Statistical significance was determined by Fisher's Least Significant Difference (LSD) test, which does not correct for multiple comparisons. Statistical significance of MR data acquired from the MR-compatible cell perfusion system was determined by multiple t-tests without correction for multiple comparisons. Extreme Studentized Deviate (ESD) method was performed. This test is applied to identify one outlier within each set of data, which is by far larger or smaller than the rest [384, 385]. It is indicated in the respective figure legend when a data point has been removed based on a two-sided Grubbs' test. The *in vivo* experiments were not randomized, and the investigators were not blinded to allocation during the experiments or outcome assessment. For significance level determination, the commonly used notation (*** corresponds to 0.0001≤ P-value <0.001, ** corresponds to 0.001≤ P-value <0.01, * corresponds to 0.01≤ P-value <0.05, ns corresponds to a P-value ≤ 0.05) was applied.

4 Results

4.1 Tumor immune escape by IFN-γ- and acidosis-induced PD-L1 expression via the eIF4F-STAT1-PD-L1 axis

Beside the cellular composition of the TME, acidosis and hypoxia are two main features that determine tumor progression and restrict immune surveillance. Therefore, the role of acidosis and hypoxia attracted great attention in recent years. Nevertheless, the role of tumor acidosis on immune escape and the interplay between hypoxia, acidosis as well as immune cell recruitment and activation are insufficiently studied. Furthermore, it remains elusive, how acidosis contributes to immune escape by affecting the expression of immune checkpoint proteins in the context of immune cell secreted cytokines like IFN-γ.

4.1.1 Establishment of acidic cell culture media for *in vitro* experiments

The pH_e of tumors is acidic due to the high demand and turnover of energy metabolites like glucose by cancer cells. Upon conversion of glucose into pyruvate, lactate is subsequently generated in a well-described process termed the Warburg effect. Lactate together with H^+ is exported by MCT1 or MCT4 symporters and acidifies the tumor pH_e. Furthermore, energy which is required for tumor progression is generated by ATPase activity, leading to an increase in extracellular H^+ [46, 55].

In order to study the effect of acidic pH_e on membrane-bound PD-L1 expression by cancer cells *in vitro*, the pH_e of the cell culture media was adjusted by either lowering the $NaHCO_3$ concentration or by adding an acid like HCl [386, 387]. In the first place, unbuffered DMEM media was supplemented with 10% FBS, 100 U ml^{-1} penicillin-streptomycin and different concentrations of $NaHCO_3$ ranging from 0 mM to 44.05 mM. The cell culture media was incubated at 37 °C and a 5% CO_2 atmosphere to allow pH_e adjustment. The pH_e was measured with a pH_e electrode after 5 h and 24 h and no significant difference in pH_e was observed between both time points. This indicates a 5% CO_2 atmosphere-related pH_e adjustment and stabilization as early as after 5 h. A moderate acidic pH_e of 6.8 was measured at a concentration of 4 mM $NaHCO_3$ in DMEM cell culture media (**Figure 11 A**). A change of pH_e in the cell culture media upon varying $NaHCO_3$ concentrations could further be visualized by a change in color from red (pH_e 7.4)

to orange (pH_e 6.8) and to yellow (pHe 6.4) due to the phenol red pH_e indicator (**Figure 11 B**). A pH_e of 6.8 was chosen for the continuative *in vitro* experiments, as it represents the approximate pH_e detected in several solid tumor entities [77, 324, 388]. The concentration of 4 mM $NaHCO_3$ resulting in a pH_e of 6.8 is slightly higher than the concentration reported by others (2 mM $NaHCO_3$) [386, 387]. This might be related to small differences in CO_2 partial pressure in the cell culture incubators between individual labs or due to different cell culture media preparation protocols. Kondo *et al.* autoclaved their cell culture media after dissolving the DMEM powder and $NaHCO_3$ in water [387], whereas in the presented thesis the prepared cell culture media was sterile filtered. Furthermore, the buffering capacity of FBS can vary between batches and therefore might explain the slightly higher $NaHCO_3$ concentration determined and applied for *in vitro* experiments in this thesis. The neutral cell culture media with a concentration of 44.05 mM $NaHCO_3$ resulted in a pH_e of 7.7 in the absence of cells to ensure sufficient buffering capacity over a time course of maximum 72 h when cancer cells proliferate and acidify the cell culture media.

Another way of establishing an acidic cell culture media is to use fully buffered DMEM (44.05 mM $NaHCO_3$) media supplemented with 10% FBS, 100 U ml^{-1} penicillin-streptomycin and gradually increasing HCl concentrations ranging from 0 mM to 50 mM. Titration resulted in a HCl concentration between 30 mM and 40 mM associated with a pH_e of approximately 6.8 in the cell culture media. The acidic pH_e was measured by a pH_e electrode and visualized by phenol red (**Figure 11 C, D**).

Although both methods are equally well suited to lower the pH_e, a defined cell culture media pH_e of 6.8 was established by adjusting the $NaHCO_3$ concentration to 4 mM in DMEM for all *in vitro* experiments with murine $MC38^{wt}$ and $B16\text{-}F10^{wt}$ as well as human HCA-7 colony 29 cells, MCF-7, MIA-PaCa-2, SK-MEL-28, and U87 MG cells.

Next, the pH_e was titrated for RPMI-1640 cell culture media supplemented with 10% FBS, 100 U ml^{-1} penicillin-streptomycin and varying concentrations of $NaHCO_3$ ranging from 0 mM to 23.81 mM. The cell culture media pH_e was again adjusted at 37 °C in a 5% CO_2 atmosphere and determined after 5 h and 24 h. This resulted in a pH_e of 6.8 when applying a $NaHCO_3$ concentration of 1 mM (**Figure 11 E, F**). Respectively a concentration of 23.81 mM (pH_e 7.5) or 1 mM $NaHCO_3$ (pH_e 6.8) in

RPMI-1640 was applied for all *in vitro* experiments with murine CT26^{wt} and 4T1^{wt} cells.

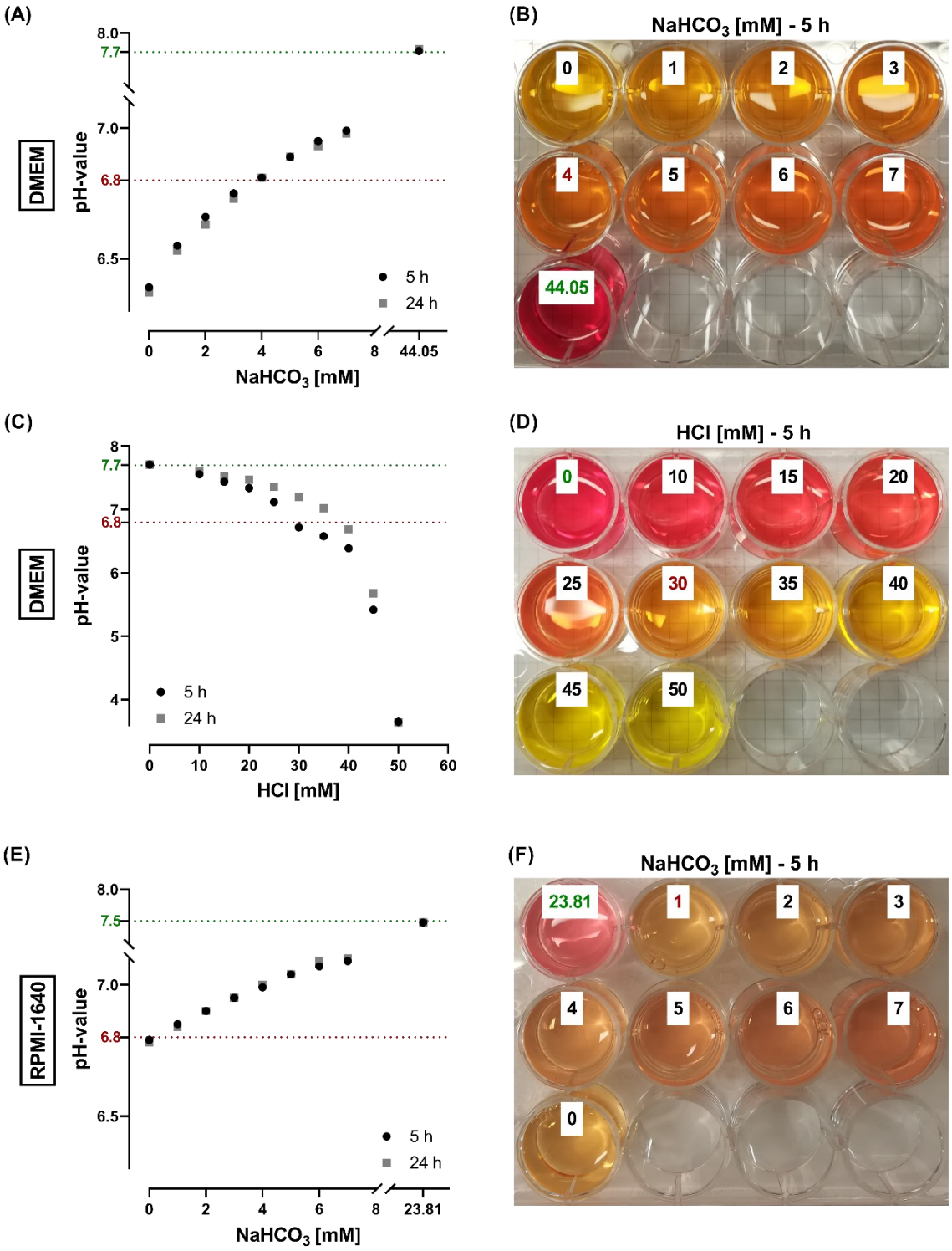

Figure 11: Establishment of neutral and acidic cell culture media for *in vitro* experiments. The DMEM-based cell culture media pH_e values were determined by a pH_e electrode **(A, C)** or the media pH_e was visualized by the pH_e color indicator phenol red **(B, D)** in DMEM supplemented with 10% FBS, 100 U ml^{-1} penicillin-streptomycin and different concentrations (0 - 44.05 mM) of

$NaHCO_3$ or different concentrations (0 - 50 mM) of HCl in a 12-well cell culture plate. The RPMI-based cell culture media pH_e values were determined by a pH_e electrode **(E)** or the media pH_e was visualized by the pH_e color indicator phenol red **(F)** in RPMI-1640 supplemented with 10% FBS, 100 U ml^{-1} penicillin-streptomycin and different concentrations (0 - 23.81 mM) of $NaHCO_3$ in a 12-well cell culture plate. The pH_e of the cell culture media was adjusted at 37 °C and 5% CO_2 atmosphere in a cell culture incubator and determined after 5 h and 24 h.

For all *in vitro* experiments, a consistent terminology was chosen, independent whether cells were maintained in DMEM or RPMI cell culture media. Neutral cell culture conditions (pH_e 7.7 for DMEM, pH_e 7.5 for RPMI) are abbreviated with N, whereas acidic cell culture conditions (pH_e 6.8) are abbreviated with A. In the presence of IFN-γ the abbreviations $N^{IFN\text{-}\gamma}$ and $A^{IFN\text{-}\gamma}$ were applied, respectively.

4.1.2 Expression of surrogate markers and inhibition of proliferation upon acidic cell culture conditions

To confirm pH_e adjustment of acidic cell culture media *in vitro* and its effect on $MC38^{wt}$ cells, expression of acidosis surrogate markers was determined. Therefore, $MC38^{wt}$ cells were cultured in neutral or acidic media for 24 h followed by RNA isolation. Next, the gene expression of the previously reported acidosis surrogate markers *Stat2* (supplement information Table S2 in [389]), *Mmp-2* and *Mmp-9* [390] was determined by qRT-PCR analysis. Due to the far-reaching effects of extracellular acidosis on cancer cells and the expression of various genes, the three well known and frequently applied housekeeping genes *Gapdh*, *Aldolase* and *β-actin* were selected. Expression of the target genes *Stat2*, *Mmp-2* and *Mmp-9* was normalized to the mean of the three mentioned housekeeping genes. $MC38^{wt}$ cells exhibited a significant, two-fold elevation in *Stat2*, *Mmp-2* and *Mmp-9* gene expression upon acidic cell culture conditions (**Figure 12 A**). Furthermore, fluorescence microscopy revealed a reduced expression of the proliferation marker Ki67 in $MC38^{wt}$ cells *in vitro* upon extracellular acidosis (**Figure 12 B**).

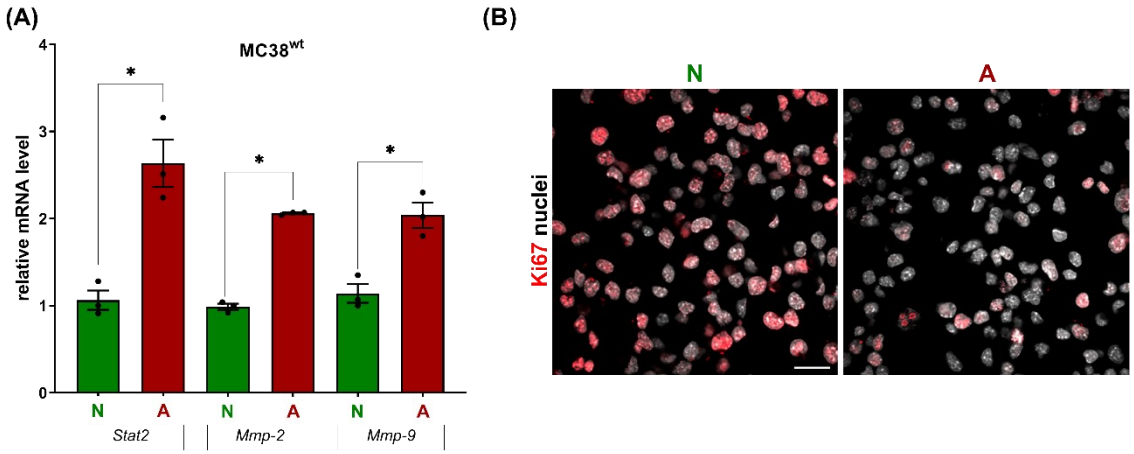

Figure 12: Induction of gene expression of acidosis surrogate markers and inhibition of cell proliferation of MC38^{wt} cells upon acidic cell culture conditions.

(A) Relative *Stat2*, *Mmp-2* and *Mmp-9* mRNA expression normalized to the mean expression of the three housekeeping genes *Gapdh*, *Aldolase* and *β-actin* determined in MC38^{wt} cells upon neutral or acidic cell culture conditions for 24 h (1 independent experiment, n = 3). Data is presented as mean ± SEM. Statistics: one-tailed Mann-Whitney test. **(B)** Fluorescent microscopy visualizing the nuclear expression of the proliferation marker Ki67 (red) and nuclei (white) in MC38^{wt} cells upon neutral or acidic cell culture conditions (1 independent experiment). Scale bar 20 µm. Abbreviations: N = neutral media, A = acidic media.

Taken together, acidic cell culture conditions increased *Stat2*, *Mmp-2* and *Mmp-9* gene expression and reduced Ki67 protein expression in MC38^{wt} cells.

4.1.3 Delineating the effect of acidosis and lactic acidosis on IFN-γ-induced PD-L1 expression in murine cancer cell lines

The initial focus was on delineating the effect of acidosis, lactic acidosis, lactosis and IFN-γ as well as conjoint treatment on PD-L1 expression *in vitro* in murine hypermutated/MSI MC38^{wt} colon adenocarcinoma cells [194, 195]. Therefore, four defined cell culture conditions were established, namely neutral (44.05 mM $NaHCO_3$, N) acidic (4 mM $NaHCO_3$, A), lactic acidic (4 mM $NaHCO_3$, 20 mM sodium L-lactate, LA) and lactosis media (44.05 mM $NaHCO_3$, 20 mM sodium L-lactate, L). In contrast to Braumüller *et al.* where a concentration of 100 ng ml^{-1} IFN-γ was applied [244], a concentration of only 10 ng ml^{-1} IFN-γ was applied in the following *in vitro* experiments taking into account the strongly reduced immune cell-derived IFN-γ protein concentrations in acidic tumor regions. To account for the long-term effects of IFN-γ and acidosis (A$^{IFN-γ}$), lactic acidosis (LA$^{IFN-γ}$) or

lactosis ($L^{IFN-\gamma}$) exposure, $MC38^{wt}$ cells were cultured in the respective defined cell culture media in the absence or presence of 10 ng ml^{-1} IFN-γ for 72 h. Cells were harvested and membrane-bound PD-L1 expression was determined by flow cytometric analysis (**Figure 13 A**). Acidic cell culture conditions significantly increased PD-L1 expression when compared to neutral conditions. Lactic acidic cell culture conditions further elevated PD-L1 expression values (**Figure 13 B**). The increase most likely originates from the acidic media, as lactate alone (L) did not affect PD-L1 cell surface expression in murine $MC38^{wt}$ cells. As expected, stimulation of $MC38^{wt}$ cells with IFN-γ upon neutral cell culture conditions impressively increased membrane-bound PD-L1 expression. Most importantly, IFN-γ stimulation upon acidic cell culture conditions further elevated cell surface PD-L1 expression. This effect was significantly extenuated upon conjoint IFN-γ and lactic acidic media treatment of $MC38^{wt}$ cells. Nevertheless, conjoint IFN-γ and lactic acidic media treatment yielded an increased PD-L1 cell surface expression compared to IFN-γ treatment upon neutral cell culture conditions. Conjoint IFN-γ and lactosis stimulation of $MC38^{wt}$ cancer cells resulted in elevated PD-L1 cell surface expression compared to lactosis cell culture conditions in the absence of IFN-γ. Nevertheless, PD-L1 expression was slightly lower compared to IFN-γ stimulation in neutral cell culture media (**Figure 13 B**).

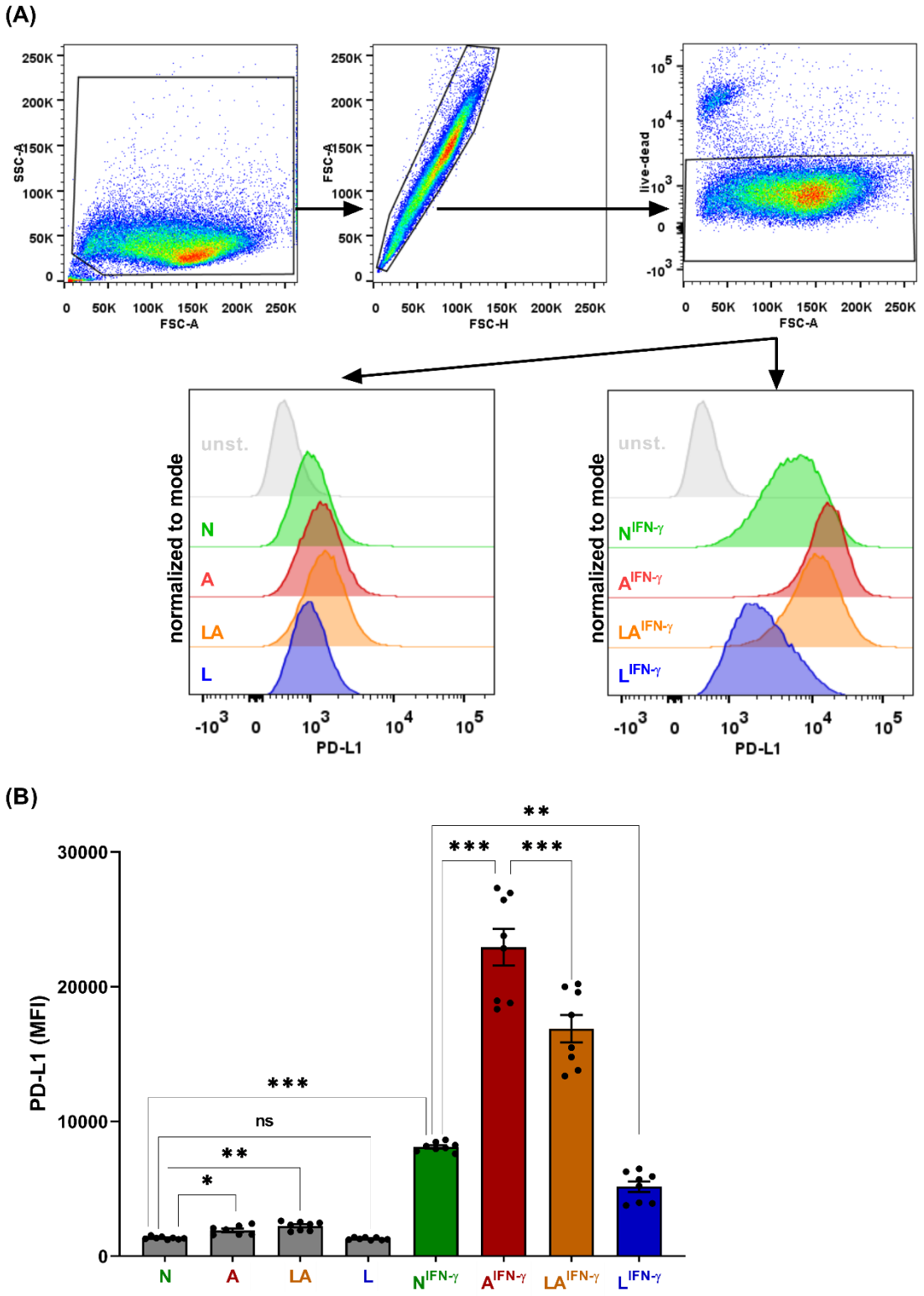

Figure 13: Effect of acidosis, lactic acidosis and lactosis in the absence and presence of IFN-γ treatment on membrane-bound PD-L1 expression on murine MC38^{wt} cancer cells.

MC38^{wt} cancer cells were treated with neutral, acidosis, lactic acidosis or lactosis cell culture media in the absence or presence of IFN-γ (10 ng ml^{-1}) for 72 h. Membrane-bound PD-L1 expression was determined by flow cytometry. **(A)** Gating strategy and histograms normalized to mode of PD-L1 cell surface expression are shown for the different cell culture conditions in the absence (left panel)

or presence (right panel) of IFN-γ. **(B)** PD-L1 mean fluorescence intensity (MFI) on MC38^{wt} cells was determined and quantified (3 independent experiments, n = 8). Data is presented as mean ± SEM. Statistics: Tukey's multiple comparison test. Abbreviations: N = neutral media, A = acidic media, LA = lactic acidic media, L = lactosis media, N$^{IFN-\gamma}$ = neutral media plus IFN-γ, A$^{IFN-\gamma}$ = acidic media plus IFN-γ, LA$^{IFN-\gamma}$ = lactic acidic media plus IFN-γ, L$^{IFN-\gamma}$ = lactosis media plus IFN-γ.

Taken together, acidosis and lactic acidosis increased membrane-bound PD-L1 expression of MC38^{wt} cancer cells whereas lactate alone had no effect. Furthermore, conjoint IFN-γ and acidosis treatment of MC38^{wt} cancer cells increased cell surface PD-L1 expression compared to IFN-γ treatment upon neutral cell culture conditions. Lactate extenuates acidosis-induced PD-L1 expression upon IFN-γ stimulation. These results suggest an important role of acidosis and lactate on the induction of PD-L1 cell surface expression in MC38^{wt} cancer cells in the absence or presence of IFN-γ.

4.1.4 Conjoint IFN-γ- and acidic media-induced PD-L1 gene expression in murine cancer cell lines

Several studies have shown that IFN-γ induces membrane-bound PD-L1 expression. In the IFN-γ signaling cascade, translation of *Stat1* mRNA via the eIF4F complex is crucial for the upregulation of PD-L1 on the cancer cell surface [30].

To investigate the mechanism of PD-L1 upregulation upon conjoint IFN-γ and acidosis treatment compared to IFN-γ stimulation upon neutral cell culture conditions, the induction of *Pd-l1* gene expression was evaluated. Therefore, anti-PD-L1 mAb therapy responsive MC38^{wt} cancer cells were cultured in neutral or acidic cell culture conditions with or without IFN-γ for 72 h and analyzed by qRT-PCR. MC38^{wt} cells cultured in acidic cell culture media failed to up-regulate *Pd-l1* on the mRNA level. In contrast stimulation of MC38^{wt} cells with IFN-γ for 72 h induced *Pd-l1* mRNA expression (**Figure 14 A**). As previously reported in chapter 4.1.3., conjoint treatment of MC38^{wt} cells with IFN-γ and acidic compared to neutral cell culture media further increased membrane-bound PD-L1 expression, which was accompanied by an induction of *Pd-l1* gene expression (**Figure 14 A**). This implies a contribution of acidosis in the IFN-γ-eIF4F-STAT1-PD-L1 pathway.

To proof that upon IFN-γ stimulation, acidosis further induces PD-L1 protein expression compared to neutral cell culture conditions in MC38^{wt} cells, total PD-L1 protein levels were determined by WB analysis. Acidic cell culture media alone failed to up-regulate total PD-L1 protein levels in MC38^{wt} cells. Relative to β-actin, IFN-γ- and neutral media-induced total PD-L1 protein expression in MC38^{wt} cells, whereas conjoint IFN-γ and acidosis treatment significantly enhanced total PD-L1 protein levels by a factor of two when WB bands were analyzed by densitometry (**Figure 14 B, C**). Similar results in terms of PD-L1 induction patterns in MC38^{wt} cells upon IFN-γ and acidosis treatment were obtained by fluorescence imaging. Strikingly, almost no PD-L1 expression could be detected under neutral conditions. Upon acidic cell culture conditions without IFN-γ stimulation, MC38^{wt} cells exhibited only few PD-L1 positive cells. Upon IFN-γ treatment in neutral or acidic cell culture media, PD-L1 could be detected in clusters by fluorescence microscopy (**Figure 14 D**).

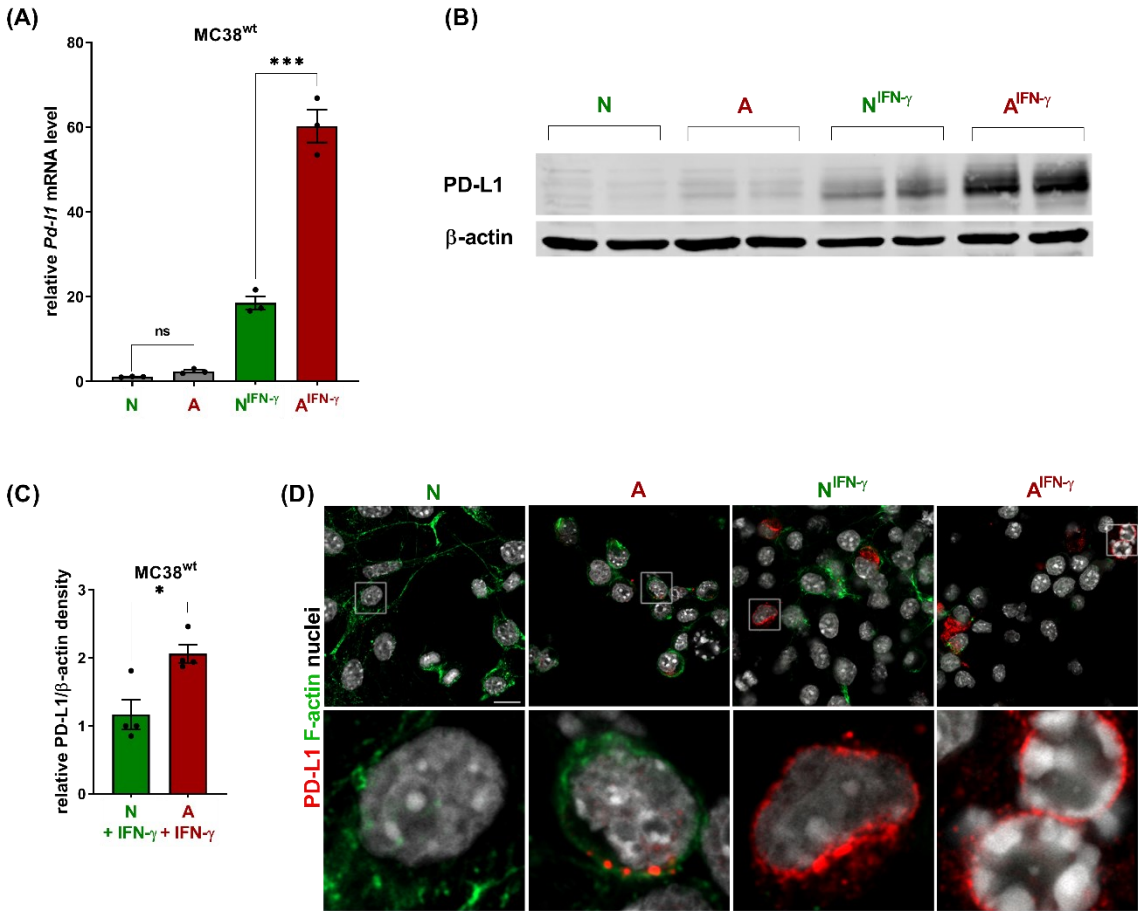

Figure 14: IFN-γ and acidic media treatment induces PD-L1 expression in MC38^{wt} cells.

(A) Relative *Pd-l1* mRNA expression normalized to the mean housekeeping gene expression (1 independent experiment, n = 3, statistics: Tukey's multiple comparison test), **(B)** WB analysis and **(C)** densitometry of total PD-L1 and β-actin (2 independent experiments, n = 4, statistics: two-tailed Mann-Whitney test, *P<0.05) in anti-PD-L1 mAb therapy responder $MC38^{wt}$ cells treated with acidic media and/or IFN-γ (10 ng ml^{-1}) for 72 h. Data is presented as mean ± SEM. **(D)** Fluorescent staining for PD-L1 (red), nuclei (white) and F-actin (green) of $MC38^{wt}$ cells cultured in neutral or acidic media and/or IFN-γ (10 ng ml^{-1}) for 72 h (n = 1 independent experiment). Scale bar 10 µm. White rectangles in the upper images indicate the cells depicted enlarged in the images below. Abbreviations: N = neutral media, A = acidic media, $N^{IFN-\gamma}$ = neutral media plus IFN-γ, $A^{IFN-\gamma}$ = acidic media plus IFN-γ.

Similar results were obtained using anti-PD-L1 mAb therapy responsive non-hypermutated/MSI $CT26^{wt}$ colon carcinoma cells [194]. Acidic cell culture conditions did not result in elevated *Pd-l1* mRNA levels compared to neutral conditions in $CT26^{wt}$ cells. On the gene expression level, conjoint treatment of $CT26^{wt}$ cells with IFN-γ under neutral cell culture conditions increased *Pd-l1* mRNA expression levels. Interestingly, conjoint IFN-γ and acidic media treatment resulted in an almost threefold increase in *Pd-l1* mRNA expression compared to IFN-γ stimulation in neutral cell culture media (**Figure 15 A**). Culture of $CT26^{wt}$ cancer cells in acidic cell culture media failed to increase membrane-bound PD-L1 expression. Stimulation of $CT26^{wt}$ cells with IFN-γ in neutral media significantly increased cell surface PD-L1 expression, which was further elevated, upon combined IFN-γ and acidic cell culture media treatment (**Figure 15 B**). Interestingly, the magnitude of PD-L1 cell surface induction upon conjoint treatment with IFN-γ and acidic media compared to IFN-γ and neutral media was less prominent in $CT26^{wt}$ compared to $MC38^{wt}$ cells (**Figure 15 B**, **Figure 13 B**). WB analysis confirmed the IFN-γ-induced increase in PD-L1 protein expression of $CT26^{wt}$ cells under neutral cell culture conditions (**Figure 15 C**). Combined IFN-γ and acidic cell culture media treatment resulted in an almost threefold elevation of *Pd-l1* mRNA levels and a slight, but nevertheless significant elevation of membrane-bound PD-L1 which was not reflected in total PD-L1 protein expression when compared to IFN-γ stimulation under neutral cell culture conditions (**Figure 15**).

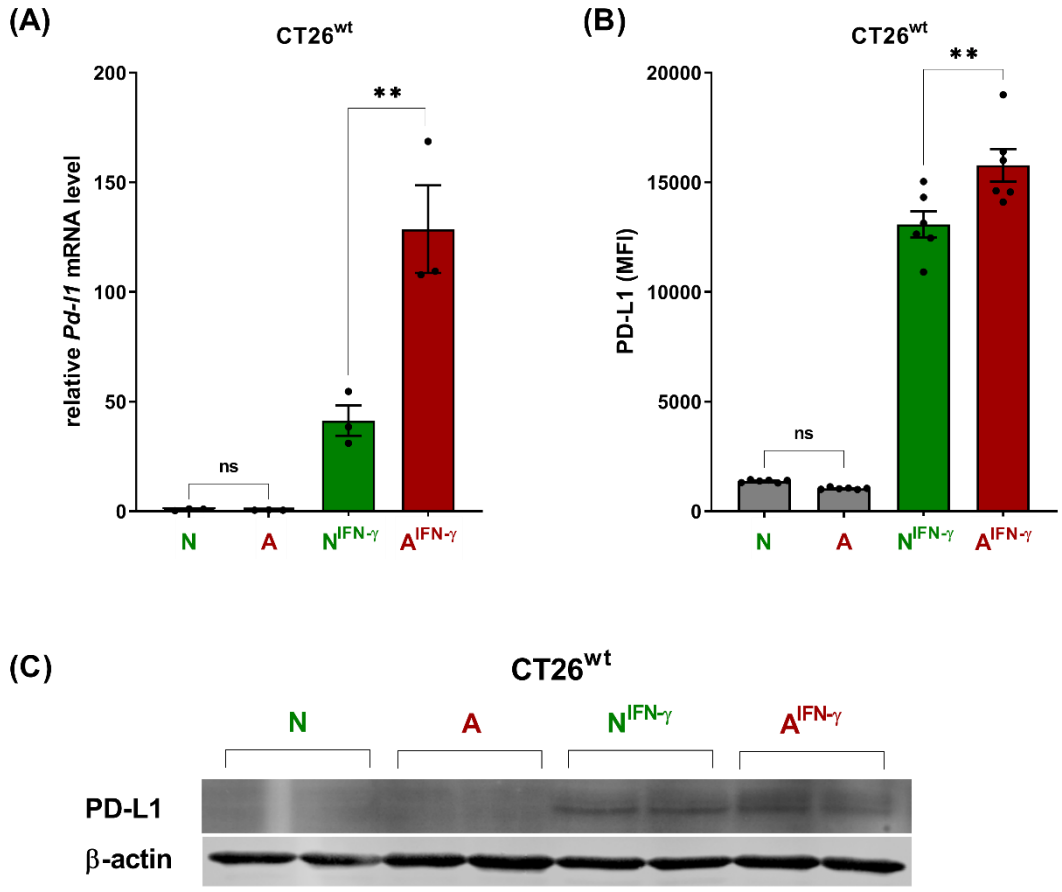

Figure 15: IFN-γ and acidic media treatment induces PD-L1 expression in CT26^{wt} cells.
(A) Relative *Pd-l1* mRNA normalized to the mean housekeeping gene expression (1 independent experiment, n = 3), **(B)** PD-L1 MFI measured by flow cytometry (2 independent experiments, n = 6) and **(C)** WB analysis of PD-L1 and β-actin protein levels (1 independent experiment, n = 2) in the murine anti-PD-L1 mAb therapy responder CT26^{wt} cell line treated with acidic media and/or IFN-γ (10 ng ml^{-1}) for 72 h. Data is presented as mean ± SEM. Statistics: Tukey's multiple comparison test. Abbreviations: N = neutral media, A = acidic media, N$^{IFN-γ}$ = neutral media plus IFN-γ, A$^{IFN-γ}$ = acidic media plus IFN-γ.

Next, we raised the question, whether conjoint IFN-γ- and acidosis-mediated PD-L1 expression is exclusively a characteristic of anti-PD-L1 mAb therapy responsive cancer cell lines like MC38^{wt} and CT26^{wt} and therefore might represent a response biomarker. The anti-PD-L1 mAb therapy low-/non-responsive cancer cell lines B16-F10^{wt} and 4T1^{wt} were identically treated with IFN-γ in neutral and acidic cell culture media as MC38^{wt} and CT26^{wt} cancer cells and analyzed by flow cytometry for membrane-bound PD-L1 expression. IFN-γ stimulation in neutral media increased PD-L1 cell surface expression of B16-F10^{wt} cells which was not further elevated by conjoint IFN-γ and acidic media treatment (**Figure 16 A**). Like B16-

F10^{wt} cancer cells acidic media alone did not impair PD-L1 cell surface expression of 4T1^{wt} cancer cells. IFN-γ stimulation in neutral media significantly elevated PD-L1 expression, whereas a combined IFN-γ and acidic media treatment even reduced membrane-bound PD-L1 expression in 4T1^{wt} cancer cells (**Figure 16 B**).

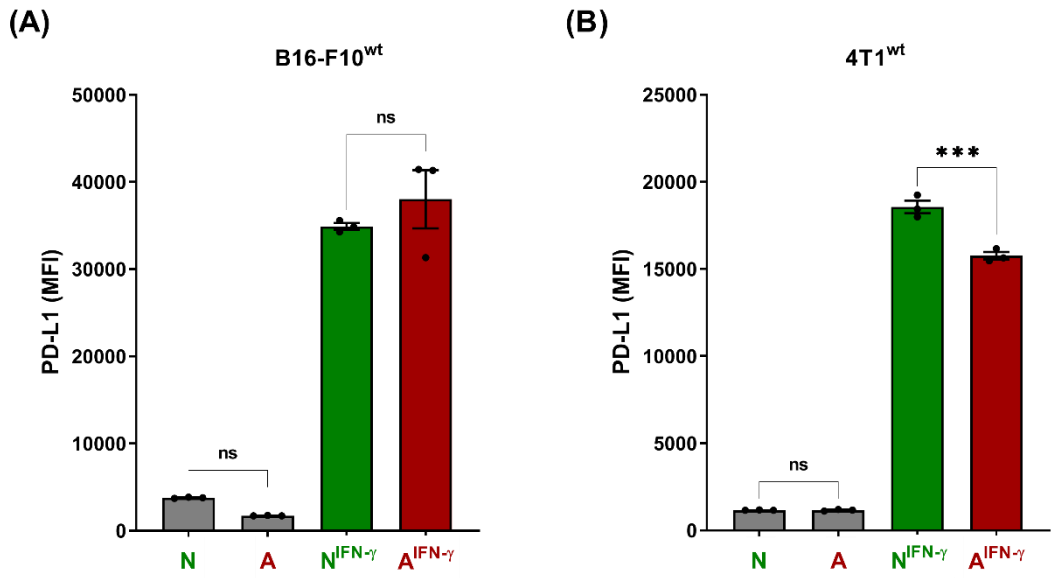

Figure 16: IFN-γ and acidic media treatment fails to induce membrane-bound PD-L1 expression in B16-F10^{wt} and 4T1^{wt} cells.

PD-L1 MFI measured by flow cytometry of the murine anti-PD-L1 mAb therapy non-responsive **(A)** B16-F10^{wt} and **(B)** 4T1^{wt} cell lines treated with acidic media and/or IFN-γ (10 ng ml^{-1}) for 72 h (1 independent experiments, n = 3). Data is presented as mean ± SEM. Statistics: Tukey's multiple comparison test. Abbreviations: N = neutral media, A = acidic media, N$^{IFN-γ}$ = neutral media plus IFN-γ, A$^{IFN-γ}$ = acidic media plus IFN-γ.

Taken together, IFN-γ stimulation in neutral media increased membrane-bound PD-L1 expression in murine MC38^{wt}, CT26^{wt}, B16-F10^{wt} and 4T1^{wt} cells. Conjoint IFN-γ and acidic media treatment further increased cell surface PD-L1 expression only in anti-PD-L1 mAb therapy responsive MC38^{wt} and CT26^{wt} cells but not in the anti-PD-L1 mAb therapy low-/non-responder cancer cell lines B16-F10^{wt} and 4T1^{wt}. Therefore, the conjoint IFN-γ- and acidosis-mediated PD-L1 induction might serve as a positive prognostic biomarker for an anti-PD-L1 mAb therapy response, at least in the four studied murine cancer cell lines.

4.1.5 *In silico* analysis of *Pd-l1* expression in different human tumors

In order to delineate the role of basal PD-L1 from IFN-γ-induced PD-L1 expression, various human cancer tissues collected and curated by the TCGA RNA-seq database were analyzed for *Pd-l1* RNA expression *in silico* [205].

Tumor tissues derived from cancer patients was analyzed for *Pd-l1* expression by RNA-seq and evaluated across various tumor entities. For instance, lung, head and neck as well as cervical cancer exhibited elevated *Pd-l1* mRNA levels compared to liver, prostate, ovarian and endometrial cancers illustrating the heterogeneity in terms of *Pd-l1* expression levels across different tumor entities. Significant correlations between *Pd-l1* expression and overall survival were found for colorectal and breast cancer in an analysis performed by The Human Protein Atlas, with high *Pd-l1* expression being a favorable prognostic marker (**Figure 17 A**) [364].

Next a correlation analysis of *Pd-l1*, *Ifn-γ* and *Stat1* mRNA expression was performed in colorectal cancer tissue of 597 patients. *Ifn-γ* mRNA expression by tumor resident immune cells like T_h1 cells, cytotoxic $CD8^+$ T cells and NK cells significantly correlated with *Pd-l1* mRNA expression ($r = 0.7427$; $p<0.0001$). According to Havel *et al.* elevated *Ifn-γ* mRNA expression patterns in tumor tissue indicate the presence of activated immune cells, a characteristic of immune-inflamed tumors [126]. The correlation between *Ifn-γ* and *Pd-l1* also underlines that IFN-γ induces *Pd-l1* expression (**Figure 17 B**). Studies in malignant melanoma suggest, that *Ifn-γ* induces *Pd-l1* expression via the eIF4F-STAT1 axis [30]. Therefore, the dataset was analyzed for a correlation between *Stat1* and *Pd-l1* mRNA levels. In line with other studies [30, 172, 391], *Stat1* and *Pd-l1* mRNA levels also significantly correlated ($r = 0.8085$; $p<0.0001$) in the studied dataset of colorectal cancers (**Figure 17 C**).

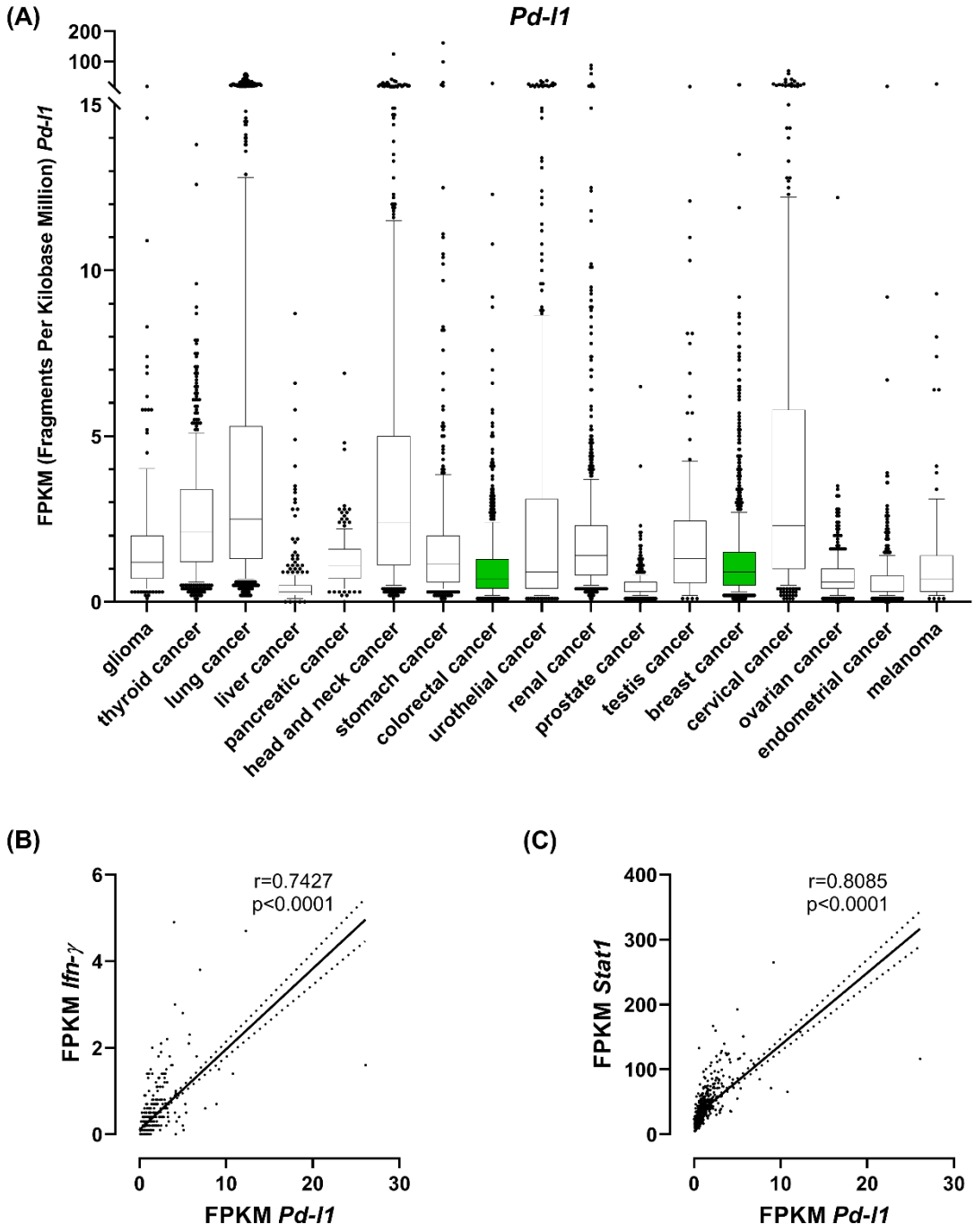

Figure 17: *Pd-l1* mRNA expression in different human cancer entities.

(A) Expression of *Pd-l1* (CD274) in different human cancer tissues analyzed by RNA-seq, collected, and curated by The Cancer Genome Atlas (TCGA). The RNA-seq data is shown as fragments per kilobase million (FPKM) in a box and whiskers blot with 10-95 percentile. The analysis includes glioma (153 samples), thyroid cancer (501 samples), lung cancer (994 samples), liver cancer (365 samples), pancreatic cancer (176 samples), head and neck cancer (499 samples), stomach cancer (354 samples), colorectal cancer (597 samples), urothelial cancer (406 samples), renal cancer (877 samples), prostate cancer (494 samples), testis cancer (134 samples), breast cancer (1075 samples), cervical cancer (291 samples), ovarian cancer (373 samples), endometrial cancer

(541 samples) and melanoma (102 samples). *Pd-l1* expression is a favorable prognostic marker in colorectal and breast cancer (green) according to The Human Protein Atlas (http://www.proteinatlas.org) [364]. TCGA RNA-seq data was analyzed for correlations between **(B)** *Ifn-γ* and *Pd-l1* as well as **(C)** *Stat1* and *Pd-l1* gene expression in human colorectal cancer samples. A nonparametric Spearman's rank correlation was computed with $p<0.0001$. The presented analysis here is as a whole based on data which were generated and curated by the TCGA Research Network: https://www.cancer.gov/tcga [205]. Correlation analysis and statistical analysis were performed on the extracted data derived from the TCGA Research Network.

4.1.6 IFN-γ induces PD-L1 expression via the eIF4F-STAT1 axis

Based on significant correlations between *Ifn-γ*, *Stat1* and *Pd-l1* mRNA expression in human colorectal cancers, STAT1 expression and phosphorylation was studied *in vitro* in conjoint IFN-γ- and acidosis-induced PD-L1 expression.

Murine colon adenocarcinoma MC38^{wt} cells treated with IFN-γ in neutral media showed an increased STAT1 protein expression and phosphorylation (pSTAT1) after 12 h and 24 h. Conjoint IFN-γ and acidic media treatment resulted in similar total STAT1, but higher pSTAT1 levels in contrast to IFN-γ treatment in neutral media (**Figure 18 A**). Acidic cell culture media therefore enhanced STAT1 activation via phosphorylation upon treatment with IFN-γ compared to neutral media, whereas total STAT1 protein levels remained stable.

Next, siRNA-mediated STAT1 knockdowns (siSTAT1) were performed to interfere with IFN-γ-induced STAT1 upregulation. To confirm STAT1 knockdowns and to study the effect on *Pd-l1* gene expression, mRNA levels were evaluated by qRT-PCR. MC38^{wt} cells transfected with a non-targeting siRNA (siCTL) and treated with IFN-γ combined with neutral or acidic media for 24 h showed a comparable increase in *Stat1* mRNA levels (**Figure 18 B**). This suggests that increased STAT1 phosphorylation mediates the increase in total PD-L1 expression upon conjoint IFN-γ and acidic media treatment. The STAT1 knockdown was confirmed by significantly reduced *Stat1* mRNA levels, which remain low when cells were treated with IFN-γ in neutral or acidic media (**Figure 18 B**). MC38^{wt} cells transfected with siCTL and treated with IFN-γ exhibited increased *Pd-l1* mRNA levels, which were further elevated upon conjoint IFN-γ and acidic media treatment for 24 h. A siRNA-mediated STAT1 knockdown resulted in significantly reduced *Pd-l1* mRNA levels (**Figure 18 C**). Nevertheless, slightly higher *Pd-l1* mRNA levels were detected in

siSTAT1 transfected MC38^{wt} cells upon combined IFN-γ and acidic media treatment compared to IFN-γ stimulation in neutral media. Similarly, to the 72-h treatment time point shown in **Figure 13**, siCTL transfected MC38^{wt} cancer cell exhibited an increased membrane-bound PD-L1 expression upon IFN-γ stimulation in neutral media already after 24 h. PD-L1 expression on the cell surface was again further elevated upon conjoint IFN-γ and acidic media treatment after 24 h (**Figure 18 D**). A STAT1 knockdown significantly reduced membrane-bound PD-L1 induction upon IFN-γ treatment under neutral and acidic cell culture conditions, underlining the important role of STAT1 in IFN-γ-mediated PD-L1 expression. Nevertheless, siSTAT1 transfected MC38^{wt} cells revealed a significantly higher PD-L1 expression upon conjoint IFN-γ and acidic compared to neutral media treatment, emphasizing the role of elevated STAT1 activation during acidosis (**Figure 18 D**). MC38^{wt} cells transfected with siCTL revealed increased STAT1 protein levels upon 24 h conjoint IFN-γ and neutral as well as acidic media treatment. The induction of total PD-L1 protein expression in MC38^{wt} cancer cells was only detectable upon combined IFN-γ and acidosis treatment but not upon IFN-γ and neutral media treatment (**Figure 18 E**). The STAT1 knockdown in MC38^{wt} cancer cells was confirmed by WB analysis yielding hardly any detectable total STAT1 protein expression even upon IFN-γ stimulation (**Figure 18 E**). In summary, IFN-γ-mediated PD-L1 expression is STAT1-dependent and stimulation with IFN-γ in acidic media further increases PD-L1 expression via enhanced STAT1 phosphorylation in MC38^{wt} cells.

Like MC38^{wt} cancer cells, IFN-γ and neutral as well as acidic media treatment induced *Stat1* mRNA and total protein expression levels to the same extend in murine CT26^{wt} cells (**Figure 18 F, G**). Interestingly, no difference in STAT1 phosphorylation upon IFN-γ treatment in neutral and acidic media was observed in CT26^{wt} cells (**Figure 18 G**).

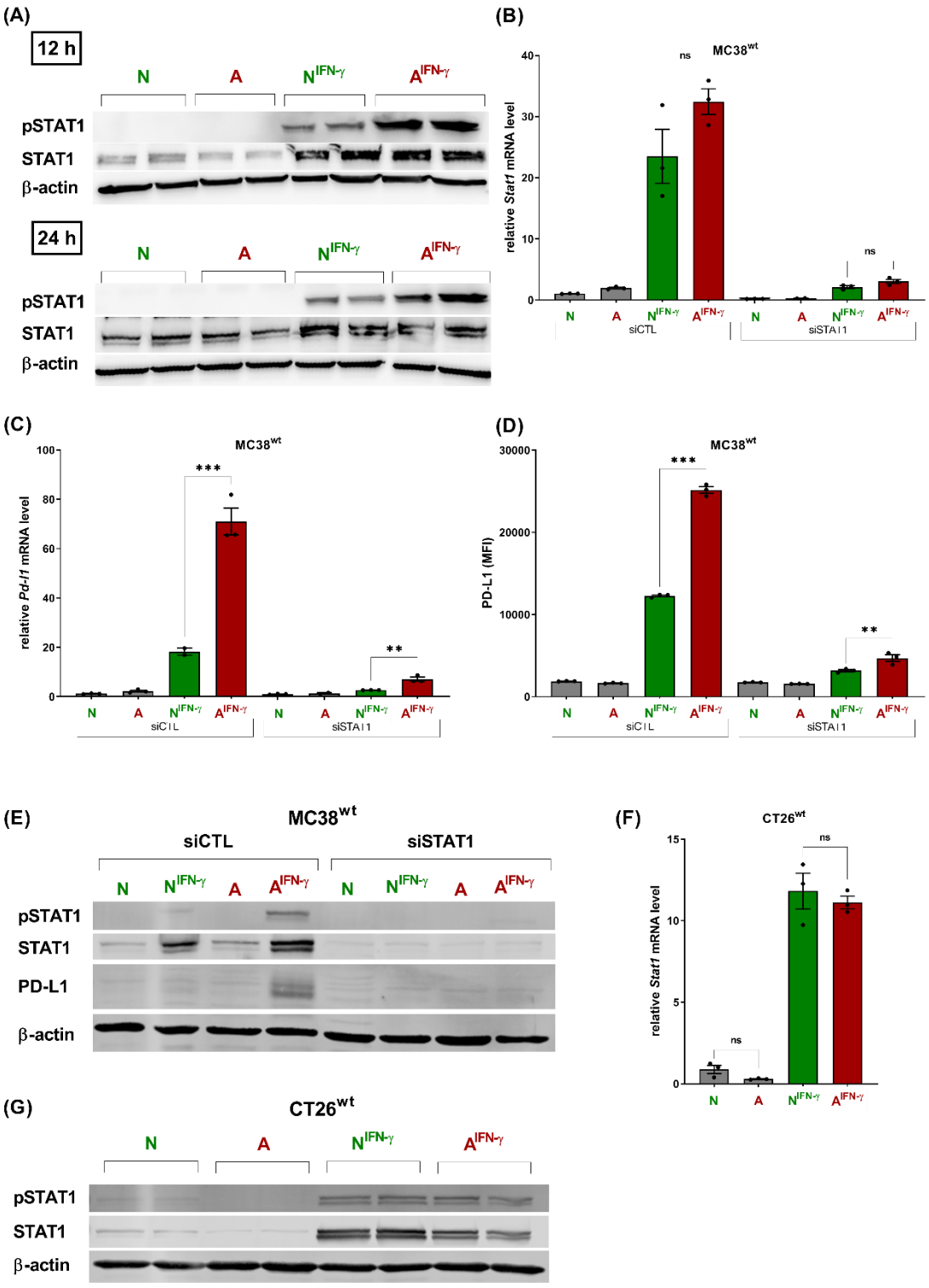

Figure 18: IFN-γ-induced STAT1 regulates acidosis and IFN-γ dependent PD-L1 expression. **(A)** WB analysis of pSTAT1, STAT1 and β-actin treated with acidic media and/or IFN-γ (10 ng ml^{-1}) for 12 h and 24 h (2 independent experiment, n = 2). MC38^{wt} cells were transfected with non-targeting siRNA control (siCTL) or siRNA against STAT1 (siSTAT1) and treated with acidic media and/or IFN-γ (10 ng ml^{-1}) for 24 h. Relative **(B)** *Stat1* and **(C)** *Pd-l1* mRNA expression levels normalized to the mean housekeeping gene expression (1 independent experiment, n = 3) and **(D)** PD-L1 visualized by flow cytometry (1 independent experiment, n = 3) were determined. **(E)** WB

analysis of pSTAT1, STAT1, PD-L1 and β-actin was performed to determine STAT1 knockdown efficiency (1 independent experiment, n = 2). **(F)** Relative *Stat1* mRNA expression normalized to the mean housekeeping gene expression was determined and **(G)** WB analysis of pSTAT1, STAT1 and β-actin in $CT26^{wt}$ cells treated with acidic media and/or IFN-γ (10 ng ml^{-1}) for 72 h (1 independent experiment, n = 3). Data is presented as mean ± SEM. Statistics: Tukey's multiple comparison test. Abbreviations: N = neutral media, A = acidic media, $N^{IFN-\gamma}$ = neutral media plus IFN-γ, $A^{IFN-\gamma}$ = acidic media plus IFN-γ.

To explore potential therapeutic strategies, *in vitro* experiments applying the highly potent pharmacological eIF4A inhibitor silvestrol which eventually blocks the eIF4F translational complex as a whole, were performed [30, 392-394]. The eIF4F complex consists of several components, including the eIF4G, eIF4E and eIF4A subunits (**Figure 19 A**). Inhibition of the helicase eIF4A by silvestrol therefore inhibits translation of mRNAs like *Stat1* with 5' untranslated regions (5' UTR) which are rich in secondary structures [392, 395, 396]. It was initially hypothesized, that extracellular acidosis might cause an increased assembly of the eIF4F complex or elevate the gene expression of the different subunits. Contrary to the initial hypothesis, neither eIF4A1, nor eIF4E expression are subject to conjoint IFN-γ- and acidosis-induced gene expression as total eIF4A1 and eIF4E protein levels remained unchanged (**Figure 19 B**). Even though WB analysis of eIF4G was performed, eIF4G proteins could not be resolved in a 10% SDS-PAGE due to the large protein size of 200-220 kDa [397-399]. As previously shown, conjoint IFN-γ and neutral or acidic media treatment increased *Stat1* mRNA levels to the same extend in the presence of dimethyl sulfoxide (DMSO, control). The pharmacological inhibitor silvestrol (30 nM) was dissolved in DMSO. Consequently, the solvent DMSO was applied for control treatment (**Figure 19 C**). Conjoint stimulation with IFN-γ and neutral media induced *Stat1* mRNA expression to the identical extend upon silvestrol treatment as compared to DMSO alone. This confirms the role of silvestrol in inhibiting *Stat1* translation. Interestingly, conjoint IFN-γ- and acidosis-stimulation further increased *Stat1* mRNA levels upon silvestrol treatment compared to DMSO, which might be due to a feedback loop that is unlocked upon acidosis (**Figure 19 C**). $MC38^{wt}$ cells treated exclusively with DMSO (control), exhibited increased *Pd-l1* mRNA expression levels upon 24 h conjoint treatment with IFN-γ under neutral or acidic cell culture conditions. Upon IFN-γ stimulation silvestrol treatment of $MC38^{wt}$ cells prevented the induction of

Pd-l1 mRNA expression (**Figure 19 D**). Like the siRNA-mediated STAT1 knockdown experiments, silvestrol treatment upon conjoint IFN-γ and acidic cell culture media stimulation significantly increased *Pd-l1* mRNA expression in MC38^{wt} cells compared to IFN-γ stimulation in neutral cell culture media (**Figure 19 D**). This supports the previous finding that an increase in STAT1 activation via phosphorylation upon conjoint IFN-γ and acidic media stimulation leads to elevated PD-L1 expression levels. Flow cytometry analysis of MC38^{wt} cells of the DMSO control group, revealed increased membrane-bound PD-L1 expression upon 24 h stimulation with IFN-γ in neutral media. This effect was further elevated when cells were stimulated with a combination of IFN-γ and acidic cell culture media. Inhibition of *Stat1* mRNA translation by silvestrol thus prevented the upregulation of membrane-bound PD-L1 upon 24 h IFN-γ stimulation under either neutral or acidic cell culture conditions (**Figure 19 E**).

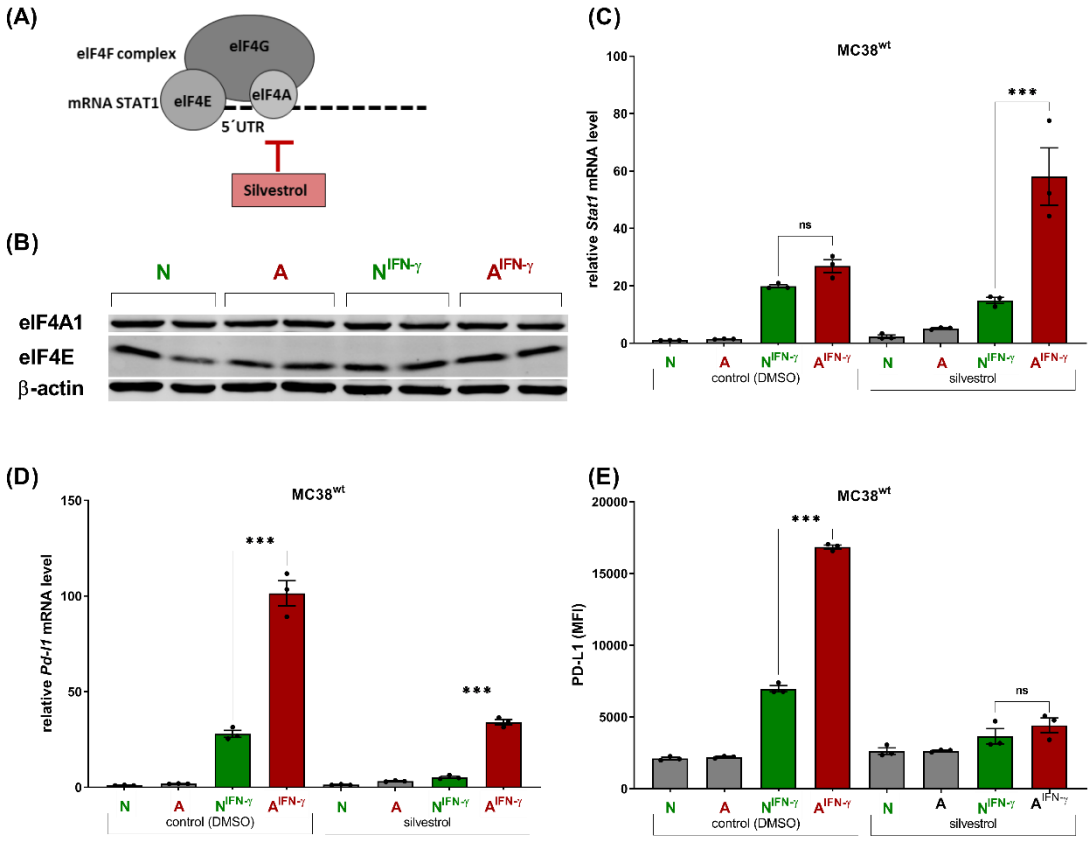

Figure 19: Inhibition of the translation initiation complex eIF4F prevents conjoint IFN-γ- and acidosis-mediated PD-L1 expression.

(A) Schematic representation of the eukaryotic translation initiation complex eIF4F composed of eIF4G, eIF4E and eIF4A which bind to the 5' UTR of the *Stat1* mRNA. The eIF4A subunit can be

inhibited by the pharmacological inhibitor silvestrol. **(B)** WB analysis of eIF4A1, eIF4E and β-actin in MC38^{wt} cells treated with acidic media and/or IFN-γ (10 ng ml^{-1}) for 72 h (1 independent experiment, n = 2). Relative **(C)** *Stat1* and **(D)** *Pd-l1* mRNA expression normalized to the mean housekeeping gene expression (1 independent experiment, n = 3) as well as **(E)** membrane-bound PD-L1 expression visualized by flow cytometry (1 independent experiment, n = 3) were determined in MC38^{wt} cells treated with acidic media and/or IFN-γ (10 ng ml^{-1}) in the presence of DMSO (control) or silvestrol (30 nM) for 24 h. Data is presented as mean ± SEM. Statistics: Tukey's multiple comparison test. Abbreviations: N = neutral media, A = acidic media, N$^{IFN-\gamma}$ = neutral media plus IFN-γ, A$^{IFN-\gamma}$ = acidic media plus IFN-γ.

In summary, IFN-γ increases PD-L1 expression via the eIF4F-STAT1-PD-L1 axis and an acidic pH_e increased IFN-γ-induced PD-L1 expression via elevated STAT1 phosphorylation. Further, IFN-γ-mediated PD-L1 expression can be pharmacologically targeted by the eIF4A inhibitor silvestrol.

4.1.7 Delineating the effect of acidosis and lactic acidosis on IFN-γ-induced PD-L1 expression in human cancer cell lines

The effect of IFN-γ treatment on PD-L1 induction and the contribution of acidic pH_e or L-lactate were studied in murine MC38^{wt} cancer cells described in chapter 4.1.3. To expand the findings on conjoint IFN-γ- and acidosis-, lactic acidosis-, or lactosis-mediated PD-L1 expression, the five human cancer cell lines HCA-7 colony 29 (colon adenocarcinoma), MCF-7 (mammary gland adenocarcinoma), U-87 MG (likely glioblastoma), SK-MEL-28 (malignant melanoma) and MIA PaCa-2 (pancreas carcinoma) were screened. Briefly, human cancer cells were cultured for 72 h in neutral, acidic, lactic acidic or lactic cell culture media (as described in chapter 4.1.3) in the absence or presence of 10 ng ml^{-1} IFN-γ. Then cancer cells were harvested and membrane-bound PD-L1 expression was analyzed by flow cytometry. The gating strategy shown in **Figure 13 A** was applied and only living cells were analyzed.

Like murine MC38^{wt} and CT26^{wt} cells, three out of the five human cell lines exhibited an elevated membrane-bound PD-L1 expression upon conjoint IFN-γ and acidosis treatment. Nevertheless, these three cell lines namely HCA-7 colony 29, MCF-7 and U-87 MG exhibited differential magnitudes of inducible PD-L1 expression upon conjoint IFN-γ and acidic cell culture media treatment (**Figure 20 A**). Like in murine MC38^{wt} cells, acidic and lactic acidic media alone

only slightly increased PD-L1 cell surface expression in human HCA-7 colony 29 and MCF-7 cells, whereas the PD-L1 expression was unchanged in U-87 MG cells. In contrast to murine MC38^{wt} cells, where conjoint IFN-γ and lactic acidic media treatment resulted in remarkably reduced PD-L1 cell surface expression (**Figure 13 B**), human MCF-7 cells exhibited significantly elevated PD-L1 levels (**Figure 20 A**), whereas only slight changes were observed in HCA-7 colony 29 and U-87 MG cancer cells. Conjoint lactosis and IFN-γ treatment resulted in similar PD-L1 cell surface expression levels compared to IFN-γ stimulation in neutral media (**Figure 20 A**).

The two human cancer cell lines SK-MEL-28 and MIA-PaCa-2 exhibited differential membrane-bound PD-L1 expression patterns upon conjoint IFN-γ and acidic media treatment when compared to murine MC38^{wt} cells (**Figure 20 B**). SK-MEL-28 cells exhibited reduced membrane-bound PD-L1 levels upon conjoint IFN-γ and acidic media treatment compared to IFN-γ stimulation in neutral media. In MIA PaCA-2 cancer cells PD-L1 levels remained unchanged upon conjoint IFN-γ and neutral or acidic media treatment. In addition, conjoint IFN-γ and lactic acidic media treatment further reduced membrane-bound PD-L1 expression in comparison to combined IFN-γ and acidic media treatment in SK-MEL-28 but not as prominent in MIA PaCa-2 cancer cells. Finally, conjoint IFN-γ and lactic media treatment slightly reduced PD-L1 cell surface expression on SK-MEL-28 and MIA PaCa-2 cancer cells when compared to IFN-γ stimulation in neutral media (**Figure 20 B**).

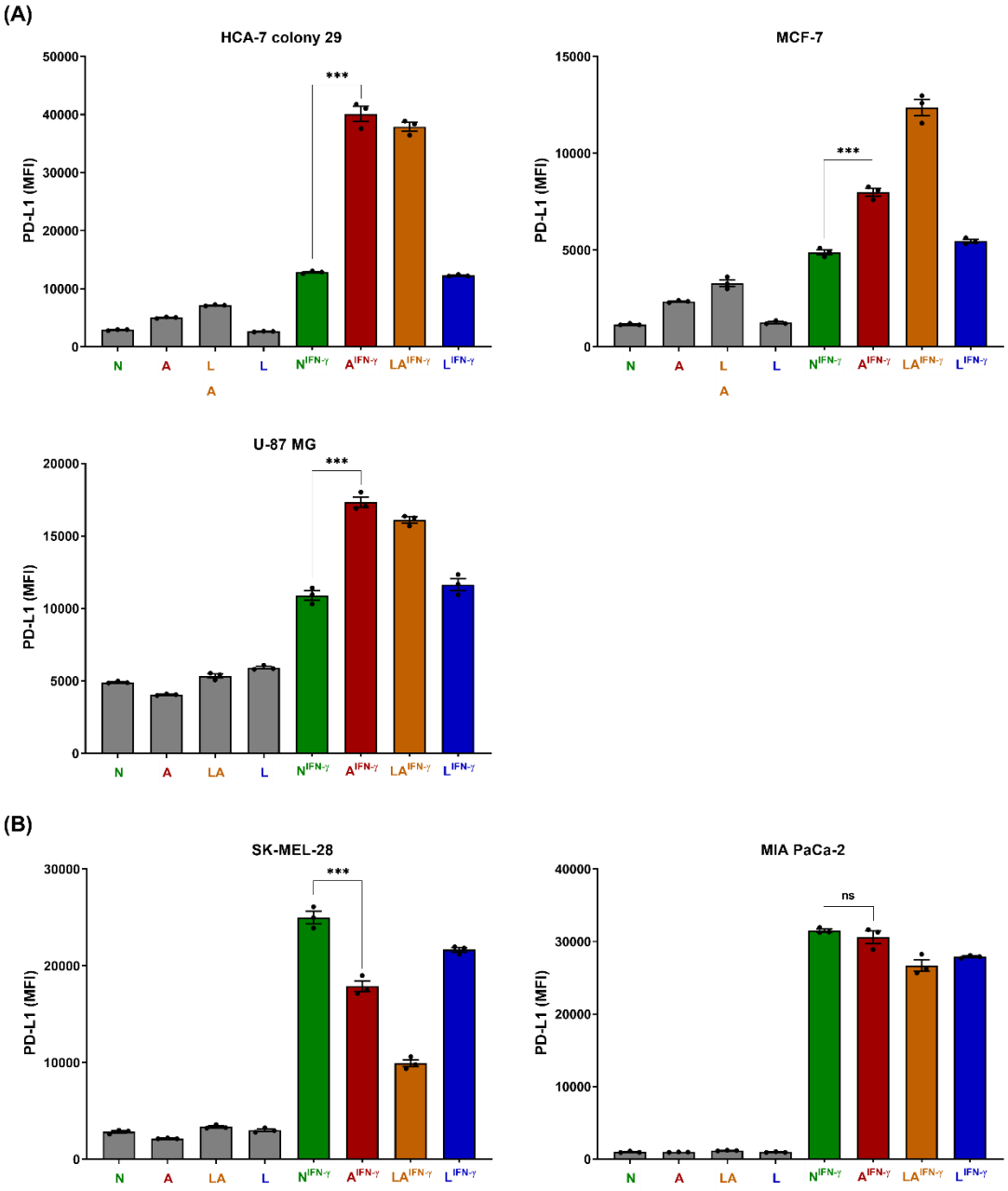

Figure 20: Effect of acidosis, lactic acidosis and lactosis in the absence and presence of IFN-γ treatment on membrane-bound PD-L1 expression on human cancer cell lines.

(A) Human HCA-7 colony 29, MCF-7 and U-87 MG cells exhibit elevated PD-L1 expression patterns upon conjoint IFN-γ (10 ng ml^{-1}) and acidic cell culture media treatment, whereas **(B)** SK-MEL-28 and MIA PaCa-2 cells do not. PD-L1 MFI was determined by flow cytometry of the respective cell lines treated with acidosis, lactic acidosis or lactosis media and/or IFN-γ (10 ng ml^{-1}) for 72 h (1 independent experiment, n = 3). Data is presented as mean ± SEM. Statistics: Tukey's multiple comparison test. Abbreviations: N = neutral media, A = acidic media, LA = lactic acidic media, L = lactosis media, N$^{IFN-γ}$ = neutral media plus IFN-γ, A$^{IFN-γ}$ = acidic media plus IFN-γ, LA$^{IFN-γ}$ = lactic acidic media plus IFN-γ, L$^{IFN-γ}$ = lactosis media plus IFN-γ.

To elucidate and confirm the underlying mechanism of IFN-γ- and acidosis-inducible PD-L1 expression in human colon adenocarcinoma HCA-7 colony 29 cells, qRT-PCR, WB analysis and siRNA-mediated STAT1 knockdown experiments were performed. Conjoint treatment of HCA-7 colony 29 cells with IFN-γ and neutral media increased *Stat1* mRNA levels to the identical extend as conjoint IFN-γ and neutral media treatment (**Figure 21 A**). In contrast to *Stat1*, *Pd-l1* mRNA levels were significantly increased upon conjoint IFN-γ and acidosis treatment compared to IFN-γ stimulation in neutral media (**Figure 21 A**). Elevated PD-L1 and unchanged STAT1 levels upon conjoint IFN-γ and acidosis stimulation were confirmed by WB analysis and densitometry (**Figure 21 B, C**). The significant increase in total PD-L1 protein level was accompanied by significantly enhanced acidosis-induced STAT1 activation via phosphorylation in the context of IFN-γ stimulation (**Figure 21 B, C**). Interference with a pool of four siRNAs directed against STAT1 prevented IFN-γ- as well as conjoint IFN-γ- and acidosis-mediated STAT1 and subsequently total PD-L1 protein induction (**Figure 21 D**).

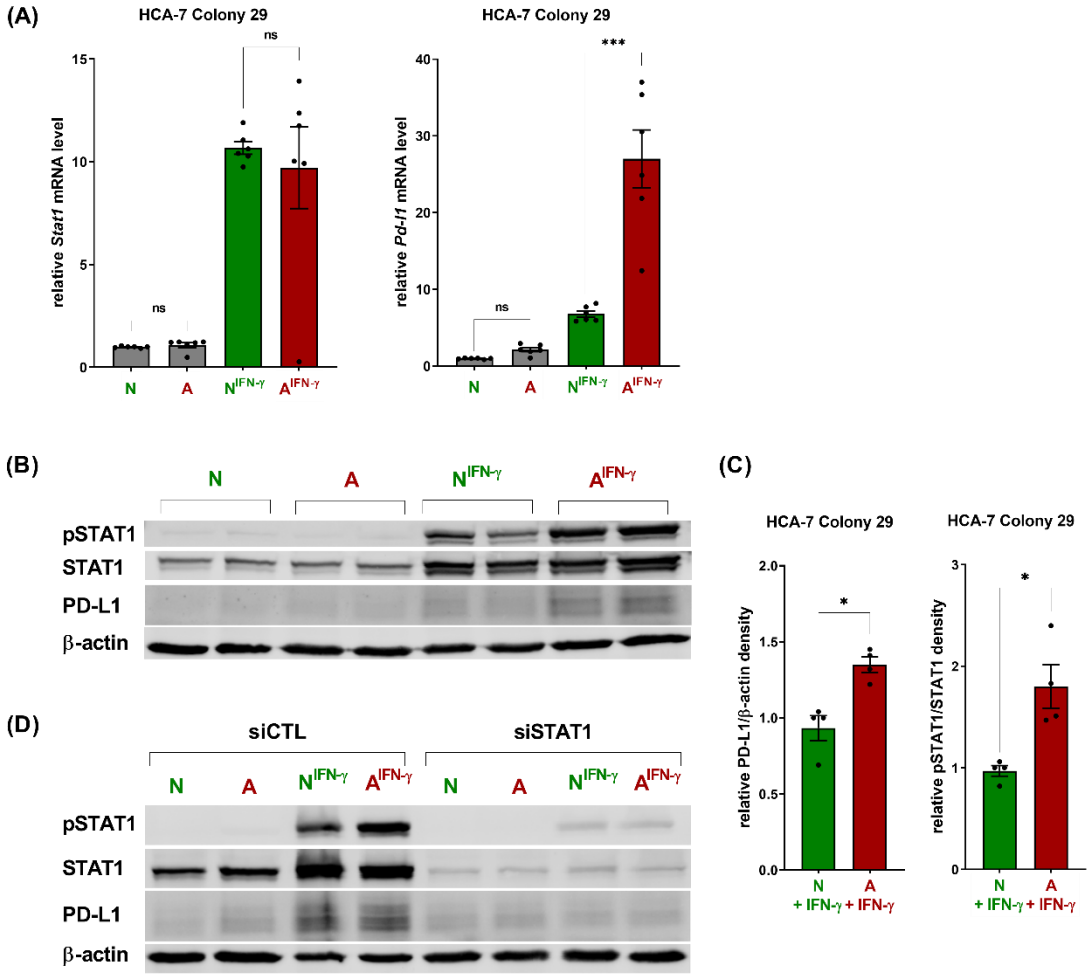

Figure 21: IFN-γ and acidic media treatment induces PD-L1 expression in human HCA-7 colony 29 cells.

(A) Relative *Stat1* and *Pd-l1* mRNA expression normalized to the mean housekeeping gene expression (2 independent experiment, n = 5-6, statistics: Tukey's multiple comparison test) as well as **(B, C)** WB analysis and densitometry of pSTAT1, STAT1, PD-L1 and β-actin in the HCA-7 colony 29 cell line treated with acidic media and/or IFN-γ (10 ng ml^{-1}) for 72 h (2 independent experiment, n = 4, statistics: two-tailed Mann-Whitney test). HCA-7 colony 29 cells were transfected with siRNA control (siCTL) or siRNA against STAT1 and treated with acidic media and/or IFN-γ (10 ng ml^{-1}) for 24 h. **(D)** WB analysis of pSTAT1, STAT1, PD-L1 and β-actin was performed to determine STAT1 knockdown efficiency (1 independent experiment, n = 2). Data is presented as mean ± SEM. Abbreviations: N = neutral media, A = acidic media, $N^{IFN-γ}$ = neutral media plus IFN-γ, $A^{IFN-γ}$ = acidic media plus IFN-γ.

These findings in human HCA-7 colony 29 cells imply a key role of STAT1 induction and phosphorylation in conjoint IFN-γ- and acidosis-mediated PD-L1 expression like in the two studied murine cancer cell lines. Therefore, these results imply a conserved mechanism across species.

4.1.8 Role of STAT2 in conjoint IFN-γ- and acidosis-mediated PD-L1 expression

It is widely accepted and well-studied, that IFN-γ induces an intracellular signaling cascade which involves the homodimerization of the transcription factor STAT1 [172]. Type I IFNs, including IFN-α, IFN-β, IFN-ε, IFN-κ and IFN-ω as well as type III IFNs involved in antiviral response induce phosphorylation of STAT1 or STAT2. Phosphorylated STAT1 can heterodimerize with phosphorylated STAT2 inducing gene expression of interferon-sensitive response element (ISRE) controlled genes [400, 401]. A gene expression dataset of human pancreatic carcinoma PANC-1 and AsPC-1 cells, revealed that exclusively *Stat2* but not *Stat1* gene expression was upregulated in response to extracellular acidic conditions [389]. Therefore, *Stat2* mRNA expression upon 72 h IFN-γ treatment of MC38^{wt} and CT26^{wt} cells under neutral or acidic cell culture conditions was studied. In MC38^{wt} but not in CT26^{wt} cancer cells a slight increase of *Stat2* on the mRNA level was observed under acidic cell culture conditions (**Figure 22 A, B**). Like the induction of *Stat1* gene expression, combined treatment of MC38^{wt} and CT26^{wt} cells with IFN-γ upon neutral cell culture conditions significantly enhanced *Stat2* mRNA levels (**Figure 22 A, B**). In contrast, conjoint IFN-γ and acidic media treatment significantly enhanced *Stat2* mRNA levels in MC38^{wt}, but not CT26^{wt} cancer cells in comparison to IFN-γ stimulation in neutral media (**Figure 22 A, B**). This observation might be one potential explanation for the only faint effect of an acidic pH_e on IFN-γ-induced PD-L1 cell surface expression in CT26^{wt} cells (**Figure 15 B**). Next RNA interference experiments were performed to elucidate the interplay between the two transcription activators STAT1 and STAT2. Again 24 h combined IFN-γ and acidic media treatment of siCTL transfected MC38^{wt} cells significantly increased *Stat2* mRNA levels. Knockdown of STAT1 significantly reduced *Stat2* mRNA levels even upon IFN-γ stimulation in neutral or acidic media. These results suggest that STAT1 is involved in conjoint IFN-γ- and acidosis-mediated induction of *Stat2* gene expression (**Figure 22 C**). Furthermore, it outlines the interdependence between *Stat1* and *Stat2* gene expression. Therefore, in a next step, the role of STAT2 on *Stat1* and *Pd-l1* expression was investigated. A siRNA-mediated knockdown of STAT2 resulted in significantly reduced *Stat2* mRNA levels confirming the knockdown efficiency, even when MC38^{wt} cells were treated with IFN-γ in the presence of neutral or acidic media (**Figure 22 D**). A

STAT2 knockdown resulted in significantly enhanced *Stat1* mRNA levels in MC38^{wt} cells treated with IFN-γ and neutral media compared to siCTL transfected cells. Conjoint IFN-γ and acidosis treatment of MC38^{wt} cells transfected with STAT2 siRNAs resulted in only minor changes in *Stat1* mRNA expression levels when compared to siCTL (**Figure 22 E**). These finding are accompanied by significantly elevated *Pd-l1* mRNA and protein cell surface expression levels in STAT2 knockdown MC38^{wt} cells upon IFN-γ stimulation in neutral media when compared to siCTL transfected cells. Subsequently, the differences in PD-L1 enhancement upon conjoint IFN-γ and acidic media stimulation compared to neutral conditions was less prominent upon knockdown of STAT2 (**Figure 22 F, G**), suggesting that STAT2 negatively regulates PD-L1 expression under neutral but not acidic conditions. In MC38^{wt} cancer cells a siRNA-mediated STAT2 knockdown did not significantly affect PD-L1 expression upon conjoint IFN-γ and acidosis stimulation compared siCTL (**Figure 22 F, G**).

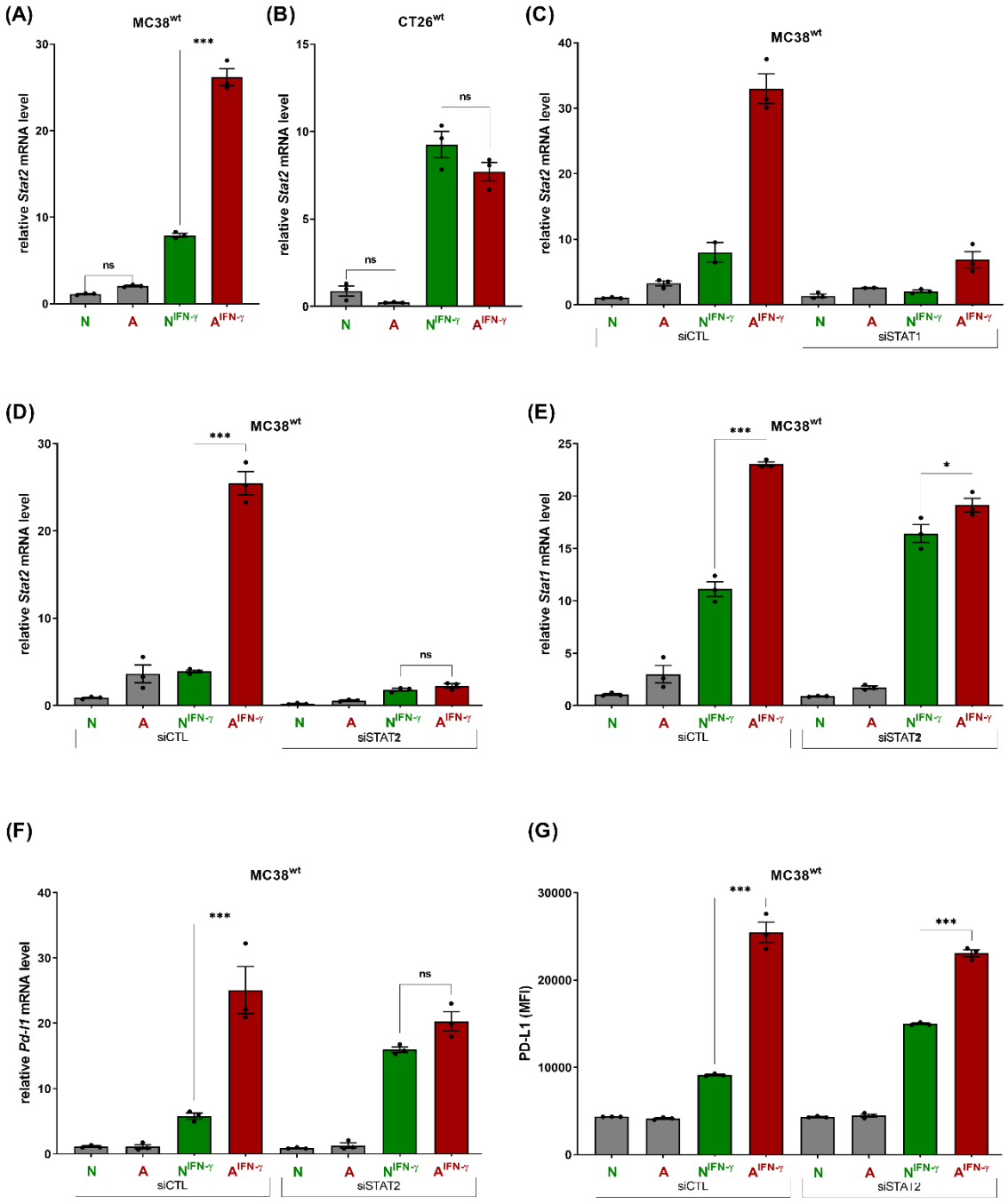

Figure 22: IFN-γ and acidic media treatment induces *Stat2* expression.

Relative *Stat2* mRNA expression normalized to the mean housekeeping gene expression was determined in **(A)** MC38^{wt} and **(B)** CT26^{wt} cells treated with acidic media and/or IFN-γ (10 ng ml^{-1}) for 72 h (1 independent experiment, n = 3). **(C)** Relative *Stat2* mRNA expression levels normalized to the mean housekeeping gene expression (1 independent experiment, n = 2-3; no C_t value was detectable for one replicate in the siCTL-N$^{IFN-γ}$ and the siSTAT1-A group). MC38^{wt} cells were transfected with siRNA control (siCTL) or siRNA against STAT1 (siSTAT1) and treated with acidic media and/or IFN-γ (10 ng ml^{-1}) for 24 h. **(D-F)** Relative *Stat2*, *Stat1* and *Pd-l1* mRNA expression levels normalized to the mean housekeeping gene expression (1 independent experiment, n = 3) and **(G)** PD-L1 expression visualized by flow cytometry (1 independent experiment, n = 3) in

MC38^{wt} cells transfected with siRNA control (siCTL) or siRNA against STAT2 (STAT2) and treated with acidic media and/or IFN-γ (10 ng ml^{-1}) for 24 h. Data is presented as mean ± SEM. Statistics: Tukey's multiple comparison test. Abbreviations: N = neutral media, A = acidic media, N$^{IFN-γ}$ = neutral media plus IFN-γ, A$^{IFN-γ}$ = acidic media plus IFN-γ.

Taken together, these findings suggest an unsuspected and so far, not described potential regulatory role of STAT2 in IFN-γ-mediated PD-L1 expression. Furthermore, the transcription factor STAT1 seems to be involved in conjoint IFN-γ- and acidosis-mediated *Stat2* gene expression, whereas STAT2 itself regulates *Stat1* mRNA as well as *Pd-l1* mRNA and PD-L1 cell surface protein expression levels.

4.1.9 Tumor acidification-targeting therapeutic strategies, PD-L1 expression and immune cell recruitment

To further validate the relevance of IFN-γ- and acidosis-inducible PD-L1 expression, *in vivo* experiments in immune competent mice were performed.

To study the role of tumor pH_e neutralization, immune cell recruitment, activation and IFN-γ secretion *in vivo*, four tumor models originating from two mice strains were applied. Two tumor models, namely MC38^{wt} and B16-F10^{wt} originate from C57BL/6 mice, which are characterized by T_h1 polarization, high TNF, IL-12 and IFN-γ levels as well as low IL-13 production by CD4$^+$ T cells [226, 227]. In contrast, CT26^{wt} and 4T1^{wt} tumors originate from BALB/c strains, which are T_h2 prone and characterized by high IL-4 levels [226, 228]. In this regard, two syngeneic murine tumor models were selected that respond to an anti-PD-L1 mAb therapy (MC38^{wt} and CT26^{wt}) and two tumor models classified as low-/non-responders to an anti-PD-1 and/or anti-PD-L1 mAb therapy (B16-F10^{wt} and 4T1^{wt}) [196, 197, 208, 217, 402-404]. Most importantly, the tumor models applied in the *in vivo* studies range from low (CT26^{wt} and 4T1^{wt} [218]) to medium (MC38^{wt} and B16-F10^{wt}) basal PD-L1 cell surface expression (**Figure 23 A**). Classification into the categories low and medium basal PD-L1 expression is based on the MFI difference of cancer cell surface PD-L1 expression in neutral media and unstained living cells. This equation yields the Δ basal PD-L1 of the respective cancer cell line and reveals a value smaller or greater than the arbitrary number 250 discriminating low and medium basal PD-L1 cell surface expression (**Figure 23 B, C**). Furthermore, PD-L1 expression was inducible by IFN-γ stimulation in all four studied murine cancer

cell lines (**Figure 23 A**).

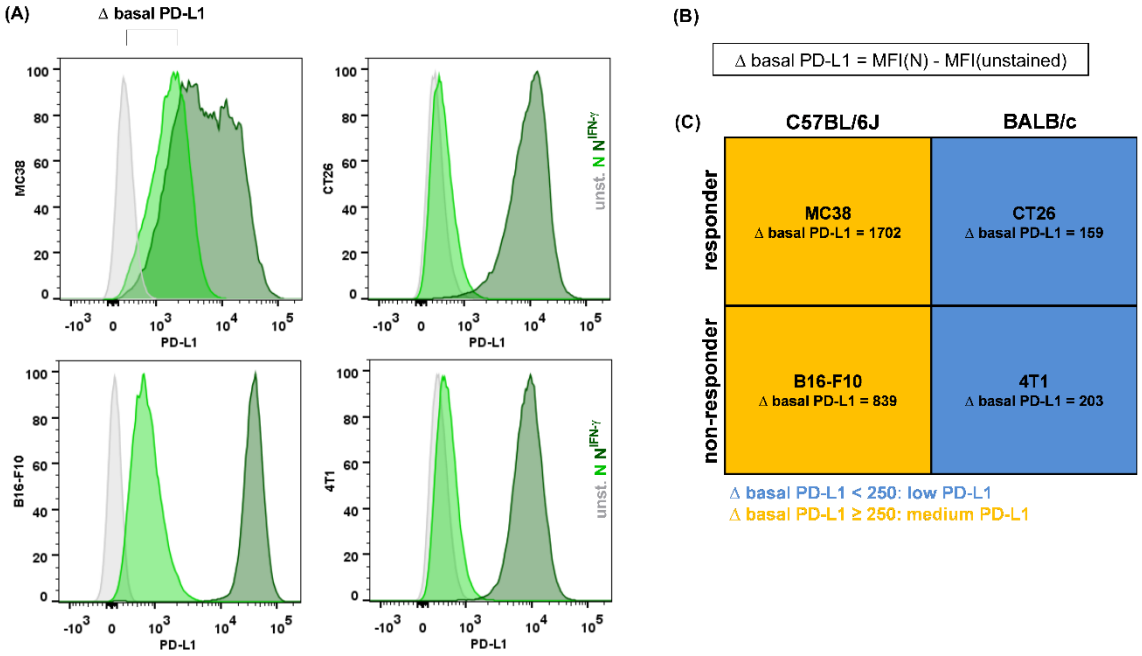

Figure 23: Basal and IFN-γ-inducible PD-L1 expression on murine cancer cell lines.
(A) Flow cytometry analysis of basal (light green) and IFN-γ-induced (10 ng ml^{-1}; 24 h; dark green) PD-L1 expression of $MC38^{wt}$, $CT26^{wt}$, $B16\text{-}F10^{wt}$ and $4T1^{wt}$ cells. Unstained cells (out of the live gate) are depicted in grey (1 independent experiment, n = 1). **(B)** Equation applied to calculate the basal level of PD-L1 in the four different cancer cell lines to classify them into low basal PD-L1 (Δbasal PD-L1 < 250) and medium basal PD-L1(Δbasal PD-L1 ≥ 250) expression. **(C)** Schematic overview of $MC38^{wt}$, $CT26^{wt}$, $B16\text{-}F10^{wt}$ and $4T1^{wt}$ cells, their classification as anti-PD-L1 mAb therapy responders and non-responders as well as their mouse strain of origin. Abbreviations: N = neutral media, $N^{IFN\text{-}\gamma}$ = neutral media plus IFN-γ.

For *in vivo* studies, the terminology was adjusted according to the terminology used for *in vitro* experiments. Immune competent mice with intact IFN-γ signaling that received sodium bicarbonate-enriched drinking water and therefore exhibit a neutral tumor pH_e are referred to as '$neutral^{IFN\text{-}\gamma}$', whereas mice that received regular drinking water and therefore exhibit an acidic tumor pH_e are termed '$acidosis^{IFN\text{-}\gamma}$'. Equivalently, mice deficient in IFN-γ signaling that received sodium bicarbonate-enriched drinking water are termed 'neutral' and mice of the group that received regular drinking water are termed 'acidosis'.
To study the role of tumor pH_e on PD-L1 expression and immune cell recruitment *in vivo*, tumor-bearing mice were treated with sodium bicarbonate *ad libitum*

starting three days prior cancer cell inoculation as previously described [76-78, 81]. $MC38^{wt}$ cancer cells with basal and IFN-γ-inducible PD-L1 expression were injected *s.c.* on the right shoulder of immune competent C57BL6J mice with intact IFN-γ signaling. Treatment with sodium bicarbonate ($neutral^{IFN\text{-}\gamma}$) resulted in a slightly reduced (P-value = 0.0895) $MC38^{wt}$ tumor volume at day 15 post cancer cell inoculation (**Figure 24 A**). In other words, tumor $acidosis^{IFN\text{-}\gamma}$ resulted in an increased tumor volume, suggesting $acidosis^{IFN\text{-}\gamma}$-mediated tumor immune escape. Moreover, mice treated with the anti-PD-L1 mAb clone 10F.9G2 (Bio X Cell, West Lebanon, NH, USA) which blocks the interaction between PD-L1 and PD-1 as well as B7-1 (CD80) yielded a significant reduction in $MC38^{wt}$ tumor volume (responder tumor model, **Figure 24 A**). Interestingly, a combination of sodium bicarbonate and anti-PD-L1 mAb therapy did not further reduce the tumor volume, indicating no synergistic effect when both therapeutic components are combined (**Figure 24 A**). The role of basal and IFN-γ-inducible PD-L1 expression as a prognostic biomarker is therefore the subject of this study. In contrast to $MC38^{wt}$ cancer cells which are sensitive to IFN-γ-mediated PD-L1 cell surface induction (**Figure 24 B**), $MC38^{PD\text{-}L1\text{-}/\text{-}}$ cells deficient in PD-L1 [196] were also used for *in vivo* experiments. The constitutive PD-L1 knockout was confirmed by flow cytometry of $MC38^{PD\text{-}L1\text{-}/\text{-}}$ cells which were cultured in neutral media in the absence or presence of IFN-γ (100 ng ml^{-1}). $MC38^{PD\text{-}L1\text{-}/\text{-}}$ cells revealed a significant reduction in basal PD-L1 expression which was indistinguishable from the histogram of unstained live cells. Furthermore, stimulation of $MC38^{PD\text{-}L1\text{-}/\text{-}}$ cells with IFN-γ did not result in an induction of membrane-bound PD-L1 expression (**Figure 24 D**). *In vivo*, $MC38^{PD\text{-}L1\text{-}/\text{-}}$ tumor-bearing mice exhibited an overall reduced tumor growth when compared to $MC38^{wt}$ tumors (**Figure 24 C**). This reduced tumor growth and the rejection of $MC38^{PD\text{-}L1\text{-}/\text{-}}$ cancer cells in one experimental mouse of the $acidosis^{IFN\text{-}\gamma}$ group underlines the importance of PD-L1 expression on cancer cells to inhibit an anti-tumor immune response. This supports the hypothesis of acidosis and IFN-γ-mediated tumor immune evasion via induction of PD-L1 expression by cancer cells. Furthermore, $MC38^{PD\text{-}L1\text{-}/\text{-}}$ tumor-bearing mice in the $neutral^{IFN\text{-}\gamma}$ group did not exhibit a significant reduction in tumor volume in comparison to $MC38^{wt}$ tumor-bearing mice that received sodium bicarbonate. The large SEM at day 20 and day 21 is due to one very large tumor in the $acidosis^{IFN\text{-}\gamma}$ group. The respective

mouse had to be removed subsequently from the experiment due to the federal animal welfare regulations at day 21 (**Figure 24 C**).

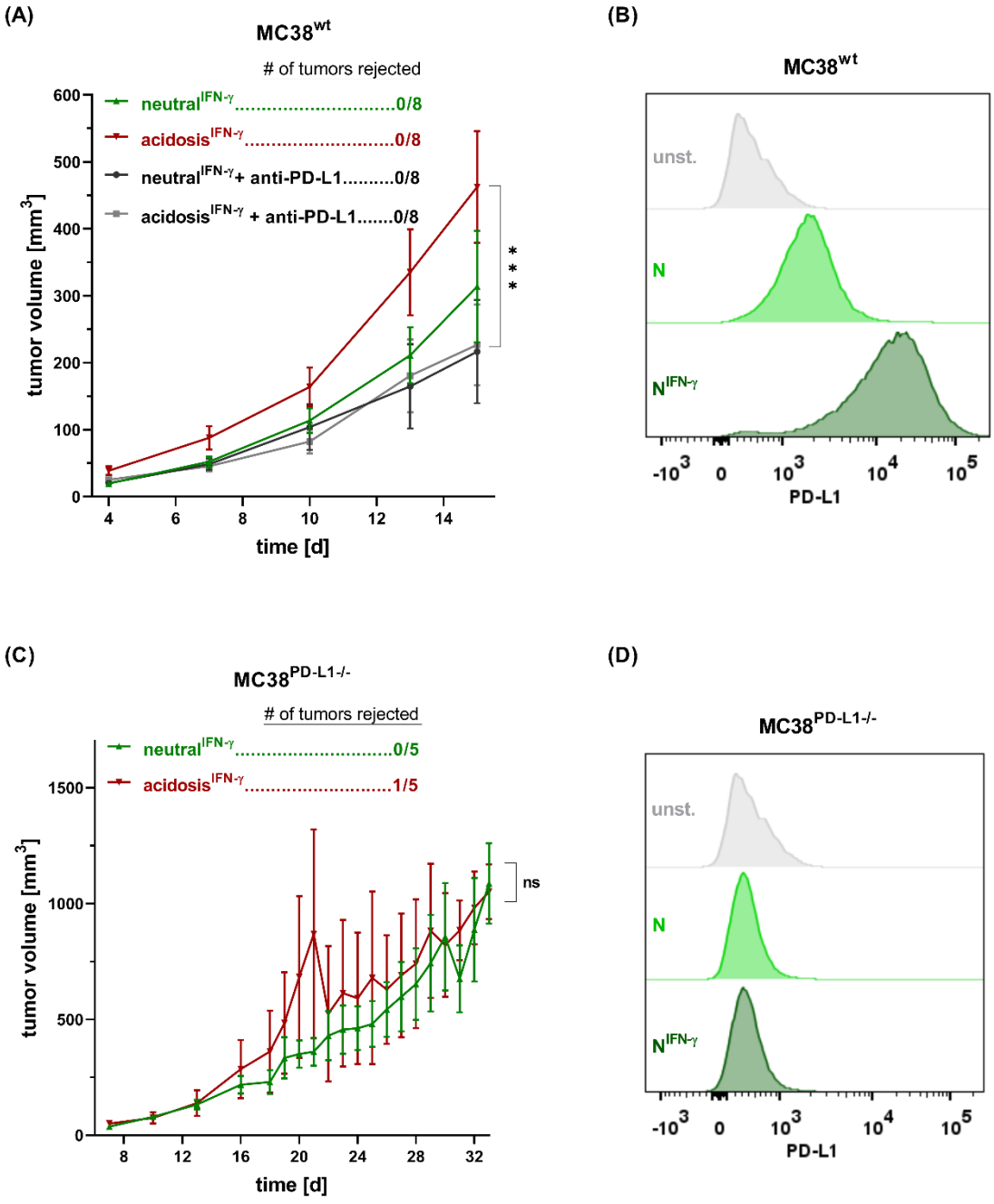

Figure 24: Effect of sodium bicarbonate and/or anti-PD-L1 mAb therapy on MC38^{wt} and MC38$^{PD\text{-}L1\text{-}/\text{-}}$ tumor growth *in vivo*.

(A) Tumor volume of MC38^{wt} (n = 8 animals per group; 1 independent experiment, statistics: Tukey's multiple comparison test) and **(C)** MC38$^{PD\text{-}L1\text{-}/\text{-}}$ (n = 4-5 animals per group; 1 independent experiment, statistics: Sidak's multiple comparison test) tumors in C57BL/6J mice treated with sodium bicarbonate-enriched water *ad libitum* starting three days prior to cancer cell injection and/or anti-PD-L1 mAb (200 µg per mouse) treatment every third day, starting from day 4 post

cancer cell injection. Data is presented as mean ± SEM. Flow cytometry histograms of **(B)** $MC38^{wt}$ and **(D)** $MC38^{PD\text{-}L1\text{-}/\text{-}}$ cells cultured in neutral media in the absence (light green) or presence (dark green) of IFN-γ (100 ng ml^{-1}) for 24 h to confirm the CRISP/Cas9-mediated PD-L1 knockout. Abbreviations: $neutral^{IFN\text{-}\gamma}$ = mice with intact IFN-γ signaling treated with sodium bicarbonate-enriched drinking water leading to tumor pH_e neutralization, $acidosis^{IFN\text{-}\gamma}$ = mice with intact IFN-γ signaling receiving regular drinking water leading to tumor pH_e acidification.

In the field of immunotherapy, tumors are often defined as hot (T cell 'inflamed'), altered, and cold tumors (not T cell 'inflamed'). These classifications are based on the composition of the TIME and the pro-inflammatory cytokine patterns, with hot tumors usually exhibiting a better response rate to immunotherapy [405, 406]. Therefore, histology and IHC of $MC38^{wt}$ and $MC38^{PD\text{-}L1\text{-}/\text{-}}$ tumor tissue was performed. H&E staining of $MC38^{wt}$ tumors revealed large cells with marked pleomorphism, abundant cytoplasm and large and pleomorphic nuclei with prominent nucleoli. Tumors of $acidosis^{IFN\text{-}\gamma}$ mice exhibited focal central necrosis and mild acute inflammation in the periphery of the tumor tissue (**Figure 25 A**). $MC38^{wt}$ tumors of $neutral^{IFN\text{-}\gamma}$ animals exhibited mild to intense necrosis. Necrosis was found in the center but also as necrotic foci in the periphery of the tumor. Quantification of the necrotic area revealed more necrosis in $MC38^{wt}$ tumors of the $neutral^{IFN\text{-}\gamma}$ compared to the $acidosis^{IFN\text{-}\gamma}$ group (**Figure 25 B**). This finding is consistent with the results reported by Faes *et al.* for the same tumor model [78]. Further $MC38^{wt}$ tumors are characterized by a high macrophage content detected by ionized calcium binding adaptor molecule 1 (Iba1) IHC staining. CD3 staining revealed abundant T cells in the tumor periphery and some in the center of the tumor. Medium to large tumors showed fewer $CD3^+$ T cells, mainly located in the periphery of the tumor (**Figure 25 A**). Similar necrosis patterns could be observed in $MC38^{wt}$ tumors from mice treated with anti-PD-L1 mAb. In the $acidosis^{IFN\text{-}\gamma}$ + anti-PD-L1 group, tumors showed mild necrosis arranged in cords and variable CD3 staining depending on the tumor volume. Small to medium size tumors showed focal patchy necrosis with $CD3^+$ T cells in the periphery and the center of the tumor, whereas larger tumors exhibited less $CD3^+$ T cells. Taken together, a combined treatment with sodium bicarbonate and anti-PD-L1 mAb ($neutral^{IFN\text{-}\gamma}$ + anti-PD-L1) increased the recruitment of $CD3^+$ T cells to the tumor periphery. Furthermore, tumors with higher amounts of $CD3^+$ T cells were predominantly smaller in volume. PD-L1 staining of $MC38^{wt}$ tumors revealed that almost all cells

of the tumor mass stained positive for PD-L1 in the acidosis$^{IFN-\gamma}$ and neutral$^{IFN-\gamma}$ group. To validate the PD-L1 IHC staining, MC38^{wt} tumors of anti-PD-L1 mAb treated mice underwent PD-L1 staining. These MC38^{wt} tumors showed a clear reduction in PD-L1 staining, due to blocking of the target antigen with the therapeutic anti-PD-L1 mAb administered to these animals (**Figure 25 A**). Furthermore, tumors of the neutral$^{IFN-\gamma}$ group revealed a higher and more intense PD-L1 staining compared to tumors of the acidosis$^{IFN-\gamma}$ group. PD-L1 expression was heterogeneous across the neutral$^{IFN-\gamma}$ tumors, with more intense and clustered PD-L1 staining nearby necrotic regions (**Figure 25 A**). These necrotic regions in MC38^{wt} tumors of the neutral$^{IFN-\gamma}$ group were characterized by palisading macrophages detected by Iba1 IHC staining (**Figure 25 A**).

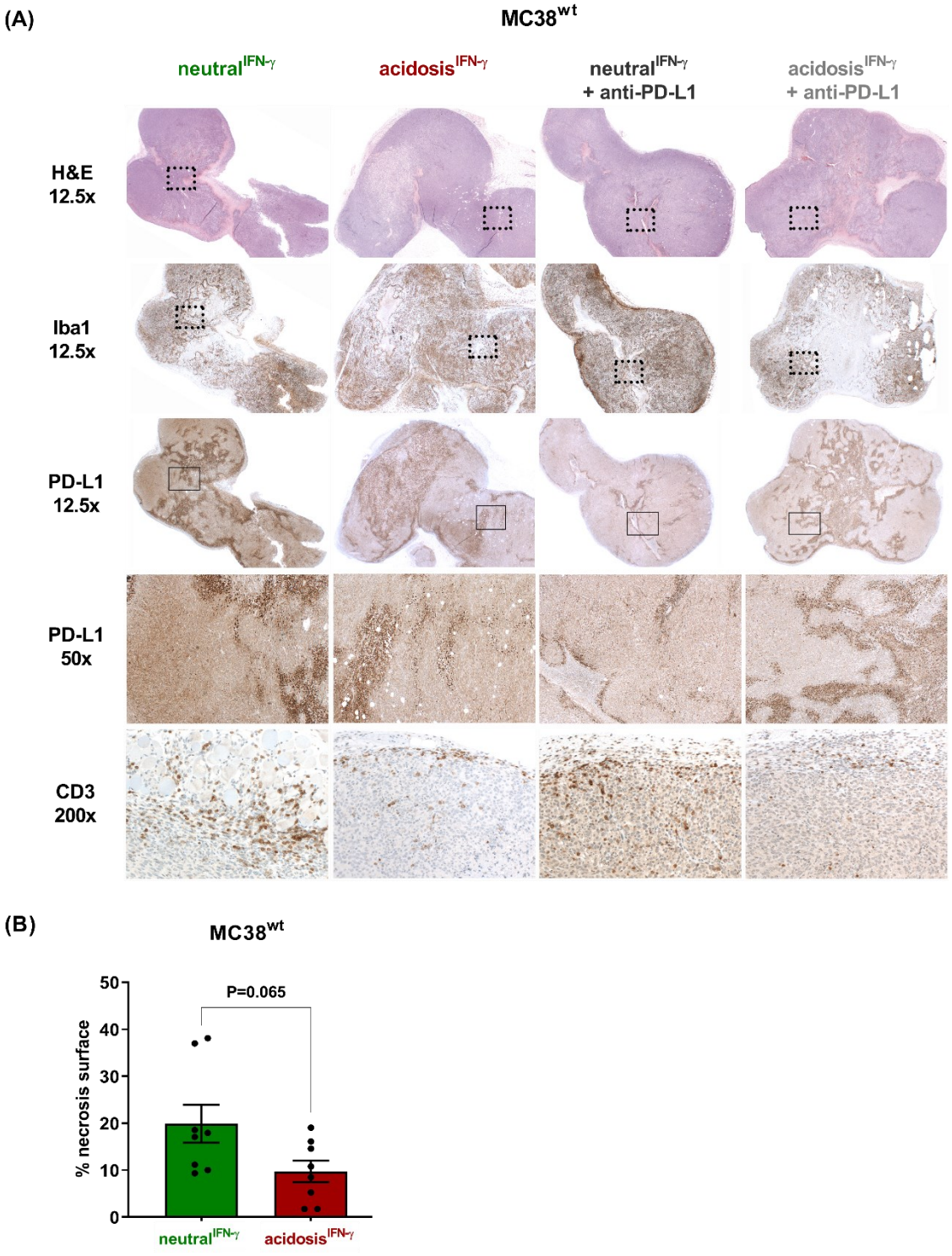

Figure 25: Histology and IHC of murine MC38^{wt} tumors.

(A) Representative H&E, Iba1, PD-L1 and CD3 staining of *s.c.* MC38^{wt} tumors harvested at day 18 after onset of treatment with sodium bicarbonate (neutral$^{IFN-\gamma}$) enriched drinking water. Animals were treated with sodium bicarbonate-enriched water *ad libitum* starting three days prior to cancer cell inoculation and/or repetitive anti-PD-L1 mAb (200 µg per mouse; every third day) treatment, starting from day 4 post cancer cell inoculation. All MC38^{wt} tumors (n = 8 animals per group) underwent H&E staining. Based on H&E staining, representative tumors were selected for Iba1,

PD-L1 and CD3 IHC. Dotted and solid rectangles indicate the identical tumor region in the 12.5x H&E, Iba1 and PD-L1 images. The 50x magnification of the PD-L1 stained tumor region is equivalent to the excerpt indicated by the solid rectangle in the 12.5x magnification. The images in 200x magnification of the CD3 staining were obtained from the tumor periphery and tumor areas are not indicated in the 12.5x H&E images. **(B)** The percentage of the necrotic area was quantified (quantification of pink surface area greater than 0.01 mm^2 in $MC38^{wt}$ tumors stained with H&E) in $MC38^{wt}$ tumors from mice treated with sodium bicarbonate ($neutral^{IFN\text{-}\gamma}$) or regular drinking water ($acidosis^{IFN\text{-}\gamma}$). Data is presented as mean ± SEM. Statistics: two-tailed Mann-Whitney test. Abbreviations: $neutral^{IFN\text{-}\gamma}$ = mice with intact IFN-γ signaling treated with sodium bicarbonate-enriched drinking water leading to tumor pH_e neutralization; $acidosis^{IFN\text{-}\gamma}$ = mice with intact IFN-γ signaling receiving regular drinking water leading to tumor pH_e acidification.

$MC38^{wt}$ tumors derived from mice with intact IFN-γ signaling without any treatment developed tumor acidosis ($acidosis^{IFN\text{-}\gamma}$) and revealed elevated cancer cell PD-L1 expression when compared to tumors of mice with intact IFN-γ signaling and sodium bicarbonate treatment ($neutral^{IFN\text{-}\gamma}$; **Figure 26 A, B**). This *ex vivo* discovery confirms the *in vitro* findings on conjoint IFN-γ- and acidosis-induced elevation of membrane-bound PD-L1 expression on $MC38^{wt}$ cancer cells presented in Figure 13 B. Interestingly, $MC38^{wt}$ tumors of the $neutral^{IFN\text{-}\gamma}$ group exhibited higher PD-L1 expression on TILs when compared to the $acidosis^{IFN\text{-}\gamma}$ group (**Figure 26 A, B**). These findings are substantiated by quantitative analysis of the immune fluorescence microscopy images, revealing significantly higher PD-L1 positive areas per $MC38^{wt}$ cancer cell and significantly lower PD-L1 positive area per immune cell within tumors of the $acidosis^{IFN\text{-}\gamma}$ compared to the $neutral^{IFN\text{-}\gamma}$ group (**Figure 26 C, D**). In conclusion, elevated PD-L1 expression on $MC38^{wt}$ cancer cells in the $acidosis^{IFN\text{-}\gamma}$ group is associated with a higher tumor volume compared to the $neutral^{IFN\text{-}\gamma}$ group suggesting a so far unknown mechanism of tumor immune escape (**Figure 26**, **Figure 24 A**).

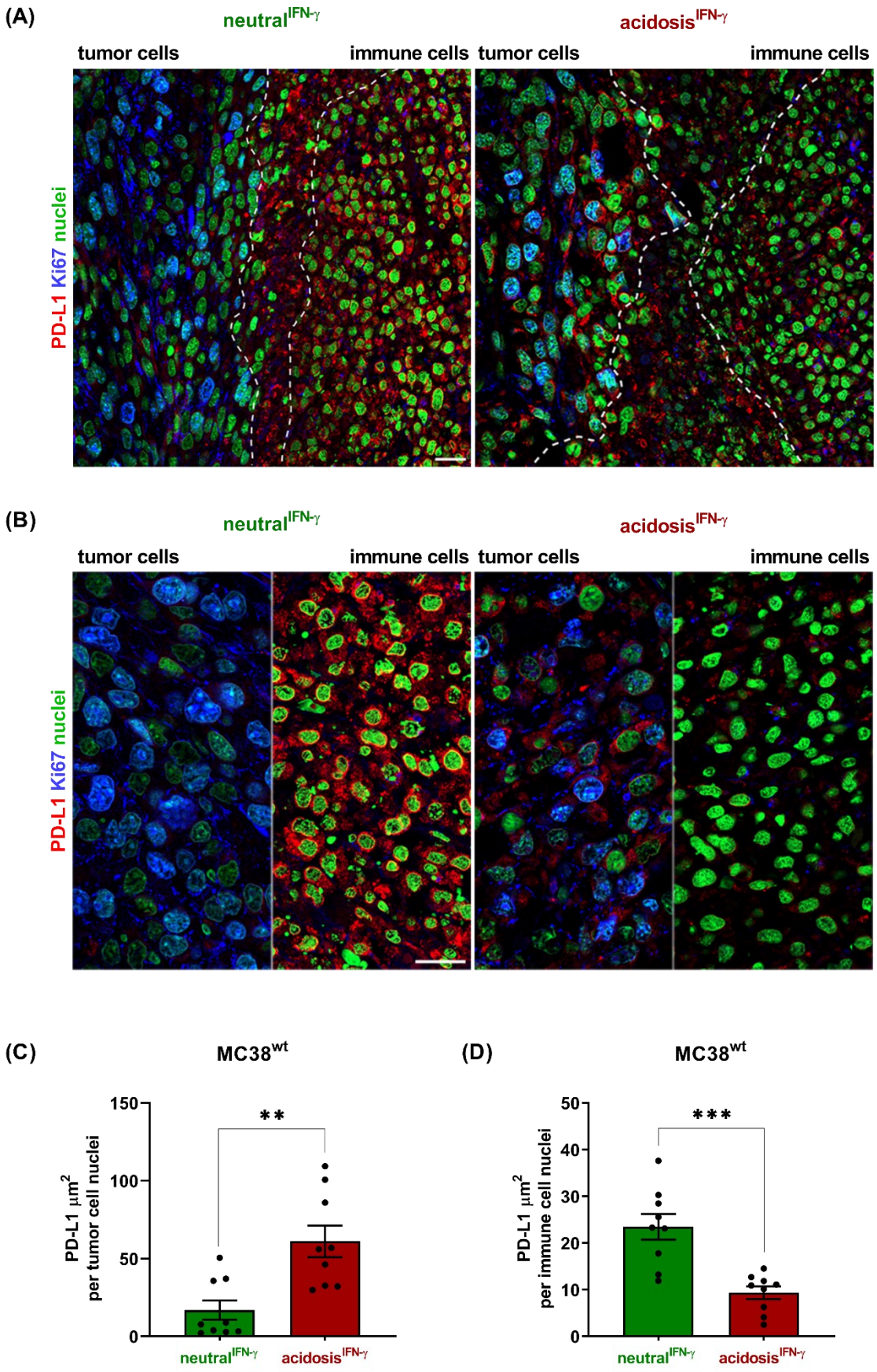

Figure 26: Tumor acidosis elevates PD-L1 expression on cancer cells.

(A, B) Representative fluorescence microscopy images of *s.c.* MC38^{wt} tumors isolated at day 18 (post treatment start with sodium bicarbonate) from sodium bicarbonate (neutral$^{IFN\text{-}\gamma}$) and regular drinking water (acidosis$^{IFN\text{-}\gamma}$) treated mice and stained for PD-L1 and the proliferation marker Ki67. The dotted line separates proliferating MC38^{wt} cancer cells on the left from non-proliferating immune cells on the right side. Tumor and immune cells were identified based on morphological characteristics as well as Ki67, CD4, CD8 and Iba1 staining performed in serial slices. **(C, D)** PD-L1 fluorescence area was quantified in MC38^{wt} tumor regions high (cancer cells) and low (immune cells) in Ki67 expression and normalized to the number of nuclei. Data is presented as mean ± SEM. Statistics: two-tailed Mann-Whitney test. Abbreviations: neutral$^{IFN\text{-}\gamma}$ = mice with intact IFN-γ signaling treated with sodium bicarbonate-enriched drinking water leading to tumor pH_e neutralization, acidosis$^{IFN\text{-}\gamma}$ = mice with intact IFN-γ signaling receiving regular drinking water leading to tumor pH_e acidification.

Furthermore, tumor pH_e neutralization led to enhanced early activation of $CD4^+$ T cells, determined by CD69 immune fluorescence microscopy (**Figure 27**). Interestingly, no pH_e neutralization induced changes in $CD8^+$ T cell and macrophage homing patterns were observed by fluorescence microscopy (**Figure 27**).

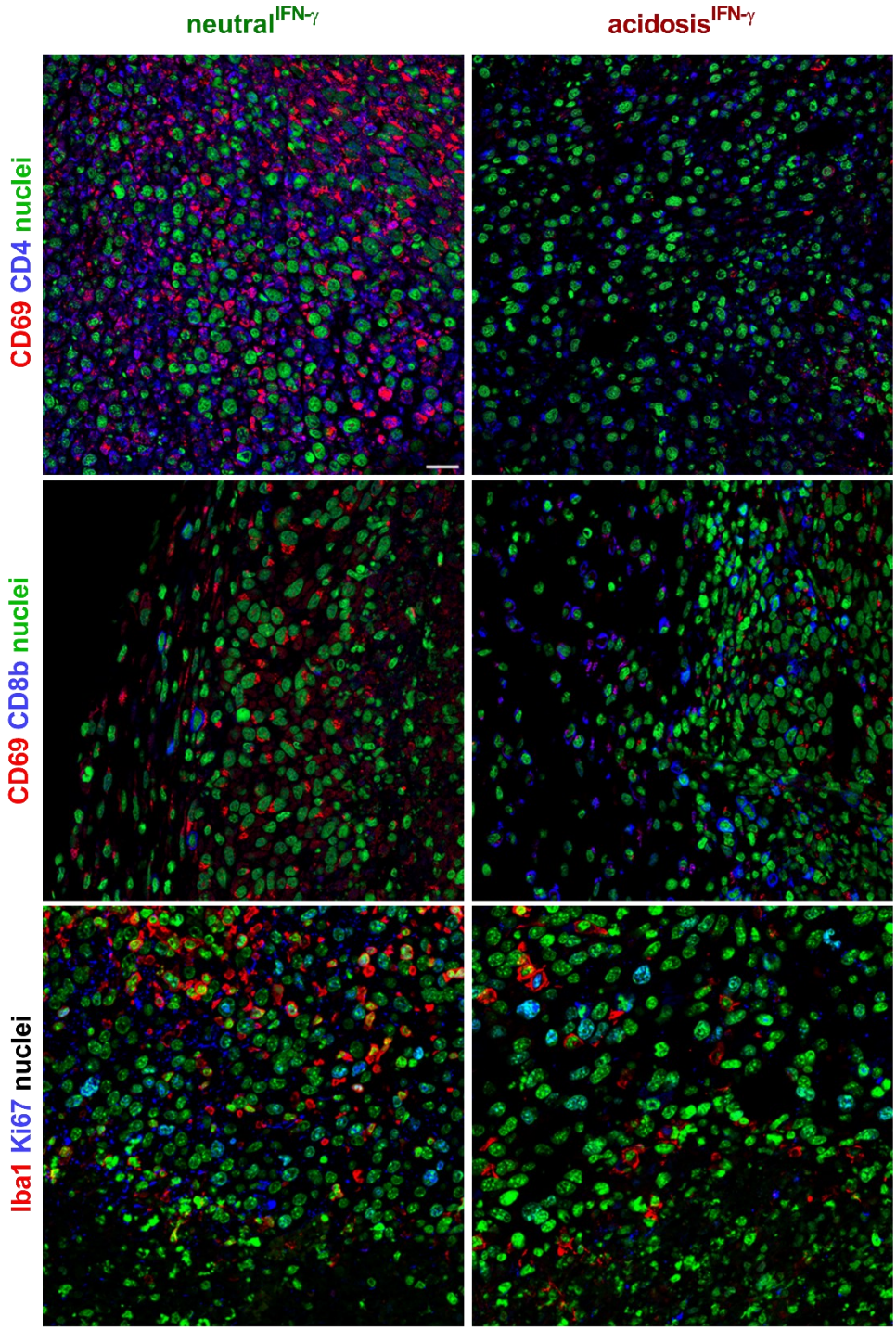

Figure 27: Tumor pH_e neutralization elevates immune cell activation.

(A) Representative fluorescence microscopy images of *s.c.* MC38^{wt} tumors isolated at day 18 (post treatment start with sodium bicarbonate) from sodium bicarbonate (neutral$^{IFN-\gamma}$) and regular drinking water (acidosis$^{IFN-\gamma}$) treated mice and stained for CD69 (early activation marker), CD4 (CD4$^+$ T cells), CD8b (CD8$^+$ T cells), Ki67 (proliferation marker) and Iba1 (macrophages). Abbreviations: neutral$^{IFN-\gamma}$ = mice with intact IFN-γ signaling treated with sodium bicarbonate-enriched drinking water leading to tumor pH_e neutralization, acidosis$^{IFN-\gamma}$ = mice with intact IFN-γ signaling receiving regular drinking water leading to tumor pH_e acidification.

Histological analysis of H&E staining of MC38$^{PD\text{-}L1\text{-}/\text{-}}$ tumors revealed marked pleomorphism, abundant cytoplasm and large and pleomorphic nuclei. Both, tumors from the acidosis$^{IFN\text{-}\gamma}$ and neutral$^{IFN\text{-}\gamma}$ group showed a prominent central necrosis (**Figure 28 A**). Apart from significantly less necrosis in MC38$^{PD\text{-}L1\text{-}/\text{-}}$ tumors of the neutral$^{IFN\text{-}\gamma}$ compared to the acidosis$^{IFN\text{-}\gamma}$ group, there were no additional histological differences between both groups (**Figure 28 A, B**). PD-L1 IHC of MC38$^{PD\text{-}L1\text{-}/\text{-}}$ tumors revealed a heterogeneous PD-L1 staining, with PD-L1 negative cancer cells and regions of PD-L1 positive cells (not cancer cells) within the tumor. Furthermore, Iba1 IHC of MC38 tumors, which are known to be rich in macrophages [407-411], confirmed a high content of activated macrophages [412, 413] in MC38$^{PD\text{-}L1\text{-}/\text{-}}$ tumors (Figure 28 **B**). The distribution of these activated macrophages in MC38$^{PD\text{-}L1\text{-}/\text{-}}$ tumors was heterogeneous with clusters of more and clusters of less intense Iba1 staining. Interestingly, Iba1 staining matched with regions of high PD-L1 expression. This suggests that the PD-L1 expression in PD-L1 deficient MC38$^{PD\text{-}L1\text{-}/\text{-}}$ tumors originates from tumor resident macrophages (**Figure 28 A**). For both, tumors from the acidosis$^{IFN\text{-}\gamma}$ and neutral$^{IFN\text{-}\gamma}$ group a CD3 IHC revealed few CD3^{+} T cells in the tumor periphery (**Figure 28 A**).

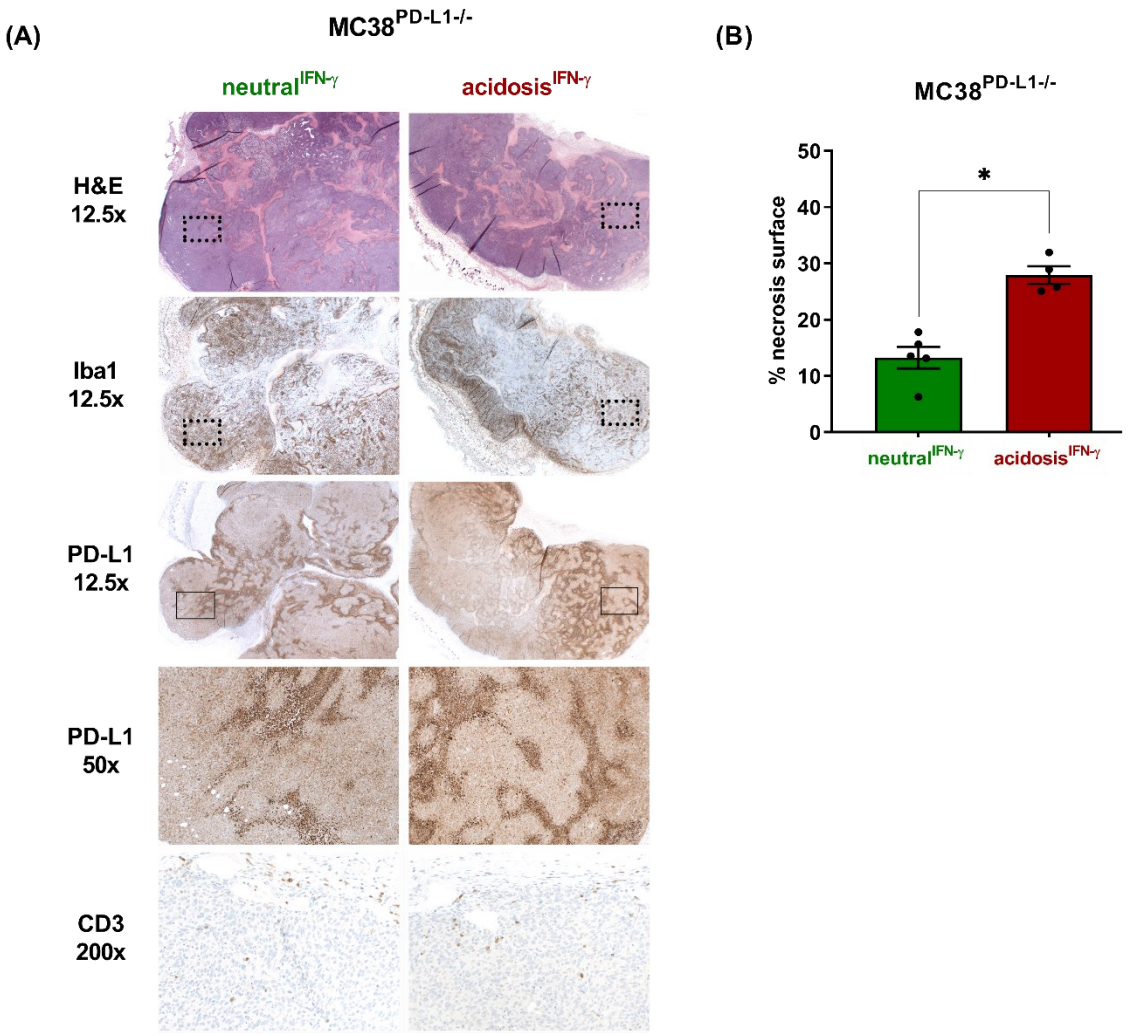

Figure 28: Histology and IHC of murine MC38$^{PD\text{-}L1\text{-}/\text{-}}$ tumors.

(A) Representative H&E, Iba1, PD-L1 and CD3 staining of *s.c.* MC38$^{PD\text{-}L1\text{-}/\text{-}}$ tumors harvested at day 38 after onset of treatment with sodium bicarbonate (neutral$^{IFN\text{-}\gamma}$) enriched drinking water. Animals were treated with sodium bicarbonate-enriched water *ad libitum* starting three days prior to cancer cell inoculation. MC38$^{PD\text{-}L1\text{-}/\text{-}}$ tumors (n = 3-4 animals per group) underwent H&E staining. Based on H&E staining, representative tumors were selected for Iba1, PD-L1 and CD3 IHC. Dotted and solid rectangles indicate the identical tumor region in the 12.5x H&E, Iba1 and PD-L1 images. The 50x magnification of the PD-L1 stained tumor region is equivalent to the excerpt indicated by the solid rectangle in the 12.5x magnification. The images in 200x magnification of the CD3 staining were obtained from the tumor periphery and tumor areas are not indicated in the 12.5x H&E images. **(B)** The percentage of the necrotic area was quantified (quantification of pink surface area greater than 0.01 mm^2 in MC38$^{PD\text{-}L1\text{-}/\text{-}}$ tumors stained with H&E) in MC38$^{PD\text{-}L1\text{-}/\text{-}}$ tumors from mice treated with sodium bicarbonate (neutral$^{IFN\text{-}\gamma}$) or regular drinking water (acidosis$^{IFN\text{-}\gamma}$). Data is presented as mean ± SEM. Statistics: two-tailed Mann-Whitney test. Abbreviations: neutral$^{IFN\text{-}\gamma}$ = mice with intact IFN-γ signaling treated with sodium bicarbonate-enriched drinking water leading to tumor pH_e neutralization; acidosis$^{IFN\text{-}\gamma}$ = mice with intact IFN-γ signaling receiving regular drinking water leading to tumor pH_e acidification.

Mice on a C57BL/6J background are known to exhibit an augmented IL-12 production by macrophages and an increased IFN-γ production [226, 227]. In order to investigate the role of IFN-γ secretion by various immune cells including $CD8^+$ T cells on PD-L1 expression during sodium bicarbonate treatment, $MC38^{wt}$ cancer cells were inoculated in IFN-γ-deficient mice. Genetically engineered B6.129S7-$Ifng^{tm1Ts}$/J mice are deficient in IFN-γ secretion and exhibit impaired MHC II antigens [365]. As an internal control, C57BL/6J mice from the same room within a breeding facility were used to ensure that the determined effects are not due to potential differences in the mouse microbiome originating from different husbandry conditions. Again, as shown before, $MC38^{wt}$ tumor bearing C57BL/6J mice with intact IFN-γ signaling exhibited a significant reduction in tumor volume upon sodium bicarbonate treatment at day 13 post $MC38^{wt}$ cancer cell inoculation ($neutral^{IFN\text{-}\gamma}$ vs. $acidosis^{IFN\text{-}\gamma}$; **Figure 29 A**). In contrast to this finding, neither a sodium bicarbonate (neutral vs. acidosis) nor an anti-PD-L1 mAb treatment resulted in a reduction in $MC38^{wt}$ tumor volume in IFN-γ-deficient mice. Also, the combination of sodium bicarbonate and anti-PD-L1 mAb treatment was inefficient in IFN-γ-deficient mice (**Figure 29 B**).

Taken together, these findings suggest that the effect of a sodium bicarbonate as well as anti-PD-L1 mAb therapy depends on the secretion of IFN-γ by various immune cells within the tumors. Or in other words, $MC38^{wt}$ tumors escape immune control via IFN-γ signaling and tumor acidosis most likely mediated by induction of PD-L1 expression, which is associated with higher tumor volumes in the $acidosis^{IFN\text{-}\gamma}$ compared to the $neutral^{IFN\text{-}\gamma}$ group and unaltered tumor volumes between the acidosis and neutral group.

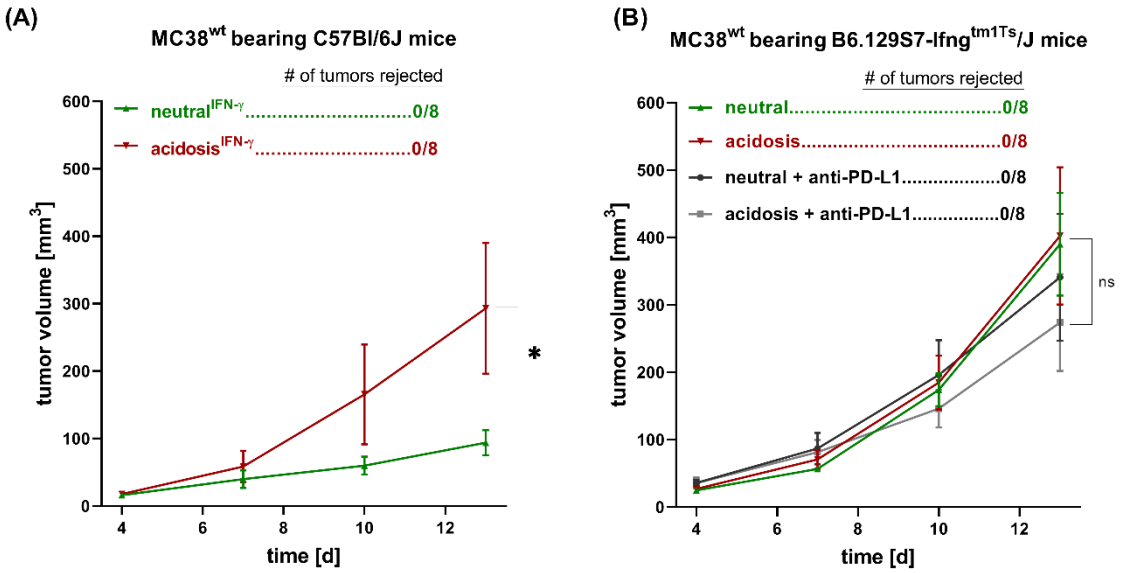

Figure 29: Effect of sodium bicarbonate and/or anti-PD-L1 mAb therapy on MC38^{wt} tumor growth in wild type and IFN-γ-deficient mice.

Tumor volume of MC38^{wt} tumor-bearing **(A)** C57BL/6J (wild type) and **(B)** B6.129S7-Ifng^{tm1Ts}/J (IFN-γ-deficient) mice (1 independent experiment, n = 7-8 animals per group) treated with sodium bicarbonate-enriched water *ad libitum* starting three days prior to cancer cell injection and/or anti-PD-L1 mAb (200 µg per mouse) treatment every third day, starting from day 4 post cancer cell injection. Data is presented as mean ± SEM. Statistics: Tukey's multiple comparison test. Abbreviations: neutral$^{IFN-γ}$ = mice with intact IFN-γ signaling treated with sodium bicarbonate-enriched drinking water leading to tumor pH_e neutralization, acidosis$^{IFN-γ}$ = mice with intact IFN-γ signaling receiving regular drinking water leading to tumor pH_e acidification, neutral = mice deficient in IFN-γ treated with sodium bicarbonate-enriched drinking water leading to tumor pH_e neutralization, acidosis = mice deficient in IFN-γ receiving regular drinking water leading to tumor pH_e acidification.

Histological analysis again revealed marked pleomorphism, abundant cytoplasm as well as large and pleomorphic nuclei with conspicuous nucleolus. MC38^{wt} tumors from C57BL/6J wild type mice from the neutral$^{IFN-γ}$ group exhibited again a slightly more intense PD-L1 staining compared to the acidosis$^{IFN-γ}$ group. Interestingly, the overall PD-L1 staining was more intense in MC38^{wt} tumors from IFN-γ-deficient B6.129S7-Ifng^{tm1Ts}/J mice compared to MC38^{wt} tumors from wild type C57BL/6J mice suggesting an engagement of other compensatory pathways that regulate PD-L1 expression on cancer cells apart from the IFN-γ- eIF4F-STAT1-PD-L1 axis. Noteworthy is the slightly weaker PD-L1 staining in MC38^{wt} tumors of the neutral$^{IFN-γ}$ compared to the acidosis$^{IFN-γ}$ group of IFN-γ-deficient B6.129S7-

Ifng^{tm1Ts}/J mice, without any additional differences in Iba1 and CD3 staining between the four experimental treatment groups (**Figure 30**).

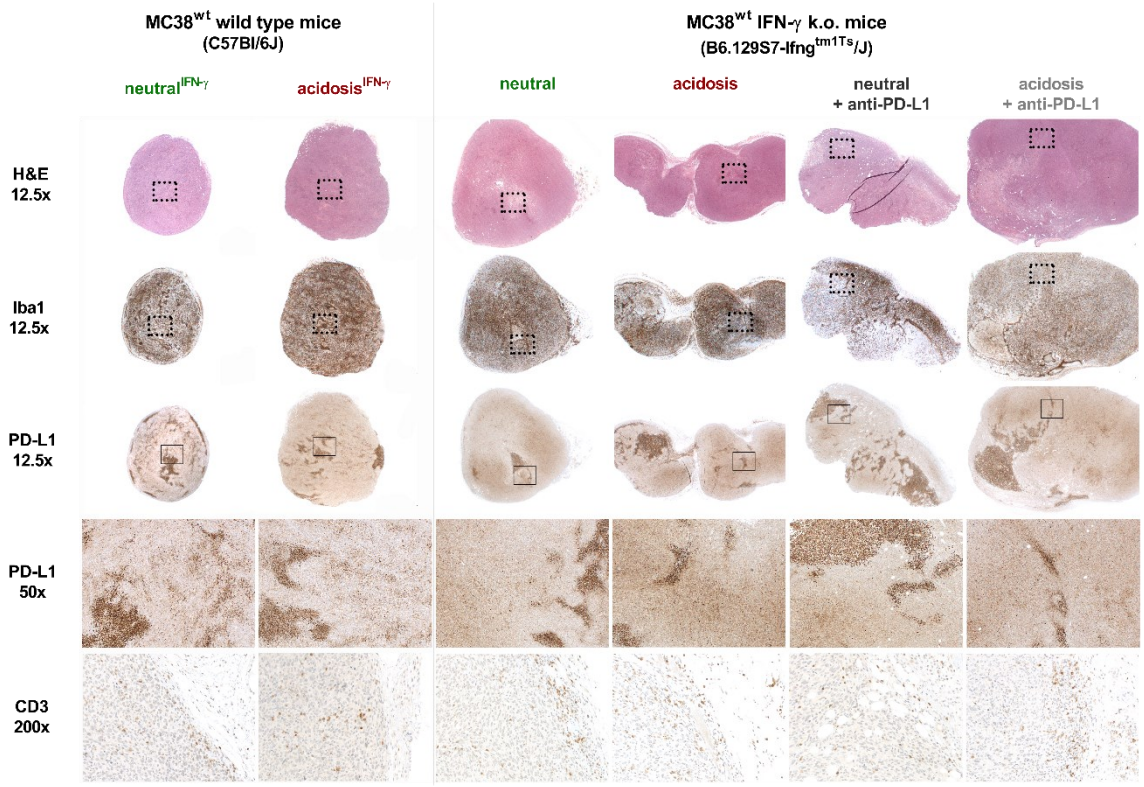

Figure 30: Histology and IHC of murine MC38^{wt} tumors in wild type and IFN-γ-deficient mice. Representative H&E, Iba1, PD-L1 and CD3 staining of *s.c.* MC38^{wt} tumors grown in C57BL/6J wild type or IFN-γ knockout (k.o.) B6.129S7-Ifngtm1Ts/J mice harvested at day 16 after onset of treatment with sodium bicarbonate (neutral$^{IFN-γ}$) enriched drinking water. Animals were treated with sodium bicarbonate-enriched water *ad libitum* starting three days prior to cancer cell inoculation and/or repetitive anti-PD-L1 mAb (200 µg per mouse; every third day) treatment, starting from day 4 post cancer cell inoculation. MC38^{wt} tumors (n = 4-5 animals per group) underwent H&E staining. Based on H&E staining, representative tumors were selected for Iba1, PD-L1 and CD3 IHC. Dotted and solid rectangles indicate the identical tumor region in the 12.5x H&E, Iba1 and PD-L1 images. The 50x magnification of the PD-L1 stained tumor region is equivalent to the excerpt indicated by the solid rectangle in the 12.5x magnification. The images in 200x magnification of the CD3 staining were obtained from the tumor periphery and tumor areas are not indicated in the 12.5x H&E images. Abbreviations: neutral$^{IFN-γ}$ = mice with intact IFN-γ signaling treated with sodium bicarbonate-enriched drinking water leading to tumor pH_e neutralization, acidosis$^{IFN-γ}$ = mice with intact IFN-γ signaling receiving regular drinking water leading to tumor pH_e acidification, neutral = mice deficient in IFN-γ treated with sodium bicarbonate-enriched drinking water leading to tumor pH_e neutralization, acidosis = mice deficient in IFN-γ receiving regular drinking water leading to tumor pH_e acidification.

As experimentally proven in chapter 4.1.6 and shown by Cerezo *et al.* [30], IFN-γ induces PD-L1 expression via the eIF4F-STAT1 axis. Therefore, MC38 cells deficient in STAT1 ($MC38^{STAT1-/-}$) were generated by the CRISP/Cas9 gene editing technology. MC38 cells were transfected with a non-targeting gRNA (control) and either pooled ($MC38^{control}$ pool) or subjected to clonal expansion ($MC38^{control}$ # F1). For a constitutive STAT1 knockout, MC38 cells were transfected with three individual STAT1 targeting gRNAs and clonally expanded ($MC38^{STAT1-/-}$ # 3F7, $MC38^{STAT1-/-}$ # 2A7). The hashtag indicates that the STAT1 knockout cell line was generated by clonal selection. The number indicates the gRNA that resulted in STAT1 depletion. The individual clone number originates from the position in a 96-well plate where the clones were expanded. WB analysis was applied to confirm the STAT1 knockout in both clones ($MC38^{STAT1-/-}$ # 3F7, $MC38^{STAT1-/-}$ # 2A7). STAT1 levels were similar in $MC38^{control}$ pool and $MC38^{control}$ # F1 cells (**Figure 31 A**). Next the generated STAT1 knockout ($MC38^{STAT1-/-}$ # 3F7, $MC38^{STAT1-/-}$ # 2A7) as well as control MC38 cancer cells ($MC38^{control}$ pool, $MC38^{control}$ # F1) were studied focusing on their potential to engraft after *s.c.* inoculation *in vivo* and their ability to form solid tumors. Two out of five $MC38^{control}$ pool tumors were rejected in immune competent C57BL/6J mice. $MC38^{control}$ # F1 cancer cells did not engraft, and all tumors were rejected. This indicates, that through clonal expansion of $MC38^{control}$ cells a cancer cell clone might have been selected that is more immunogenic and unable to engraft in immune-competent C57BL/6J mice. In contrast, all $MC38^{STAT1-/-}$ # 3F7 tumors successfully engrafted and only two out of five $MC38^{STAT1-/-}$ # 2A7 tumors were rejected. Surprisingly, the tumor growth curves of $MC38^{STAT1-/-}$ # 3F7 and $MC38^{STAT1-/-}$ # 2A7 tumors were significantly different. $MC38^{STAT1-/-}$ # 3F7 tumors featured a significantly increased tumor volume compared to $MC38^{control}$ pool tumors, whereas the $MC38^{STAT1-/-}$ # 2A7 tumor volume was significantly reduced (**Figure 31 B**). These differences between pooled and clonal $MC38^{control}$ tumors as well as the two STAT1 knockout tumor clones most likely can be attributed to clonal effects.

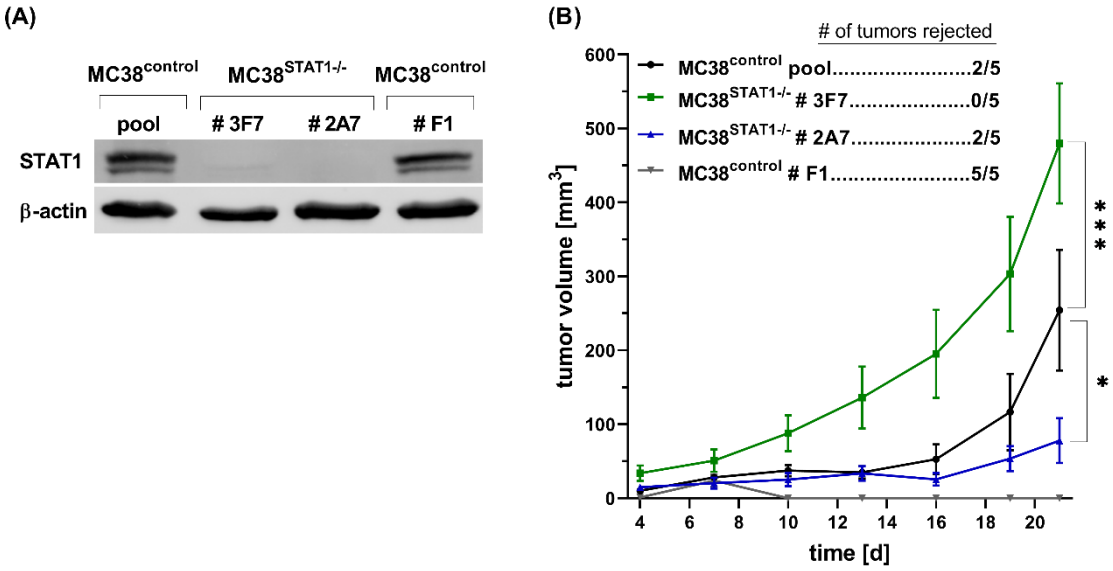

Figure 31: Role of STAT1 on MC38$^{STAT1-/-}$ tumor growth *in vivo*.

(A) CRISP/Cas9-mediated STAT1 knockout in MC38 cells were confirmed by WB analysis of STAT1 and β-actin. Control MC38^{wt} cells were transfected with a non-targeting gRNA and either pooled (MC38^{control} pool) or subjected to clonal expansion indicating the clone selected (MC38^{control} # F1). MC38$^{STAT1-/-}$ cells were generated by transfection of MC38^{wt} cells with 3 different STAT1 targeting gRNAs and subjected to clonal expansion, resulting in the two clones # 3F7 and #2A7. **(B)** Tumor volume of MC38^{control} pool, MC38$^{STAT1-/-}$ # 3F7, MC38$^{STAT-/-}$ # 2A7 and MC38^{control} # F1 tumor-bearing mice (n = 5 animals per group; 1 independent experiment). Data is presented as mean ± SEM. Statistics: Tukey's multiple comparison test.

Taken together, the tumor volume reduction upon sodium bicarbonate mediated tumor pH_e neutralization in T_h1 prone C57BL/6J mice depends on the inducible expression of the checkpoint inhibitor PD-L1 in MC38^{wt} tumors.

Next the findings on sodium bicarbonate treatment-mediated tumor volume reduction and increased PD-L1 expression were further validated *in vivo* applying CT26^{wt} cancer cells with a low basal, but IFN-γ-inducible PD-L1 expression (**Figure 32 A, B**). CT26^{wt} cells originate from BALB/c mice, which are T_h2 prone [226, 228]. CT26^{wt} cancer cells were injected *s.c.* in BALB/c mice which received either regular drinking water or sodium bicarbonate-enriched water *ad libitum* starting three days prior to cancer cell inoculation [77, 81]. In accordance with the MC38^{wt} *in vivo* experiments, CT26^{wt} tumor-bearing mice were treated with a blocking anti-PD-L1 mAb or an isotype control antibody. BALB/c mice yielded a significant reduction in CT26^{wt} tumor volume upon monotherapy with sodium bicarbonate (neutral$^{IFN-γ}$) or anti-PD-L1 mAb as well as a combination of both

(**Figure 32 A**). In other words, tumor acidosis$^{IFN\text{-}\gamma}$ in immune competent mice resulted in elevated tumor volumes compared to sodium bicarbonate treated mice with neutral$^{IFN\text{-}\gamma}$ tumor pH_e, suggesting a mechanism of tumor immune escape via acidosis and IFN-γ. Nevertheless, no additive effect of sodium bicarbonate and anti-PD-L1 mAb treatment (neutral$^{IFN\text{-}\gamma}$ + anti-PD-L1) was observed (**Figure 32 A**). In contrast, CT26$^{PD\text{-}L1\text{-}/\text{-}}$ tumors deficient in basal and IFN-γ-inducible PD-L1 expression, did not respond to sodium bicarbonate-mediated pH_e neutralization (**Figure 32 C, D**). These findings are in accordance with the results obtained for MC38$^{PD\text{-}L1\text{-}/\text{-}}$ tumors (**Figure 24 C**).

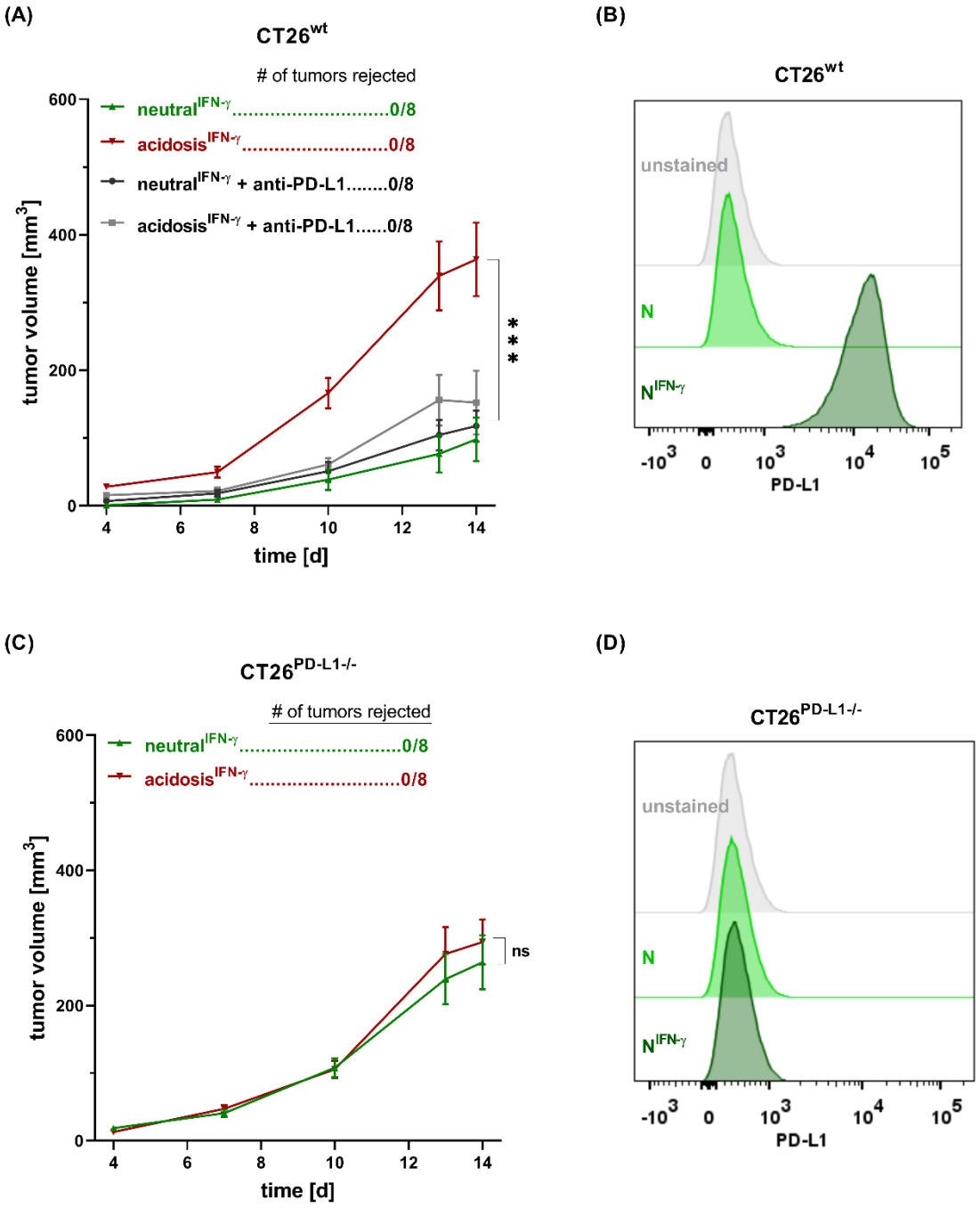

Figure 32: Effect of sodium bicarbonate and/or anti-PD-L1 mAb therapy on CT26^{wt} and CT26$^{PD\text{-}L1\text{-}/\text{-}}$ tumor growth *in vivo*.

(A) Tumor volume of CT26^{wt} (n = 7-8 animals per group; 1 independent experiment, statistics: Tukey's multiple comparison test) and **(C)** CT26$^{PD\text{-}L1\text{-}/\text{-}}$ (n = 8 animals per group; 1 independent experiment, statistics: Sidak's multiple comparison test) tumors in BALB/c mice treated with sodium bicarbonate water *ad libitum* starting three days prior to cancer cell injection and/or anti-PD-L1 mAb (200 µg per mouse) treatment every third day, starting from day 4 post cancer cell injection. Data is presented as mean ± SEM. Flow cytometry histograms of **(B)** CT26^{wt} and **(D)** CT26$^{PD\text{-}L1\text{-}/\text{-}}$ cells cultured in the absence (light green) or presence (dark green) of IFN-γ (100 ng ml^{-1}) for 48 h to confirm the CRISP/Cas9-mediated PD-L1 knockout. Abbreviations: neutral$^{IFN\text{-}\gamma}$ = mice with intact

IFN-γ signaling treated with sodium bicarbonate-enriched drinking water leading to tumor pH_e neutralization, acidosis$^{IFN-\gamma}$ = mice with intact IFN-γ signaling receiving regular drinking water leading to tumor pH_e acidification.

To study intra-tumor heterogeneity in terms of necrosis and immune cell recruitment upon sodium bicarbonate and anti-PD-L1 mAb treatment, H&E staining and IHC was performed. CT26^{wt} tumors derived from mice of the acidosis$^{IFN-\gamma}$ group showed mild, mostly central necrosis. In contrast, small CT26^{wt} tumors of neutral$^{IFN-\gamma}$ mice showed small multifocal necrosis, whereas medium sized CT26^{wt} tumors of this group revealed mild, mostly central necrosis. Surprisingly, quantification of necrosis revealed significantly less necrosis in tumors of experimental mice from the neutral$^{IFN-\gamma}$ compared to acidosis$^{IFN-\gamma}$ group (**Figure 33 A, B**). CT26^{wt} tumors derived from anti-PD-L1 mAb as well as anti-PD-L1 mAb and sodium bicarbonate treated mice exhibited mild to intense focal necrosis in dependence of the tumor volume. While no significant inflammation could be observed in tumors of the acidosis$^{IFN-\gamma}$ and neutral$^{IFN-\gamma}$ group, treatment with the anti-PD-L1 mAb resulted in low to mild acute inflammation. CT26^{wt} tumors characterized by a low basal PD-L1 expression exhibited minor PD-L1 IHC staining. PD-L1 expression patterns were heterogeneous and more pronounced on cells nearby necrotic regions. Tumors of the neutral$^{IFN-\gamma}$ group showed a slightly higher PD-L1 staining in CT26^{wt} tumors compared to the acidosis$^{IFN-\gamma}$ group (**Figure 33 A**). Further, CT26^{wt} tumors of mice treated with sodium bicarbonate or anti-PD-L1 yielded an increased $CD3^+$ T cell homing to the tumor periphery, which was more pronounced, when both treatments were combined (**Figure 33 A**).

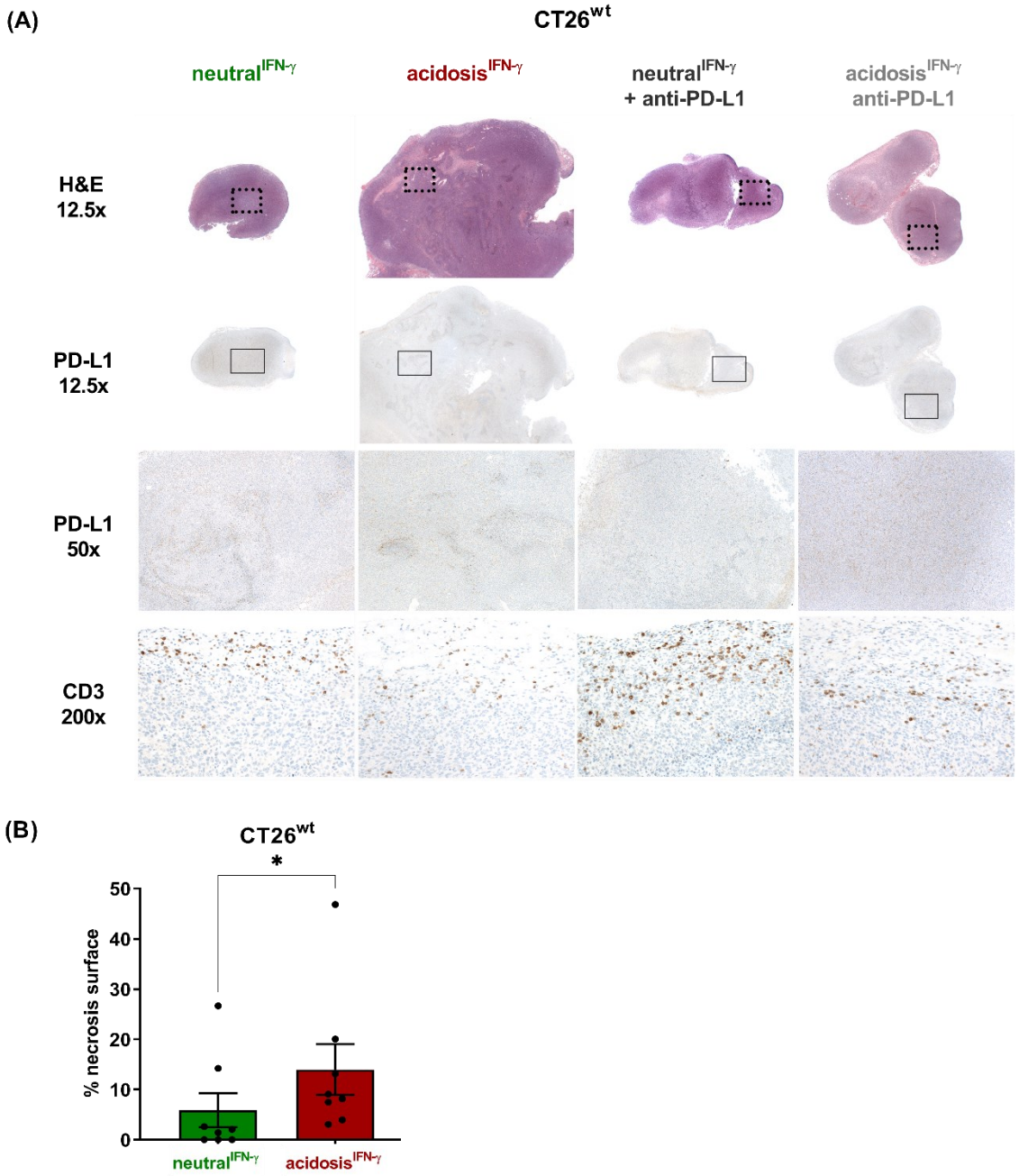

Figure 33: Histology and IHC of murine CT26^{wt} tumors.

(A) Representative H&E, PD-L1 and CD3 staining of *s.c.* CT26^{wt} tumors harvested at day 17 after onset of treatment with sodium bicarbonate (neutral$^{IFN-\gamma}$) enriched drinking water. Animals were treated with sodium bicarbonate-enriched water *ad libitum* starting three days prior to cancer cell inoculation and/or repetitive anti-PD-L1 mAb (200 µg per mouse; every third day) treatment, starting from day 4 post cancer cell inoculation. CT26^{wt} tumors (n = 8 animals per group) underwent H&E staining. Based on H&E staining, representative tumors were selected for PD-L1 and CD3 IHC. Dotted and solid rectangles indicate the identical tumor region in the 12.5x H&E and PD-L1 images. The 50x magnification of the PD-L1 stained tumor region is equivalent to the excerpt indicated by the solid rectangle in the 12.5x magnification. The images in 200x magnification of the CD3 staining were obtained from the tumor periphery and tumor areas are not indicated in the

12.5x H&E images. **(B)** The percentage of the necrotic area was quantified (quantification of pink surface area greater than 0.01 mm^2 in $CT26^{wt}$ tumors stained with H&E) in $CT26^{wt}$ tumors from mice treated with sodium bicarbonate ($neutral^{IFN-\gamma}$) or regular drinking water ($acidosis^{IFN-\gamma}$). Data is presented as mean ± SEM. Statistics: two-tailed Mann-Whitney test. Abbreviations: $neutral^{IFN-\gamma}$ = mice with intact IFN-γ signaling treated with sodium bicarbonate-enriched drinking water leading to tumor pH_e neutralization, $acidosis^{IFN-\gamma}$ = mice with intact IFN-γ signaling receiving regular drinking water leading to tumor pH_e acidification.

Interestingly, quantification of $CT26^{PD-L1-/-}$ tumor necrosis of the $neutral^{IFN-\gamma}$ group exhibited significantly more and larger necrotic areas compared to tumors of the $acidosis^{IFN-\gamma}$ group (**Figure 34 A, B**). Next, $CT26^{PD-L1-/-}$ tumors were stained for Iba1-positive, activated macrophages and PD-L1 expression. PD-L1 positive cells were mainly found in the outer margin of $CT26^{PD-L1-/-}$ tumors. Cells that stained positive for PD-L1 were identified by Iba1 IHC as activated macrophages (**Figure 34 A**), as described by others [412, 413]. Interestingly, macrophages are mainly located at the margin of $CT26^{PD-L1-/-}$ tumors and fewer macrophages were found in the center perfectly co-localizing with the PD-L1 IHC (**Figure 34 A**). Furthermore, in $CT26^{PD-L1-/-}$ tumors no differences in terms of $CD3^+$ T cell homing were observed between the two treatment groups. Like $CT26^{wt}$ tumors, $CD3^+$ T cells were mostly identified in the periphery of $CT26^{PD-L1-/-}$ tumors (**Figure 34 A**).

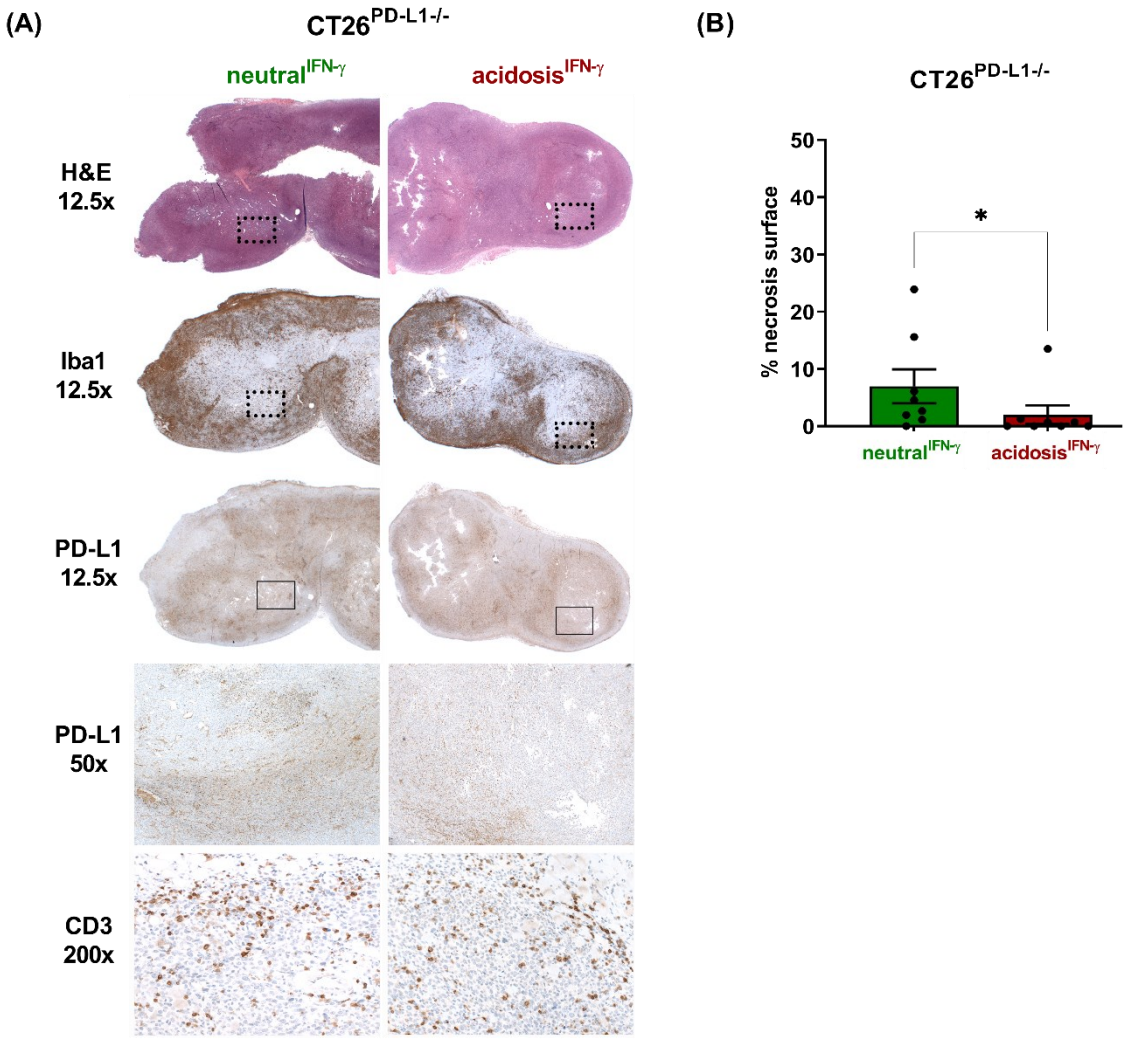

Figure 34: Histology and IHC of murine CT26$^{PD\text{-}L1\text{-}/\text{-}}$ tumors.

(A) Representative H&E, Iba1, PD-L1 and CD3 staining of *s.c.* CT26$^{PD\text{-}L1\text{-}/\text{-}}$ tumors harvested at day 17 after onset of treatment with sodium bicarbonate (neutral$^{IFN\text{-}\gamma}$) enriched drinking water. Animals were treated with sodium bicarbonate-enriched water *ad libitum* starting three days prior to cancer cell inoculation. CT26$^{PD\text{-}L1\text{-}/\text{-}}$ tumors (n = 8 animals per group) underwent H&E staining. Based on H&E staining, representative tumors were selected for Iba1, PD-L1 and CD3 IHC. Dotted and solid rectangles indicate the identical tumor region in the 12.5x H&E, Iba1 and PD-L1 images. The 50x magnification of the PD-L1 stained tumor region is equivalent to the excerpt indicated by the solid rectangle in the 12.5x magnification. The images in 200x magnification of the CD3 staining were obtained from the tumor periphery and tumor areas are not indicated in the 12.5x H&E images. **(B)** The percentage of the necrotic area was quantified (quantification of pink surface area greater than 0.01 mm^2 in CT26$^{PD\text{-}L1\text{-}/\text{-}}$ tumors stained with H&E) in CT26$^{PD\text{-}L1\text{-}/\text{-}}$ tumors from mice treated with sodium bicarbonate (neutral$^{IFN\text{-}\gamma}$) or regular drinking water (acidosis$^{IFN\text{-}\gamma}$). Data is presented as mean ± SEM. Statistics: two-tailed Mann-Whitney test. Abbreviations: neutral$^{IFN\text{-}\gamma}$ = mice with intact IFN-γ signaling treated with sodium bicarbonate-enriched drinking water leading to tumor pH_e neutralization, acidosis$^{IFN\text{-}\gamma}$ = mice with intact IFN-γ signaling receiving regular drinking water leading to tumor pH_e acidification.

Taken together, sodium bicarbonate-mediated tumor pH_e neutralization increases PD-L1 expression in tumors of immune competent mice. Based on the investigated cell lines, this effect seems to be independent of the basal PD-L1 expression level as well as independent of the mouse strain.

To expand these findings to tumor models classified as low-/non-responders to an anti-PD-1 and/or anti-PD-L1 mAb therapy, murine B16-F10^{wt} and 4T1^{wt} cancer cells were inoculated in C57BL/6J or BALB/c mice respectively. As expected, an anti-PD-L1 mAb treatment only slightly reduced the B16-F10^{wt} tumor volume (**Figure 35 A**). Furthermore, treatment with sodium bicarbonate did not result in a reduction in tumor volume, whereas a combined treatment approach with sodium bicarbonate and anti-PD-L1 mAb resulted in slightly increased B16-F10^{wt} tumor volumes (**Figure 35 A**). Similar results were obtained for 4T1^{wt} tumors, where neither sodium bicarbonate, nor an anti-PD-L1 mAb monotherapy, nor the combination was associated with a tumor volume reduction (**Figure 35 B**). In other words, tumor acidosis in immune competent mice with intact IFN-γ signaling (acidosis$^{IFN\text{-}\gamma}$) did not result in a tumor immune escape reflected by increased B16-F10^{wt} or 4T1^{wt} tumor volumes when compared to neutral$^{IFN\text{-}\gamma}$. In this context it is important to mention, that 4T1^{wt} tumor-bearing BALB/c mice died from a fatal hypersensitivity reaction between the fourth and fifth administration of the therapeutic anti-PD-L1 mAb. This life threatening hypersensitivity reaction has been described by Mall *et al.* for repeated anti-PD-L1 mAb and anti-PD-1 mAb administration in 4T1^{wt} tumor-bearing BALB/c mice [414]. Upon mAb treatment Mall *et al.* found a systemic accumulation of IgG1 antibodies against the therapeutic anti-PD-L1 mAb, finally leading, together with an accumulation of GR-1^{high} neutrophils in the lungs, to death [414].

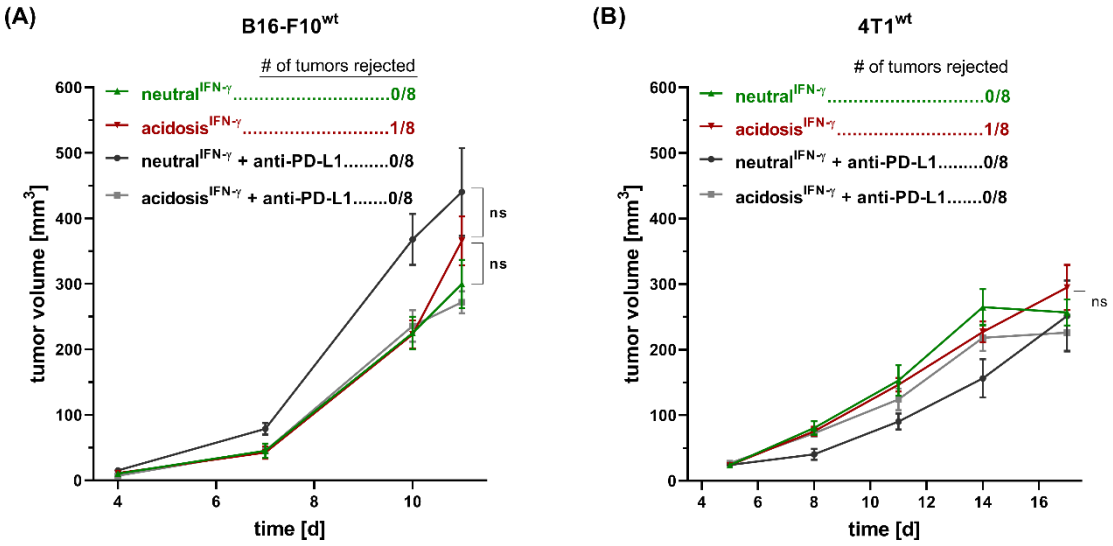

Figure 35: Effect of sodium bicarbonate and/or anti-PD-L1 mAb therapy on B16-F10^{wt} and 4T1^{wt} tumor growth *in vivo*.

(A) Tumor volume of B16-F10^{wt} (n = 5-8 animals per group; 1 independent experiment) and **(B)** 4T1^{wt} (n = 5-8 animals per group; 1 independent experiment) tumors in C57BL/6J and BALB/c mice treated with sodium bicarbonate-enriched water *ad libitum* starting three days prior to cancer cell injection and/or anti-PD-L1 mAb (200 µg per mouse) treatment every third day, starting from day 4 (B16-F10^{wt}) or 5 (4T1^{wt}) post cancer cell injection. Data is presented as mean ± SEM. Statistics: Tukey's multiple comparison test. Abbreviations: neutral$^{IFN-\gamma}$ = mice with intact IFN-γ signaling treated with sodium bicarbonate-enriched drinking water leading to tumor pH_e neutralization, acidosis$^{IFN-\gamma}$ = mice with intact IFN-γ signaling receiving regular drinking water leading to tumor pH_e acidification.

Histology of B16-F10^{wt} melanomas revealed a moderate, central necrosis and marginal signs of inflammation in the periphery across all four treatment groups. A pronounced PD-L1 staining was observed on cancer cells around necrotic areas. In melanomas derived from the neutral$^{IFN-\gamma}$ group, PD-L1 staining was more homogeneous compared to the acidosis$^{IFN-\gamma}$ group (**Figure 36**). In B16-F10^{wt} melanomas of the acidosis$^{IFN-\gamma}$ group, CD3$^+$ T cells were mainly located in the periphery and only few T cells were found within the tumor. Surprisingly, tumors of the neutral$^{IFN-\gamma}$ group revealed even less CD3$^+$ T cells compared to the acidosis$^{IFN-\gamma}$ group. B16-F10^{wt} melanomas from anti-PD-L1 mAb treated mice yielded a slightly higher T cell homing, whereas tumors from the combined treatment group (neutral$^{IFN-\gamma}$ + anti-PD-L1) exhibited similar numbers of CD3$^+$ T cells as in the acidosis$^{IFN-\gamma}$ group (**Figure 36**).

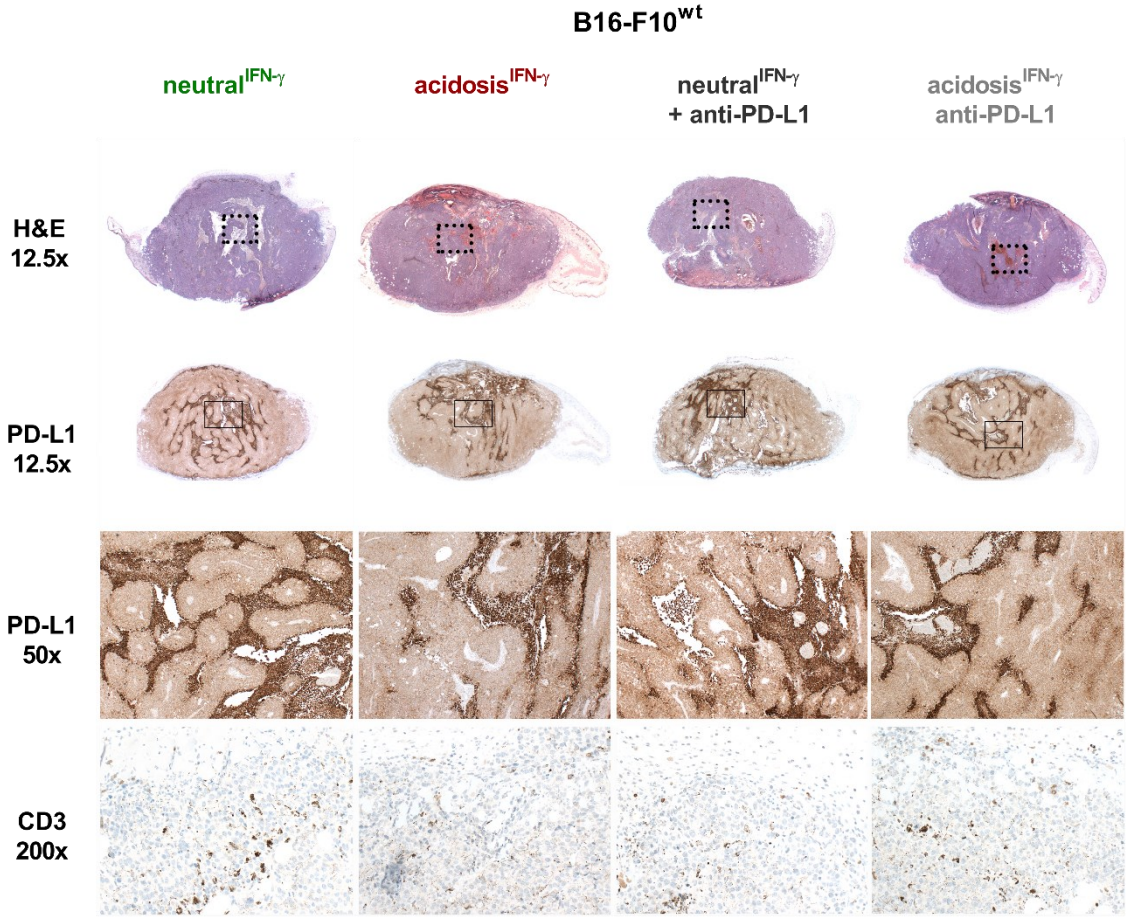

Figure 36: Histology and IHC of murine B16-F10^{wt} tumors.
Representative H&E, PD-L1 and CD3 staining of *i.c.* B16-F10^{wt} tumors harvested at day 14 after onset of treatment with sodium bicarbonate (neutral$^{IFN-\gamma}$) enriched drinking water. Animals were treated with sodium bicarbonate-enriched water *ad libitum* starting three days prior to cancer cell inoculation and/or repetitive anti-PD-L1 mAb (200 µg per mouse; every third day) treatment, starting from day 4 post cancer cell inoculation. B16-F10^{wt} tumors (n = 8 animals per group) underwent H&E staining. Based on H&E staining, representative tumors were selected for PD-L1 and CD3 IHC. Dotted and solid rectangles indicate the identical tumor region in the 12.5x H&E and PD-L1 images. The 50x magnification of the PD-L1 stained tumor region is equivalent to the excerpt indicated by the solid rectangle in the 12.5x magnification. The images in 200x magnification of the CD3 staining were obtained from the tumor periphery and tumor areas are not indicated in the 12.5x H&E images. Abbreviations: neutral$^{IFN-\gamma}$ = mice with intact IFN-γ signaling treated with sodium bicarbonate-enriched drinking water leading to tumor pH_e neutralization, acidosis$^{IFN-\gamma}$ = mice with intact IFN-γ signaling receiving regular drinking water leading to tumor pH_e acidification.

The 4T1^{wt} tumor-bearing mice of the acidosis$^{IFN-\gamma}$ and neutral$^{IFN-\gamma}$ group showed some degree of tumor necrosis. Further, a heterogeneous PD-L1 expression was found in 4T1^{wt} tumors of all experimental groups. Cells with pronounced PD-L1

expression were found in clusters around necrotic tumor regions, as well as in areas without necrosis. 4T1^{wt} tumors of the neutral$^{IFN-\gamma}$ group yielded abundant CD3^{+} T cells in the periphery as well as across the entire tumor, which was more prominent than in the acidosis$^{IFN-\gamma}$ group (**Figure 37**).

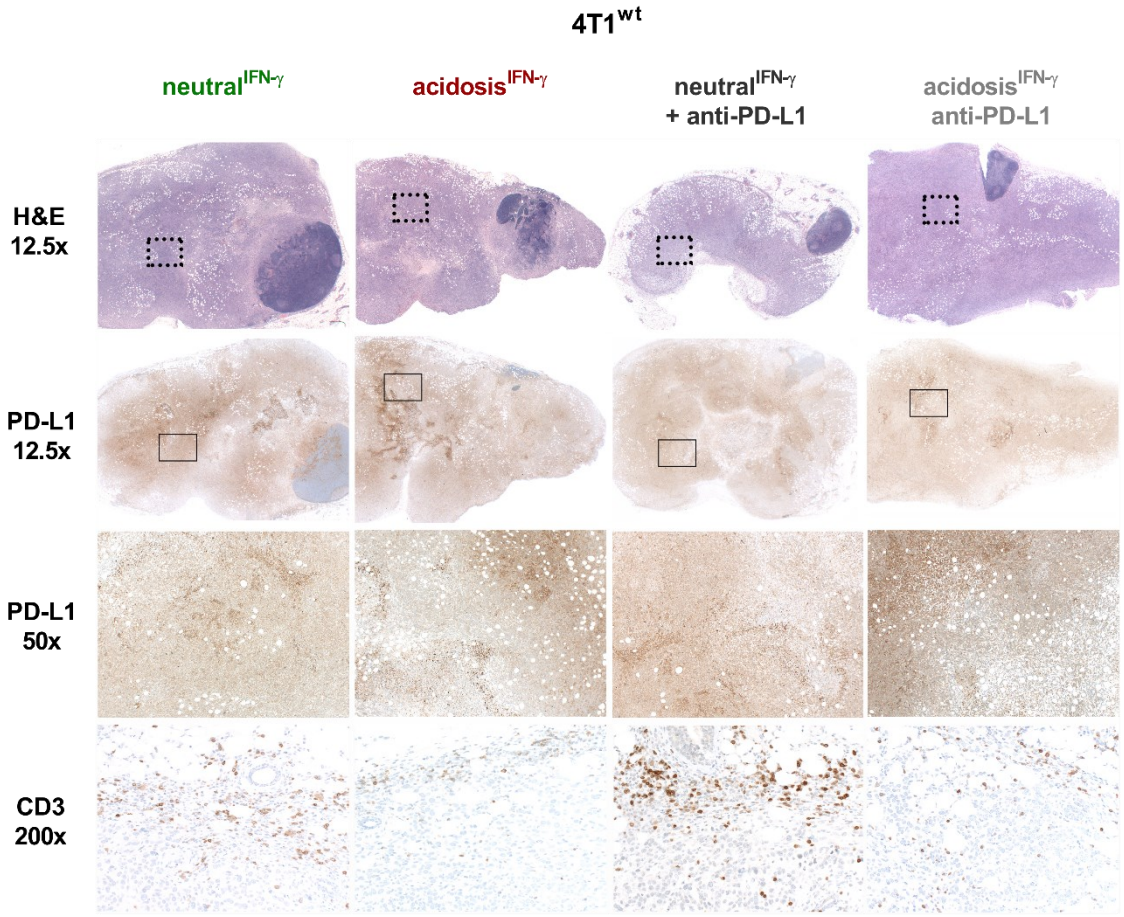

Figure 37: Histology and IHC of murine 4T1^{wt} tumors.
Representative H&E, PD-L1 and CD3 staining of orthotropic 4T1^{wt} tumors harvested at day 20 after onset of treatment with sodium bicarbonate (neutral$^{IFN-\gamma}$) enriched drinking water. Animals were treated with sodium bicarbonate-enriched water *ad libitum* starting three days prior to cancer cell inoculation and/or repetitive anti-PD-L1 mAb (200 µg per mouse; every third day) treatment, starting from day 5 post cancer cell inoculation. 4T1^{wt} tumors (n = 5-8 animals per group) underwent H&E staining. Based on H&E staining, representative tumors were selected for PD-L1 and CD3 IHC. Dotted and solid rectangles indicate the identical tumor region in the 12.5x H&E, Iba1 and PD-L1 images. The 50x magnification of the PD-L1 stained tumor region is equivalent to the excerpt indicated by the solid rectangle in the 12.5x magnification. The images in 200x magnification of the CD3 staining were obtained from the tumor periphery and tumor areas are not indicated in the 12.5x H&E images. Abbreviations: neutral$^{IFN-\gamma}$ = mice with intact IFN-γ signaling treated with sodium bicarbonate-enriched drinking water leading to tumor pH_e neutralization, acidosis$^{IFN-\gamma}$ = mice with intact IFN-γ signaling receiving regular drinking water leading to tumor pH_e

acidification.

Taken together, induction of membrane-bound cancer cell PD-L1 expression upon acidosis$^{IFN-\gamma}$ seems to represent a not yet described mechanism of tumor immune escape. Furthermore, sodium bicarbonate-mediated tumor pH_e neutralization did not result in a significant tumor volume reduction in the selected low-/non-responder tumor models when immune competent mice with intact IFN-γ signaling were applied. Furthermore, sodium bicarbonate treatment was not applicable to elevate PD-L1 expression in the selected low-/non-responder tumor models when compared to the anti-PD-L1 mAb therapy responder models MC38^{wt} and CT26^{wt}. In summary, these findings suggest that sodium bicarbonate treatment enforces the recruitment of T cells and elevates immune cell PD-L1 expression patterns. Tumor acidosis together with IFN-γ results in elevated cancer cell PD-L1 expression and increased tumor volumes, representing a mechanism of immune escape, targetable by an anti-PD-L1 mAb therapy.

4.1.10 Imaging tumor acidosis non-invasively *in vivo* using acidoCEST-MRI

AcidoCEST-MRI represents a promising technology to evaluate the tumor pH_e non-invasively *in vivo*.

Therefore, the tumor pH_e of *s.c.* MC38^{wt} tumors at the right shoulder of C57BL/6J mice was neutralized by treatment with sodium bicarbonate-enriched (200 mM) water administered *ad libitum* three days prior cancer cell inoculation. The tumor pH_e was measured by non-invasive *in vivo* acidoCEST-MRI [76, 77, 81, 375]. AcidoCEST-MRI measurements with iopamidol were conducted at day 10 post cancer cell inoculation. Mice that received regular drinking water revealed tumor pH_e values ranging from 6.48 to 6.85 (**Figure 38 A**). Of note, the linear calibration range was between 6.2 and 7.4. Therefore, the MC38^{wt} tumor of mouse 4 of the acidosis$^{IFN-\gamma}$ group (pH_e 5.15) and of mouse 4 of the neutral$^{IFN-\gamma}$ group (pH_e 7.53) had to be excluded. Most importantly, sodium bicarbonate treated mice of the neutral$^{IFN-\gamma}$ group exhibited a significantly higher tumor pH_e ranging from 7.04 to 7.27. In summary sodium bicarbonate treatment significantly increased the pH_e of MC38^{wt} tumors at day 10 post cancer cell inoculation (**Figure 38 A, B**).

H&E staining of MC38^{wt} tumors of the neutral$^{IFN-\gamma}$ group revealed minimal to moderate focal necrosis, whereas tumors of the acidosis$^{IFN-\gamma}$ group exhibited a lack

of massive central necrosis at day 10 post cancer cell inoculation. In the untreated acidosis$^{IFN-\gamma}$ group, the macrophage population within MC38^{wt} tumors was homogeneous and was surrounding the necrotic areas, whereas less macrophages were identified in tumors of the neutral$^{IFN-\gamma}$ group (**Figure 38 C**). In addition, a more intense PD-L1 staining of the MC38^{wt} tumors derived from the neutral$^{IFN-\gamma}$ group was observed (**Figure 38 C**) and is in line with the findings shown in **Figure 25** for MC38^{wt} tumors which were isolated at day 15 post cancer cell inoculation. In tumors of the experimental acidosis$^{IFN-\gamma}$ group, the PD-L1 staining was associated with necrotic tumor regions. The association between PD-L1 and tumor necrosis observed at day 15 in MC38^{wt} tumors of the sodium bicarbonate-treated neutral$^{IFN-\gamma}$ group (**Figure 25 A**) was not determined at day 10. Furthermore, CD3 IHC yielded a similar number of T cells within tumors of both experimental groups (**Figure 38 C**).

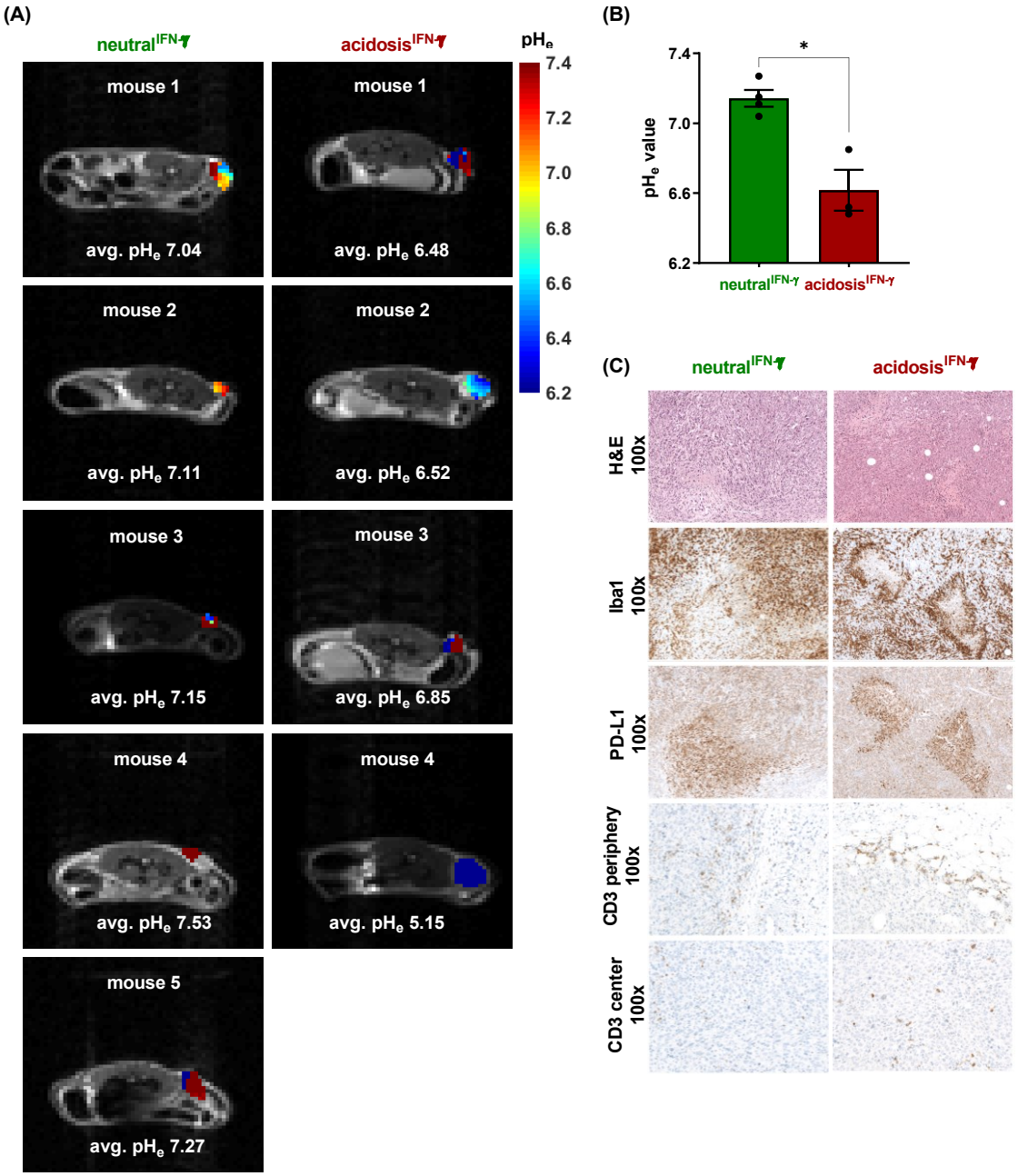

Figure 38: Imaging of tumor pH_e neutralization via sodium bicarbonate treatment using non-invasive *in vivo* acidoCEST-MRI.

(A) pH_e-maps overlaid over T_2-weighted axial MRI images of MC38^{wt} tumor (*s.c.*, right shoulder) bearing mice injected with iopamidol (*i.v.*) at day 13 post treatment start with sodium bicarbonate water. Mice received either sodium bicarbonate (neutral$^{IFN-\gamma}$) water or regular drinking (acidosis$^{IFN-\gamma}$) water three days prior cancer cell injection. **(B)** Average pH_e across the whole tumor. Sodium bicarbonate treatment significantly increased tumor pH_e measured by acidoCEST-MRI at day 13 (n = 3-4 animals per group; 1 independent experiment; mouse 4 of the neutral$^{IFN-\gamma}$ and mouse 4 of the acidosis$^{IFN-\gamma}$ group were excluded from quantitative analysis as measured pH_e-value were out of calibration range). Data is presented as mean ± SEM. Statistics: one-tailed nonparametric Mann Whitney test. **(C)** Representative images of *s.c.* MC38^{wt} tumors isolated at day 13 post treatment

start with sodium bicarbonate water and stained for H&E, Iba1, PD-L1 and CD3 (acidosis$^{IFN-\gamma}$: n = 4, neutral$^{IFN-\gamma}$: n = 5). Abbreviations: neutral$^{IFN-\gamma}$ = mice with intact IFN-γ signaling treated with sodium bicarbonate-enriched drinking water leading to tumor pH_e neutralization, acidosis$^{IFN-\gamma}$ = mice with intact IFN-γ signaling receiving regular drinking water leading to tumor pH_e acidification.

Taken together, sodium bicarbonate-mediated pH_e neutralization was confirmed in MC38^{wt} tumors at day 10 post cancer cell inoculation by acidoCEST-MRI. Tumors of experimental mice of the neutral$^{IFN-\gamma}$ group yielded enhanced PD-L1 expression patterns at day 10, confirming our results within MC38^{wt} tumors isolated at day 15. Nevertheless, contradictory results were obtained for CD3 and macrophage IHC at day 10 and day 15, highlighting the dynamics of immune cell homing to the tumor site.

4.2 Non-invasive *in vivo* BLI of tumor hypoxia using 5xHRE-ODD-luc reporter cell lines

As shown in the previous chapter, immune cell-derived IFN-γ and acidosis together induce PD-L1 expression on cancer cells. Furthermore, other authors reported an elevation of PD-L1 expression upon hypoxia [161, 415]. Therefore, hypoxia was imaged and correlated with PD-L1 expression.

4.2.1 *In vitro* validation of hypoxia reporter 5xHRE-ODD-luc cell lines

Tumor hypoxia is one of the main features of the TME and is an interesting condition to study and image non-invasively. Beside the widely studied PET tracers ^{18}F-FMISO [416, 417] and ^{18}F-FAZA [418-421], hypoxia reporter genes attracted attention in recent years. To image hypoxia non-invasively by BLI, cells are transduced with a 5xHRE-ODD-luc construct. Upon hypoxia, *Luciferase* gene expression is induced and luciferase activity can be measured by BLI [267, 275].

To generate murine hypoxia reporter cell lines, MC38, CT26, B16-F10 and 4T1 cells were transduced with the 5xHRE-ODD-luc construct and selected by increasing puromycin concentrations. Reporter gene expression was detected and validated by culturing cancer cells either under normoxic (20% O_2) or under hypoxic (1% O_2) conditions. Hypoxic conditions were generated by an incubator chamber with a gas mixture containing 1% O_2, 5% CO_2 and 94% N_2. Induction of *Luciferase* gene expression upon hypoxia was determined after 24 h by qRT-PCR analysis. Hypoxia resulted in increased *Luciferase* mRNA levels in MC38-HRE-

ODD-luc (~ 3-fold), CT26-HRE-ODD-luc (~ 5-fold), B16-F10-HRE-ODD-luc (~ 8-fold) and 4T1-HRE-ODD-luc (~ 4-fold) cells (**Figure 39 A**). Next, the hypoxia reporter cancer cell lines were evaluated for the expression of functional luciferase under hypoxia. Therefore, cancer cells were cultured under normoxic and hypoxic conditions for 48 h. Then cells were harvested, and the luciferase enzyme activity was measured. Hypoxia resulted in increased relative luciferase activity in MC38-HRE-ODD-luc (~ 4-fold), CT26-HRE-ODD-luc (~ 10-fold), B16-F10-HRE-ODD-luc (~ 3-fold) and 4T1-HRE-ODD-luc (~ 16-fold) cells (**Figure 39 B**). Interestingly the measured luciferase mRNA expression and activity matched for all cell lines apart from B16-F10-ODD-luc melanoma cells. Under hypoxia the B16-F10-ODD-luc melanoma cells revealed the highest *Luciferase* induction on the mRNA level amongst all investigated cancer cell lines but yielded the lowest luciferase activity (**Figure 39 A, B**). The reduced luciferase activity compared to the *Luciferase* mRNA expression level in B16-F10-HRE-ODD-luc melanoma cells under hypoxic conditions might be due to the photon absorbing effect of the melanin [422, 423]. Next, detection of hypoxia was evaluated using the IVIS® Spectrum OI system. Therefore, induction of hypoxia was mimicked chemically by $CoCl_2$ treatment. $CoCl_2$ blocks prolyl hydroxylation by exchanging Fe with Co and thereby stabilizes HIF1-α via inhibition of its degradation [424-427]. Treatment of the four hypoxia reporter cancer cells lines resulted in increased luciferase activity measured by BLI in the IVIS® Spectrum OI system, confirming the hypoxia related induction of functional luciferase expression (**Figure 39 C**).

In summary, induction of luciferase gene and functional enzyme expression upon hypoxia could be confirmed *in vitro* in the four generated hypoxia reporter cancer cells lines MC38-HRE-ODD-luc, CT26-HRE-ODD-luc, B16-F10-HRE-ODD-luc and 4T1-HRE-ODD-luc. Nevertheless, the magnitude of luciferase gene expression induction and enzyme activity varies between the four investigated cancer cell lines.

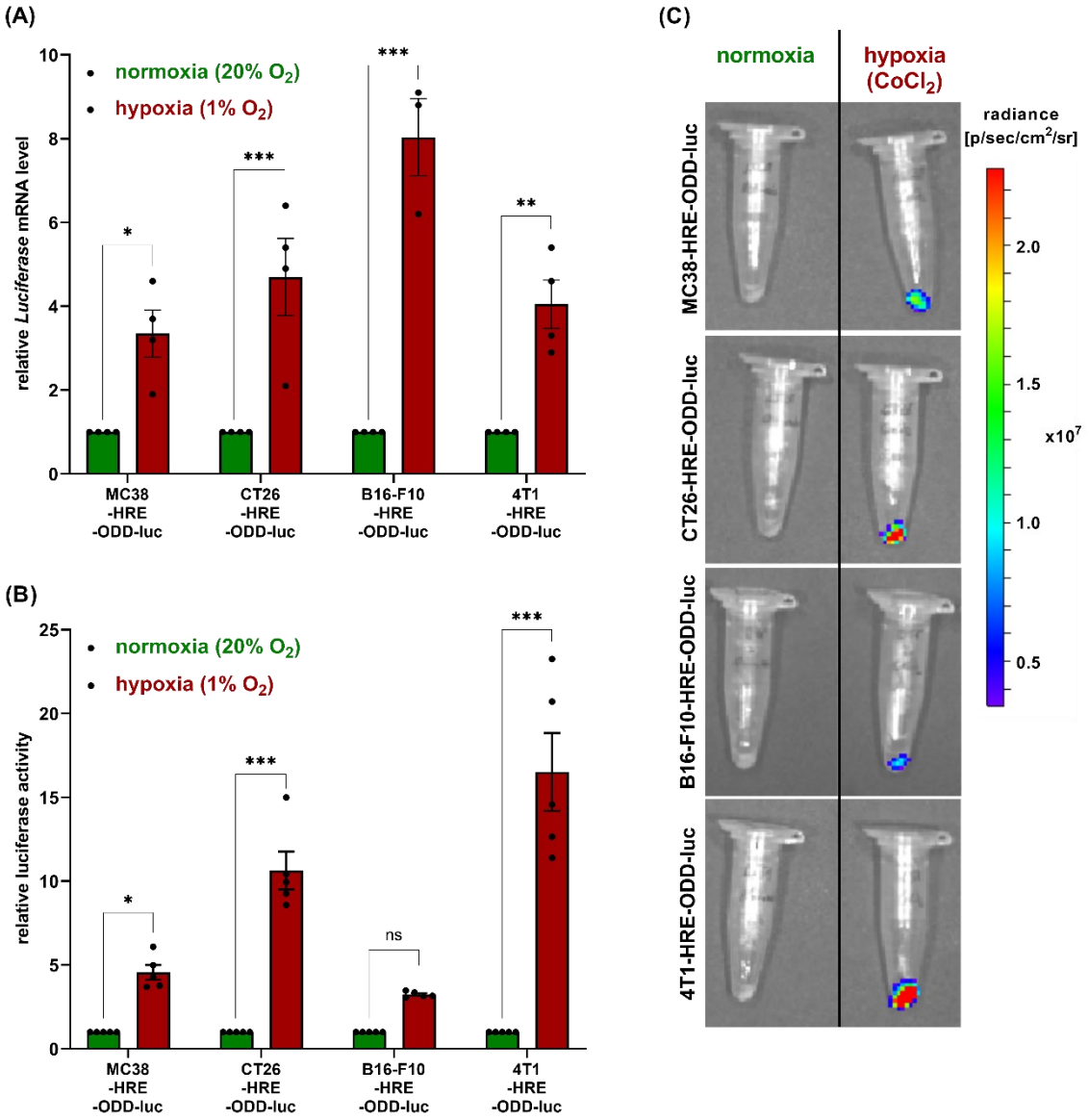

Figure 39: *In vitro* validation of four cell lines transfected with the HRE-ODD-luc construct. **(A)** Relative *Luciferase* mRNA expression normalized to the housekeeping gene *18S* of MC38-HRE-ODD-luc, CT26-HRE-ODD-luc, B16-F10-HRE-ODD-luc and 4T1-HRE-ODD-luc cells selected by puromycin and cultured under normoxic (20% O_2) or hypoxic (1% O_2) conditions for 24 h (4 independent experiments, n = 4). **(B)** Luciferase activity of the respective cancer cell lines was measured after 48 h of normoxic (20% O_2) or hypoxic (1% O_2) culture conditions using a Victor 3V plate reader (3-4 independent experiments, n = 5). Data is presented as mean ± SEM. Statistics: Sidak's multiple comparison test. **(C)** *In vitro* BLI of the indicated cell lines treated with $CoCl_2$ (200 µM) for 48 h. The cell number for the respective cell lines and conditions was adjusted to $1.5*10^6$ cells each.

4.2.2 Interplay between tumor hypoxia, PD-L1 expression and T cell homing

Next, CT26-HRE-ODD-luc reporter cancer cells were evaluated *in vivo* for functional luciferase enzyme activity upon tumor hypoxia with the IVIS® Spectrum

OI system. Tumor hypoxia naturally evolves due to either increased oxygen consumption or inadequate oxygen supply *in vivo* [428].

In week three post CT26-HRE-ODD-luc cancer cell inoculation tumor-bearing mice revealed variable BLI signal intensities within the tumor. Mouse 2 exhibited a relatively high and mouse 6 a relatively low BLI signal intensity suggesting that the CT26-HRE-ODD-luc tumor from mouse 2 is more hypoxic than from mouse 6 (**Figure 40 A**). The BLI signal intensity and therefore tumor hypoxia developed to a similar extend as the CT26-HRE-ODD-luc tumor volume over time (**Figure 40 B, C**). Several studies have shown that hypoxia directly regulates PD-L1 expression on cancer cells via HIF-1α binding to the HRE in the PD-L1 promoter region [161, 162]. Therefore, *Pd-l1* mRNA and PD-L1 total protein levels within the CT26-HRE-ODD-luc tumor mass were evaluated by qRT-PCR and WB analysis. Overall, ∆*Pd-l1* mRNA expression levels ranging from 19.0 to 20.7 were similar across all 8 evaluated CT26-HRE-ODD-luc tumors. The CT26-HRE-ODD-luc tumor of mouse 2 that exhibited a higher BLI signal intensity at day 20 post cancer cell inoculation also exhibited a lower ∆*Pd-l1* mRNA expression level compared to the CT26-HRE-ODD-luc tumor of mouse 1 (**Figure 40 D**). The elevated BLI signal intensity in the tumor of mouse 2 correlated with increased total PD-L1 expression compared to the tumor of mouse 1 and mouse 3 in this experiment (**Figure 40 E**). Nevertheless, this effect was not as prominent anymore when the number of experimental animals was increased (mouse 4-8; **Figure 40 A-E**). As the average radiance across the whole tumor was evaluated, spatial heterogeneity in terms of hypoxic clusters cannot be evaluated. To overcome this drawback, sampling tumor tissue from highly hypoxic and less hypoxic tumor regions and then subjecting them to PD-L1 expression analysis might leverage more significant correlations between hypoxia and PD-L1 expression. Next, the presence of $CD3^+$ T cells within CT26-HRE-ODD-luc tumors was evaluated by IHC and correlated with BLI signal intensities obtained by *in vivo* OI of CT26-HRE-ODD-luc tumor-bearing mice (**Figure 40 F, G**). Tumors exhibited heterogeneous amounts of $CD3^+$ T cells equally distributed throughout the tumor section. Furthermore, no significant correlation between the BLI signal intensity and the $CD3^+$ T cell infiltrate could be determined (**Figure 40 G**).

In summary, CT26-HRE-ODD-luc hypoxia reporter cancer cells exhibited increased BLI signal intensities correlating with increasing tumor volumes *in vivo*.

In contrast to the initial hypothesis, neither a correlation between the BLI signal and therefore tumor hypoxia with PD-L1 expression nor with $CD3^+$ T cell infiltration could be determined *in vivo*.

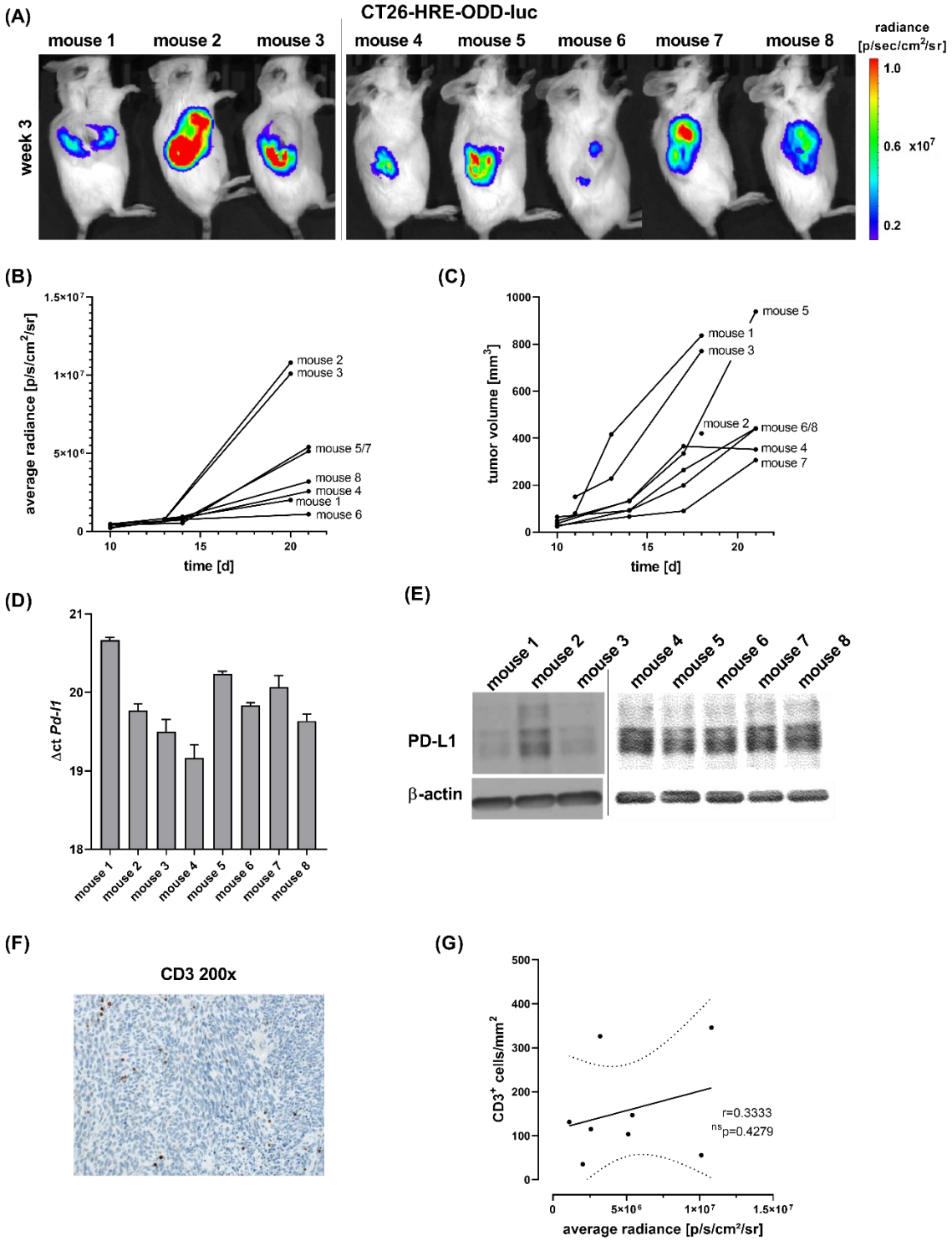

Figure 40: *In vivo* hypoxia imaging using CT26-HRE-ODD-luc cancer cells.

(A) BLI of CT26-HRE-ODD-luc tumor-bearing mice 20 days (mouse 1-3) or 21 days (mouse 4-8) post *s.c.* cancer cell inoculation into the right shoulder of experimental mice (medium binning, FOV: 13.2, exposure: 10 s). **(B)** BLI signal intensity was acquired and quantified (10% threshold) and **(C)**

the tumor volume was determined by a caliper over the time course of 21 days (n = 8 animals; 2 independent experiment). **(D)** *Pd-l1* expression was determined in CT26-HRE-ODD-luc tumors, normalized to *18S,* and presented as ∆*Pd-l1* (n = 8 animals; triplicates; 2 independent experiment). Data is presented as mean ± SEM. **(E**) WB analysis of PD-L1 and β-actin in CT26-HRE-ODD-luc tumors (3 s exposure for mouse 1-3 and 2 s exposure time for mouse 4-8). **(F)** Representative CD3 IHC of one *s.c.* CT26-HRE-ODD-luc tumor isolated at day 21 post cancer cell inoculation. **(G)** $CD3^+$ T cells were counted and correlated with the BLI signal intensity. Between 2,604 and 24,241 $CD3^+$ T cells were counted per tumor and normalized to the tumor area [mm^2]. A nonparametric Spearman's rank correlation between the number of $CD3^+$ T cells mm^2 and the average radiance [$p/s/cm^2/sr$] was computed with $^{ns}p = 0.4279$.

4.3 Identification of TDLNs of a *s.c.* colon adenocarcinoma

In the previous chapters, the interplay between the immune system and cancer cells in terms of PD-L1 expression was studied. As TDLNs and the lymphatic vascular network play an essential role in the anti-tumor T cell immune response [429], checkpoint-inhibitor therapies [208] and metastasis [366, 430, 431], non-invasive *in vivo* imaging was evaluated for the identification of TDLNs [432]. In this regard, the three imaging modalities OI, PET and MRI were applied to identify the TDLNs of a $MC38^{wt}$ colon adenocarcinoma on the right shoulder of C57BL/6J mice. Beside different imaging modalities, two contrast agents were evaluated for OI. The characteristics of the applied imaging agents and their application in previous studies are described in the respective **Material and Method** section. Most importantly the investigated imaging agents differ in their molecular weight, with [^{18}F]FDG representing the molecule with the lowest and IRDye® 800CW poly(ethylene glycol) (PEG) with the highest molecular weight. Furthermore, the OI agents non-specifically accumulate within the TDLN, whereas [^{18}F]FDG is taken up by activated immune cells within the TDLN exhibiting a higher glucose metabolism. Therefore, [^{18}F]FDG represents are more functional imaging agent.

4.3.1 Non-invasive *in vivo* imaging of TDLN with OI

Patent Blue V is a clinically approved dye. Upon subdermal injection Patent Blue V is trapped in the lymph and stains sentinel LNs for resection in e.g., breast cancer patients [433-435].

For *in vivo* measurements in this experimental setting, three LNs, the proper axillary, accessory axillary and subiliac LN were of main interest, due to their proximity to the *s.c.* $MC38^{wt}$ tumor at the right shoulder of the mouse

(**Figure 41 A,B**). The Patent Blue V uptake was higher in the LN of the tumor-bearing site, thereafter, named TDLN, compared to the uptake in the LN of the contralateral site, thereafter, named NTDLN. Enrichment of the synthetic dye Patent Blue V in the accessory axillary, proper axillary and slightly in the subiliac TDLN was visible by eye and was more pronounced than in the LNs of the contralateral site (**Figure 41 C**). Interestingly, accumulation of Patent Blue V in the subiliac TDLN varied depending on the actual position of the MC38^{wt} tumor representing the injection site of the dye. The subiliac TDLN staining was more pronounced when the tumor was located slightly lower (inferior; **Figure 41 C**).

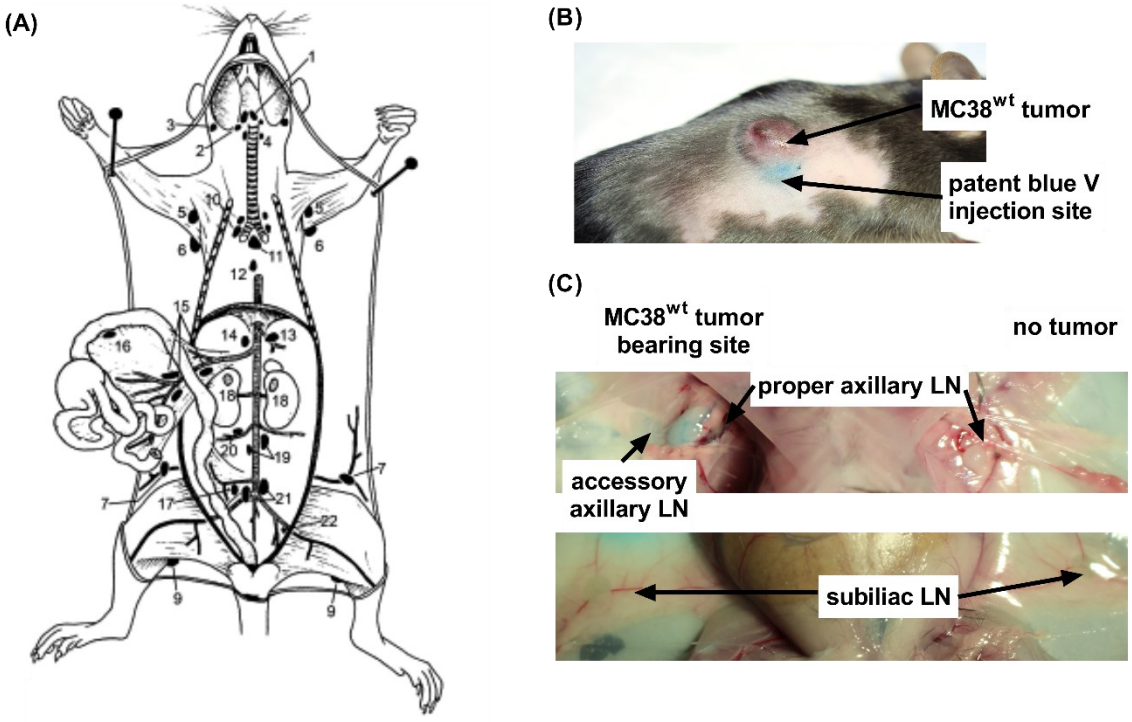

1 mandibular LN	9 popliteal LN	17 caudal mesenteric LN
2 accessory mandibular LN	10 cranial mediastinal LN	18 renal LN
3 superficial parotid LN	11 tracheobronchal LN	19 lumbar aortic LN
4 cranial deep cervical LN	12 caudal mediastinal LN	20 lateral iliac LN
5 proper axillary LN	13 gastric LN	21 medial iliac LN
6 accessory axillary LN	14 pancreaticoduodenal LN	22 external iliac LN
7 subiliac LN	15 jejunal LN	
8 sciatic LN	16 colic LN	

Figure 41: Localization of LNs in mice.

(A) Schematic representation of the localization and nomenclature of murine LNs adapted from [436]. **(B)** Indication of the MC38^{wt} tumor location at the right shoulder and the Patent Blue V injection site next to the tumor. **(C)** Indication of the tumor-draining and non-tumor-draining lymph nodes (TDLN and NTDLN respectively) of a MC38^{wt} colon adenocarcinoma at the right shoulder, namely proper axillary LN, accessory axillary LN and subiliac LN.

To proof the suitability of Patent Blue V for non-invasive fluorescence *in vivo* OI, phantoms were applied to determine the optimal excitation and emission filter settings. Tellier *et al.* have shown, that only the human serum albumin (HSA) bound Patent Blue V emits light upon excitation, whereas free Patent Blue V doesn't [354]. Therefore, 15 ml phantoms with PBS and a concentration of 4 µmol l^{-1} Patent Blue V (sodium salt) without or with (33 g l^{-1}) BSA were generated and subsequently imaged with different excitation and emission filter settings. For each excitation and emission filter pair, the exposure time was documented (**Figure 42 A**). Furthermore, phantom images were assessed for auto-fluorescence for each individual filter setting (**Figure 42 B**). An excitation filter of 675 nm and an emission filter of 720 nm were chosen for *in vivo* measurements due to the low exposure time of 3 s, low auto-fluorescence, and the relatively high excitation wavelength.

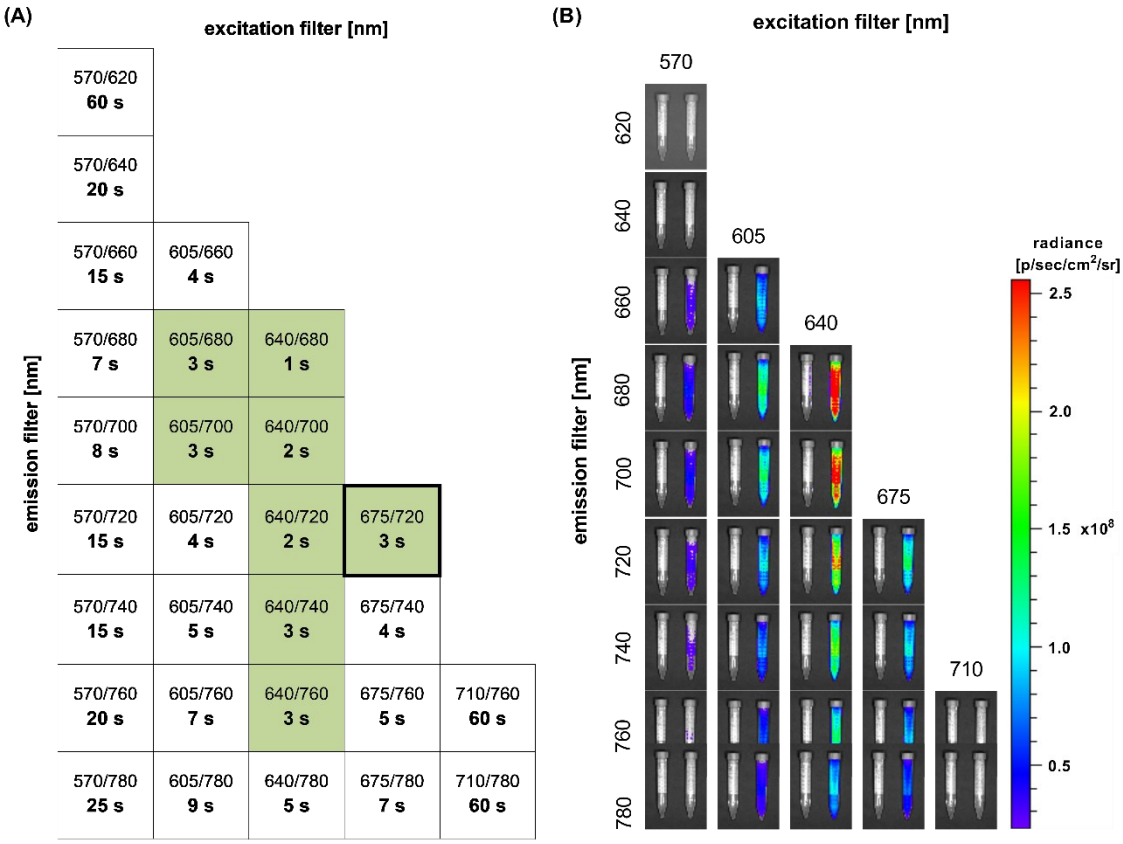

Figure 42: Patent Blue V phantom measurements.

Different excitation (570 nm, 605 nm, 640 nm, 675 nm, 710 nm) and emission (620 nm, 640 nm, 680 nm, 700 nm, 720 nm, 740 nm, 760 nm, 780 nm) filters were applied and the **(A)** exposure time as well as **(B)** images of 15 ml phantoms with 4 µmol l^{-1} Patent Blue V in PBS (left phantom) or

PBS with 33 g l^{-1} BSA (right phantom, [354]) were acquired with the IVIS® system (medium binning, FOV: 25, f-stop:2).

As accumulation of Patent Blue V in the respective TDLN was already detectable by eye (**Figure 41 C**), in a next step the dye was applied for *in vivo* OI due to its fluorescent characteristics [354]. TDLNs were visualized using *in vivo* and *ex vivo* fluorescence OI. As previously described, mice were injected with Patent Blue V *s.c.* in proximity to the $MC38^{wt}$ tumor of an approximate size of 80 mm^3 (**Figure 43 A**). *In vivo* imaging yielded a weak fluorescence signal in the axilla on the tumor-bearing site of two out of five experimental mice (**Figure 43 B**). Overall the *in vivo* detected fluorescence signal intensity was fairly weak, most likely due to light absorption, auto-fluorescence and a limited penetration depth of approximately 4 mm [266]. Furthermore, the *in vivo* determined fluorescence signal intensity was cross-validated *ex vivo*. Accessory axillary and proper axillary LNs yielded an elevated Patent Blue V uptake at the tumor-bearing compared to the contralateral site of experimental mice. *Ex vivo* quantification of the fluorescence signal confirmed the accessory axillary and proper axillary LNs at the tumor-bearing site as the main TDLN. In one experimental mouse a marginal Patent Blue V uptake in the subiliac LN at the tumor-bearing site was observed. Nevertheless, there was no significant difference in Patent Blue V uptake in the subiliac LN on the tumor-bearing compared to the contralateral site (**Figure 43 C,D**).

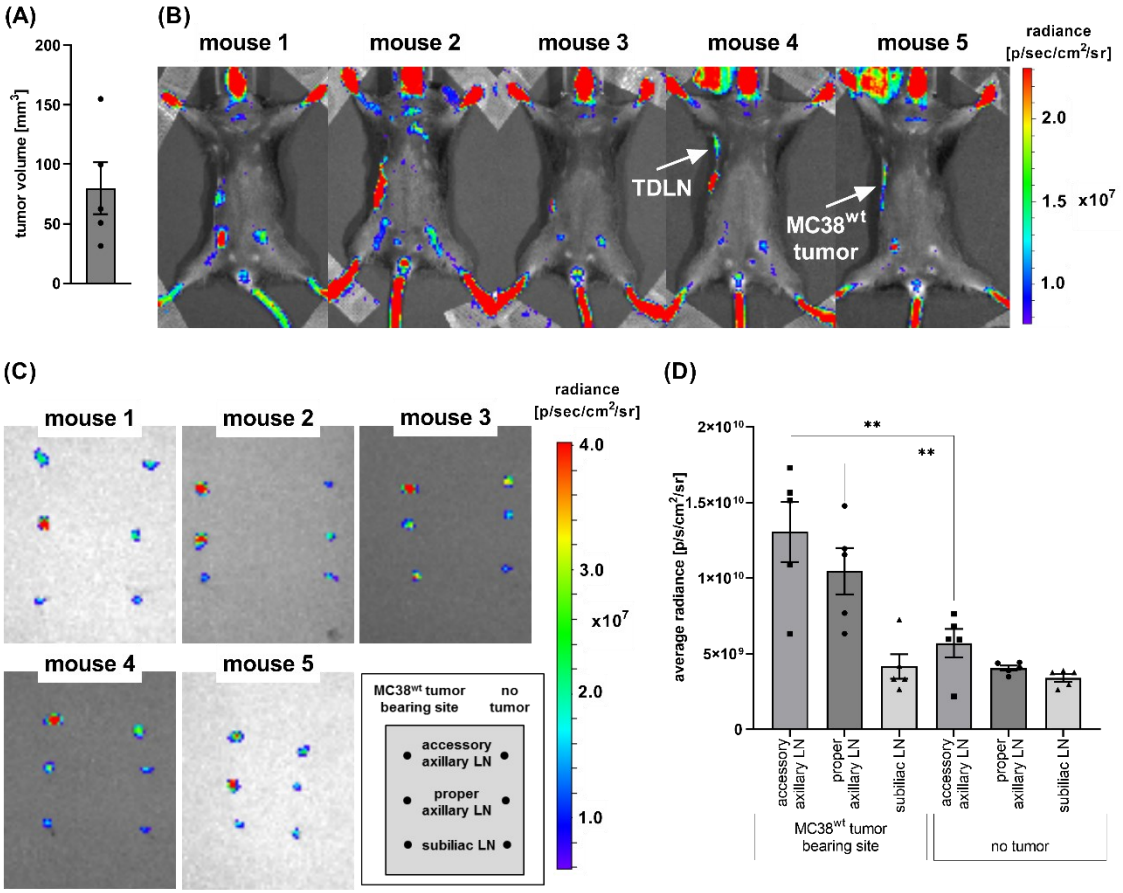

Figure 43: *In vivo* and *ex vivo* Patent Blue V OI of TDLNs.

(A) MC38^{wt} tumor volumes (mm^3) at day 7 post cancer cell inoculation. **(B)** Mice bearing a MC38^{wt} colon adenocarcinoma at the right shoulder were *s.c.* injected with Patent Blue V (25 mg ml^{-1}) in tumor proximity for *in vivo* OI (ventral position, uptake time: 5 min, medium binning, FOV: 14, f-stop:2, exposure: 10 s, excitation filter: 675 nm, emission filter: 720 nm). The tumor-draining lymph node (TDLN) and the MC38^{wt} tumor are indicated with an error. **(C)** Mice were sacrificed, and the indicated LNs were isolated and analyzed by *ex vivo* OI. **(D)** *Ex vivo* quantification of the Patent Blue V uptake in the LNs (n = 5 animals). Data is presented as mean ± SEM. Statistics: Tukey's multiple comparison test. Abbreviation: LN = lymph node, TDLN = tumor-draining lymph node.

Next the NIR contrast agent IRDye® 800CW conjugated to PEG was studied. The molecular weight of IRDye® 800CW PEG ranges between 25-60 kDa and is therefore markedly larger than the molecular weight of the Patent Blue V sodium salt [367, 368]. Similarly, as for Patent Blue V, mice were injected with IRDye® 800CW PEG *s.c.* in proximity to MC38^{wt} tumors with an approximate size of 75 mm^3 on the right shoulder of the experimental mouse (**Figure 44 A**). *In vivo* imaging revealed an accumulation of IRDye® 800CW PEG in the axilla on the tumor-bearing site of one out of five mice (**Figure 44 B**). As a strong signal

intensity was detected at the injection site, the absence of IRDye® 800CW PEG uptake in the LNs most likely does not reflect a detection problem, but rather an insufficient or weaker accumulation of the tracer in the TDLN when compared to Patent Blue V. This might be related to the larger molecular weight of IRDye® 800CW PEG which impedes or delays lymph vessel penetration. Although being used as a contrast agent for *in vivo* visualization of LNs by others [366, 368], *ex vivo* analysis revealed no IRDye® 800CW PEG NIR signal neither in the TDLN, nor in the NTDLN (**Figure 44 C**). In this regard, Proulx *et al.* reported a slow clearance of the dye from the injection site at a higher molecular weight [366]. Therefore, an even longer uptake duration might be recommended for IRDye® 800CW PEG OI measurements.

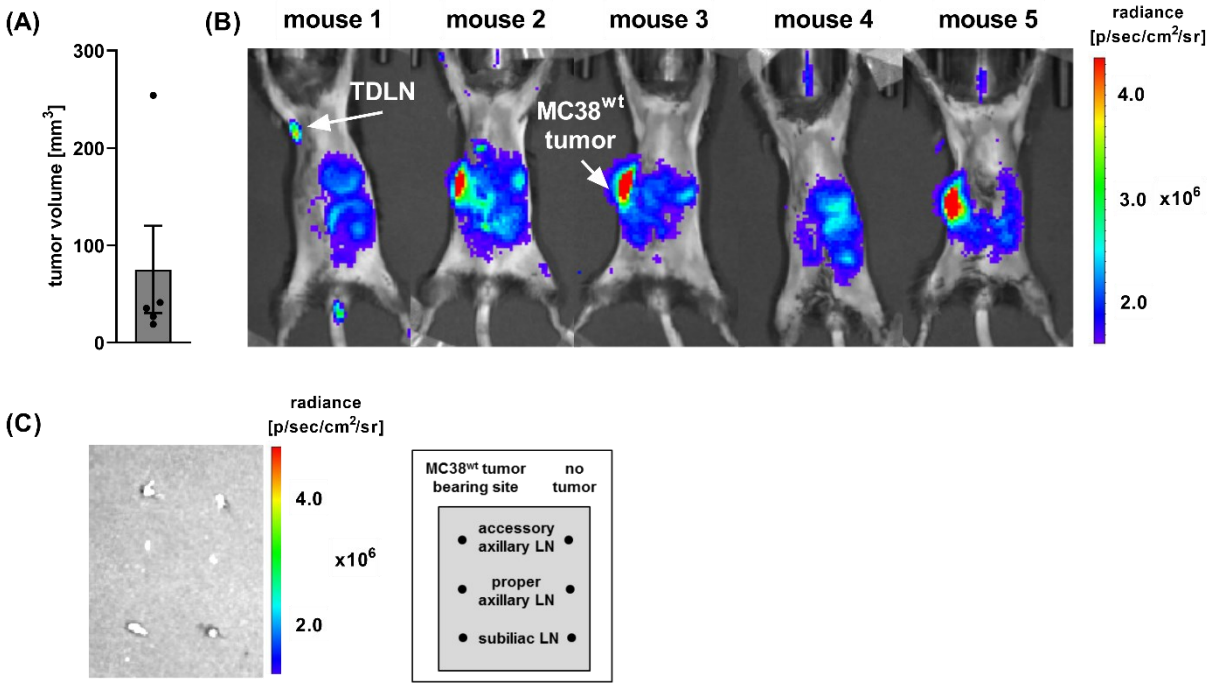

Figure 44: *In vivo* IRDye® 800CW PEG OI of TDLNs.

(A) MC38^{wt} tumor volumes (mm^3) at day 7 post cancer cell inoculation. **(B)** Mice bearing a MC38^{wt} colon adenocarcinoma at the right shoulder were *s.c.* injected with IRDye® 800CW PEG (~0.1 nmol; [368]) in tumor proximity. *In vivo* OI was performed 30 min post IRDye® 800CW PEG injection (ventral position, n = 5 animals, medium binning, FOV: 25, f-stop: 2, auto exposure, excitation filter: 745 nm, emission filter: 800 nm). The tumor-draining lymph node (TDLN) and the MC38^{wt} tumor are indicated with an error. **C)** Mice were sacrificed, and the indicated LNs were isolated and analyzed by *ex vivo* OI. Data is presented as mean ± SEM. Abbreviation: LN = lymph node, TDLN = tumor-draining lymph node.

Taken together, exclusively Patent Blue V OI was qualified to identify the accessory axillary and proper axillary LNs as the main TDLNs. This information on TDLNs obtained by *in vivo* and *ex vivo* imaging is crucial, as Fransen *et al.* have experimentally shown that the TDLNs are pivotal for a successful anti-PD-1 mAb checkpoint inhibitor therapy [208].

4.3.2 Non-invasive *in vivo* imaging of TDLN with PET/MRI

Next, the in clinical oncology commonly applied [^{18}F]FDG-PET/MRI technology, enabling three-dimensional, quantitative and high-resolution imaging, was evaluated for the feasibility of detecting TDLNs of *s.c.* MC38^{wt} tumors at the right shoulder of experimental mice using the previously described set-up. The rational for this study was to overcome the limitations of OI in terms of light absorption, penetration depth and the lack of three-dimensional quantitative imaging by PET/MRI. Combined PET/MRI measurements enable functional [^{18}F]FDG imaging of activated immune cells in the TDLN together with MRI qualified to provide essential anatomical information about the respective [^{18}F]FDG uptake site. Therefore, combined [^{18}F]FDG-PET/MRI measurements represent a clinically highly relevant approach to identify TDLNs.

Thus, mice were injected *s.c.* with 3.3 - 4.0 MBq [^{18}F]FDG in proximity to the *s.c.* MC38^{wt} tumors of about 50 mm^3 on the right shoulder of the mice. *In vivo* [^{18}F]FDG-PET/MRI revealed in the axilla of experimental mice a higher [^{18}F]FDG tracer uptake at the tumor-bearing when compared to the contralateral site (**Figure 45 A,B**). LNs were identified based on the MR images, but it was not possible to distinguish the [^{18}F]FDG uptake of the accessory axillary from the proper axillary LN *in vivo*. Furthermore, the subiliac LN was not detectable by [^{18}F]FDG-PET/MRI. *Ex vivo* biodistribution analysis of the [^{18}F]FDG-uptake by gamma counting, identified the accessory axillary LN as the main TDLN of a *s.c.* MC38^{wt} tumor at the right shoulder. These findings were confirmed by *ex vivo* [^{18}F]FDG autoradiography analysis of the respective LNs (**Figure 45 C-E**).

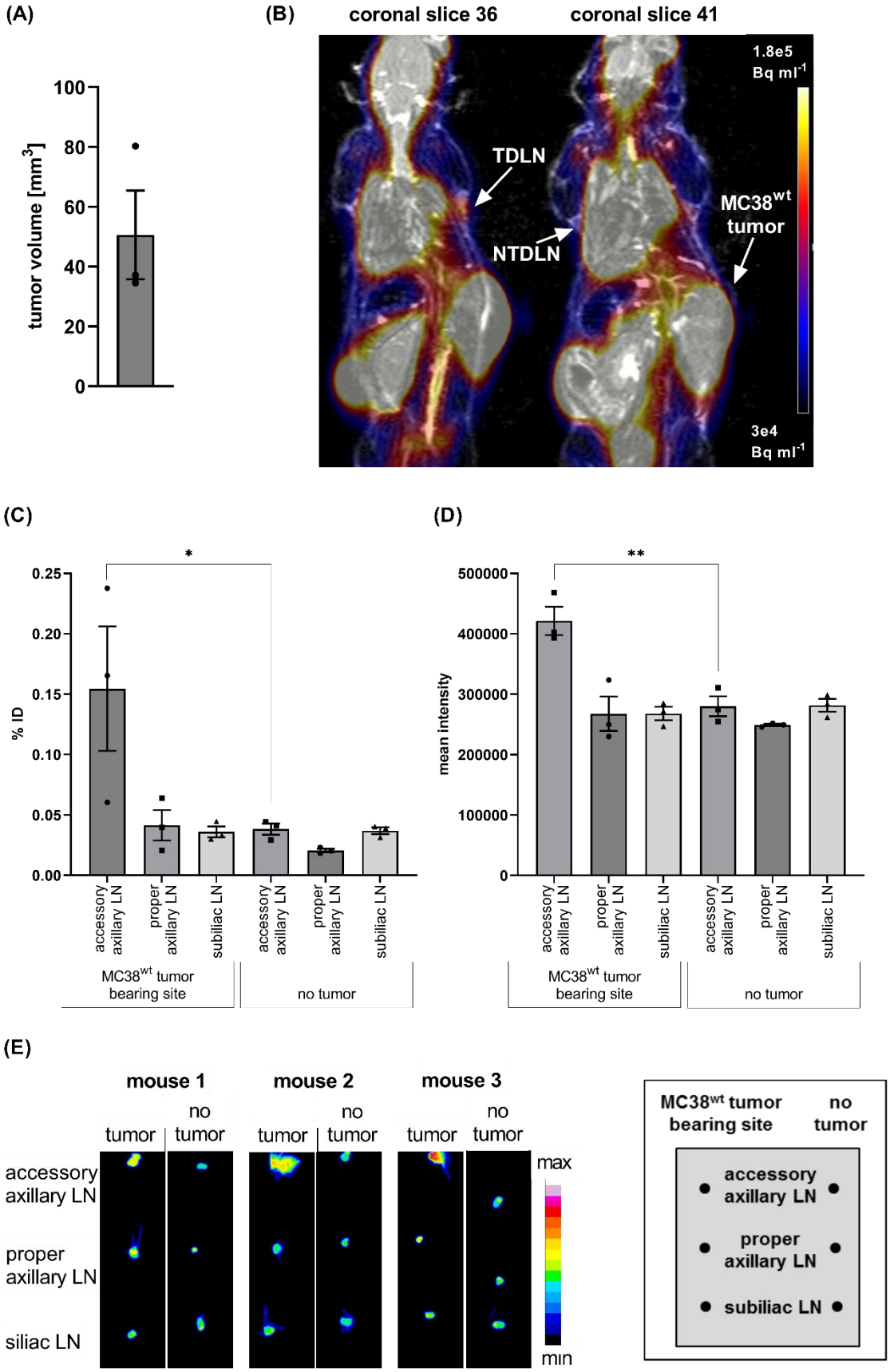

Figure 45: Imaging of TDLNs by [^{18}F]FDG-PET/MRI *in vivo* and *ex vivo*.

(A) MC38^{wt} tumor volumes (mm^3) at day 7 post cancer cell injection. **(B)** Mice bearing a MC38^{wt}

colon adenocarcinoma at the right shoulder were injected with [^{18}F]FDG in tumor proximity for *in vivo* PET/MR imaging. Representative PET images of the last 10 min frame of a 60 min dynamic PET scan were merged with the respective MR image, indicating the tumor-draining (TDLN, coronal slice 36) and non-tumor-draining (NTDLN, coronal slice 41) LN as well as the MC38^{wt} tumor at the right shoulder of the mouse. **(C)** %ID corrected for radioactive decay of tumor-draining and non-tumor-draining accessory axillary, proper axillary and subiliac LNs. **(D)** Quantitative *ex vivo* [^{18}F]FDG-autoradiography analysis and **(E)** autoradiography images of the respective LNs (n = 3 animals). Data is presented as mean ± SEM. Statistics: Tukey's multiple comparison test. Abbreviation: LN = lymph node, TDLN = tumor-draining lymph node, NTDLN = non-tumor-draining lymph node.

Taken together *in vivo* [^{18}F]FDG-PET/MRI is applicable to identify TDLNs. Nevertheless, separation of the [^{18}F]FDG signal originating from the accessory and proper axillary LN was not possible *in vivo* due to their proximity in the axilla of the mouse.

4.4 Characterization of tumor metabolism during p53 re-activation induced senescence

After studying the effect of IFN-γ, acidosis and hypoxia on PD-L1 expression and imaging the respective TDLNs of a MC38^{wt} tumor, this chapter focuses on cancer senescence, a cellular status that can be enforced i.a. by immune cell cytokines. Nevertheless, detecting senescence *in vivo* remains a challenge, why in this study senescent cancer cells were investigated for a distinct metabolic fingerprint.

4.4.1 Confirmation of senescence induction in H-Ras cells

To study metabolic and ECM degradation characteristics of senescent cells, the genetic modified murine shp53;H-RasV12 (H-Ras) liver carcinoma cell line was applied, where expression of p53, a senescence inducer, is controlled by a shRNA. The expression of the reporter gene GFP indicates the presence of the shRNA and the suppression of p53 expression. In contrast, the absence of GFP indicates the downregulation of the shRNA expression and subsequent p53 re-activation leading to senescence. As previously described, expression of the shRNA and subsequent induction of senescence is mediated by doxycycline hyclate withdrawal. Senescence induction upon doxycycline hyclate withdrawal was confirmed at two stages. Fluorescence microscopy confirms shRNA downregulation, by reduced expression of the GFP reporter and therefore represents an early indicator for subsequent senescence induction. Further down-

stream of the senescence induction process in H-Ras cells, re-activation of p53 expression, the driver for senescence in this cancer model, as well as reduced Ki67 expression, indicting a proliferation arrest were confirmed in the following studies by WB analysis.

To perform cell perfusion experiments, cells were grown around microcarrier beads in a 3D-like configuration forming 2-3 cell layers close to each other. To test whether our shRNA driven model was inducing senescence in this 3D-like configuration, we compared the results with cells grown in monolayer at low and high cell density. GFP expression was significantly reduced in H-Ras cells grown in monolayer independent of the initial seeding cell density at 3- and 5-days post doxycycline hyclate withdrawal, indicating shRNA downregulation (**Figure** 46 **A, B**). H-Ras cells grown on microcarrier beads showed a heterogeneous GFP reduction at 3- and 5-days post doxycycline hyclate withdrawal, which was more pronounced at the later time points (**Figure 46 A,B**). The reduction in GFP expression was more pronounced when the cells were grown on microcarrier beads and maintained in the cell perfusion system for 2 days. These results indicate a heterogeneous shRNA downregulation and therefore reduced GFP expression most likely due to an insufficient doxycycline hyclate washout in cells grown on microcarriers. Nevertheless, this effect is reduced when cells are placed in the cell perfusion system, where they are continuously perfused with fresh, doxycycline hyclate-deficient media for 2 days (**Figure 46 A,B**).

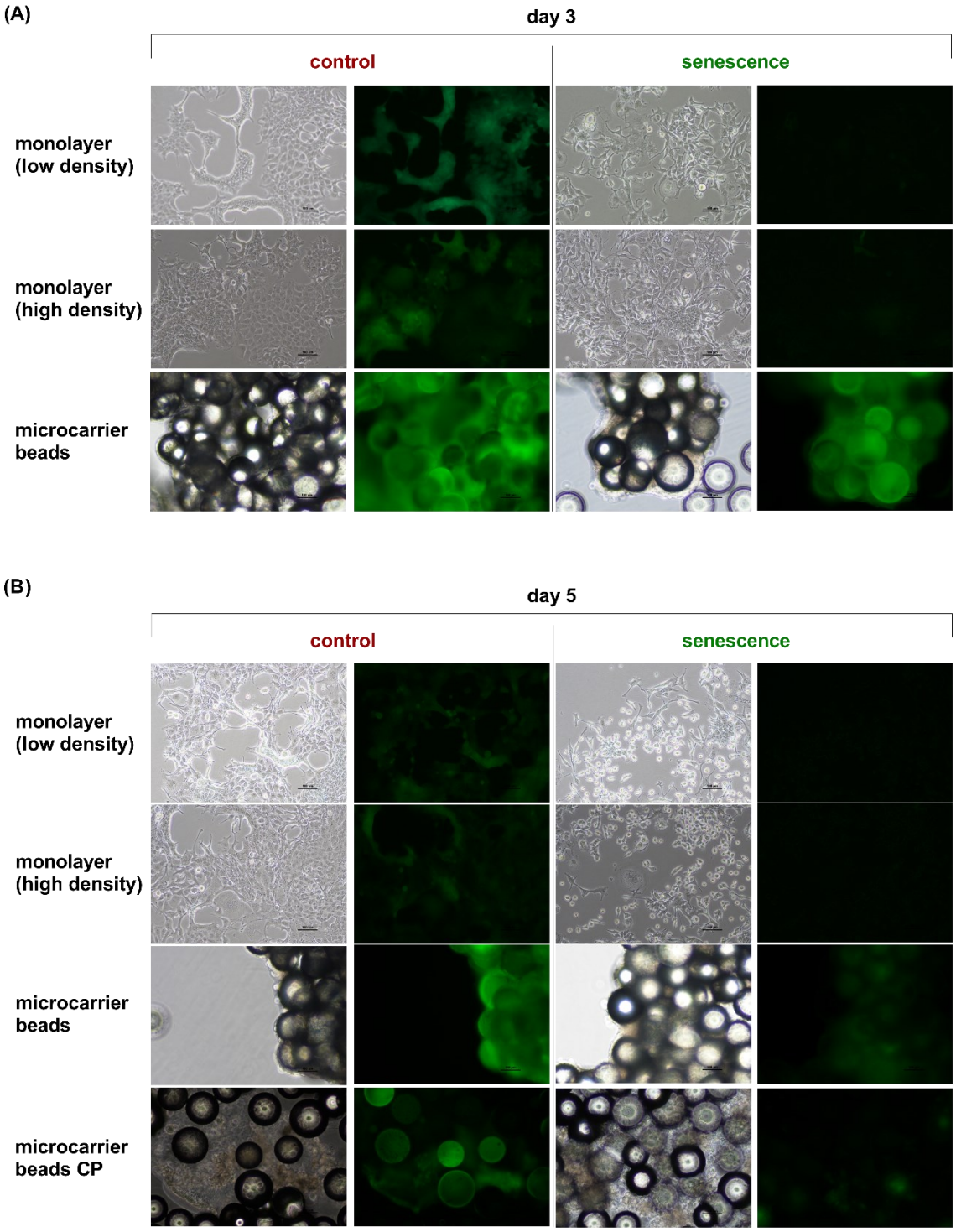

Figure 46: Doxycycline hyclate withdrawal reduces expression of the GFP reporter gene indicating reduced expression of shRNA against p53.

Bright field (left image, 70 ms) and GFP fluorescence images (right image, 20 s for cell monolayer, 4 s for cells coated on microcarrier beads) of control and senescent H-Ras cells grown as cell monolayer at low (control = $8*10^4$ cells, senescence = $16*10^4$ cells, 100 mm TC-dish) or high (control = $16*10^4$ cells, senescence = $32*10^4$ cells, 100 mm TC-dish) initial seeding cell density as well as cells coated and cultured on microcarrier beads according to the scheme illustrated in **Figure 10** at day 3 **(A)** or day 5 **(B)** post doxycycline hyclate withdrawal or harvested form the MR-

compatible cell perfusion system at day 5. For H-Ras cells grown as cell monolayers two (high and low) initial seeding cell densities were chosen, to mimic the proximity of cells when they are grown in 2-3 cell layers on microcarrier beads. Scale bar: 100 µm. Abbreviation: CP = MR-compatible cell perfusion system.

Further downstream in the process of senescence induction, p53 re-activation upon doxycycline hyclate withdrawal in H-Ras cells grown in monolayer was confirmed by WB analysis (**Figure 47**). Senescent cells exhibited a clear induction of p53 expression at day 3 and day 5 at both, low and high initial seeding cell density when compared to control. Expression of the proliferation marker Ki67 was significantly reduced in the senescence group compared to the control group at day 3. This reduction in Ki67 was even more pronounced at day 5, independent of the initial seeding cell density (**Figure 47 A**). In good agreement with the fluorescence microscopy results, p53 re-activation was less pronounced in H-Ras cells grown on microcarrier beads at day 3 and day 5 when compared to cells grown in monolayer. Furthermore, expression of p53 upon doxycycline hyclate withdrawal could also be confirmed in H-Ras cells grown on microcarrier beads and maintained in the cell perfusion system (**Figure 47 B**). For H-Ras cells grown on microcarrier beads, cells were harvested either by trypsin including several centrifugations and washing steps or by direct addition of the RIPA protein lysis buffer to the H-Ras cells on the microcarrier beads. Minor differences for Ki67 total protein expression were observed between the two harvesting methods and might be explained by differences in the time required for protein isolation. Notably, H-Ras cells grown on microcarrier beads in the senescence group exhibited an elevated Ki67 expression at day 3 and less pronounced also at day 5 independent of the harvesting method (trypsin vs. direct addition of RIPA protein lysis buffer) when compared to the control group (**Figure 47 B**). One explanation for this increase in Ki67 expression in the senescence group might be the heterogeneous depletion of shRNA against p53 and therefore heterogeneous senescence induction, even promoting proliferation of nearby non-senescent cells. This hypothesis is supported by several studies on the SASP of senescent fibroblasts which are promoting cell proliferation [437, 438] and carcinogenesis [439]. At day 5, H-Ras cells harvested by direct addition of RIPA protein lysis buffer, which is the more time efficient method, exhibited equal Ki67 levels in the control and the senescence group (**Figure 47 B**). These findings support the theory of delayed

and heterogeneous senescence induction in H-Ras cells grown on microcarrier beads. Senescent H-Ras cells harvested from the well-perfused MR-compatible cell perfusion system at day 5 by direct addition of RIPA protein lysis buffer exhibited significantly reduced total Ki67 protein levels when compared to the control group (**Figure 47 B**).

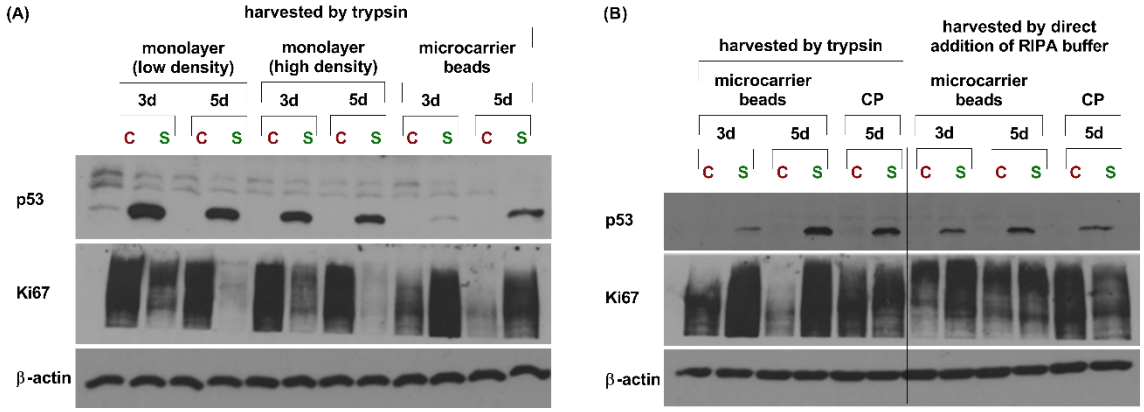

Figure 47: Doxycycline hyclate withdrawal re-activates p53 expression and reduces expression of the proliferation marker Ki67.

WB analysis of p53, Ki67 and β-actin of control and senescent H-Ras cells grown as **(A)** cell monolayer at low (control = $8*10^4$ cells, senescence = $16*10^4$ cells, 100 mm TC-dish) and high (control = $16*10^4$ cells, senescence = $32*10^4$ cells, 100 mm TC-dish) initial seeding cell density as well as **(B)** cells coated and cultured on microcarrier beads according to the scheme illustrated in **Figure 10** at day 3 or day 5 post doxycycline hyclate withdrawal or harvested form the MR-compatible cell perfusion system at day 5. Protein lysates were either obtained by first harvesting the cells with trypsin, followed by a washing step and addition of RIPA protein lysis buffer or direct addition of RIPA protein lysis buffer on the washed cells grown on microcarrier beads. Different exposure times for detection of the respective proteins have been applied in (A) and (B) (n = 1 independent experiment). Abbreviations: c = control, s = senescence, CP = MR-compatible cell perfusion system.

Taken together, these findings confirm senescence induction in H-Ras monolayer cell cultures. H-Ras cells grown on microcarrier beads exhibited a delayed and heterogeneous downregulation of the shRNA against p53, leading to a delayed senescence induction and proliferation inhibition. However, cells from the senescence group harvested from the MR-compatible cells perfusion system exhibited reduced shRNA expression determined by GFP fluorescence microscopy, increased p53 total protein expression and reduced Ki67 expression, confirming the at least partial senescence induction.

4.4.2 ECM degradation by senescent H-Ras cells

Cellular cancer senescence is characterized by a stable cell-cycle arrest. This is a characteristic that contrasts with the highly proliferative phenotype of cancer cells. Senescent cancer cells are characterized by the SASP and either themselves exhibit an elevated tissue invasion [249], or they promote invasion of surrounding non-senescent cancer cells [440]. This explains the great interest in finding a biomarker, characteristic for senescent cancer cells, so that they can be detected non-invasively *in vivo*.

To study ECM degradation by senescent H-Ras cancer cells, a MR-compatible cell perfusion system was applied [326] and the interplay between p53 re-activation induced senescence, metabolic changes and the ability to degrade ECM was investigated. Both non-senescent and senescent H-Ras cells exhibited the capability to degrade ECM in the MR-compatible cell perfusion system, but senescent cells exhibited a higher degradation index (**Figure 48**). This result highlights the invasive potential of senescent cells, outlining the clinical significance to identify and target senescent cancer cells to avoid or reduce cancer cell invasion and metastasis driven by senescent cells.

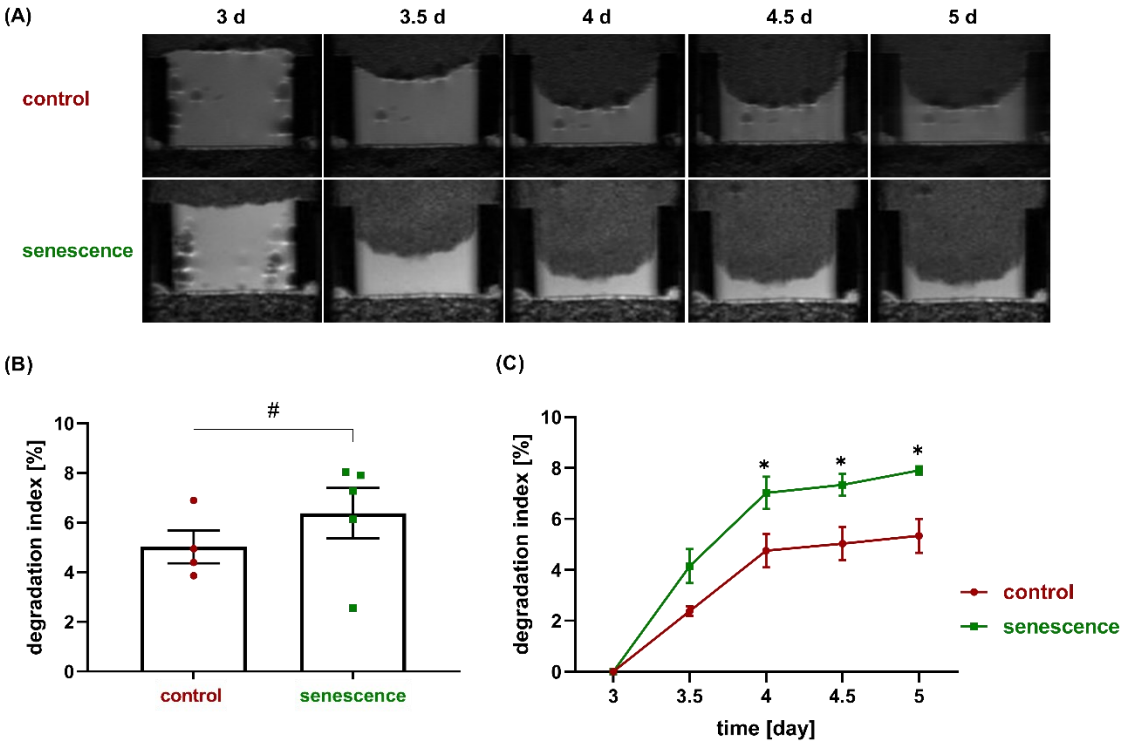

Figure 48: Senescent H-Ras cells exhibit an elevated ECM degradation phenotype.

Dynamic quantification of the ECM degradation of non-senescent control and senescent H-Ras

cells. **(A)** Representative T_1-weighted ^{1}H MR images of the ECM chamber between day 3 and day 5 post senescence induction by doxycycline hyclate withdrawal (for a detailed schematic illustration of the experimental set-up and the chronological sequence of operations see **Figure 10**). **(B)** Calculated degradation index [%] based on the T_1-weighted MR images showing an increased degradation of the ECM by senescent compared to non-senescent control cells at day 4.5 (# P≤0.286, statistics: two-tailed nonparametric Mann Whitney test). **(C)** Degradation index [%] of the ECM calculated based on the T_1-weighted MR images between day 3 and day 5 (outlier identified and excluded based on a two-sided Grubbs' test, n = 3-5, statistics: Sidak's multiple comparison test). Data is presented as mean ± SEM.

4.4.3 Identification of metabolic alterations of senescent H-Ras cell extracts by ^{1}H MR spectroscopy

Senescent cancer cells differ from proliferating cancer cells in various means. Therefore, the focus of this study is to identify metabolic changes, characteristic for cancer senescence. MR spectroscopy is a powerful technique that allows studying metabolic alterations. Therefore, dual-phase extracts of control and senescent H-Ras cells were generated, and the lipophilic and hydrophilic phases were studied by high-resolution ^{1}H spectroscopy.

The hydrophilic phase showed an increased GPC/PC ratio due to elevated GPC levels in senescent compared to control cells (**Figure 49**), indicating an impact of senescence on phospholipid metabolism. These results are in good agreement with previous studies that proposed a switch from PC to GPC as a marker of senescence [256]. Senescent cells also exhibited elevated ATP levels, which might be due to the reduced energy demand in non-proliferating senescent cancer cells when compared to proliferating control H-Ras cells (**Figure 49**). These changes were accompanied by elevated PCr levels in the senescence group, supporting the hypothesis of a lower energy demand in senescent compared to proliferating control cancer cells (**Figure 49**). In contrast to PCr, which is a mobilizable reserve of energy, ATP generated in glycolysis represents an immediate source of energy upon hydrolysis to ADP and might energize processes involved in the SASP. Furthermore, several amino acids, including arginine and aspartate, were increased in senescent H-Ras cells. This increase in amino acids was accompanied by increased lactate and myo-inositol levels in the senescent compared to the control group (**Figure 49**). Increased intracellular lactate levels in senescent H-Ras cells imply that although energy demand for proliferation dried up; lactate as a product of energy generating glycolysis is produced. Further it

might be that lactate is not exported to the same extend from senescent as from control H-Ras cancer cells. Experiments with H-Ras cells and a slightly altered culturing and harvesting protocol revealed inconsistent results on lactate (data not shown) suggesting that lactate is an imperfect biomarker for senescence. Interestingly, the increase in myo-inositol in senescent cancer cells might be specific and exclusive for p53 re-activation induced senescence (**Figure 49**). In a microarray screen, Koguchi *et al.* revealed that p53 induces genes related to myo-inositol metabolism, including the enzyme inositol 3-phosphate synthase (ISYNA1) which is essential for myo-inositol biosynthesis [441].

In summary these results suggest major changes in hydrophilic metabolites involved in phospholipid and energy metabolism.

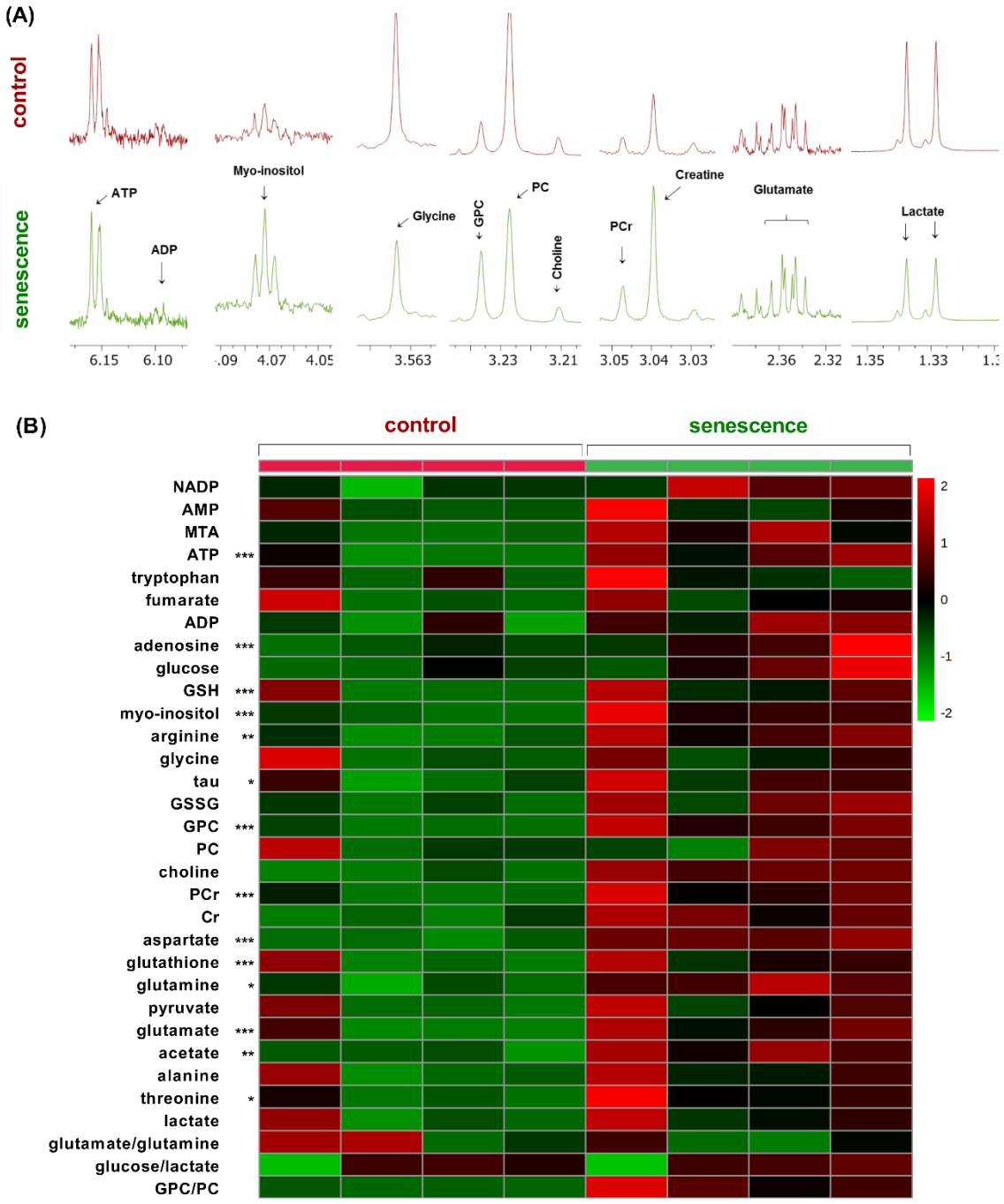

Figure 49: Senescent H-Ras cells exhibit distinct alterations in water soluble metabolites. **(A)** Individual high-resolution ^{1}H spectra of selected metabolites and **(B)** heat map of metabolites in the hydrophilic phase of control (red) and senescent (green) H-Ras cell extracts grown in monolayer and processed as illustrated in **Figure 8**. Heat maps were generated based on the normalized concentration of metabolites, mean-centered and divided by the standard deviation of each variable (600 MHz, n = 4 independent experiments, statistics: Fisher's LSD test). Abbreviations: ADP = adenosine diphosphate, AMP = adenosine monophosphate, ATP = adenosine triphosphate, Cr = creatine, GPC = sn-glycero-3-phosphocholine, GSH = glutathione, GSSG = glutathione disulfide, MTA = S-methyl-5´-thioadenosine,

NADP = nicotinamide adenine dinucleotide phosphate, PC = O-phosphocholine, PCr = creatine phosphate.

Changes in the lipophilic phase were also studied, as the alterations in GPC suggest important changes in lipid metabolism during senescence. Senescent cancer cells exhibited a significantly elevated lipid content compared to proliferating control tumor cells (**Figure 50**). Furthermore, glycerol, PtCho, sphingomyelin (SM), PE, linoleic acid, docosahexaenoic acid (DHA), omega-3 fatty acids and cholesterol did not significantly change but showed a trend towards elevated levels in non-proliferating senescent compared to proliferating control H-Ras cells.

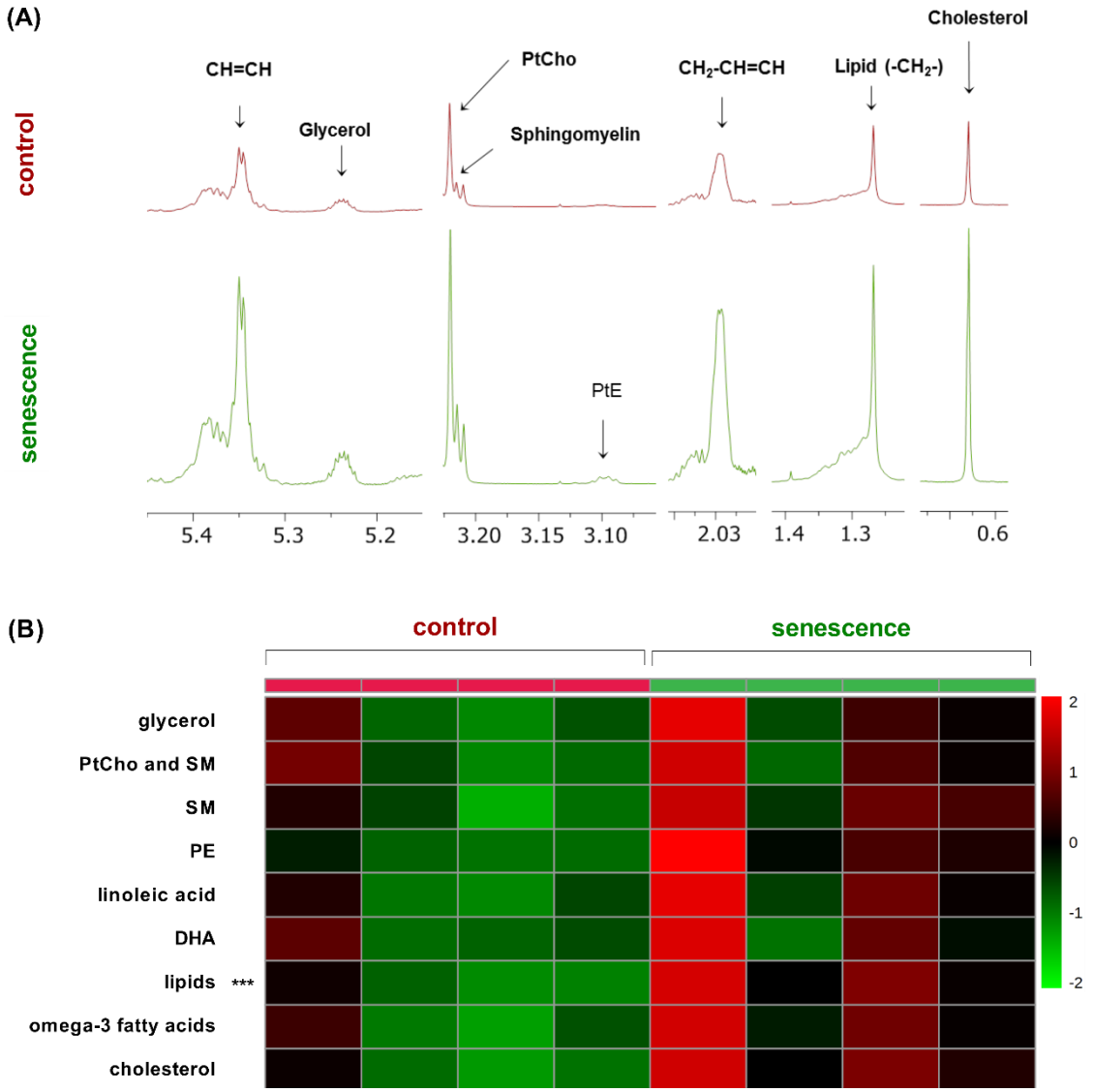

Figure 50: Senescent H-Ras cells exhibit alterations in lipophilic metabolites.

(A) Individual ^{1}H NMR spectra of selected metabolites and **(B)** heat map of top 9 metabolites in the

lipophilic phase of control (red) and senescent (green) H-Ras cell extracts grown in monolayer and processed as illustrated in **Figure 8**. Heat maps were generated based on the normalized concentration of metabolites, mean-centered and divided by the standard deviation of each variable (600 MHz, n = 4 independent experiments, statistics: Fisher's LSD test). Abbreviations: DHA = docosahexaenoic acid, PtCho = phosphatidylcholine, SM = sphingomyelin, PE = phosphatidylethanolamine.

Taken together, these findings indicate a higher lipid and membrane content in senescent compared to control H-Ras cell extracts. These major alterations of different metabolites upon senescence in H-Ras cells highlight the far-reaching consequences of senescence on cellular metabolism. Furthermore, these results provide a list of metabolites that probably can be used as biomarkers for senescence. Nevertheless, these biomarker candidates must be further evaluated in pre-clinical studies.

4.4.4 *In vitro* analysis of metabolic alterations of senescent H-Ras cells using the MR-compatible cell perfusion system

Comparative analysis of senescent and control H-Ras cancer cell extracts by ^{1}H NMR spectroscopy allows the identification of potential senescence biomarkers. Nevertheless, one drawback of this method is that the temporal dynamics of metabolic changes cannot be studied. Subsequently, the MR-compatible cell perfusion system allows longitudinal studies of the metabolic characteristics of senescent compared to control cells. Noteworthy, the MR-compatible cell perfusion system only allows measurements of the relative temporal dynamics in the respective experimental groups.

Both control and senescent H-Ras cells exhibited a significant decrease in GPC between day 3 and day 5, and a significant increase of PC between day 3 and day 4. Nevertheless, apart from day 3.5 for GPC, no significant difference in GPC and PC was observed between control and senescent H-Ras cells (**Figure 51 A**). These findings in the MR-compatible cell perfusion system are contrary to the increased GPC levels in senescence detected by high-resolution ^{1}H NMR spectroscopy. This might be explained by the delayed and heterogeneous senescence induction in H-Ras cells which are cultured on microcarrier beads and maintained in the MR-compatible cell perfusion system (see **Figure 46** and **Figure** 47). The effect of non-senescent, proliferating control H-Ras cells might outplay metabolic changes in senescent cells, at least in terms of GPC and PC. The

increase in PC over time was accompanied by stable choline and triglyceride levels, indistinguishable between the senescent and the control group (**Figure** 51 **A**). Increased PC levels can not be explained by altered choline kinase (ChK) protein expression, as total ChK protein levels remained stable in control and senescent cells approved by WB analysis (**Figure 51 B**).

Taken together, although suggested by the high-resolution ^{1}H NMR spectroscopy data no major changes in the temporal dynamics of GPC and PC between senescent and control H-Ras cancer cells could be identified with the MR-compatible cell perfusion system. This might be due to the heterogeneous induction of senescence on microcarrier beads in this model.

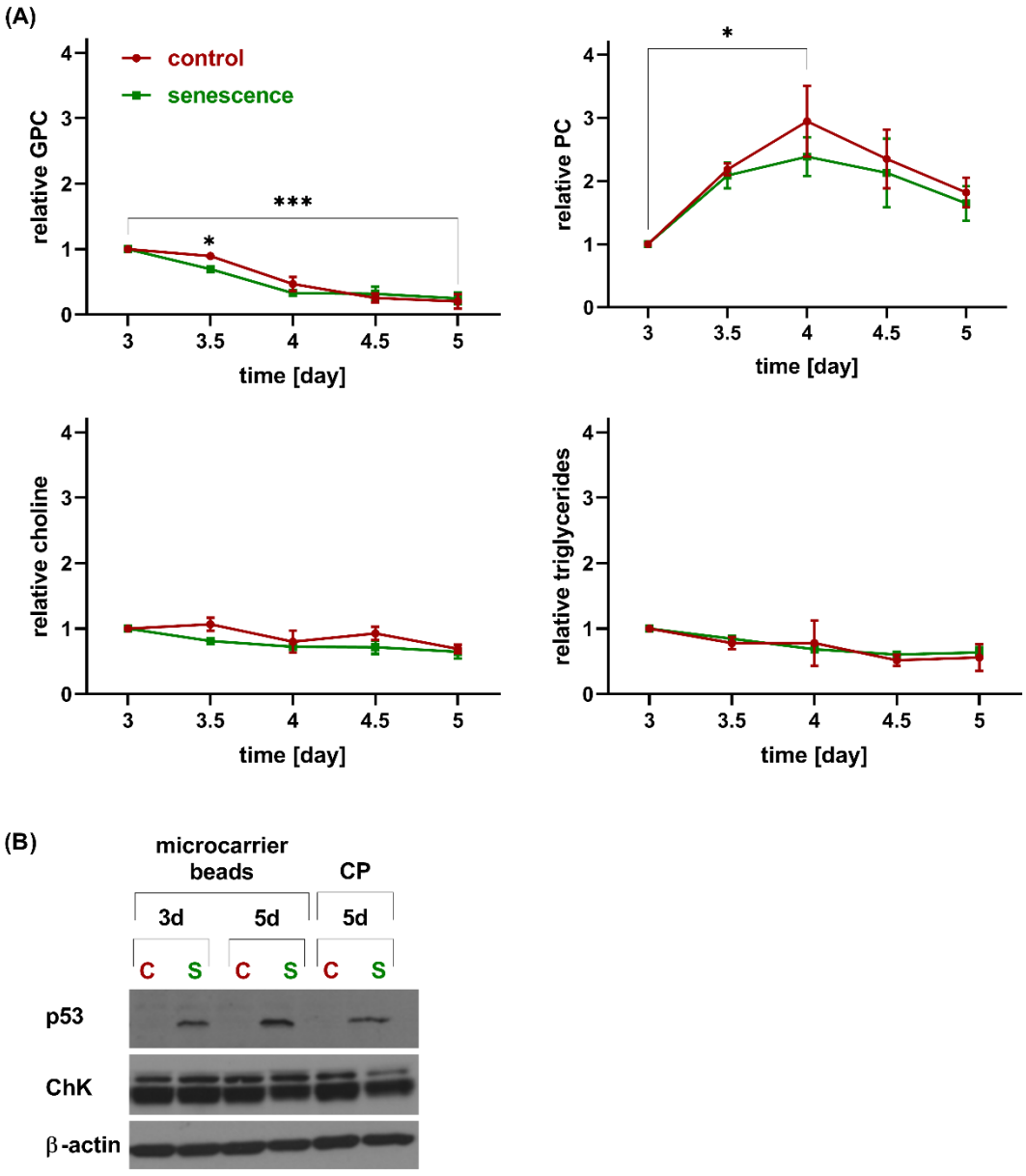

Figure 51: Changes in the temporal dynamics of the choline and triglyceride metabolism in control and senescent H-Ras cells determined by ^{1}H and ^{31}P MRS in a MR-compatible cell perfusion system.

(A) Quantification of GPC, PC, choline, and triglycerides from ^{1}H and ^{31}P MR spectra of control and senescent H-Ras cells grown on microcarrier beads and maintained in a MR-compatible cell perfusion system between day 3 and day 5 post senescence induction according to the scheme illustrated in **Figure 10**. Spectra were quantified, normalized to the 1) water phase and to the 2) first time point (n=3-5, values represent mean ± SEM, statistics: Tukey's multiple comparison test and unpaired t-test). **(B)** WB analysis of p53, choline kinase (ChK) and β-actin of control and senescent H-Ras cells coated and cultured on microcarrier beads and harvested at day 3 or day 5 post doxycycline hyclate withdrawal or harvested form the MR-compatible cell perfusion system at day 5. Abbreviations: GPC = sn-glycero-3-phosphocholine, PC = O-phosphocholine, c = control, s = senescence, CP = MR-compatible cell perfusion system, ChK = choline kinase.

Senescent cells developed significantly increased PCr levels compared to control cells, which were stable over two days (**Figure 52**). This was accompanied by the development of significantly increased Cr levels over time in both groups (**Figure** 52). The higher amount of the mobilizable energy source PCr in senescent cells either suggests a lower demand or an increased rate of Cr phosphorylation in senescent cells and is in accordance with the high-resolution ^{1}H NMR results (**Figure 49**).

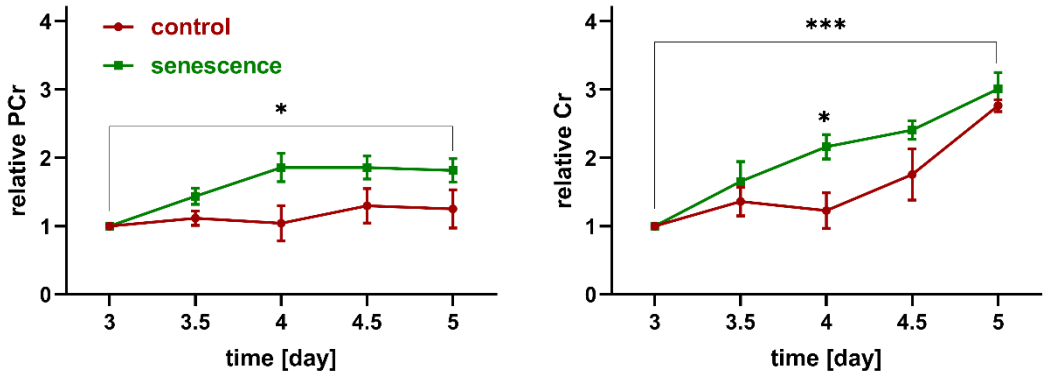

Figure 52: Changes in the temporal dynamics of the energy metabolism in control and senescent H-Ras cells determined by ^{1}H and ^{31}P MRS in a MR-compatible cell perfusion system.

Quantification of PCr and Cr from ^{1}H and ^{31}P MR spectra of control and senescent H-Ras cells grown on microcarrier beads and maintained in a MR-compatible cell perfusion system between day 3 and day 5 post senescence induction according to the scheme illustrated in **Figure 10**. Spectra were quantified, normalized to the 1) water phase and to the 2) first time point (n=3-5, values represent mean ± SEM, statistics: Tukey's multiple comparison test and unpaired t-test). Abbreviations: PCr = creatine phosphate, Cr = creatine.

Besides temporal changes in the energy reserves between senescent and control cells, control cells developed slightly, although not significant higher lactate levels than senescent H-Ras tumor cells (**Figure 53**). In contradiction to this, but in line with the high-resolution ^{1}H NMR spectroscopy data (**Figure 49**), the senescence group developed a slightly, but not significantly lower pH in the cell culture media (**Figure 53**).

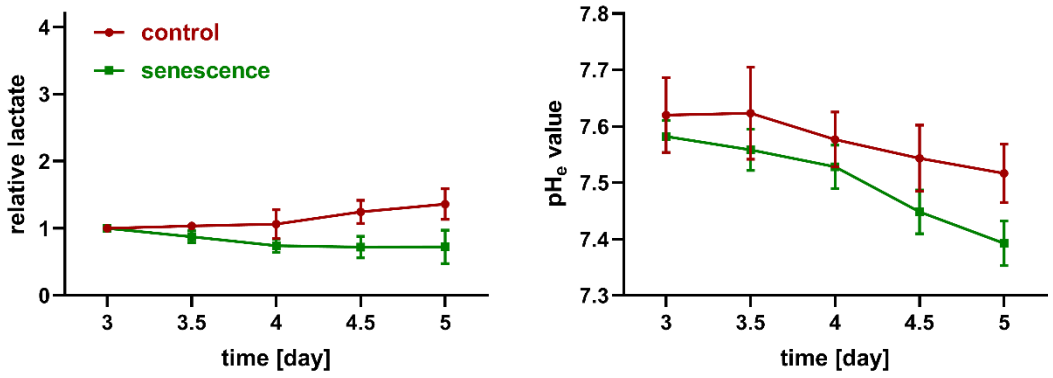

Figure 53: Changes in the temporal dynamic of the lactate metabolism in control and senescent H-Ras cells determined by ^{1}H and ^{31}P MRS in a MR-compatible cell perfusion system.
Quantification of lactate and determination of pH_e from ^{1}H and ^{31}P MR spectra of control and senescent H-Ras cells grown on microcarrier beads and maintained in a MR-compatible cell perfusion system between day 3 and day 5 post senescence induction according to the scheme illustrated in **Figure 10**. Spectra were quantified, normalized to the 1) water phase and to the 2) first time point (n=3-5, values represent mean ± SEM, statistics: Tukey's multiple comparison test and unpaired t-test).

In summary, these results are in good agreement with high-resolution spectroscopy data, revealing that PCr may serve as a potential biomarker to detect senescence non-invasively *in vivo*.

5 Discussion

Avoiding immune destruction proclaimed as an emerging hallmark of cancer by Hanahan and Weinberg in 2011 accentuates the importance of the immune system for tumor immune evasion and illustrates the emerging role of immunotherapy in recent years [4]. The FDA approval of ipilimumab for advanced melanoma targeting the immune checkpoint protein CTLA-4 [115] introduced for the first time a cancer treatment approach based on targeted re-activation of the immune system. In recent years, this led to the approval of several drugs targeting different immune checkpoint proteins like PD-1 and PD-L1 in various cancer entities [44, 134, 442]. Despite these great advances, reliable biomarkers to predict response or resistance are still missing. Nevertheless, immunotherapy has been evolved to the fifth and most promising pillar of the cancer therapy. Treatment efficacy of immune checkpoint inhibitor-based therapies is often closely linked to pre-treatment of patients with surgery, radiotherapy, chemotherapy, or precision therapy. A recent study revealed that TDLNs, which are often resected in cancer patients (e.g. melanoma and breast cancer), are pivotal in PD-1/PD-L1 mAb checkpoint inhibitor therapies [208]. This outlines the importance of methods for non-invasive clinical identification of TDLNs prior lymphadenectomy and immunotherapy. Especially, when taking into consideration that resection of the respective TDLNs also might diminish the anti-tumor therapeutic effect of immune checkpoint inhibitor-based cancer immunotherapies [208]. One of the tumor regression mechanisms upon immune checkpoint blocking therapies is the cytokine mediated cell cycle arrest, termed tumor senescence [333]. Depending on the tumor entity and the mechanism of senescence induction, this process is either detrimental or beneficial for malignant tumors. Therefore, non-invasive *in vivo* MR imaging and spectroscopy techniques can potentially assist to identify and specifically target senescent cancer cells by senolytic drugs.

Therefore, in this thesis three key aspects were investigated. Firstly, the induction of PD-L1 expression upon IFN-γ and acidosis on cancer cells was evaluated. Further, hypoxia known as an PD-L1 inducer was imaged non-invasively and correlated with tumor PD-L1 expression. Secondly, due to the importance of the immune system for a successful checkpoint inhibitor therapy, different imaging agents and modalities were assessed for non-invasive TDLNs imaging. Thirdly,

due to the connection of senescence with checkpoint inhibitor therapies, the metabolome of senescent cancer cells was analysed for characteristic metabolic patterns, that can serve as *in vivo* biomarkers in future.

5.1 Acidosis promotes cancer immune escape by IFN-γ-induced PD-L1 expression via the eIF4F-STAT1 axis

Malignant tumors exhibit various mechanisms to escape the control of the immune system. The intrinsic characteristics of cancer cells, including the overall tumor mutational burden or elevated PD-L1 expression by gene amplification [138], shape the TIME as well as the systemic anti-tumor immune response. Cancer cells only constitute parts of the tumor mass and are embedded in a complex network of cellular and non-cellular structures. The TME also comprises cancer cell extrinsic factors such as tumor acidosis, which leads to an unfavorable environment for immune cells. Furthermore, the expression of the immune checkpoint protein PD-L1 can be regulated by factors like hypoxia [161] or TIL-derived IFN-γ, representing another mechanism of immune escape [168, 172, 443].

5.1.1 Aim and rational for applied cell lines and mouse models

The aim of the presented work is to elucidate the complex spatial and temporal interactions between IFN-γ secreting TILs, tumor acidosis and immune checkpoint PD-L1 expression as well as the impact on an anti-PD-L1 mAb therapy response. This complexity and the interplay between cancer cell intrinsic and extrinsic factors, which are regulating the PD-L1 expression has been addressed by investigating various cancer cell lines across different tumor entities in syngeneic, immune competent mice. In this regard, the effect of the tumor mutational burden on conjoint IFN-γ- and acidosis-mediated PD-L1 expression was studied in anti-PD-1 and/or anti-PD-L1 mAb therapy responder cell lines [196, 206, 208, 217], including the hypermutated MC38^{wt} [194, 195] and the non-hypermutated CT26^{wt} adenocarcinoma cell line [194]. Beside these responder cancer cell lines, B16-F10^{wt} and 4T1^{wt} cancer cells, both described as low-/non-responsive in several studies were applied [206, 217, 218]. Moreover, the differences in the host immune cell composition were displayed by using T_h1 prone C57BL/6 [226, 227] and T_h2 prone BALB/c [226, 228] mice. In summary, a study set-up involving *in vitro,* and *in vivo* experiments allows holistic conclusions about the complex interactions and provides insights into the underlying mechanisms, which regulate PD-L1

expression patterns and determine immune checkpoint inhibitor therapy response.

5.1.2 Regulation of PD-L1 upon IFN-γ and acidosis

Predicting clinical response as well as identifying and counteracting resistance mechanisms to an anti-PD-L1 mAb therapy remains as a major clinical issue. In the TME, acidosis has been reported to be a negative prognostic factor for an anti-tumor immune response [77, 83, 167]. Moreover, several studies outlined the importance of TIL-derived IFN-γ for an anti-CTLA-4 or anti-PD-1 mAb therapy mediated elimination of cancer cells [444, 445]. Tumors are a heterogeneous mass with spatially separated acidic and immune cell rich areas. Therefore, in the present thesis, the hypothesis that cytokines like IFN-γ might diffuse to acidic tumor regions, induce PD-L1 expression and thereby mediate immune escape has been formulated. The data in the present thesis shows for the first time that conjoint IFN-γ and acidosis treatment significantly increases membrane-bound PD-L1 expression compared to IFN-γ treatment in neutral cell culture conditions. This effect was present in the immune checkpoint inhibitor responsive cancer cell lines MC38^{wt} and CT26^{wt} (**Figure 13**, **Figure 15**). In contrast, this conjoint effect was not observed in the non-responsive cancer cell lines B16-F10^{wt} and 4T1^{wt} (**Figure 16**). Furthermore, three out of five studied human cancer cell lines exhibited a conjoint IFN-γ- and acidosis-mediated elevation in PD-L1 expression. These findings suggest a new conserved mechanism of tumor immune escape that has not been described in literature so far.

As shown in this thesis, conjoint IFN-γ- and acidosis-induced PD-L1 expression on cancer cells is mediated via the eIF4F-STAT1-PD-L1 axis in the applied murine and human colon carcinoma cell lines (**Figure 18**, **Figure 19**). In addition, acidosis contributed to elevated PD-L1 expression via enhanced phosphorylation of the transcription factor STAT1 (**Figure 18 A**, **Figure 21 B,C**). In line with this data, Nakayama *et al.* described that T cell derived IFN-γ leads to an elevated STAT1 phosphorylation and PD-L1 expression via the JAK/STAT1 pathway in breast cancer cell lines [446]. Likewise, these findings are underpinned by Garcia-Diaz *et al.* delineating the signaling pathways which are involved in IFN-γ-inducible PD-L1 expression in melanoma cells [172]. Accordingly, it has been identified by Cerezo *et al.* that the eukaryotic translation initiation complex eIF4F binds to and initiates translation of *Stat1* mRNA into protein [30]. Therefore, the eIF4F complex

is a key factor in IFN-γ-induced PD-L1 expression on cancer cells. Consequently, the authors propose eIF4A inhibitors as a promising, novel cancer immunotherapeutic approach to overcome tumor immune escape [30]. In the context of these data, enhanced STAT1 phosphorylation at tyrosine 701 (Y701) upon conjoint IFN-γ and acidosis treatment can be explained by either enhanced tyrosine kinase or decreased tyrosine phosphatase activity. Accordingly, it has been reported that upon treatment with IFN-γ, the transcription factor STAT1 is activated by phosphorylation at Y701, migrates to the nucleus and becomes fully activated by phosphorylation of the amino acid serine 727 (S727) [447-449]. Kovarik *et al.* reported stress-induced phosphorylation of STAT1 at S727 upon exposure of macrophages to LPS, UV irradiation or TNF. The authors have experimentally proven that in macrophages the p38 mitogen-activated protein kinase (MAPK) is activated in response to stress, leading to enhanced STAT1 phosphorylation at S727, whereas IFN-γ-induced S727 phosphorylation seems to be independent from this pathway [450].

Extracellular acidosis is also considered as a cellular stress factor. To this aspect, Riemann *et al.* reported that metabolic acidosis induces the elevation of COX-2 and nitric oxide synthase (iNOS) which is mediated by p38 MAPK activity in fibroblasts [451]. As described, extracellular acidosis (pH_e 6.6) decreases serine and threonine protein phosphatase activity, which leads to increased p38 phosphorylation [451]. Similar results were reported by the same authors for prostate carcinoma cells, where extracellular acidosis was associated with enhanced p38 and extracellular signal-regulated kinase 1/2 (ERK1/2) phosphorylation [452].

In summary, several studies suggest enhanced phosphorylation of various proteins upon acidic pH_e in different cell entities. Nevertheless, the data of present thesis revealed for the first time an enhanced phosphorylation of STAT1 at Y701 upon conjoint IFN-γ and acidic media treatment compared to IFN-γ treatment in neutral cell culture conditions (**Figure 18 A**, **Figure 21 B,C**). However, the exact mechanism of acidosis-induced enhanced STAT1 phosphorylation in the IFNGR-JAK-STAT1 pathway remains unknown. In this context as shown by several authors, a *in silico* database analysis using PhosphoSite [453] and Phospho.ELM [454] also identified the two predicted STAT1 phosphorylation sites Y701 and S727. Continuative experiments focusing on the temporal phosphorylation dynamics of

the amino acids Y701 and S727 might lead to the identification of potential kinases and phosphatases involved. Furthermore, phosphoproteomics together with a screen of several pharmacological tyrosine and serine kinase as well as phosphatase inhibitors could reveal the engaged enzymes with altered activity during extracellular acidosis. In this context it is of interest that in the present thesis, the magnitude of conjoint IFN-γ- and acidosis-mediated PD-L1 induction was more pronounced in hypermutated MC38^{wt} compared to non-hypermutated CT26^{wt} cancer cells. Further experiments with more hypermutated and non-hypermutated cancer cell lines across several tumor entities are required to uncover whether there is a link between the mutational burden and conjoint IFN-γ- and acidosis-induced PD-L1 expression. Notably, Yu *et al.* did not find any correlation between PD-L1 expression neither on cancer nor on tumor infiltrating immune cells with tumor mutational burden. Furthermore, the tumor mutational burden did also not correlate with the IFN-γ gene signature [455]. This study therefore most likely suggests that the different magnitudes of PD-L1 induction upon conjoint IFN-γ and acidosis treatment are exclusively a coincidence and not related to the mutational burden of the respective cancer cell line.

In summary, by various approaches, it could be demonstrated that conjoint IFN-γ- and acidosis-mediated induction of PD-L1 expression represents a mechanism of tumor immune escape in anti-PD-L1 mAb therapy responsive MC38^{wt} and CT26^{wt} cancer cells. Interestingly, this mechanism of conjoint IFN-γ- and acidosis-mediated tumor immune escape via PD-L1 induction is absent in non-responsive B16-F10^{wt} and 4T1^{wt} cancer cells. To this aspect, Efremova *et al.* performed an immunogenic and transcriptomic characterization of MC38^{wt} cancer cells and reported that upregulation of immune checkpoints represents a tumor immune escape mechanism [194]. In the mentioned study, the authors reported tumor PD-L1 upregulation in wild type mice due to immune cell-derived IFN-γ compared to immune deficient RAG1$^{-/-}$ mice [194]. The IFN-γ-induced upregulation of PD-L1 was sufficient for a tumor immune escape [194]. Likewise, Bullock *et al*. reported that IFNGR1-deficient tumors which are incapable of PD-L1 upregulation were non-responsive to an anti-PD-1 mAb therapy [456]. Further, Kleinovink *et al.* reported a reduced tumor growth of PD-L1 deficient compared to wild type cancer cells. Nevertheless PD-L1-deficient tumors were still responsive to an anti-PD-L1 mAb therapy *in vivo* [196]. The authors together with others attributed the

effectiveness to an anti-PD-L1 therapy of tumors deficient in PD-L1 on cancer cells to the expression of PD-L1 on various immune cells [196, 202, 457, 458].

The cancer cell metabolism relies on aerobic glycolysis leading to elevated lactate production and accumulation in the TME, a phenomenon caused by the Warburg effect [4, 16, 165, 459]. Acidification of the TME is furthermore driven by CO_2, which is hydrated by carbonic anhydrases into HCO_3^- and H^+ ions [46, 460]. In the present thesis, deconvoluting the effect of acidosis and lactate on conjoint IFN-γ-mediated cancer cell PD-L1 expression revealed that acidosis might represent the main contributor (**Figure 13**). Surprisingly, conjoint IFN-γ and lactic acidosis (20 mM sodium L-lactate) treatment even reduced PD-L1 cell surface expression on $MC38^{wt}$ cancer cells when compared to conjoint IFN-γ and acidosis treatment (**Figure 13**). Amongst the investigated murine and human cell lines, only the breast cancer MCF-7 cell line exhibited elevated membrane-bound PD-L1 expression upon conjoint IFN-γ and lactic acidosis treatment in comparison to IFN-γ stimulation in acidic media. The effect of lactate on IFN-γ- induced membrane-bound PD-L1 expression is rather negligible in most of the here examined murine and human cancer cell lines. Interestingly, Feng *et al.* showed that lactate induces PD-L1 expression in the two human lung adenocarcinoma A549 and H1299 cell lines via binding to the lactate receptor GPR81. Upon treatment with 20 mM extracellular lactate and subsequent binding to the G-protein coupled receptor (GPCR) the receptor becomes activated, leading to decreased intracellular cyclic AMP (cAMP) levels and inhibition of the cAMP dependent protein kinase A (PKA). Reduced PKA activity entails the activation of the transcriptional co-activator TAZ and subsequently mediates PD-L1 expression [166]. Moreover, Daneshmandi *et al.* determined by flow cytometry analysis an enhanced PD-L1 expression on B16-F10 melanoma cells upon 24 h treatment with 10 mM lactate [167]. In summary, the data presented in this dissertation as well as the two studies by Feng *et al.* and Daneshmandi *et al.* indicate a cell line specific effect of lactate on PD-L1 cell surface expression. So far however, the contribution of acidic pH_e upon conjoint treatment with IFN-γ seems to be more predominant in terms of PD-L1 upregulation in comparison to lactate.

Taken together, conjoint IFN-γ and acidic media treatment induces PD-L1 expression in various cancer cell lines via the eIF4F-STAT1 axis, whereas acidic pH_e contributes to elevated PD-L1 expression by enhanced phosphorylation of

STAT1. A schematic representation summarizing the *in vitro* and *in vivo* findings obtained within this thesis and the proposed a mechanism of conjoint IFN-γ- and acidosis-mediated PD-L1 expression is illustrated in **Figure 54**.

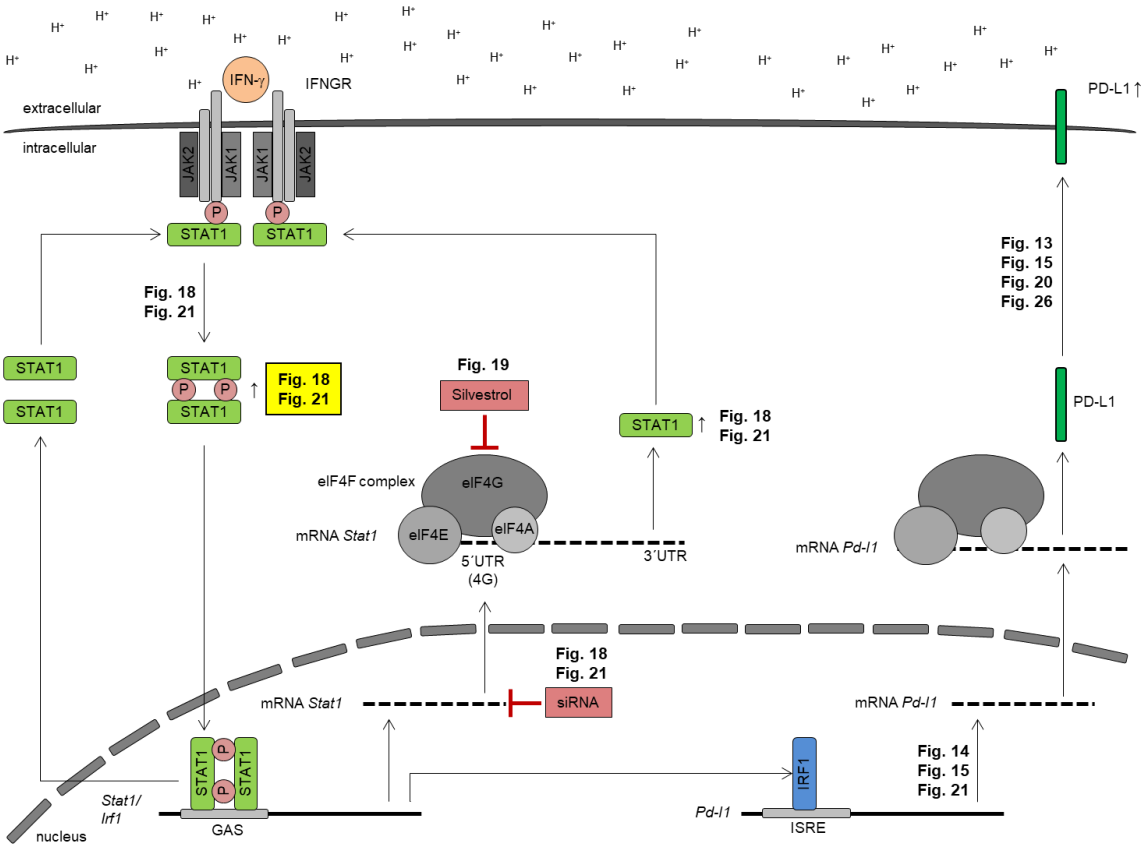

Figure 54: Schematic summary of the potential regulatory mechanism of combined IFN-γ- and acidosis-mediated cancer cell PD-L1 expression.

The findings in the presented dissertation are indicated by cross referencing the respective figures in section 4.1. It is proposed that acidosis elevates PD-L1 expression by increased STAT1 expression via the eIF4F complex and enhanced STAT1 phosphorylation (yellow box) upon IFN-γ binding to the IFNGR. Briefly, IFN-γ binds to the IFNGR leading to STAT1 phosphorylation, homodimerization and translocation to the nucleus. The phosphorylated STAT1 homodimer binds to GAS and induces STAT1 transcription. The resulting *Stat1* mRNA is translated by the eIF4F translational complex leading to increased STAT1 protein levels. Furthermore, IRF1 is transcribed upon STAT1 binding to GAS, which then induces PD-L1 transcription. The *Pd-l1* mRNA is then translated into protein and transferred to the cell membrane. IFN-γ stimulation in the context of acidosis further increases STAT1 phosphorylation and subsequently elevates PD-L1 expression. The underlying structure of the schematic representation is based on [30, 172, 400, 461].

5.1.3 Effect of PD-L1 regulation by IFN-γ and acidosis *in vivo*

These *in vitro* results on PD-L1 regulation upon IFN-γ and acidosis stimulation are clinically highly relevant. As shown herein, both anti-PD-L1 mAb therapy

responsive cancer cell lines, $MC38^{wt}$ and $CT26^{wt}$ exhibited reduced tumor volumes upon sodium bicarbonate-mediated tumor pH_e neutralization (**Figure 24, Figure 32**). The tumor volume reduction was less pronounced for $MC38^{wt}$ tumors at day 15 post cancer cell inoculation. Similarly, Faes *et al.* reported a reduction in $MC38^{wt}$ tumor volumes in sodium bicarbonate-treated mice, which was less pronounced at day 15 but significant at day 18 post cancer cell inoculation [78]. In other words, tumor acidosis in immune competent wild type mice with intact IFN-γ signaling resulted in elevated tumor volumes and thus might represent a mechanism of tumor immune escape. In accordance with the *in vitro* results of this thesis, development of acidosis in $MC38^{wt}$ tumors of wild type mice with intact IFN-γ signaling resulted in elevated cancer cell PD-L1 expression (**Figure 26**). In contrast, under the same experimental *in vivo* conditions, PD-L1 expression on immune cells was reduced under acidic tumor pH_e. These results indicate that conjoint IFN-γ- and acidosis-induced PD-L1 expression on cancer cells mediate tumor immune escape, which is associated with elevated tumor volumes. In this context, Daneshmandi *et al.* performed a shRNA mediated knockdown of LDH-A in B16-F10 melanoma cells, which exhibited significantly reduced tumor volumes and resulted in an elevated fraction of IFN-γ producing cells [167]. Interestingly, in the present thesis sodium bicarbonate treated wild type mice with intact IFN-γ signaling and neutralized $MC38^{wt}$ tumor pH_e, PD-L1 expression on immune cells was higher compared to tumors with acidic tumor pH_e. Moreover, in $MC38^{wt}$ tumors no additional effect of the combined sodium bicarbonate and anti-PD-L1 treatment was observed. In contrast to this, Daneshmandi *et al.* reported an almost completely abrogated tumor growth upon anti-PD-L1 mAb treatment of shLDH-A B16-F10 melanomas [167]. As also other factors including CO_2 contribute to an acidic TME, the conclusions made by Daneshmandi *et al.* are restricted to the effect of cancer cell-derived lactate and only partly allow conclusions on tumor acidosis [167]. In line with data in the present thesis, Pilon-Thomas *et al.* revealed elevated $CD8^+$ and IFN-γ^+ T cells and an enhanced IFN-γ secretion upon neutral cell culture conditions, which explains the higher immune cell PD-L1 expression in $MC38^{wt}$ tumors with neutralized pH_e. Interestingly IFN-γ gene expression by T cells was unaffected by acidic cell culture media (pH 6.6), whereas cytokine secretion was completely abolished [77]. Furthermore, the authors have shown, that sodium bicarbonate (200 mM) treatment resulted in a tumor pH_e neutralization *in vivo*

improves an anti-CTLA-4 or an anti-PD-1 mAb therapy in B16 melanomas [77].

Tumors consist of numerous cell types. Besides cancer cells, other resident and infiltrating cell types contribute to the acidification of the TME. To address this topic, Seth *et al.* generated LysM-Cre:LDH-A$^{fl/fl}$:K-Ras mice with tamoxifen-mediated macrophage-specific LDH-A deletion [462]. Mice with macrophages deficient in lactate production exhibited reduced lung tumor volumes accompanied with decreased VEGF expression, angiogenesis and an increased number of $CD3^+$ T cells and activated, IL-17- and IFN-γ-producing $CD8^+$ T cells [462]. This study supports the results in this thesis, that an increased PD-L1 expression on immune cells in MC38^{wt} tumors with neutralized pH_e is IFN-γ-mediated. In addition, Seth *et al.* reported for a myeloid-specific LDH-A deletion an increased M1 macrophage phenotype [462]. In line with this, El-Kenawi *et al.* described that a neutral tumor pH_e favors a M1 phenotype. In addition, extracellular acidic pH_e promotes an IL-4 driven M2 macrophage polarization [83]. Furthermore, tumors of mice deficient in LDH-A exhibited significantly reduced PD-L1 expression levels compared to tumors with intact lactate production indicating that LDH-A induces PD-L1 on cancer cells [462]. This finding is in line with the enhanced PD-L1 expression on MC38^{wt} cancer cells in the experimental acidosis$^{IFN-\gamma}$ group in present thesis. Nevertheless, Seth *et al.* suspected that accumulation of lactate within the TME is the main driver of PD-L1 induction, whereas the results in this thesis suggest a conjoint effect of acidic pH_e and IFN-γ as the main driver for induced cancer cell PD-L1 expression and subsequent tumor immune escape. This contradiction accentuates the differential effects of lactate as a signaling molecule and of tumor acidosis on PD-L1 expression. In this regard the *in vitro* as well as *in vivo* results suggest a negligible role of lactate in the studied tumor models.

The differential PD-L1 expression on cancer and immune cells upon tumor acidosis raises the questions about the drivers for tumor immune escape and the response markers for an efficient immune checkpoint inhibitor therapy. The results in this thesis suggest that the induction of PD-L1 on cancer cells upon IFN-γ and acidosis exposure results in immune escape and increased tumor volumes, whereas PD-L1 induction on immune cells determines response to an anti-PD-L1 mAb therapy. In 2017 four independent research groups by using different tumor and mouse models addressed the question whether PD-L1 expression on cancer

or immune cells is pivotal for an anti-tumor immune response [457]. In this context, Juneja *et al.* generated PD-L1 deficient MC38 cancer cells using the CRISP/Cas9 technology. These $MC38^{PD\text{-}L1\text{-}/\text{-}}$ tumors exhibited a reduced tumor growth in comparison to $MC38^{wt}$ tumors, suggesting that PD-L1 expression on cancer cells is required for suppression of an anti-tumor immune response [201]. In line with our results, Kleinovink *et al.* reported a delayed outgrowth of $MC38^{PD\text{-}L1\text{-}/\text{-}}$ and $CT26^{PD\text{-}L1\text{-}/\text{-}}$ tumors when compared to $MC38^{wt}$ and $CT26^{wt}$ tumors. This study supports the concept of cancer cell PD-L1 expression conveying $CD8^+$ T cell suppression and thus mediating tumor immune escape [196]. Moreover, Noguchi *et al.* evaluated the temporal PD-L1 expression patterns on cancer and immune cells and confirmed the key role of PD-L1 on cancer cells in promoting tumor immune escape. In line with the hypothesis and the results of this thesis, the authors described the IFN-γ dependency of PD-L1 induction on cancer cells [458]. Beside spontaneous regression or growth slow-down of PD-L1 knockout cells, Lau *et al.* showed that PD-L1 on cancer, myeloid or other immune cells modulate the extend and degree of T cell cytotoxicity within the TME [202]. Absence of PD-L1 on host immune and cancer cells yields in the most profound tumor regression accompanied by cytolytic gene expression patterns, characteristic for T cell activation and function [202]. These results underline the importance of cancer and host cell PD-L1 expression for suppressing T cell functioning and mediating tumor immune escape. In line with the research hypothesis of this work, that conjoint IFN-γ- and acidosis-mediated PD-L1 induction on cancer cells represents a tumor immune escape mechanism, several recent studies outline the role of induced PD-L1 expression for tumor immune escape. Similar to IFN-γ-mediated $MC38^{wt}$ tumor PD-L1 induction leading to increased tumor volumes and therefore presenting a mechanism of immune escape, Iwai *et al.* reported the involvement of cancer cell PD-L1 expression in immune escape [463]. The authors reported that overexpression of PD-L1 on murine P815 mastocytoma cells conveys the formation of progressive local tumors, whereas PD-L1 negative $P815^{wt}$ mastocytoma cells formed only transient tumors in syngeneic mice due to the high T cell immunogenicity [463]. The *in vivo* $MC38^{wt}$ tumor studies in this thesis confirm the *in vitro* findings that extracellular tumor acidosis fosters IFN-γ-induced PD-L1 expression on cancer cells, whereas sodium bicarbonate-mediated pH_e neutralization of the TME increased immune cell PD-L1 expression levels.

Investigating the temporal PD-L1 expression patterns on cancer and host immune cells of murine methylcholanthrene-induced sarcomas with distinct immunogenicity, Noguchi *et al.* showed transient induction of PD-L1 expression on sarcoma cells and very stable PD-L1 expression on TAMs, which was only partly IFN-γ dependent [458]. Notably, by treatment of tumor-bearing mice with IFN-γ neutralizing mAb the authors confirmed an IFN-γ dependency of cancer cell PD-L1 expression but were unable to rule out a potential contribution of host cell PD-L1 expression for immune escape [458].

In the present study only anti-PD-L1 mAb therapy responsive cell lines exhibited a conjoint IFN-γ- and acidosis-mediated increase in PD-L1 expression *in vitro* as well as elevated PD-L1 expression in clusters close to necrotic tumor regions palisaded by macrophages *in vivo*. This supports the theory, that immune cell-induced PD-L1 expression determines the anti-tumor immune response. To uncover inducible PD-L1 expression Cerezo *et al.* correlated in a coherent study CD8 and PD-L1 expression with eIF4F formation in melanomas from 59 patients [30]. Thus, the clinical response to anti-PD-1 mAb treatment significantly correlated with eIF4F complex activation, which in turn correlated with PD-1/PD-L1 engagement [30]. In line with the results of this thesis, the authors recommend eIF4F complex formation as a response marker for an anti-PD-1 mAb therapy [30]. Building on the hypothesis of inducible PD-L1 expression being a better response biomarker, 17 nivolumab treated NSCLC patients with high IFN-γ expression exhibited a significantly higher progression-free survival [444]. Similarly, based on the study of Karachaliou *et al.,* the overall survival of 21 melanoma patients treated with pembrolizumab was higher in patients with high compared to low IFN-γ expression levels [444]. Based on these data, the authors propose IFN-γ to be a more accurate biomarker compared to PD-L1 itself. Nevertheless, the mutual causality between the pre-existing immune infiltrate and the treatment-induced increase in immune cell infiltration remains ambiguous. In this regard IFN-γ producing $CD4^+$ T cells with high expression of the inducible T cell co-stimulator (ICOS) were present in peripheral blood and tumor tissue of 6 anti-CTLA-4 mAb treated urothelial carcinoma patients as described by Liakou *et al.* [464]. In a second study they expanded their finding to prostate cancer and proposed immunologic biomarkers such as the infiltration of IFN-γ-secreting $CD4^+$ T cells for anti-CTLA-4 mAb treatment monitoring [445]. Similar to the upregulation of PD-L1 on tumor

infiltrating immune cells upon sodium bicarbonate-mediated pH_e neutralization, Peng *et al.* showed that PD-1 is up-regulated on transferred T cells at the tumor site [465]. Furthermore, it has been shown that tumor acidosis prevents IFN-γ secretion by T cells [77]. The findings by Peng *et al.* on PD-1 blockade-induced T cell recruitment to the tumor site and tumoral IFN-γ expression [465] are in line with enhanced $CD3^+$ T cell homing to $MC38^{wt}$ tumors in the combined sodium bicarbonate and anti-PD-L1 treatment group. In this thesis IFN-γ dependency was proven in IFN-γ-deficient mice, whereas Peng *et al.* transplanted bone-marrow derived from IFNGR knockout mice into wild type mice [465]. Together these studies outline the importance of immune cell-derived IFN-γ during cancer immunotherapy. In 46 patients with metastatic melanoma, Tumeh *et al.* nicely described that responding patients exhibited elevated $CD8^+$ T cell levels and were generally high in PD-1 and PD-L1 expression levels before treatment when compared to patients with progressive disease [466]. These studies support our findings of inducible PD-L1 expression being a more reliable biomarker for response. Further the authors revealed increased STAT1 phosphorylation in the response group, proposing that anti-PD-1 mAb therapy inhibits adaptive immune escape via e.g. PD-L1 upregulation and thereby induces response [466]. Therefore, stable STAT1 knockout MC38 cells were generated in this thesis. Nevertheless, variable tumor growth was observed in the STAT1 knockout cells, most likely due to clonal effects. Manguso *et al.* performed a genetic screen using the CRISPR/Cas9 technology and identified defects in IFN-γ signaling which are causing resistance to cancer immunotherapy [467]. The authors reported a significant growth advantage of B16 melanoma cells with a deficient IFN-γ signaling pathway when compared to wild type melanoma cells [467]. Furthermore, the authors reported a growth advantage of STAT1 deficient B16 melanomas compared to wild type melanoma cells in mice upon combined cancer immunotherapy [467].

In summary, the presented results propose conjoint IFN-γ and acidosis inducible cancer cell PD-L1 expression to be a novel, so far not described tumor immune escape mechanism, which can be targeted by an anti-PD-L1 mAb therapy.

5.2 Non-invasive *in vivo* BLI of tumor hypoxia using 5xHRE-ODD-luc reporter cell lines

Tumor acidosis and tumor hypoxia are closely related and linked to each other. Tumor regions of deep hypoxia distant from blood vessels and therefore deficient in oxygen supply also exhibit an acidic pH_e [46].

To study the effect of hypoxia on PD-L1 expression and $CD3^+$ T cell homing in a syngeneic mouse model *in vivo*, murine MC38-HRE-ODD-luc, CT26-HRE-ODD-luc, B16-F10-HRE-ODD-luc and 4T1-HRE-ODD-luc reporter cancer cell lines for short-lived hypoxia were generated. Danhier *et al.* developed the hypoxia reporter cell construct where the luciferase enzyme expression is under control of the HRE and transcription is induced upon HIF binding. As a model for short-lived hypoxia, the authors reported an ODD-luc half-life of 34 min in human prostate cancer PC3 cells [267]. Exposure of hypoxia reporter cells to 1% O_2 resulted in increased *Luciferase* mRNA expression levels (**Figure 39**). The generated CT26-HRE-ODD-luc cells exhibited an increase in luciferase activity upon 48 h hypoxia which was similar to the human PC3-HRE-GFP/HRE-ODD-luc/tdTomato cells studied by Danhier *et al.* [267]. Noteworthy is the variable magnitude of *Luciferase* mRNA expression and luciferase activity upon hypoxia, which might be explained by cancer cell line specific characteristics. Scharping *et al.* reported in this context different oxygen consumption rates for B16-F10 and MC38 cancer cells, which also suggests a difference with respect to the hypoxia response of the individual cancer cell lines in terms of hypoxia-induced gene expression [468]. Noman *et al.* support this assumption by cancer cell line specific PD-L1 expression patterns upon hypoxia [161]. Furthermore, Tiffen *et al.* attributed cell line-specific BLI signal intensities to the differences in promoter and transduction efficiencies as well as the photon absorbing effect of the melanin in B16-F10-HRE-ODD-luc cancer cells [422, 423]. Based on data presented in this thesis, short-lived hypoxia characterized by luciferase expression and activity developed in CT26-HRE-ODD-luc tumors *in vivo* and increased with tumor progression. Nevertheless, short-lived acute hypoxia varied substantially between individual tumors in the present thesis, representing a weakness of the reporter system. However, a dual hypoxia reporter cell system, where chronic and long-term tumor hypoxia is displayed by eGFP expression and short-lived acute hypoxia is displayed by luciferase activity [267, 275], might provide a more holistic picture and allow dissecting these two types of

tumor hypoxia.

Imaging the development and characterizing the type of tumor hypoxia is of paramount clinical relevance as hypoxia can promote tumor progression [469], invasion and metastasis [470]. To this aspect, Bharti *el at.* applied a dual imaging hypoxia reporter system in a xenograft model of prostate cancer and demonstrated that cancer cells residing in the metastatic lesions highly express the long-term hypoxia marker eGFP but only faintly the short-lived hypoxia marker luciferase [471]. These findings suggest that metastatic cancer cells were exposed to hypoxia before, when residing at the primary tumor site leading to a metastatic phenotype [471]. In chapter 4.1 of the present thesis, the conjoint IFN-γ- and acidosis-mediated PD-L1 expression was described for the first time *in vitro* and *in vivo*. To elucidate the effect of combined IFN-γ and hypoxia on PD-L1 expression, CT26-HRE-ODD-luc tumors harvested from syngeneic, immune competent mice with intact IFN-γ signaling were evaluated for PD-L1 expression on mRNA and total protein level. However, neither a correlation between short-lived hypoxia with *Pd-l1* mRNA levels nor with total PD-L1 expression could be identified in CT26-HRE-ODD-luc whole tumor lysates. In contrast to this data, Noman *et al.* and Barsoum *et al.* reported a significant hypoxia-induced upregulation of PD-L1 on various murine and human cancer cell lines, macrophages and DCs *in vitro* [161, 162]. One reason for the lack of correlation between the luciferase BLI signal intensity and PD-L1 expression could be that the luciferase hypoxia reporter system detects only short-lived hypoxia. For short-lived hypoxia, the luciferase expression increased already within 4 h under hypoxic conditions and exhibits a half-life of approximately 34 min [267]. Therefore, only regions within CT26-HRE-ODD-luc tumors which are currently hypoxic show a high BLI signal. This argument is supported by findings from Noman *et al.*, who reported a significant membrane-bound PD-L1 upregulation on splenic MDSCs of CT26 tumor-bearing mice after 48 h of hypoxia and on B16-F10 melanoma cells after 24 h of hypoxia suggesting that mainly long-term hypoxia mediates PD-L1 induction on cancer cells [161]. Therefore, a correlation of PD-L1 with the long-term hypoxia reporter eGFP might be more illuminating as well as spatially resolving the BLI signal and correlating it to PD-L1 expression voxel by voxel. Furthermore, contrary to the initial research hypothesis short-lived hypoxia did not inversely correlate with CD3 staining in CT26-HRE-ODD-luc tumors. In this context, in pre-clinical prostate cancers,

Jayaprakash *et al.* revealed that therapeutic hypoxia reduction or elimination partly reversed T cell exclusion and sensitized tumors to immune checkpoint blockade [472]. To further study the relationship between hypoxia and T cell infiltration, fluorescence microscopy might reveal and spatially resolve the distribution of T cells in hypoxic and normoxic regions.

Finally it is worth noting, as also explicated by Bharti *et al.* that the inability to quantify oxygen tension as well as signal attenuation represents major limitations of optical hypoxia reporter systems [471].

5.3 Identification of TDLNs of a *s.c.* colon adenocarcinoma

With the emergence of immune checkpoint inhibitor therapies, which are based on the engagement of the host immune system to battle against cancer, identification of primary as well as secondary lymphoid organs via non-invasive *in vivo* imaging gained importance. In a translational study Schwenck *et al.* identified metabolic changes in the bone marrow and spleen upon immune checkpoint based cancer immunotherapy by [^{18}F]FDG-PET imaging that allowed to distinguish therapy responders from non-responders [473]. These results are supported by a study from Fransen *et al.* which revealed that immune cell homing and activation in the TDLN upon an anti-PD-L1 mAb therapy is pivotal for an efficient treatment response [208]. Another recent publication by Wu *et al.* indicates that activated T cells characterized by a high glucose metabolism and lactic acid secretion lead to acidic niches in LNs and thereby suppress T cell effector functions, including reduced IFN-γ or IL-2 cytokine release. T cells are therefore subject to a physiological process of immune regulation by acidification of paracortical zones within the LNs [474]. Taken together, these studies accentuate the need to identify TDLNs by non-invasive *in vivo* imaging in a pre-clinical as well as clinical setting. In recent years, several studies focused on lymphatic vessel and LN imaging using Isosulfan Blue, Patent Blue V, Evans Blue, radionuclide scintigraphy, technetium-99m (^{99m}Tc) single photon emission computed tomography (SPECT)/CT, MRI and [^{18}F]FDG-PET/CT or [^{18}F]FDG-PET/MRI [432, 475, 476].

The presented work focuses on the comparison and suitability of the two fluorescent dyes Patent Blue V and IRDye® 800CW PEG for OI as well as combined [^{18}F]FDG-PET/MRI to identify the TDLN of a *s.c.* MC38^{wt} tumor on the right shoulder of an experimental mouse.

The OI dyes Patent Blue V and IRDye® 800CW PEG only revealed limited

suitability for *in vivo* detection of TDLN, with a detectable uptake in one out of five mice for Patent Blue V and IRDye® 800CW PEG in the respective axilla. In contrast to IRDye® 800CW PEG, Patent Blue V was suitable to identify the accessory and the axillary LN as the main TDLN *ex vivo* (**Figure 43**). One reason for the lack of IRDye® 800CW PEG accumulation in the respective LNs might be the higher molecular weight compared to Patent Blue V (25-60 kDa vs. 582.7 g mol^{-1} [367] [368]). Nevertheless, IRDye® 800CW PEG has been shown suitable for *in vivo* LN imaging when injected intradermally and also blood vessel imaging 30 min post *i.v.* injection by others [368]. In the experimental set-up of this thesis the accumulation in the LN might be significantly slower due to the high molecular weight of IRDye® 800CW PEG in combination with the *s.c.* administration route. The clinically approved NIR dye indocyanine green (ICG) with a similar molecular weight as Patent Blue V (775 g mol^{-1}) [477] has been extensively and successfully applied for *in vivo* LN imaging in several animal species as well as in humans [478-481]. In contrast to IRDye® 800CW which is conjugated to PEG, ICG is an unconjugated fluorophore resulting in a lower molecular weight, which might lead to a fast and therefore more pronounced uptake of the contrast agent in the LN. As other NIR dyes, ICG is characterized by a reduced background auto-fluorescence and increased tissue penetration [480], which is an advantage over Patent Blue V, emitting light in the visible light spectrum. Nevertheless, OI of Patent Blue V was applicable to identify the TDLNs in a fast and cost-effective manner. Taken together, Patent Blue V, IRDye® 800CW PEG and ICG non-specifically accumulate in the TDLN and therefore do not provide functional information on e.g., immune cell activation.

Beside the two evaluated OI dies, [^{18}F]FDG-PET/MRI was performed due to the specific uptake of the radiotracer by immune cells with a high glucose demand. By [^{18}F]FDG *in vivo* imaging a higher uptake in the axilla of the MC38^{wt} tumor-bearing site was detected. In contrast to Patent Blue V OI, where the accessory axillary and the proper axillary LN were identified as TDLNs, *ex vivo* biodistribution and autoradiography analysis of the [^{18}F]FDG-uptake only revealed the accessory axillary LN as the main TDLN (**Figure 45**). This sophisticated picture might be due to the different characteristics of the two applied tracers, as [^{18}F]FDG is taken up predominantly by activated immune cells with an increased metabolic demand, suggesting that immune cell homing, and activation rather takes place in the

accessory axillary LN. In contrast to OI, combined [^{18}F]FDG-PET/MRI allows detection of functional TDLN with high glucose metabolism and furthermore provides anatomical information on the exact location of the LN at high spatial resolution [432]. Nevertheless, neither OI, nor PET/MRI was applicable to differentiate between the accessory axillary and the proper axillary LN *in vivo* and therefore required *ex vivo* biodistribution analysis. [^{18}F]FDG, the most common clinically applied PET tracer, has also been applied by Singh *et al.* to identify sentinel LNs in malignant melanoma patients. Like the results of this thesis, Singh *et al.* reported, that non-invasive pre-operative [^{18}F]FDG-PET/CT imaging cannot substitute lymphoscintigraphy or LN biopsy, due to the low sensitivity of [^{18}F]FDG-PET [313]. Beside immunotherapies, there is a great interest to identify TDLN for sentinel LN resection to anticipate metastatic spread or detect LN metastases. In this regard, Bae *et al.* claim that [^{18}F]FDG PET/CT is superior to CT/MRI in term of LN metastasis identification in patients with oral cavity squamous cell carcinoma [312]. Beside these clinical studies, [^{18}F]FDG is non-specifically taken up by cells with elevated metabolic demand including T cells as well as tumor metastases in the LN. Therefore, direct T cell labeling represents a promising approach to identify the T cell homing directly. Griessinger *et al.* specifically labeled adoptively transferred T cells with the ^{64}Cu-pyruvaldehyde-bis(N4-methylthiosemicarbazone) (^{64}Cu-PTSM) radiotracer for PET imaging, which allows to monitor T cell homing in single LNs [482]. This T cell-specific labeling approach is probably the most specific way for T cell homing sites identification.

In summary, OI with Patent Blue V as well as [^{18}F]FDG-PET/MRI identified the accessory axillary LN on the tumor-bearing site of the mouse as the main TDLN. These findings have broad pre-clinical as well as clinical implications for LN resections and the consequences for immune checkpoint inhibitor therapies as reported by Fransen *et al.* [208].

5.4 Metabolomics of p53 re-activation induced senescence

Tumor senescence is characterized by a stable cell cycle arrest and involves major cellular changes including metabolic alterations [483].

Co-culture experiments by Krtolica *et al.* revealed that senescent fibroblasts induce hyperproliferation and carcinogenesis of the human epidermal keratinocyte cell line HaCAT or the murine mammary epithelial cell line SCp2 [438]. This

interplay between infiltrating and resident cell types in the TME and cancer cells, their cellular characteristics in terms of senescence and the impact on tumor progression versus regression are also highlighted in a study by Brenner *et al.* [333]. Moreover, the authors describe that cytokine-induced senescence is required for cancer immune control [333]. These studies underline the importance of identifying senescent cancer cells within the tumor. In this regard, metabolic alterations specific for senescent cancer cells might therefore represent a valuable source for potential biomarkers.

In the present study, a model of p53 re-activation induced senescence based on a hepatocellular carcinoma H-Ras cell line was used. This model has been previously described and validated in a slightly modified form [235], with the main difference being the regulation of the p53 expression. In the present study, senescence is induced upon doxycycline hyclate withdrawal, whereas p53 expression is re-activated in the presence of doxycycline hyclate as proven in a study by Xue and Zender *et al.* [235]. As described, the p53 re-activation is accompanied by induction of cellular senescence, the expression of inflammatory cytokines and an innate immune response [235].

In the current work, the first step of senescence induction in the H-Ras cancer cell model was proven by GFP expression, a reporter for the expression of the shRNA targeting p53. In addition, WB analysis revealed p53 expression and inhibition of cell proliferation (Ki67) upon senescence induction. As shown herein, tumor cell growth in monolayer exhibited a marked reduction in GFP expression, indicating an increased p53 and a reduced Ki67 protein expression 3 days post senescence induction. However, tumor senescence induction in the 3D-like model was two days delayed and more heterogeneous when compared to the monolayer H-Ras cancer cell model. This effect is most likely to be explained by the fact that the washout of doxycycline hyclate in a 3D united cell structure was insufficient compared to a 2D monolayer H-Ras cancer cell culture. In good agreement with this hypothesis, previous studies by Yin *et al.* reported delayed senescence induction in a 3D compared to a 2D adipose-derived mesenchymal stem cell culture model [484]. Senescence in adipose-derived mesenchymal stem cells was measured by SA-β-GAL staining and determination of genomic p16, p21 and p53 expression [484].

In addition, senescent H-Ras cancer cells were evaluated for ECM degradation. In

the present thesis, ECM degradation in senescent H-Ras cancer cells was elevated when compared to proliferating control cells suggesting that senescent cells exhibit an increased ECM degradation phenotype. This effect is likely to be explained by the fact that the senescence induction might be heterogeneous, which causes a mixture of senescent and non-senescent H-Ras cancer cells within the MR-compatible cell perfusion system. Thus, the senescent H-Ras cancer cell-induced SASP induces a higher ECM degradation by their non-senescent counterparts. These findings are supported by a study of Kim *et al.* who described a higher invasiveness of senescent cells associated with the SASP, which is determined by elevated CXCL12 expression patterns in papillary thyroid carcinoma [249].

Senescence is associated with cell cycle arrest as well as major alterations of the cell secretome and metabolome [439, 485]. In this context, metabolic alterations are of outstanding importance as they help to understand the underlying molecular processes involved in cancer cell senescence and thus represent a potential source of novel biomarkers. In the present thesis, senescence in the H-Ras cancer model is characterized by increased GPC levels (**Figure 49**). Several studies have shown that malignant transformation and tumor progression trigger PtCho breakdown, leading to an increase in PC and the characteristic GPC to PC switch [258-260]. In line with these studies, Gey *et al.* reported reduced PC and increased GPC levels in the different models of replicative, oncogene-induced and etoposide mediated DNA damage induced senescence in the human embryonic lung fibroblast cell line WI-38 [256]. This study reported that increased GPC levels most likely arise from phospholipase A1 and/or A2 and lysophospholipase activity [256]. This is in good agreement with studies reporting an impairment of phospholipase D/diacylglycerol pathway in senescent cells [256, 486]. Interestingly, a knockout of the phospholipase A2 receptor (PLA2R) prevented replicative and decreased stress-induced senescence in WI-38 human fibroblast cells [487] indicating an important role of PLA2R in cellular senescence induction [487]. For the premature aging disease, the Hutchinson-Gilford progeria syndrome, cellular senescence is induced by progerin. In this context, Griveau *et al.* reported that targeting PLA2R improves premature aging [488]. This author has shown that inhibition of farnesyl diphosphate synthase reduces senescence. Noteworthy, it has been demonstrated that increased expression of farnesyl diphosphate

synthase in progerin-expressing human fibroblasts is p53-mediated [488]. Interestingly, several studies described a reduced activity of the transphosphatidylase PLD, an enzyme that converts PtCho to phosphatidic acid and choline, in senescent human umbilical vein endothelial cells and human dermal fibroblasts [486, 489, 490].

Importantly, senescence induction by p53 re-activation is accompanied by major changes in energy metabolism. Within this thesis, MRS measurements of senescent H-Ras cells exhibited an increased PCr levels between day 3 and day 5 post senescence induction (**Figure 52**). The gradual increase in PCr between day 3 and day 5 after senescence induction was accompanied by an increase in creatine in both, senescent and control cells. Both metabolites, PCr and creatine, are essential in energy storage and transmission. Especially, Elevated PCr levels in senescent H-Ras cancer cells indicate a lower energy demand when compared to control cells. Similar results were reported by James *et al.* for human fibroblasts, where replicative senescence resulted in elevated PCr levels and increased creatine metabolism [491]. The authors attributed these metabolic changes to an altered energy storage and/or utilization in senescent cells [491]. Nevertheless, other studies exhibited a trend towards decreased PCr levels in replicative and oncogene-induced senescence in the human fibroblast cell line WI-38 [256]. Based on the data presented in this thesis, the high-resolution MR measurements indicated alterations in lactate levels in H-Ras cancer cells whereas no differences were determined with the MR-compatible cell perfusion system. However, other studies on human fibroblasts reported a decreased lactate level in replicative, oncogene-induced and etoposide-induced senescence, suggesting either reduced glycolysis or a switch in energy generation [256]. Furthermore, it has been demonstrated that the transcription factor p53 plays a key role in senescence [492]. In this context, Schwartzenberg-Bar-Yoseph *et al.* by applying p53 overexpression experiments demonstrated that p53 reduces the *Glut1* and *Glut4* gene expression and therefore antagonizes the glucose up-take in osteosarcoma-derived SaOS-2 and rhabdomyosarcoma-derived RD cells [493]. In addition, this effect was absent for mutated p53, suggesting that overexpression of wild type p53 modulates glucose metabolism in cancer cells by regulation of *Glut1* and *Glut4* gene expression [493]. Further, Wiley *et al.* reviewed several pathways by which p53 likely reduces glycolysis and favors mitochondrial respiration in senescent cells

[494].

In the present thesis, myo-inositol is another metabolite that is increased upon p53 re-activation in senescent H-Ras cancer cells. This result is in very good agreement with the data published by Koguchi *et al.* describing that ISYNA1 expression, a key enzyme for myo-inositol synthesis [495-497], is regulated by p53 activation [441]. The authors also showed that DNA damage in response to adriamycin treatment resulted in increased p53, ISYNA1 and myo-inositol levels in human HCT116 cells, whereas no change was observed in p53 deficient HCT116 cells [441]. These basic mechanistic findings might also explain the increase in myo-inositol in the p53 re-activation induced model of senescence applied in the presented dissertation.

In summary, a distinct metabolic profile of senescent H-Ras cancer cells could be identified in the here presented dissertation, including alterations in phospholipid and energy metabolism. Therefore, GPC and PCr might represent novel senescence biomarkers that should be further evaluated in various tumor models *in vitro* and *in vivo*.

6 Summary

Immunotherapy is a promising approach in cancer treatment. In recent years, several antibodies targeting immune checkpoint proteins have been approved and are now applied in clinical routine. Immune escape mechanisms as well as response biomarkers and resistance mechanisms of an immune checkpoint inhibitor therapy are of great interest and are subject to many research studies. The TME and its role during immunotherapies attracted special attention in recent years. Different factors in the TME including immune cell-derived IFN-γ and hypoxia induce expression of the checkpoint protein PD-L1 and thereby mediate T cell exhaustion or apoptosis.

In the first chapter of this thesis, the role of an acidic TME and IFN-γ on cancer cell PD-L1 expression and subsequent immune escape was studied. It is proposed that PD-L1 induction by an acidic tumor pH_e combined with IFN-γ represents an immune escape mechanism which can be targeted by an anti-PD-L1 mAb therapy. This conjoint acidosis- and IFN-γ-mediated PD-L1 induction was exclusively found in immunotherapy-responsive murine cancer cell lines. Therefore, it might serve as a biomarker to distinguish immunotherapy responders from non-responders. Further it could be shown that acidosis- and IFN-γ-induced PD-L1 is mediated by the expression and activation of the transcription factor STAT1. The translation of the *Stat1* mRNA was experimentally proven to be eIF4F-dependent, whereas the translation initiation complex eIF4F can be inhibited by silvestrol representing an additional therapeutic option. Most importantly, the *in vitro* findings on conjoint acidosis- and IFN-γ-mediated cancer cell PD-L1 expression could be confirmed *in vivo*. The tumor pH_e neutralization with sodium bicarbonate was proven *in vivo* by acidoCEST-MRI measurements in $MC38^{wt}$ tumors and IFN-γ-dependency of the immune escape was confirmed by IFN-$\gamma^{-/-}$ mice. In summary, conjoint IFN-γ- and acidosis-inducible cancer cell PD-L1 expression represents a novel immune escape mechanism and might display a biomarker for immunotherapy response.

In the second chapter, hypoxia which, besides acidosis and IFN-γ induces PD-L1 expression, was imaged non-invasively *in vivo*. Imaging tumor hypoxia by *in vivo* OI with reporter cancer cell lines did not prove to be suitable serving as a non-invasive surrogate marker for tumor PD-L1 expression. Short-lived tumor hypoxia neither correlated with tumor PD-L1 expression, nor with $CD3^+$ T cell infiltration.

In addition to tumor-resident immune cells, a systemic immune response including the lymphoid system is pivotal for anti-tumor immunity. Lymph nodes are secondary lymphoid organs and play an essential role in the anti-tumor immune response during a checkpoint inhibitor therapy. This underlines the importance of non-invasive *in vivo* imaging of TDLNs prior to lymphadenectomy. Therefore, in the third chapter of this thesis, different contrast agents of varying molecular weight were assessed for their suitability to detect TDLNs. Further, the non-invasive imaging technologies OI and PET/MRI were compared. In contrast to OI with Patent Blue V, which was only suitable for *ex vivo* identification of the accessory and proper axillary TDLNs, functional *in vivo* together with *ex vivo* [^{18}F]FDG-PET/MRI revealed the accessory axillary LN as the main TDLN of a *s.c.* MC38^{wt} tumor on the right shoulder of mice.

Due to the link between immune checkpoint inhibitor therapies and senescence, the final chapter of this thesis addressed the identification of cancer senescence metabolic biomarkers. Several anti-tumor therapies, as well as immune cell-derived cytokines which are released upon immunotherapy induce cancer cell senescence. Thus, potential biomarkers for senescence including GPC and PCr were successfully identified by ^{1}H MRS and must be further studied and evaluated in continuative pre-clinical *in vivo* studies.

In summary, within this thesis a so far unknown mechanism of immune escape by cancer cells was uncovered enabling the identification of anti-PD-1 or anti PD-L1 mAb immune checkpoint inhibitor responsive patients. Further non-invasive *in vivo* imaging modalities to identify the TDLNs were evaluated. Finally, metabolic studies on cancer senescence revealed several potential biomarkers of a cancer cell growth arrest.

7 Zusammenfassung

Die Immuntherapie ist ein neuer und vielversprechender Ansatz in der Krebstherapie. In den letzten Jahren wurden mehrere Immuncheckpoint-Proteine blockierende Antikörper zugelassen und werden nunmehr in der klinischen Routine eingesetzt. Immunevasionsmechanismen, Biomarker für ein Therapieansprechen sowie Resistenzmechanismen einer Immuncheckpoint-Inhibitor-Therapie sind von großem Interesse und Gegenstand umfangreicher Studien. Das Tumormikroenvironment und seine Rolle im Rahmen von Immuntherapien haben in den letzten Jahren große Aufmerksamkeit erfahren. Verschiedene Faktoren des Tumormikroenvironments, wie von Immunzellen sekretiertes IFN-γ sowie Tumorhypoxie, induzieren die Expression des Immuncheckpoint-Proteins PD-L1 und vermitteln dadurch die Erschöpfung oder Apoptose von T-Zellen.

Im ersten Kapitel dieser Forschungsarbeit wurde der Effekt eines angesäuerten (azidotischen) Tumormikroenvironments sowie von IFN-γ auf die Expression von PD-L1 auf Krebszellen und die hierdurch vermittelte Immunevasion untersucht. Im Rahmen dieser Arbeit konnte erfolgreich gezeigt werden, dass die Induktion der PD-L1 Genexpression mittels eines erniedrigten (sauren) tumoralen pH_e-Werts in Kombination mit von Immunzellen sezernierten IFN-γ einen *Immune Escape* Mechanismus darstellt, mit dessen Hilfe sich der Tumor der Kontrolle des Immunsystems entzieht. Diesem *Immune Escape* Mechanismus wirkt eine anti-PD-L1 Antikörpertherapie erfolgreich entgegen. Diese, durch Azidose- und IFN-γ-vermittelte Steigerung der PD-L1 Expression wurde ausschließlich in Krebszelllinien identifiziert die empfänglich für eine Immuncheckpoint-Inhibitor-Therapie sind. Entsprechend könnte die Erfassung der Azidose- und IFN-γ-vermittelten Steigerung der PD-L1 Expression als Biomarker dienen, um ein Ansprechen auf eine anti-PD-1 oder anti-PD-L1 Antikörper basierte Immuncheckpoint-Inhibitor-Therapie vorherzusagen. Weiterhin konnte gezeigt werden, dass die Azidose- und IFN-γ-induzierte PD-L1 Expression durch die gesteigerte Expression und Aktivierung des Transkriptionsfaktors STAT1 vermittelt wird und die Translation der *Stat1*-mRNA eIF4F-abhängig ist. Die Hemmung des Translationsinitiationskomplexes eIF4F durch Silvestrol stellt folglich eine weitere therapeutische Interventionsmöglichkeit dar. Die *in vitro* Ergebnisse zur Azidose-

und IFN-γ-vermittelten Induktion von PD-L1 Expression auf Krebszellen konnten zudem erfolgreich im Rahmen von umfangreichen *in vivo* Studien bestätigt werden. Die pH_e-Wert Neutralisierung des Tumors mit Natriumhydrogencarbonat konnte mit Hilfe nicht-invasiver *in vivo* acidoCEST-MRI-Messungen von $MC38^{wt}$-Tumoren bestätigt werden. Die IFN-γ-Abhängigkeit der Azidose- und IFN-γ-induzierten Immunevasion wurde mittels $IFN^{-/-}$ Mäusen experimentell belegt. Zusammenfassend lässt sich sagen, dass die Azidose- und IFN-γ-induzierte PD-L1 Expression auf Krebszellen einen neuartigen bisher nicht beschriebenen Immunevasionsmechanismus repräsentiert und folglich einen potenten Biomarker, der in der Lage ist, das Ansprechen auf eine die PD-1/PD-L1-Achse blockierende Immuncheckpoint-Inhibitor-Therapie vorherzusagen.

Im zweiten Kapitel wurde die Tumorhypoxie, welche neben Azidose und IFN-γ ebenfalls die Expression von PD-L1 auf Krebszellen induziert, mittels Bildgebung *in vivo* dargestellt. Die bildgebende Darstellung der Tumorhypoxie unter Zuhilfenahme der optischen *in vivo* Bildgebung und von Reporter-Krebszelllinien stellte jedoch keinen geeigneten Surrogat-Marker zur nicht-invasiven Visualisierung einer gesteigerten Tumor-PD-L1-Expression dar. Die kurzlebige Tumorhypoxie korrelierte weder mit der PD-L1 Expression noch mit der Infiltration von $CD3^+$ T-Zellen.

Zusätzlich zu den intra-tumoralen Immunzellen ist eine systemische Immunantwort unter Beteiligung der primär und sekundär lymphatischen Organe entscheidend für die anti-tumorale Immunität. Lymphknoten gehören zu den sekundär lymphatischen Organen und sind maßgeblich für eine effiziente anti-tumorale Immunantwort während einer Immuncheckpoint-Inhibitor-Therapie verantwortlich. Dies unterstreicht die Bedeutung der nicht-invasiven *in vivo* Bildgebung zur sicheren Identifizierung der Tumor-drainierenden Lymphknoten vor Lymphadenektomie. Entsprechend wurden im Rahmen des dritten Kapitels dieser Arbeit verschiedene Kontrastmittel mit unterschiedlichem Molekulargewicht auf ihre Eignung zur Identifikation der Tumor-drainierenden Lymphknoten mittels zweier nicht-invasiver *in vivo* Bildgebungsverfahren, dem *Optical Imaging* und der PET/MR-Bildgebung evaluiert. Das Patent Blue V *Optical Imaging* ist lediglich für die *ex vivo* Identifikation der akzessorischen und axillären Tumor-drainierenden Lymphknoten qualifiziert. Im Gegensatz hierzu eignet sich die funktionelle [^{18}F]FDG-PET/MR Bildgebung sehr gut um die akzessorischen axillären

Lymphknoten als Tumor-drainierenden Lymphknoten eines *s.c.* MC38^{wt} Tumors an der rechten Schulter von Versuchsmäusen nicht-invasiv *in vivo* zu identifiziert.

Aufgrund des Zusammenhangs zwischen Immuncheckpoint-Inhibitor-Therapien und Seneszenz, befasste sich das letzte Kapitel dieser Forschungsarbeit mit der Identifizierung von metabolischen Biomarkern seneszenter Krebszellen. Verschiedene Krebstherapien sowie von aktivierten Immunzellen sekretierte Zytokine, wie TNF und IFN-γ, sind in der Lage Seneszenz der Krebszellen zu induzieren. Mittels ^{1}H MRS konnten erfolgreich potenzielle Seneszenzbiomarker, wie GPC und PCr identifiziert werden, welche im Rahmen weiterführender präklinischer *in vivo* Studien validiert werden müssen.

Zusammenfassend wurde im Rahmen dieser Arbeit ein bisher unbekannter Mechanismus der Immunevasion von Krebszellen beschrieben der die vorzeitige Identifikation von Therapieansprechern einer anti-PD-1 oder anti-PD-L1 Antikörper basierten Immuncheckpoint-Inhibitor-Therapie ermöglicht. Ferner wurden zwei etablierte bildgebenden Verfahren zur *in vivo* Identifizierung der Tumor-drainierenden Lymphknoten validiert und im Rahmen von Stoffwechselstudien zur Krebszellseneszenz mehrere, potenzielle Biomarker für den Wachstumsarrest von Krebszellen identifiziert.

8 Statement

Ich erkläre hiermit, dass ich die zur Promotion eingereichte Arbeit mit dem Titel „Role of Tumor Acidosis and Hypoxia in Immune Escape by IFN-γ-induced Transcriptional Induction of PD-L1 via the eIF4F Axis on Cancer Cells - Comparison of Imaging Technologies for Non-Invasive *In Vivo* Imaging of Tumor-Draining Lymph Nodes - Monitoring of Metabolic Alterations during Tumor Senescence by ^{1}H MRS" selbständig verfasst, nur die angegebenen Quellen und Hilfsmittel benutzt und wörtlich oder inhaltlich übernommene Stellen als solche gekennzeichnet habe. Ich erkläre, dass die Richtlinien zur Sicherung guter wissenschaftlicher Praxis der Universität Tübingen (Beschluss des Senats vom 25.05.2000) beachtet wurden. Ich versichere Eides statt, dass diese Angaben wahr sind und dass ich nichts verschwiegen habe. Mir ist bekannt, dass die falsche Abgabe einer Versicherung an Eides statt mit Freiheitsstrafe bis zu drei Jahren oder mit Geldstrafe bestraft wird.

Tübingen, 2021

8.1 Declaration of contributions

Murine tissue culture procedures (cancer cell culture, transfections, virus production, transductions, CRISP/Cas9 clonal expansion), molecular biology procedures (RNA isolation, cDNA synthesis, qRT-PCR analysis, flow cytometry, WB antibody selection, luciferase activity measurements), tumor induction, imaging procedures (PET, MRI, CP-MRI, OI) were performed by me. The *in silico* analysis was performed by me and the Animal Experiment Application required for *in vivo* experiments at the University of Tübingen were written by me. The general project idea and the project outline have been generated by me. Further I planned, analysed, prepared, and interpreted the data in this thesis.

Dr. Omelyan Trompak from the Department of Internal Medicine VIII, University Hospital Tübingen designed the gRNAs for the CRISP/Cas9-mediated knockouts. The WB analysis was performed by Natalie Herrmann at the Department of Preclinical Imaging and Radiopharmacy, University of Tübingen, Dr. Daniela Kramer at the Interfaculty Institute of Biochemistry, University of Tübingen and by Yelena Mironchik at the Department of Radiology and Radiological Science, The

Johns Hopkins University School of Medicine.

Human cell culture of HCA-7 colony 29 cells for qRT-PCR and WB analysis was performed by Valentina Bucher. She was a master intern enrolled in Molecular Medicine at the University of Tübingen and was supervised by me. Respectively, experiments were designed and planned by me. Reagents like siRNAs, qRT-PCR primers as well as WB antibodies were furthermore selected by me.

Optical, PET and MRI measurements were performed by me, partially supported by technical staff at the Department of Preclinical Imaging and Radiopharmacy, University of Tübingen as well as Dr. Balaji Krishnamachary and Dr. Jesus Pacheco Torres at the Department of Radiology and Radiological Science, The Johns Hopkins University School of Medicine. acidoCEST-MR measurements were performed by Dr. Sabrina Hoffmann and analyzed by Dr. Sanhita Sinharay and Prof. Dr. Mark D. Pagel from the Department of Cancer Systems Imaging, MD Anderson Cancer Center. MRI and MRS measurements with the MR-compatible cell perfusion system were performed and analyzed by me and approved by Dr. Jesus Pacheco Torres.

[^{18}F]FDG synthesis was performed by staff of the Radiopharmacy, Department of Preclinical Imaging and Radiopharmacy, University of Tübingen.

NMR measurements were performed and analyzed by Dr. Jesus Pacheco Torres and Dr. Christoph Trautwein at the Department of Preclinical Imaging and Radiopharmacy, University of Tübingen.

Histological staining was performed by Birgit Fehrenbacher at the Department of Dermatology, University of Tübingen as well as Dr. Irene Gonzalez-Menendez and Prof. Dr. Leticia Quintanilla-Fend at the Department of Pathology, University of Tübingen.

I would like to thank Dr. Manfred Kneilling for critical proofreading of this dissertation. Further, I would like to thank Dr. Jesus Pacheco Torres for proofreading the chapters 1.4, 3.2.11, 3.2.12, 4.4 and 5.1.3; Dr. Balaji Krishnamachary for proofreading the chapters 1.5.1, 3.2.4, 3.2.10, 4.2 and 5.2; Dr. Julia Mannheim for proofreading the chapters 1.5.2 and 1.5.3; Dr. Nicolas Bézière for proofreading the chapter 1.5.1.

All contributions to this dissertation are further indicated in the **Materials and Methods** section.

9 List of Publications

9.1 Publications in scientific journals

Sonanini D, Griessinger CM, Schörg BF, **Knopf P**, Dittmann K, Röcken M, Pichler BJ, Kneilling M. Low-dose total body irradiation facilitates antitumoral Th1 immune response. Theranostics. 2021 Jun 16;11(16):7700-7714.

Seitz CM, Schroeder S, **Knopf P**, Krahl AC, Hau J, Schleicher S, Martella M, Quintanilla-Martinez L, Kneilling M, Pichler B, Lang P, Atar D, Schilbach K, Handgretinger R, Schlegel P. GD2-targeted chimeric antigen receptor T cells prevent metastasis formation by elimination of breast cancer stem-like cells. Oncoimmunology. 2019 Nov 7;9(1):1683345.

Schwenck J, Maurer A, Fehrenbacher B, Mehling R, **Knopf P**, Mucha N, Haupt D, Fuchs K, Griessinger CM, Bukala D, Holstein J, Schaller M, Menendez IG, Ghoreschi K, Quintanilla-Martinez L, Gütschow M, Laufer S, Reinheckel T, Röcken M, Kalbacher H, Pichler BJ, Kneilling M. Cysteine-type cathepsins promote the effector phase of acute cutaneous delayed-type hypersensitivity reactions. Theranostics. 2019 May 31;9(13):3903-3917.

Fransen MF, Schoonderwoerd M, **Knopf P**, Camps MG, Hawinkels LJ, Kneilling M, van Hall T, Ossendorp F. Tumor-draining lymph nodes are pivotal in PD-1/PD-L1 checkpoint therapy. JCI Insight. 2018 Dec 6;3(23):e124507.

9.2 Contributions to scientific meetings

9.2.1 Oral presentation at scientific meetings

Knopf P, Hoffmann SHL, Hermann N, Maurer A, Bucher V, Poxleitner M, Tako B, Sonanini D, Sinharay S, Fehrenbacher B, Gonzalez-Menendez I, Kramer D, Schaller M, Quintanilla-Martinez L, Schulze-Osthoff K, Pagel MD, Ferreira Martins A, Fransen MF, Pichler BJ, Ghoreschi K, Kneilling M. Acidosis promotes immune escape by interferon-γ-induced transcriptional induction of PD-L1 via the eIF4F-STAT1-PD-L1 axis on cancer cells. Working Group Dermatological Research (Arbeitsgemeinschaft Dermatologische Forschung), 2021, March 04-06, virtual.

Knopf P, Mucha N, Maurer A, Poxleitner M, Trompak O, Tako B, Harant M, Zender L, Fransen MF, Gonzalez-Menendez I, Krishnamachary B, Fehrenbacher B, Kramer D, Quintanilla-Martinez L, Schulze-Osthoff K, Bhujwalla ZM, Ghoreschi K, Pichler BJ, Kneilling M. Tumor immune escape via tumor hypoxia and acidosis mediated PD-L1 expression as a prognostic biomarker. TOPIM-Imaging Immunity Conference, 2020, January 12-17, Les Houches, France.

9.2.2 Poster presentation at scientific meetings

Knopf P, Pacheco-Torres J, Wildes F, Trautwein C, Zhou B, Krishnamachary B, Zender L, Pichler BJ, Bhujwalla ZM. Investigating metabolism and invasion of hepatocellular carcinoma cells during p53 re-activation induced senescence using a MR-compatible cell perfusion system. European Molecular Imaging Meeting (EMIM), 2019, March 19-22, Glasgow, UK.

Knopf P, Pacheco-Torres J, Wildes F, Trautwein C, Zhou B, Pichler BJ, Bhujwalla ZM. Investigating metabolism and invasion of hepatocellular carcinoma cells during p53 re-activation induced senescence. World Molecular Imaging Congress (WMIC), 2018, September 12-15, Seattle, USA.

Knopf P, Schörg B, Mehling R, Sonanini D, Altmeyer N, Haupt D, Aidone S, Griessinger CM, Pichler BJ, Kneilling M. *In vivo* bioluminescence imaging (BLI) of the sites of immune cell action and ex vivo characterization of the tumor microenvironment (TME) during a combined T cell, anti-PD-L1 and anti-LAG-3 based cancer immunotherapy. Cancer Immunotherapy (CIMT) Meeting, 2017, September 06-09, Mainz, Germany.

10 References

1. Heron, M., *Deaths: Leading Causes for 2017.* Natl Vital Stat Rep, 2019. 68(6): p. 1-77.
2. Mullard, A., *2018 FDA drug approvals.* Nat Rev Drug Discov, 2019. 18(2): p. 85-89.
3. Vogelstein, B. and K.W. Kinzler, *The multistep nature of cancer.* Trends Genet, 1993. 9(4): p. 138-41.
4. Hanahan, D. and R.A. Weinberg, *Hallmarks of cancer: the next generation.* cell, 2011. 144(5): p. 646-674.
5. Hanahan, D. and R.A. Weinberg, *The hallmarks of cancer.* Cell, 2000. 100(1): p. 57-70.
6. Pylayeva-Gupta, Y., E. Grabocka, and D. Bar-Sagi, *RAS oncogenes: weaving a tumorigenic web.* Nature Reviews Cancer, 2011. 11(11): p. 761-774.
7. Sharma, S.V., et al., *Epidermal growth factor receptor mutations in lung cancer.* Nature Reviews Cancer, 2007. 7(3): p. 169-181.
8. Chen, H., H. Liu, and G. Qing, *Targeting oncogenic Myc as a strategy for cancer treatment.* Signal Transduction and Targeted Therapy, 2018. 3(1): p. 5.
9. Nilsson, J.A. and J.L. Cleveland, *Myc pathways provoking cell suicide and cancer.* Oncogene, 2003. 22(56): p. 9007-9021.
10. Mantovani, F., L. Collavin, and G. Del Sal, *Mutant p53 as a guardian of the cancer cell.* Cell Death & Differentiation, 2019. 26(2): p. 199-212.
11. Bates, S.E., et al., *Expression of transforming growth factor alpha and its messenger ribonucleic acid in human breast cancer: its regulation by estrogen and its possible functional significance.* Mol Endocrinol, 1988. 2(6): p. 543-55.
12. Humphreys, R.C. and L. Hennighausen, *Transforming growth factor alpha and mouse models of human breast cancer.* Oncogene, 2000. 19(8): p. 1085-1091.
13. Hayflick, L., *Mortality and immortality at the cellular level. A review.* Biochemistry (Mosc), 1997. 62(11): p. 1180-90.
14. Simons, M., E. Gordon, and L. Claesson-Welsh, *Mechanisms and regulation of endothelial VEGF receptor signalling.* Nature Reviews Molecular Cell Biology, 2016. 17(10): p. 611-625.
15. Goel, H.L. and A.M. Mercurio, *VEGF targets the tumour cell.* Nature Reviews Cancer, 2013. 13(12): p. 871-882.
16. Warburg, O., *On the origin of cancer cells.* Science, 1956. 123(3191): p. 309-14.
17. House, S.W., et al., *On respiratory impairment in cancer cells.* Science, 1956. 124(3215): p. 267-272.
18. Salk, J.J., E.J. Fox, and L.A. Loeb, *Mutational heterogeneity in human cancers: origin and consequences.* Annu Rev Pathol, 2010. 5: p. 51-75.
19. Negrini, S., V.G. Gorgoulis, and T.D. Halazonetis, *Genomic instability--an evolving hallmark of cancer.* Nat Rev Mol Cell Biol, 2010. 11(3): p. 220-8.
20. McGranahan, N., et al., *Clonal neoantigens elicit T cell immunoreactivity and sensitivity to immune checkpoint blockade.* Science, 2016. 351(6280): p. 1463-9.
21. Mardis, E.R., *Neoantigens and genome instability: impact on immunogenomic phenotypes and immunotherapy response.* Genome Medicine, 2019. 11(1): p. 71.
22. Murphy, K.M., *Janeway's Immunobiology*. 2011: Taylor & Francis Group.
23. O'Donnell, J.S., M.W.L. Teng, and M.J. Smyth, *Cancer immunoediting and resistance to T cell-based immunotherapy.* Nature Reviews Clinical Oncology, 2019. 16(3): p. 151-167.
24. Gonzalez, H., C. Hagerling, and Z. Werb, *Roles of the immune system in cancer:*

from tumor initiation to metastatic progression. Genes & development, 2018. 32(19-20): p. 1267-1284.
25. Mantovani, A., et al., *Tumour-associated macrophages as treatment targets in oncology.* Nature Reviews Clinical Oncology, 2017. 14(7): p. 399-416.
26. Wu, L., et al., *Tumor-Associated Neutrophils in Cancer: Going Pro.* Cancers, 2019. 11(4): p. 564.
27. Aarts, C.E.M. and T.W. Kuijpers, *Neutrophils as myeloid-derived suppressor cells.* Eur J Clin Invest, 2018. 48 Suppl 2: p. e12989.
28. Aarts, C.E.M., et al., *Activated neutrophils exert myeloid-derived suppressor cell activity damaging T cells beyond repair.* Blood advances, 2019. 3(22): p. 3562-3574.
29. Kabelitz, D., et al., *Cancer immunotherapy with γδ T cells: many paths ahead of us.* Cellular & Molecular Immunology, 2020.
30. Cerezo, M., et al., *Translational control of tumor immune escape via the eIF4F-STAT1-PD-L1 axis in melanoma.* Nat Med, 2018. 24(12): p. 1877-1886.
31. Wang, X., et al., *Inflammatory cytokines IL-17 and TNF-alpha up-regulate PD-L1 expression in human prostate and colon cancer cells.* Immunol Lett, 2017. 184: p. 7-14.
32. Balkwill, F.R., M. Capasso, and T. Hagemann, *The tumor microenvironment at a glance.* Journal of Cell Science, 2012. 125(23): p. 5591-5596.
33. Hanahan, D. and R.A. Weinberg, *Biological hallmarks of cancer.* Holland-Frei Cancer Medicine, 2016: p. 1-10.
34. Kalluri, R., *The biology and function of fibroblasts in cancer.* Nat Rev Cancer, 2016. 16(9): p. 582-98.
35. Sahai, E., et al., *A framework for advancing our understanding of cancer-associated fibroblasts.* Nat Rev Cancer, 2020. 20(3): p. 174-186.
36. Williams, J.B., et al., *Tumor heterogeneity and clonal cooperation influence the immune selection of IFN-gamma-signaling mutant cancer cells.* Nat Commun, 2020. 11(1): p. 602.
37. Yang, J., et al., *Guidelines and definitions for research on epithelial–mesenchymal transition.* Nature Reviews Molecular Cell Biology, 2020. 21(6): p. 341-352.
38. Hardin, H., et al., *The evolving concept of cancer stem-like cells in thyroid cancer and other solid tumors.* Laboratory Investigation, 2017. 97(10): p. 1142-1151.
39. De Palma, M., D. Biziato, and T.V. Petrova, *Microenvironmental regulation of tumour angiogenesis.* Nature Reviews Cancer, 2017. 17(8): p. 457-474.
40. Carmeliet, P. and R.K. Jain, *Molecular mechanisms and clinical applications of angiogenesis.* Nature, 2011. 473(7347): p. 298-307.
41. Stacker, S.A., et al., *Lymphangiogenesis and lymphatic vessel remodelling in cancer.* Nature Reviews Cancer, 2014. 14(3): p. 159-172.
42. Nazareth, M.R., et al., *Characterization of human lung tumor-associated fibroblasts and their ability to modulate the activation of tumor-associated T cells.* J Immunol, 2007. 178(9): p. 5552-62.
43. Jayasingam, S.D., et al., *Evaluating the Polarization of Tumor-Associated Macrophages Into M1 and M2 Phenotypes in Human Cancer Tissue: Technicalities and Challenges in Routine Clinical Practice.* Frontiers in oncology, 2020. 9: p. 1512-1512.
44. Administration, U.F.a.D., *FDA approves Keytruda for advanced melanoma, First PD-1 blocking drug to receive agency approval.* 2014, September 4.
45. Weber, J.S., K.C. Kähler, and A. Hauschild, *Management of immune-related adverse events and kinetics of response with ipilimumab.* Journal of Clinical Oncology, 2012. 30(21): p. 2691-2697.

46. Corbet, C. and O. Feron, *Tumour acidosis: from the passenger to the driver's seat.* Nat Rev Cancer, 2017. 17(10): p. 577-593.
47. McKeown, S.R., *Defining normoxia, physoxia and hypoxia in tumours-implications for treatment response.* Br J Radiol, 2014. 87(1035): p. 20130676.
48. Hockel, M. and P. Vaupel, *Tumor hypoxia: definitions and current clinical, biologic, and molecular aspects.* J Natl Cancer Inst, 2001. 93(4): p. 266-76.
49. Semenza, G.L., *Involvement of hypoxia-inducible factor 1 in human cancer.* Intern Med, 2002. 41(2): p. 79-83.
50. Semenza, G., *Signal transduction to hypoxia-inducible factor 1.* Biochem Pharmacol, 2002. 64(5-6): p. 993-8.
51. Krishnamachary, B., et al., *Regulation of colon carcinoma cell invasion by hypoxia-inducible factor 1.* Cancer Res, 2003. 63(5): p. 1138-43.
52. Hayashi, M., et al., *Induction of glucose transporter 1 expression through hypoxia-inducible factor 1alpha under hypoxic conditions in trophoblast-derived cells.* J Endocrinol, 2004. 183(1): p. 145-54.
53. Kay, H.H., S. Zhu, and S. Tsoi, *Hypoxia and lactate production in trophoblast cells.* Placenta, 2007. 28(8-9): p. 854-60.
54. Ullah, M.S., A.J. Davies, and A.P. Halestrap, *The plasma membrane lactate transporter MCT4, but not MCT1, is up-regulated by hypoxia through a HIF-1alpha-dependent mechanism.* J Biol Chem, 2006. 281(14): p. 9030-7.
55. Vander Heiden, M.G., L.C. Cantley, and C.B. Thompson, *Understanding the Warburg effect: the metabolic requirements of cell proliferation.* Science, 2009. 324(5930): p. 1029-33.
56. Webb, B.A., et al., *Dysregulated pH: a perfect storm for cancer progression.* Nature Reviews Cancer, 2011. 11(9): p. 671-677.
57. Gillies, R.J., et al., *MRI of the tumor microenvironment.* J Magn Reson Imaging, 2002. 16(4): p. 430-50.
58. Li, Y., et al., *Catalysis and pH control by membrane-associated carbonic anhydrase IX in MDA-MB-231 breast cancer cells.* J Biol Chem, 2011. 286(18): p. 15789-96.
59. Peppicelli, S., F. Bianchini, and L. Calorini, *Extracellular acidity, a "reappreciated" trait of tumor environment driving malignancy: perspectives in diagnosis and therapy.* Cancer Metastasis Rev, 2014. 33(2-3): p. 823-32.
60. Peppicelli, S., et al., *Extracellular acidity strengthens mesenchymal stem cells to promote melanoma progression.* Cell Cycle, 2015. 14(19): p. 3088-100.
61. Parks, S.K., J. Chiche, and J. Pouyssegur, *Disrupting proton dynamics and energy metabolism for cancer therapy.* Nat Rev Cancer, 2013. 13(9): p. 611-23.
62. Riemann, A., et al., *Acidosis Promotes Metastasis Formation by Enhancing Tumor Cell Motility.* Adv Exp Med Biol, 2016. 876: p. 215-220.
63. Dagher, R., et al., *Approval summary: imatinib mesylate in the treatment of metastatic and/or unresectable malignant gastrointestinal stromal tumors.* Clin Cancer Res, 2002. 8(10): p. 3034-8.
64. Parkkila, S., et al., *The protein tyrosine kinase inhibitors imatinib and nilotinib strongly inhibit several mammalian alpha-carbonic anhydrase isoforms.* Bioorg Med Chem Lett, 2009. 19(15): p. 4102-6.
65. Administration, U.F.a.D., *Tasigna Receives US Approval Providing New Hope to Chronic Myeloid Leukemia Patients with Resistance or Intolerance to Existing Therapies.* 2007, October 29.
66. ClinicalTrials.gov, U.N.L.o.M., *Effect of G17DT in Patients With Stage II/III Colorectal Cancer (CC5) ClinicalTrials.gov Identifier: NCT02518373.* 2015, August 7.

67. Strand, D.S., D. Kim, and D.A. Peura, *25 Years of Proton Pump Inhibitors: A Comprehensive Review.* Gut Liver, 2017. 11(1): p. 27-37.
68. ClinicalTrial.gov, U.N.L.o.M., *A Phase I Trial of AZD3965 in Patients With Advanced Cancer. ClinicalTrials.gov Identifier: NCT01791595* 2019, October 14.
69. Hernandez, A., et al., *Intracellular proton pumps as targets in chemotherapy: V-ATPases and cancer.* Curr Pharm Des, 2012. 18(10): p. 1383-94.
70. Bola, B.M., et al., *Inhibition of monocarboxylate transporter-1 (MCT1) by AZD3965 enhances radiosensitivity by reducing lactate transport.* Mol Cancer Ther, 2014. 13(12): p. 2805-16.
71. Matthews, H., M. Ranson, and M.J. Kelso, *Anti-tumour/metastasis effects of the potassium-sparing diuretic amiloride: an orally active anti-cancer drug waiting for its call-of-duty?* Int J Cancer, 2011. 129(9): p. 2051-61.
72. Rojas, E.A., et al., *Amiloride, An Old Diuretic Drug, Is a Potential Therapeutic Agent for Multiple Myeloma.* Clin Cancer Res, 2017. 23(21): p. 6602-6615.
73. Sparks, R.L., et al., *Effects of amiloride on tumor growth and intracellular element content of tumor cells in vivo.* Cancer Res, 1983. 43(1): p. 73-7.
74. Hulikova, A., et al., *Intracellular carbonic anhydrase activity sensitizes cancer cell pH signaling to dynamic changes in CO2 partial pressure.* J Biol Chem, 2014. 289(37): p. 25418-30.
75. Neri, D. and C.T. Supuran, *Interfering with pH regulation in tumours as a therapeutic strategy.* Nat Rev Drug Discov, 2011. 10(10): p. 767-77.
76. Robey, I.F., et al., *Bicarbonate increases tumor pH and inhibits spontaneous metastases.* Cancer Res, 2009. 69(6): p. 2260-8.
77. Pilon-Thomas, S., et al., *Neutralization of Tumor Acidity Improves Antitumor Responses to Immunotherapy.* Cancer Res, 2016. 76(6): p. 1381-90.
78. Faes, S., et al., *Acidic tumor microenvironment abrogates the efficacy of mTORC1 inhibitors.* Mol Cancer, 2016. 15(1): p. 78.
79. Robey, I., A. Lopez, and D. Roe, *Safety and Tolerability of Long-Term Sodium Bicarbonate Consumption in Cancer Care.* J Integr Oncol, 2015. 4(128): p. 2.
80. ClinicalTrial.gov, U.N.L.o.M., *Extended Use of Sodium Bicarbonate in Patients With Cancer. ClinicalTrials.gov Identifier: NCT02531919.* 2016, April 13.
81. Raghunand, N., et al., *Enhancement of chemotherapy by manipulation of tumour pH.* Br J Cancer, 1999. 80(7): p. 1005-11.
82. Raghunand, N. and R.J. Gillies, *pH and chemotherapy.* Novartis Found Symp, 2001. 240: p. 199-211; discussion 265-8.
83. El-Kenawi, A., et al., *Acidity promotes tumour progression by altering macrophage phenotype in prostate cancer.* Br J Cancer, 2019. 121(7): p. 556-566.
84. Leung, J.M., et al., *Safety and efficacy of intravenous Carbicarb in patients undergoing surgery: comparison with sodium bicarbonate in the treatment of mild metabolic acidosis. SPI Research Group. Study of Perioperative Ischemia.* Crit Care Med, 1994. 22(10): p. 1540-9.
85. Beloueche-Babari, M., et al., *Monocarboxylate transporter 1 blockade with AZD3965 inhibits lipid biosynthesis and increases tumour immune cell infiltration.* British Journal of Cancer, 2020. 122(6): p. 895-903.
86. Calcinotto, A., et al., *Modulation of microenvironment acidity reverses anergy in human and murine tumor-infiltrating T lymphocytes.* Cancer Res, 2012. 72(11): p. 2746-56.
87. Selleri, S., et al., *Human mesenchymal stromal cell-secreted lactate induces M2-macrophage differentiation by metabolic reprogramming.* Oncotarget, 2016. 7(21): p. 30193-210.
88. Colegio, O.R., et al., *Functional polarization of tumour-associated macrophages*

by tumour-derived lactic acid. Nature, 2014. 513(7519): p. 559-63.
89. Muller, B., B. Fischer, and W. Kreutz, *An acidic microenvironment impairs the generation of non-major histocompatibility complex-restricted killer cells.* Immunology, 2000. 99(3): p. 375-84.
90. Husain, Z., et al., *Tumor-derived lactate modifies antitumor immune response: effect on myeloid-derived suppressor cells and NK cells.* J Immunol, 2013. 191(3): p. 1486-95.
91. Potzl, J., et al., *Reversal of tumor acidosis by systemic buffering reactivates NK cells to express IFN-gamma and induces NK cell-dependent lymphoma control without other immunotherapies.* Int J Cancer, 2017. 140(9): p. 2125-2133.
92. Huber, V., et al., *Cancer acidity: An ultimate frontier of tumor immune escape and a novel target of immunomodulation.* Semin Cancer Biol, 2017. 43: p. 74-89.
93. Vermeulen, M., et al., *Acidosis improves uptake of antigens and MHC class I-restricted presentation by dendritic cells.* J Immunol, 2004. 172(5): p. 3196-204.
94. Martinez, D., et al., *Extracellular acidosis triggers the maturation of human dendritic cells and the production of IL-12.* J Immunol, 2007. 179(3): p. 1950-9.
95. Erra Diaz, F., et al., *Extracellular Acidosis and mTOR Inhibition Drive the Differentiation of Human Monocyte-Derived Dendritic Cells.* Cell Rep, 2020. 31(5): p. 107613.
96. Fischer, K., et al., *Inhibitory effect of tumor cell-derived lactic acid on human T cells.* Blood, 2007. 109(9): p. 3812-9.
97. Brand, A., et al., *LDHA-Associated Lactic Acid Production Blunts Tumor Immunosurveillance by T and NK Cells.* Cell Metab, 2016. 24(5): p. 657-671.
98. Pardoll, D.M., *The blockade of immune checkpoints in cancer immunotherapy.* Nature Reviews Cancer, 2012. 12(4): p. 252-264.
99. Croft, M., et al., *The significance of OX40 and OX40L to T-cell biology and immune disease.* Immunological reviews, 2009. 229(1): p. 173-191.
100. Chambers, C.A., et al., *CTLA-4-mediated inhibition in regulation of T cell responses: mechanisms and manipulation in tumor immunotherapy.* Annu Rev Immunol, 2001. 19: p. 565-94.
101. Leach, D.R., M.F. Krummel, and J.P. Allison, *Enhancement of antitumor immunity by CTLA-4 blockade.* Science, 1996. 271(5256): p. 1734-6.
102. Walunas, T.L., et al., *CTLA-4 can function as a negative regulator of T cell activation.* Immunity, 1994. 1(5): p. 405-13.
103. Linsley, P.S., et al., *Human B7-1 (CD80) and B7-2 (CD86) bind with similar avidities but distinct kinetics to CD28 and CTLA-4 receptors.* Immunity, 1994. 1(9): p. 793-801.
104. Sansom, D.M., *CD28, CTLA-4 and their ligands: who does what and to whom?* Immunology, 2000. 101(2): p. 169-77.
105. Ville, S., et al., *Co-Stimulatory Blockade of the CD28/CD80-86/CTLA-4 Balance in Transplantation: Impact on Memory T Cells?* Front Immunol, 2015. 6: p. 411.
106. Barnes, M.J., et al., *CTLA-4 promotes Foxp3 induction and regulatory T cell accumulation in the intestinal lamina propria.* Mucosal Immunol, 2013. 6(2): p. 324-34.
107. Peggs, K.S., et al., *Blockade of CTLA-4 on both effector and regulatory T cell compartments contributes to the antitumor activity of anti-CTLA-4 antibodies.* J Exp Med, 2009. 206(8): p. 1717-25.
108. Walker, L.S., *Treg and CTLA-4: two intertwining pathways to immune tolerance.* J Autoimmun, 2013. 45(100): p. 49-57.
109. Sharpe, A.H. and K.E. Pauken, *The diverse functions of the PD1 inhibitory pathway.* Nat Rev Immunol, 2018. 18(3): p. 153-167.

110. Ahmadzadeh, M., et al., *Tumor antigen-specific CD8 T cells infiltrating the tumor express high levels of PD-1 and are functionally impaired.* Blood, 2009. 114(8): p. 1537-44.
111. Ma, J., et al., *PD1Hi CD8+ T cells correlate with exhausted signature and poor clinical outcome in hepatocellular carcinoma.* Journal for ImmunoTherapy of Cancer, 2019. 7(1): p. 331.
112. Mbongue, J.C., et al., *The Role of Indoleamine 2, 3-Dioxygenase in Immune Suppression and Autoimmunity.* Vaccines, 2015. 3(3): p. 703-729.
113. Mellor, A.L., et al., *Cells expressing indoleamine 2,3-dioxygenase inhibit T cell responses.* J Immunol, 2002. 168(8): p. 3771-6.
114. Munder, M., et al., *Suppression of T-cell functions by human granulocyte arginase.* Blood, 2006. 108(5): p. 1627-34.
115. Ledford, H., *Melanoma drug wins US approval.* Nature, 2011. 471(7340): p. 561-561.
116. Wei, S.C., C.R. Duffy, and J.P. Allison, *Fundamental Mechanisms of Immune Checkpoint Blockade Therapy.* Cancer Discov, 2018. 8(9): p. 1069-1086.
117. Darvin, P., et al., *Immune checkpoint inhibitors: recent progress and potential biomarkers.* Exp Mol Med, 2018. 50(12): p. 1-11.
118. Oh, D.Y., et al., *Immune Toxicities Elicted by CTLA-4 Blockade in Cancer Patients Are Associated with Early Diversification of the T-cell Repertoire.* Cancer Research, 2017. 77(6): p. 1322-1330.
119. Spiers, L., N. Coupe, and M. Payne, *Toxicities associated with checkpoint inhibitors-an overview.* Rheumatology (Oxford, England), 2019. 58(Suppl 7): p. vii7-vii16.
120. Tivol, E.A., et al., *Loss of CTLA-4 leads to massive lymphoproliferation and fatal multiorgan tissue destruction, revealing a critical negative regulatory role of CTLA-4.* Immunity, 1995. 3(5): p. 541-7.
121. Waterhouse, P., et al., *Lymphoproliferative disorders with early lethality in mice deficient in Ctla-4.* Science, 1995. 270(5238): p. 985-8.
122. Latchman, Y.E., et al., *PD-L1-deficient mice show that PD-L1 on T cells, antigen-presenting cells, and host tissues negatively regulates T cells.* Proceedings of the National Academy of Sciences of the United States of America, 2004. 101(29): p. 10691-10696.
123. Nishimura, H., et al., *Immunological studies on PD-1 deficient mice: implication of PD-1 as a negative regulator for B cell responses.* Int Immunol, 1998. 10(10): p. 1563-72.
124. Garon, E.B., et al., *Pembrolizumab for the treatment of non–small-cell lung cancer.* New England Journal of Medicine, 2015. 372(21): p. 2018-2028.
125. Larkin, J., et al., *Combined nivolumab and ipilimumab or monotherapy in untreated melanoma.* New England journal of medicine, 2015. 373(1): p. 23-34.
126. Havel, J.J., D. Chowell, and T.A. Chan, *The evolving landscape of biomarkers for checkpoint inhibitor immunotherapy.* Nat Rev Cancer, 2019. 19(3): p. 133-150.
127. Le, D.T., et al., *Mismatch repair deficiency predicts response of solid tumors to PD-1 blockade.* Science, 2017. 357(6349): p. 409-413.
128. Le, D.T., et al., *PD-1 Blockade in Tumors with Mismatch-Repair Deficiency.* N Engl J Med, 2015. 372(26): p. 2509-20.
129. Ishida, Y., et al., *Induced expression of PD-1, a novel member of the immunoglobulin gene superfamily, upon programmed cell death.* Embo j, 1992. 11(11): p. 3887-95.
130. Ledford, H., H. Else, and M. Warren, *Cancer immunologists scoop medicine Nobel prize.* Nature, 2018. 562(7725): p. 20-21.

131. Tashiro, K., et al., *Signal sequence trap: a cloning strategy for secreted proteins and type I membrane proteins.* Science, 1993. 261(5121): p. 600-3.
132. Freeman, G.J., et al., *Engagement of the PD-1 immunoinhibitory receptor by a novel B7 family member leads to negative regulation of lymphocyte activation.* J Exp Med, 2000. 192(7): p. 1027-34.
133. Carter, L., et al., *PD-1:PD-L inhibitory pathway affects both CD4(+) and CD8(+) T cells and is overcome by IL-2.* Eur J Immunol, 2002. 32(3): p. 634-43.
134. Raedler, L.A., *Keytruda (Pembrolizumab): First PD-1 Inhibitor Approved for Previously Treated Unresectable or Metastatic Melanoma.* Am Health Drug Benefits, 2015. 8(Spec Feature): p. 96-100.
135. Administration, U.F.a.D. *FDA approves new, targeted treatment for bladder cancer*. 2016, May 18; Available from: https://www.fda.gov/news-events/press-announcements/fda-approves-new-targeted-treatment-bladder-cancer.
136. George, J., et al., *Genomic Amplification of CD274 (PD-L1) in Small-Cell Lung Cancer.* Clin Cancer Res, 2017. 23(5): p. 1220-1226.
137. *Comprehensive molecular characterization of gastric adenocarcinoma.* Nature, 2014. 513(7517): p. 202-9.
138. Green, M.R., et al., *Integrative analysis reveals selective 9p24.1 amplification, increased PD-1 ligand expression, and further induction via JAK2 in nodular sclerosing Hodgkin lymphoma and primary mediastinal large B-cell lymphoma.* Blood, 2010. 116(17): p. 3268-77.
139. Ikeda, S., et al., *PD-L1 Is Upregulated by Simultaneous Amplification of the PD-L1 and JAK2 Genes in Non-Small Cell Lung Cancer.* J Thorac Oncol, 2016. 11(1): p. 62-71.
140. Straub, M., et al., *CD274/PD-L1 gene amplification and PD-L1 protein expression are common events in squamous cell carcinoma of the oral cavity.* Oncotarget, 2016. 7(11): p. 12024-34.
141. Clave, S., et al., *CD274 (PDL1) and JAK2 genomic amplifications in pulmonary squamous-cell and adenocarcinoma patients.* Histopathology, 2018. 72(2): p. 259-269.
142. Lv, D., et al., *PD-L1 gene promoter methylation represents a potential diagnostic marker in advanced gastric cancer.* Oncol Lett, 2020. 19(2): p. 1223-1234.
143. Micevic, G., et al., *PD-L1 methylation regulates PD-L1 expression and is associated with melanoma survival.* Pigment Cell Melanoma Res, 2019. 32(3): p. 435-440.
144. Wrangle, J., et al., *Alterations of immune response of Non-Small Cell Lung Cancer with Azacytidine.* Oncotarget, 2013. 4(11): p. 2067-79.
145. Asgarova, A., et al., *PD-L1 expression is regulated by both DNA methylation and NF-kB during EMT signaling in non-small cell lung carcinoma.* Oncoimmunology, 2018. 7(5): p. e1423170.
146. Gevensleben, H., et al., *PD-L1 promoter methylation is a prognostic biomarker for biochemical recurrence-free survival in prostate cancer patients following radical prostatectomy.* Oncotarget, 2016. 7(48): p. 79943-79955.
147. Fujita, Y., et al., *The clinical relevance of the miR-197/CKS1B/STAT3-mediated PD-L1 network in chemoresistant non-small-cell lung cancer.* Mol Ther, 2015. 23(4): p. 717-27.
148. Chen, X.M., *MicroRNA signatures in liver diseases.* World J Gastroenterol, 2009. 15(14): p. 1665-72.
149. Chen, L., et al., *Metastasis is regulated via microRNA-200/ZEB1 axis control of tumour cell PD-L1 expression and intratumoral immunosuppression.* Nat Commun, 2014. 5: p. 5241.

150. Wang, W., et al., *A miR-570 binding site polymorphism in the B7-H1 gene is associated with the risk of gastric adenocarcinoma.* Hum Genet, 2013. 132(6): p. 641-8.
151. Wang, X., et al., *Tumor suppressor miR-34a targets PD-L1 and functions as a potential immunotherapeutic target in acute myeloid leukemia.* Cell Signal, 2015. 27(3): p. 443-52.
152. Gong, A.Y., et al., *MicroRNA-513 regulates B7-H1 translation and is involved in IFN-gamma-induced B7-H1 expression in cholangiocytes.* J Immunol, 2009. 182(3): p. 1325-33.
153. Jardim, M.J., et al., *Disruption of microRNA expression in human airway cells by diesel exhaust particles is linked to tumorigenesis-associated pathways.* Environ Health Perspect, 2009. 117(11): p. 1745-51.
154. Dong, P., et al., *Control of PD-L1 expression by miR-140/142/340/383 and oncogenic activation of the OCT4-miR-18a pathway in cervical cancer.* Oncogene, 2018. 37(39): p. 5257-5268.
155. Coelho, M.A., et al., *Oncogenic RAS Signaling Promotes Tumor Immunoresistance by Stabilizing PD-L1 mRNA.* Immunity, 2017. 47(6): p. 1083-1099.e6.
156. Lastwika, K.J., et al., *Control of PD-L1 Expression by Oncogenic Activation of the AKT-mTOR Pathway in Non-Small Cell Lung Cancer.* Cancer Res, 2016. 76(2): p. 227-38.
157. Crane, C.A., et al., *PI(3) kinase is associated with a mechanism of immunoresistance in breast and prostate cancer.* Oncogene, 2009. 28(2): p. 306-12.
158. Parsa, A.T., et al., *Loss of tumor suppressor PTEN function increases B7-H1 expression and immunoresistance in glioma.* Nat Med, 2007. 13(1): p. 84-8.
159. Tang, Y., et al., *The association between PD-L1 and EGFR status and the prognostic value of PD-L1 in advanced non-small cell lung cancer patients treated with EGFR-TKIs.* Oncotarget, 2015. 6(16): p. 14209.
160. Höckel, M. and P. Vaupel, *Tumor Hypoxia: Definitions and Current Clinical, Biologic, and Molecular Aspects.* JNCI: Journal of the National Cancer Institute, 2001. 93(4): p. 266-276.
161. Noman, M.Z., et al., *PD-L1 is a novel direct target of HIF-1alpha, and its blockade under hypoxia enhanced MDSC-mediated T cell activation.* J Exp Med, 2014. 211(5): p. 781-90.
162. Barsoum, I.B., et al., *A mechanism of hypoxia-mediated escape from adaptive immunity in cancer cells.* Cancer Res, 2014. 74(3): p. 665-74.
163. Koh, Y.W., et al., *PD-L1 protein expression in non-small-cell lung cancer and its relationship with the hypoxia-related signaling pathways: A study based on immunohistochemistry and RNA sequencing data.* Lung Cancer, 2019. 129: p. 41-47.
164. Tawadros, A.I.F. and M.M.M. Khalafalla, *Expression of programmed death-ligand 1 and hypoxia-inducible factor-1alpha proteins in endometrial carcinoma.* J Cancer Res Ther, 2018. 14(Supplement): p. S1063-s1069.
165. Warburg, O.H. and F. Dickens, *Metabolism of tumours.* 1930.
166. Feng, J., et al., *Tumor cell-derived lactate induces TAZ-dependent upregulation of PD-L1 through GPR81 in human lung cancer cells.* Oncogene, 2017. 36(42): p. 5829-5839.
167. Daneshmandi, S., B. Wegiel, and P. Seth, *Blockade of Lactate Dehydrogenase-A (LDH-A) Improves Efficacy of Anti-Programmed Cell Death-1 (PD-1) Therapy in Melanoma.* Cancers (Basel), 2019. 11(4).

168. Mimura, K., et al., *PD-L1 expression is mainly regulated by interferon gamma associated with JAK-STAT pathway in gastric cancer.* Cancer Sci, 2018. 109(1): p. 43-53.
169. Hu, X. and L.B. Ivashkiv, *Cross-regulation of signaling pathways by interferon-gamma: implications for immune responses and autoimmune diseases.* Immunity, 2009. 31(4): p. 539-50.
170. Ivashkiv, L.B., *IFNgamma: signalling, epigenetics and roles in immunity, metabolism, disease and cancer immunotherapy.* Nat Rev Immunol, 2018. 18(9): p. 545-558.
171. Arase, H., N. Arase, and T. Saito, *Interferon gamma production by natural killer (NK) cells and NK1.1+ T cells upon NKR-P1 cross-linking.* J Exp Med, 1996. 183(5): p. 2391-6.
172. Garcia-Diaz, A., et al., *Interferon Receptor Signaling Pathways Regulating PD-L1 and PD-L2 Expression.* Cell Rep, 2017. 19(6): p. 1189-1201.
173. Stark, G.R. and J.E. Darnell, Jr., *The JAK-STAT pathway at twenty.* Immunity, 2012. 36(4): p. 503-14.
174. Villarino, A.V., Y. Kanno, and J.J. O'Shea, *Mechanisms and consequences of Jak-STAT signaling in the immune system.* Nat Immunol, 2017. 18(4): p. 374-384.
175. Taube, J.M., et al., *Colocalization of inflammatory response with B7-h1 expression in human melanocytic lesions supports an adaptive resistance mechanism of immune escape.* Sci Transl Med, 2012. 4(127): p. 127ra37.
176. Chen, D.S. and I. Mellman, *Elements of cancer immunity and the cancer-immune set point.* Nature, 2017. 541(7637): p. 321-330.
177. Cottrell, T.R. and J.M. Taube, *PD-L1 and Emerging Biomarkers in Immune Checkpoint Blockade Therapy.* Cancer J, 2018. 24(1): p. 41-46.
178. Higgs, B.W., et al., *Interferon Gamma Messenger RNA Signature in Tumor Biopsies Predicts Outcomes in Patients with Non-Small Cell Lung Carcinoma or Urothelial Cancer Treated with Durvalumab.* Clin Cancer Res, 2018. 24(16): p. 3857-3866.
179. Johnson, D.B., et al., *Quantitative Spatial Profiling of PD-1/PD-L1 Interaction and HLA-DR/IDO-1 Predicts Improved Outcomes of Anti-PD-1 Therapies in Metastatic Melanoma.* Clin Cancer Res, 2018. 24(21): p. 5250-5260.
180. Bosticardo, M., et al., *Biased activation of human T lymphocytes due to low extracellular pH is antagonized by B7/CD28 costimulation.* Eur J Immunol, 2001. 31(9): p. 2829-38.
181. Chemnitz, J.M., et al., *SHP-1 and SHP-2 associate with immunoreceptor tyrosine-based switch motif of programmed death 1 upon primary human T cell stimulation, but only receptor ligation prevents T cell activation.* J Immunol, 2004. 173(2): p. 945-54.
182. Yokosuka, T., et al., *Programmed cell death 1 forms negative costimulatory microclusters that directly inhibit T cell receptor signaling by recruiting phosphatase SHP2.* J Exp Med, 2012. 209(6): p. 1201-17.
183. Hirano, F., et al., *Blockade of B7-H1 and PD-1 by monoclonal antibodies potentiates cancer therapeutic immunity.* Cancer Res, 2005. 65(3): p. 1089-96.
184. Escors, D., et al., *The intracellular signalosome of PD-L1 in cancer cells.* Signal Transduct Target Ther, 2018. 3: p. 26.
185. Azuma, T., et al., *B7-H1 is a ubiquitous antiapoptotic receptor on cancer cells.* Blood, 2008. 111(7): p. 3635-43.
186. Burnet, F.M., *The concept of immunological surveillance.* Prog Exp Tumor Res, 1970. 13: p. 1-27.
187. Dunn, G.P., L.J. Old, and R.D. Schreiber, *The Immunobiology of Cancer*

Immunosurveillance and Immunoediting. Immunity, 2004. 21(2): p. 137-148.
188. Shankaran, V., et al., *IFNgamma and lymphocytes prevent primary tumour development and shape tumour immunogenicity.* Nature, 2001. 410(6832): p. 1107-11.
189. Bray, F., et al., *Global cancer statistics 2018: GLOBOCAN estimates of incidence and mortality worldwide for 36 cancers in 185 countries.* CA: a cancer journal for clinicians, 2018. 68(6): p. 394-424.
190. *U.S. Food & Drug Administration, FDA Approves First-Line Immunotherapy for Patients with MSI-H/dMMR Metastatic Colorectal Cancer*. [cited 2020 June 29]; Available from: https://www.fda.gov/news-events/press-announcements/fda-approves-first-line-immunotherapy-patients-msi-hdmmr-metastatic-colorectal-cancer.
191. Corbett, T.H., et al., *Tumor induction relationships in development of transplantable cancers of the colon in mice for chemotherapy assays, with a note on carcinogen structure.* Cancer Res, 1975. 35(9): p. 2434-9.
192. Tan, M.H., E.D. Holyoke, and M.H. Goldrosen, *Murine colon adenocarcinomas: methods for selective culture in vitro.* J Natl Cancer Inst, 1976. 56(4): p. 871-3.
193. Rosenberg, S.A., P. Spiess, and R. Lafreniere, *A new approach to the adoptive immunotherapy of cancer with tumor-infiltrating lymphocytes.* Science, 1986. 233(4770): p. 1318-21.
194. Efremova, M., et al., *Targeting immune checkpoints potentiates immunoediting and changes the dynamics of tumor evolution.* Nat Commun, 2018. 9(1): p. 32.
195. Alexandrov, L.B., et al., *Signatures of mutational processes in human cancer.* Nature, 2013. 500(7463): p. 415-21.
196. Kleinovink, J.W., et al., *PD-L1 expression on malignant cells is no prerequisite for checkpoint therapy.* Oncoimmunology, 2017. 6(4): p. e1294299.
197. Woo, S.R., et al., *Immune inhibitory molecules LAG-3 and PD-1 synergistically regulate T-cell function to promote tumoral immune escape.* Cancer Res, 2012. 72(4): p. 917-27.
198. Hos, B.J., et al., *Identification of a neo-epitope dominating endogenous CD8 T cell responses to MC-38 colorectal cancer.* OncoImmunology, 2019: p. 1673125.
199. Diaz, L.A., Jr. and D.T. Le, *PD-1 Blockade in Tumors with Mismatch-Repair Deficiency.* N Engl J Med, 2015. 373(20): p. 1979.
200. Shinkai, Y., et al., *RAG-2-deficient mice lack mature lymphocytes owing to inability to initiate V(D)J rearrangement.* Cell, 1992. 68(5): p. 855-867.
201. Juneja, V.R., et al., *PD-L1 on tumor cells is sufficient for immune evasion in immunogenic tumors and inhibits CD8 T cell cytotoxicity.* J Exp Med, 2017. 214(4): p. 895-904.
202. Lau, J., et al., *Tumour and host cell PD-L1 is required to mediate suppression of anti-tumour immunity in mice.* Nat Commun, 2017. 8: p. 14572.
203. Griswold, D.P. and T.H. Corbett, *A colon tumor model for anticancer agent evaluation.* Cancer, 1975. 36(6 Suppl): p. 2441-4.
204. Zhang, B., et al., *Targeting transforming growth factor-β signaling in liver metastasis of colon cancer.* Cancer Letters, 2009. 277(1): p. 114-120.
205. *Comprehensive molecular characterization of human colon and rectal cancer.* Nature, 2012. 487(7407): p. 330-7.
206. Mosely, S.I., et al., *Rational Selection of Syngeneic Preclinical Tumor Models for Immunotherapeutic Drug Discovery.* Cancer Immunol Res, 2017. 5(1): p. 29-41.
207. Castle, J.C., et al., *Immunomic, genomic and transcriptomic characterization of CT26 colorectal carcinoma.* BMC Genomics, 2014. 15(1): p. 190.
208. Fransen, M.F., et al., *Tumor-draining lymph nodes are pivotal in PD-1/PD-L1*

checkpoint therapy. JCI Insight, 2018. 3(23).
209. Rath, D., et al., *The CRISPR-Cas immune system: biology, mechanisms and applications.* Biochimie, 2015. 117: p. 119-28.
210. *The Nobel Prize in Chemistry 2020. NobelPrize.org. Nobel Media AB 2020.* . [cited 2020 October, 15]; Available from: https://www.nobelprize.org/prizes/chemistry/2020/summary/.
211. Kirkland, S.C., *Dome formation by a human colonic adenocarcinoma cell line (HCA-7).* Cancer Res, 1985. 45(8): p. 3790-5.
212. Kirkland, S.C. and I.G. Bailey, *Establishment and characterisation of six human colorectal adenocarcinoma cell lines.* Br J Cancer, 1986. 53(6): p. 779-85.
213. Coffey, R.J., et al., *Epidermal growth factor receptor activation induces nuclear targeting of cyclooxygenase-2, basolateral release of prostaglandins, and mitogenesis in polarizing colon cancer cells.* Proc Natl Acad Sci U S A, 1997. 94(2): p. 657-62.
214. Liu, Y. and W.F. Bodmer, *Analysis of P53 mutations and their expression in 56 colorectal cancer cell lines.* Proceedings of the National Academy of Sciences of the United States of America, 2006. 103(4): p. 976-981.
215. Botti, G., et al., *COX-2 expression positively correlates with PD-L1 expression in human melanoma cells.* Journal of translational medicine, 2017. 15(1): p. 46-46.
216. Prima, V., et al., *COX2/mPGES1/PGE2 pathway regulates PD-L1 expression in tumor-associated macrophages and myeloid-derived suppressor cells.* Proc Natl Acad Sci U S A, 2017. 114(5): p. 1117-1122.
217. Jantscheff, P., et al., *Abstract 3216: Anti-PD-1, Anti-PD-L1 and Anti-CTLA-4 checkpoint inhibitor treatment leads to different responses in syngeneic tumor models.* Cancer Research, 2016. 76: p. 3216-3216.
218. Sagiv-Barfi, I., et al., *Therapeutic antitumor immunity by checkpoint blockade is enhanced by ibrutinib, an inhibitor of both BTK and ITK.* Proceedings of the National Academy of Sciences, 2015. 112(9): p. E966-E972.
219. *Genomic Classification of Cutaneous Melanoma.* Cell, 2015. 161(7): p. 1681-96.
220. Fidler, I.J., *Biological behavior of malignant melanoma cells correlated to their survival in vivo.* Cancer Res, 1975. 35(1): p. 218-24.
221. Fidler, I.J., *Selection of successive tumour lines for metastasis.* Nature New Biology, 1973. 242(118): p. 148-149.
222. Bosmann, H.B., et al., *Biochemical parameters correlated with tumour cell implantation.* Nature, 1973. 246(5434): p. 487-9.
223. Dexter, D.L., et al., *Heterogeneity of tumor cells from a single mouse mammary tumor.* Cancer Res, 1978. 38(10): p. 3174-81.
224. Aslakson, C.J. and F.R. Miller, *Selective events in the metastatic process defined by analysis of the sequential dissemination of subpopulations of a mouse mammary tumor.* Cancer Res, 1992. 52(6): p. 1399-405.
225. Pulaski, B.A. and S. Ostrand-Rosenberg, *Mouse 4T1 breast tumor model.* Curr Protoc Immunol, 2001. Chapter 20: p. Unit 20.2.
226. Watanabe, H., et al., *Innate immune response in Th1- and Th2-dominant mouse strains.* Shock, 2004. 22(5): p. 460-6.
227. Nishimura, T., et al., *The critical role of Th1-dominant immunity in tumor immunology.* Cancer chemotherapy and pharmacology, 2000. 46(1): p. S52-S61.
228. Yagi, J., et al., *Genetic background influences Th cell differentiation by controlling the capacity for IL-2-induced IL-4 production by naive CD4+ T cells.* Int Immunol, 2006. 18(12): p. 1681-90.
229. Sherwood, S.W., et al., *Defining cellular senescence in IMR-90 cells: a flow cytometric analysis.* Proc Natl Acad Sci U S A, 1988. 85(23): p. 9086-90.

230. Weinberg, R.A. and R.A. Weinberg, *The biology of cancer*. 2013: Garland science.
231. Hayflick, L. and P.S. Moorhead, *The serial cultivation of human diploid cell strains.* Exp Cell Res, 1961. 25: p. 585-621.
232. Collado, M. and M. Serrano, *Senescence in tumours: evidence from mice and humans.* Nat Rev Cancer, 2010. 10(1): p. 51-7.
233. Obaya, A.J. and J.M. Sedivy, *Regulation of cyclin-Cdk activity in mammalian cells.* Cell Mol Life Sci, 2002. 59(1): p. 126-42.
234. Stein, G.H., et al., *Differential roles for cyclin-dependent kinase inhibitors p21 and p16 in the mechanisms of senescence and differentiation in human fibroblasts.* Molecular and cellular biology, 1999. 19(3): p. 2109-2117.
235. Xue, W., et al., *Senescence and tumour clearance is triggered by p53 restoration in murine liver carcinomas.* Nature, 2007. 445(7128): p. 656-60.
236. Yasaei, H., et al., *Carcinogen-specific mutational and epigenetic alterations in INK4A, INK4B and p53 tumour-suppressor genes drive induced senescence bypass in normal diploid mammalian cells.* Oncogene, 2012. 32: p. 171.
237. Munoz-Espin, D. and M. Serrano, *Cellular senescence: from physiology to pathology.* Nat Rev Mol Cell Biol, 2014. 15(7): p. 482-96.
238. Campisi, J. and F. d'Adda di Fagagna, *Cellular senescence: when bad things happen to good cells.* Nat Rev Mol Cell Biol, 2007. 8(9): p. 729-40.
239. Passos, J.F., et al., *Cellular senescence: unravelling complexity.* Age (Dordr), 2009. 31(4): p. 353-63.
240. Serrano, M., et al., *Oncogenic ras provokes premature cell senescence associated with accumulation of p53 and p16INK4a.* Cell, 1997. 88(5): p. 593-602.
241. Foglesong, P.D., C. Reckord, and S. Swink, *Doxorubicin inhibits human DNA topoisomerase I.* Cancer Chemother Pharmacol, 1992. 30(2): p. 123-5.
242. Sliwinska, M.A., et al., *Induction of senescence with doxorubicin leads to increased genomic instability of HCT116 cells.* Mech Ageing Dev, 2009. 130(1-2): p. 24-32.
243. Kitada, K., F. Pu, and M. Toi, *Occurrence of senescence-escaping cells in doxorubicin-induced senescence is enhanced by PD0332991, a cyclin-dependent kinase 4/6 inhibitor, in colon cancer HCT116 cells.* Oncol Lett, 2019. 17(1): p. 1153-1159.
244. Braumuller, H., et al., *T-helper-1-cell cytokines drive cancer into senescence.* Nature, 2013. 494(7437): p. 361-5.
245. Schosserer, M., J. Grillari, and M. Breitenbach, *The Dual Role of Cellular Senescence in Developing Tumors and Their Response to Cancer Therapy.* Front Oncol, 2017. 7: p. 278.
246. Pérez-Mancera, P.A., A.R. Young, and M. Narita, *Inside and out: the activities of senescence in cancer.* Nat Rev Cancer, 2014. 14(8): p. 547-58.
247. Kuilman, T., et al., *Oncogene-induced senescence relayed by an interleukin-dependent inflammatory network.* Cell, 2008. 133(6): p. 1019-31.
248. Jayatilaka, H., et al., *Synergistic IL-6 and IL-8 paracrine signalling pathway infers a strategy to inhibit tumour cell migration.* Nat Commun, 2017. 8: p. 15584.
249. Kim, Y.H., et al., *Senescent tumor cells lead the collective invasion in thyroid cancer.* Nat Commun, 2017. 8: p. 15208.
250. Iannello, A., et al., *p53-dependent chemokine production by senescent tumor cells supports NKG2D-dependent tumor elimination by natural killer cells.* J Exp Med, 2013. 210(10): p. 2057-69.
251. Kang, T.W., et al., *Senescence surveillance of pre-malignant hepatocytes limits liver cancer development.* Nature, 2011. 479(7374): p. 547-51.
252. Faget, D.V., Q. Ren, and S.A. Stewart, *Unmasking senescence: context-dependent effects of SASP in cancer.* Nat Rev Cancer, 2019. 19(8): p. 439-453.

253. Shoemaker, A.R., et al., *Activity of the Bcl-2 family inhibitor ABT-263 in a panel of small cell lung cancer xenograft models.* Clin Cancer Res, 2008. 14(11): p. 3268-77.
254. Zhu, Y., et al., *Identification of a novel senolytic agent, navitoclax, targeting the Bcl-2 family of anti-apoptotic factors.* Aging Cell, 2016. 15(3): p. 428-35.
255. Nacarelli, T., et al., *NAD(+) metabolism governs the proinflammatory senescence-associated secretome.* Nat Cell Biol, 2019. 21(3): p. 397-407.
256. Gey, C. and K. Seeger, *Metabolic changes during cellular senescence investigated by proton NMR-spectroscopy.* Mech Ageing Dev, 2013. 134(3-4): p. 130-8.
257. Gey, C. and K. Seeger, *Metabolic Changes Investigated by Proton NMR Spectroscopy in Cells Undergoing Oncogene-Induced Senescence.* Methods Mol Biol, 2017. 1534: p. 155-163.
258. Aboagye, E.O. and Z.M. Bhujwalla, *Malignant transformation alters membrane choline phospholipid metabolism of human mammary epithelial cells.* Cancer Res, 1999. 59(1): p. 80-4.
259. Iorio, E., et al., *Alterations of choline phospholipid metabolism in ovarian tumor progression.* Cancer research, 2005. 65(20): p. 9369-9376.
260. Glunde, K., Z.M. Bhujwalla, and S.M. Ronen, *Choline metabolism in malignant transformation.* Nature Reviews Cancer, 2011. 11(12): p. 835-848.
261. Morse, D.L., et al., *Response of choline metabolites to docetaxel therapy is quantified in vivo by localized (31)P MRS of human breast cancer xenografts and in vitro by high-resolution (31)P NMR spectroscopy of cell extracts.* Magn Reson Med, 2007. 58(2): p. 270-80.
262. Inoue, C., et al., *SMARCD1 regulates senescence-associated lipid accumulation in hepatocytes.* npj Aging and Mechanisms of Disease, 2017. 3(1): p. 11.
263. Lizardo, D.Y., et al., *Regulation of lipids is central to replicative senescence.* Mol Biosyst, 2017. 13(3): p. 498-509.
264. Ntziachristos, V., A. Leroy-Willig, and B. Tavitian, *Textbook of in vivo Imaging in Vertebrates*. 2007: John Wiley & Sons.
265. Arranz, A. and J. Ripoll, *Advances in optical imaging for pharmacological studies.* Frontiers in Pharmacology, 2015. 6(189).
266. Ntziachristos, V., *Fluorescence molecular imaging.* Annu Rev Biomed Eng, 2006. 8: p. 1-33.
267. Danhier, P., et al., *Combining Optical Reporter Proteins with Different Half-lives to Detect Temporal Evolution of Hypoxia and Reoxygenation in Tumors.* Neoplasia, 2015. 17(12): p. 871-881.
268. Ntziachristos, V., et al., *Concurrent MRI and diffuse optical tomography of breast after indocyanine green enhancement.* Proceedings of the National Academy of Sciences, 2000. 97(6): p. 2767-2772.
269. Rice, B., M. Cable, and M. Nelson, *In vivo imaging of light-emitting probes.* Journal of Biomedical Optics, 2001. 6(4).
270. Ntziachristos, V., et al., *Fluorescence molecular tomography resolves protease activity in vivo.* Nat Med, 2002. 8(7): p. 757-60.
271. Välisuo, P., *Optical methods for assessing skin flap survival*, in *Biophotonics for Medical Applications*. 2015, Elsevier. p. 331-346.
272. Eisenblätter, M. and C. Bremer, *4.23 - External Transdermal Procedures*, in *Comprehensive Biomedical Physics*, A. Brahme, Editor. 2014, Elsevier: Oxford. p. 363-378.
273. Turner, G.M., et al., *Complete-angle projection diffuse optical tomography by use of early photons.* Opt Lett, 2005. 30(4): p. 409-11.
274. Mansfield, J., et al., *Autofluorescence removal, multiplexing, and automated*

analysis methods for in-vivo fluorescence imaging. Journal of Biomedical Optics, 2005. 10(4): p. 041207.
275. Krishnamachary, B., et al., *Hypoxia-Induced Reporter Genes with Different Half-Lives.* Methods Mol Biol, 2018. 1790: p. 113-125.
276. Carlsen, H., et al., *In Vivo Imaging of NF-κB Activity.* The Journal of Immunology, 2002. 168(3): p. 1441-1446.
277. Li, J., et al., *Cage the firefly luciferin! - a strategy for developing bioluminescent probes.* Chem Soc Rev, 2013. 42(2): p. 662-76.
278. de Wet, J.R., et al., *Firefly luciferase gene: structure and expression in mammalian cells.* Mol Cell Biol, 1987. 7(2): p. 725-37.
279. Badr, C.E., *Bioluminescence imaging: basics and practical limitations.* Methods Mol Biol, 2014. 1098: p. 1-18.
280. Lloyd, J.E., *Bioluminescence and communication in insects.* Annual review of entomology, 1983. 28(1): p. 131-160.
281. Marques, S.M. and J.C. Esteves da Silva, *Firefly bioluminescence: a mechanistic approach of luciferase catalyzed reactions.* IUBMB Life, 2009. 61(1): p. 6-17.
282. Lorenzo, J.R., *Principles of diffuse light propagation: light propagation in tissues with applications in biology and medicine*. 2012: World Scientific.
283. Hoelen, C.G. and F.F. de Mul, *Image reconstruction for photoacoustic scanning of tissue structures.* Appl Opt, 2000. 39(31): p. 5872-83.
284. Wang, X., et al., *Noninvasive laser-induced photoacoustic tomography for structural and functional in vivo imaging of the brain.* Nat Biotechnol, 2003. 21(7): p. 803-6.
285. Ntziachristos, V., et al., *Looking and listening to light: the evolution of whole-body photonic imaging.* Nature Biotechnology, 2005. 23(3): p. 313-320.
286. Grischke, E.M., et al., *ICG Fluorescence Technique for the Detection of Sentinel Lymph Nodes in Breast Cancer: Results of a Prospective Open-label Clinical Trial.* Geburtshilfe Frauenheilkd, 2015. 75(9): p. 935-940.
287. Sceneay, J., et al., *Tracking the fate of adoptively transferred myeloid-derived suppressor cells in the primary breast tumor microenvironment.* PLoS One, 2018. 13(4): p. e0196040.
288. Griessinger, C.M., et al., *The administration route of tumor-antigen-specific T-helper cells differentially modulates the tumor microenvironment and senescence.* Carcinogenesis, 2019. 40(2): p. 289-302.
289. Seitz, C.M., et al., *GD2-targeted chimeric antigen receptor T cells prevent metastasis formation by elimination of breast cancer stem-like cells.* Oncoimmunology, 2020. 9(1): p. 1683345.
290. Weigelin, B., G.J. Bakker, and P. Friedl, *Intravital third harmonic generation microscopy of collective melanoma cell invasion: Principles of interface guidance and microvesicle dynamics.* Intravital, 2012. 1(1): p. 32-43.
291. Weigert, R., et al., *Intravital microscopy: a novel tool to study cell biology in living animals.* Histochemistry and Cell Biology, 2010. 133(5): p. 481-491.
292. Weigelin, B., et al., *Anti-CD137 monoclonal antibodies and adoptive T cell therapy: a perfect marriage?* Cancer Immunol Immunother, 2016. 65(5): p. 493-7.
293. Chittajallu, D.R., et al., *In vivo cell-cycle profiling in xenograft tumors by quantitative intravital microscopy.* Nature Methods, 2015. 12(6): p. 577-585.
294. Phelps, M.E., et al., *Application of annihilation coincidence detection to transaxial reconstruction tomography.* J Nucl Med, 1975. 16(3): p. 210-24.
295. Ter-Pogossian, M.M., et al., *A positron-emission transaxial tomograph for nuclear imaging (PETT).* Radiology, 1975. 114(1): p. 89-98.
296. Cherry, S.R. and S.S. Gambhir, *Use of Positron Emission Tomography in Animal*

Research. ILAR Journal, 2001. 42(3): p. 219-232.
297. Phelps, M.E., *Positron emission tomography provides molecular imaging of biological processes.* Proc Natl Acad Sci U S A, 2000. 97(16): p. 9226-33.
298. Smith, T.A., *FDG uptake, tumour characteristics and response to therapy: a review.* Nuclear medicine communications, 1998. 19(2): p. 97-105.
299. Turkington, T.G., *Introduction to PET instrumentation.* J Nucl Med Technol, 2001. 29(1): p. 4-11.
300. Fukuda, H., et al., *Experimental study for cancer diagnosis with positron-labeled fluorinated glucose analogs: [18F]-2-fluoro-2-deoxy-D-mannose: a new tracer for cancer detection.* Eur J Nucl Med, 1982. 7(7): p. 294-7.
301. Baron, J.C., et al., *Noninvasive measurement of blood flow, oxygen consumption, and glucose utilization in the same brain regions in man by positron emission tomography: concise communication.* J Nucl Med, 1982. 23(5): p. 391-9.
302. Pichler, B.J., M.S. Judenhofer, and H.F. Wehrl, *PET/MRI hybrid imaging: devices and initial results.* Eur Radiol, 2008. 18(6): p. 1077-86.
303. Pichler, B.J., et al., *Positron emission tomography/magnetic resonance imaging: the next generation of multimodality imaging?* Semin Nucl Med, 2008. 38(3): p. 199-208.
304. Marzola, P., F. Osculati, and A. Sbarbati, *High field MRI in preclinical research.* Eur J Radiol, 2003. 48(2): p. 165-70.
305. Fuchs, K., et al., *In Vivo Hypoxia PET Imaging Quantifies the Severity of Arthritic Joint Inflammation in Line with Overexpression of Hypoxia-Inducible Factor and Enhanced Reactive Oxygen Species Generation.* J Nucl Med, 2017. 58(5): p. 853-860.
306. Schweifer, A., et al., *[(18)F]Fluoro-azomycin-2´-deoxy-β-d-ribofuranoside - A new imaging agent for tumor hypoxia in comparison with [(18)F]FAZA.* Nucl Med Biol, 2016. 43(12): p. 759-769.
307. Freise, A.C., et al., *ImmunoPET Imaging of Murine CD4(+) T Cells Using Anti-CD4 Cys-Diabody: Effects of Protein Dose on T Cell Function and Imaging.* Molecular imaging and biology, 2017. 19(4): p. 599-609.
308. Tavaré, R., et al., *An Effective Immuno-PET Imaging Method to Monitor CD8-Dependent Responses to Immunotherapy.* Cancer Res, 2016. 76(1): p. 73-82.
309. Kristensen, L.K., et al., *CD4(+) and CD8a(+) PET imaging predicts response to novel PD-1 checkpoint inhibitor: studies of Sym021 in syngeneic mouse cancer models.* Theranostics, 2019. 9(26): p. 8221-8238.
310. Niemeijer, A.N., et al., *Whole body PD-1 and PD-L1 positron emission tomography in patients with non-small-cell lung cancer.* Nat Commun, 2018. 9(1): p. 4664.
311. Stutvoet, T.S., et al., *Molecular imaging of PD-L1 expression and dynamics with the adnectin-based PET tracer (18)F-BMS-986192.* J Nucl Med, 2020.
312. Bae, M.R., et al., *18F-FDG PET/CT versus CT/MR imaging for detection of neck lymph node metastasis in palpably node-negative oral cavity cancer.* Journal of Cancer Research and Clinical Oncology, 2020. 146(1): p. 237-244.
313. Singh, B., et al., *Preoperative 18F-FDG-PET/CT imaging and sentinel node biopsy in the detection of regional lymph node metastases in malignant melanoma.* Melanoma Res, 2008. 18(5): p. 346-52.
314. Bloch, F., W.W. Hansen, and M. Packard, *The Nuclear Induction Experiment.* Physical Review, 1946. 70(7-8): p. 474-485.
315. Purcell, E.M., H.C. Torrey, and R.V. Pound, *Resonance Absorption by Nuclear Magnetic Moments in a Solid.* Physical Review, 1946. 69(1-2): p. 37-38.
316. *The Nobel Prize in Physics 1952.* NobelPrize.org, 10 June 2020. Nobel Media AB 2020.

317. *The Nobel Prize in Physiology or Medicine 2003. NobelPrize.org. Nobel Media AB 2020.* [cited 2020 August, 07]; Available from: https://www.nobelprize.org/prizes/medicine/2003/summary/.
318. Cherry, S.R., *In vivo molecular and genomic imaging: new challenges for imaging physics.* Phys Med Biol, 2004. 49(3): p. R13-48.
319. Emwas, A.H., et al., *NMR Spectroscopy for Metabolomics Research.* Metabolites, 2019. 9(7).
320. Grover, V.P., et al., *Magnetic Resonance Imaging: Principles and Techniques: Lessons for Clinicians.* J Clin Exp Hepatol, 2015. 5(3): p. 246-55.
321. van Geuns, R.J., et al., *Basic principles of magnetic resonance imaging.* Prog Cardiovasc Dis, 1999. 42(2): p. 149-56.
322. Shah, T., et al., *CEST-FISP: a novel technique for rapid chemical exchange saturation transfer MRI at 7 T.* Magn Reson Med, 2011. 65(2): p. 432-7.
323. Sheth, V.R., et al., *Measuring in vivo tumor pHe with CEST-FISP MRI.* Magn Reson Med, 2012. 67(3): p. 760-8.
324. Chen, L.Q., et al., *Evaluations of Tumor Acidosis Within In Vivo Tumor Models Using Parametric Maps Generated with Acido CEST MRI.* Mol Imaging Biol, 2015. 17(4): p. 488-96.
325. Ackerstaff, E., et al., *Anti-inflammatory agent indomethacin reduces invasion and alters metabolism in a human breast cancer cell line.* Neoplasia, 2007. 9(3): p. 222-35.
326. Penet, M.F., et al., *MRI and MRS of intact perfused cancer cell metabolism, invasion, and stromal cell interactions.* NMR Biomed, 2019. 32(10): p. e4053.
327. Coffelt, S.B., et al., *Elusive identities and overlapping phenotypes of proangiogenic myeloid cells in tumors.* The American journal of pathology, 2010. 176(4): p. 1564-1576.
328. DeNardo, D.G., P. Andreu, and L.M. Coussens, *Interactions between lymphocytes and myeloid cells regulate pro-versus anti-tumor immunity.* Cancer and Metastasis Reviews, 2010. 29(2): p. 309-316.
329. Murdoch, C., et al., *The role of myeloid cells in the promotion of tumour angiogenesis.* Nature reviews cancer, 2008. 8(8): p. 618-631.
330. Johansson, M., D.G. DeNardo, and L.M. Coussens, *Polarized immune responses differentially regulate cancer development.* Immunological reviews, 2008. 222(1): p. 145-154.
331. Elinav, E., et al., *Inflammation-induced cancer: crosstalk between tumours, immune cells and microorganisms.* Nature Reviews Cancer, 2013. 13(11): p. 759.
332. Erra Díaz, F., E. Dantas, and J. Geffner, *Unravelling the Interplay between Extracellular Acidosis and Immune Cells.* Mediators of inflammation, 2018. 2018.
333. Brenner, E., et al., *Cancer immune control needs senescence induction by interferon-dependent cell cycle regulator pathways in tumours.* Nat Commun, 2020. 11(1): p. 1335.
334. Reynolds, A., et al., *Rational siRNA design for RNA interference.* Nat Biotechnol, 2004. 22(3): p. 326-30.
335. de Fougerolles, A., et al., *Interfering with disease: a progress report on siRNA-based therapeutics.* Nat Rev Drug Discov, 2007. 6(6): p. 443-53.
336. Hannus, M., et al., *siPools: highly complex but accurately defined siRNA pools eliminate off-target effects.* Nucleic Acids Res, 2014. 42(12): p. 8049-61.
337. Parsons, B.D., et al., *A direct phenotypic comparison of siRNA pools and multiple individual duplexes in a functional assay.* PLoS One, 2009. 4(12): p. e8471.
338. Wiedenheft, B., S.H. Sternberg, and J.A. Doudna, *RNA-guided genetic silencing systems in bacteria and archaea.* Nature, 2012. 482(7385): p. 331-8.

339. Jinek, M., et al., *A programmable dual-RNA-guided DNA endonuclease in adaptive bacterial immunity.* Science, 2012. 337(6096): p. 816-21.
340. *Benchling [Biology Software].* 2019.
341. Wang, G.L., et al., *Hypoxia-inducible factor 1 is a basic-helix-loop-helix-PAS heterodimer regulated by cellular O2 tension.* Proc Natl Acad Sci U S A, 1995. 92(12): p. 5510-4.
342. Kõressaar, T., et al., *Primer3_masker: integrating masking of template sequence with primer design software.* Bioinformatics, 2018. 34(11): p. 1937-1938.
343. Koressaar, T. and M. Remm, *Enhancements and modifications of primer design program Primer3.* Bioinformatics, 2007. 23(10): p. 1289-91.
344. Untergasser, A., et al., *Primer3--new capabilities and interfaces.* Nucleic Acids Res, 2012. 40(15): p. e115.
345. Ye, J., et al., *Primer-BLAST: a tool to design target-specific primers for polymerase chain reaction.* BMC Bioinformatics, 2012. 13: p. 134.
346. Livak, K.J. and T.D. Schmittgen, *Analysis of relative gene expression data using real-time quantitative PCR and the 2(-Delta Delta C(T)) Method.* Methods, 2001. 25(4): p. 402-8.
347. Renart, J., J. Reiser, and G.R. Stark, *Transfer of proteins from gels to diazobenzyloxymethyl-paper and detection with antisera: a method for studying antibody specificity and antigen structure.* Proc Natl Acad Sci U S A, 1979. 76(7): p. 3116-20.
348. Towbin, H., T. Staehelin, and J. Gordon, *Electrophoretic transfer of proteins from polyacrylamide gels to nitrocellulose sheets: procedure and some applications.* Proc Natl Acad Sci U S A, 1979. 76(9): p. 4350-4.
349. McKinnon, K.M., *Flow Cytometry: An Overview.* Curr Protoc Immunol, 2018. 120: p. 5.1.1-5.1.11.
350. Cibrián, D. and F. Sánchez-Madrid, *CD69: from activation marker to metabolic gatekeeper.* European journal of immunology, 2017. 47(6): p. 946-953.
351. González-Amaro, R., et al., *Is CD69 an effective brake to control inflammatory diseases?* Trends Mol Med, 2013. 19(10): p. 625-32.
352. Marzio, R., et al., *Expression and function of the early activation antigen CD69 in murine macrophages.* J Leukoc Biol, 1997. 62(3): p. 349-55.
353. Sanderson, M.J., et al., *Fluorescence microscopy.* Cold Spring Harb Protoc, 2014. 2014(10): p. pdb.top071795.
354. Tellier, F., et al., *Sentinel lymph nodes fluorescence detection and imaging using Patent Blue V bound to human serum albumin.* Biomed Opt Express, 2012. 3(9): p. 2306-16.
355. Pacheco-Torres, J., et al., *The PD-L1 metabolic interactome intersects with choline metabolism and inflammation.* Cancer & Metabolism, 2021. 9(1): p. 10.
356. Ng, C.E., et al., *31P NMR spectroscopic study of the effects of gamma-irradiation on RIF-1 tumor cells perfused in vitro.* Magn Reson Med, 1992. 27(2): p. 296-309.
357. Pilatus, U., et al., *Real-time measurements of cellular oxygen consumption, pH, and energy metabolism using nuclear magnetic resonance spectroscopy.* Magn Reson Med, 2001. 45(5): p. 749-55.
358. McGovern, K.A., et al., *Gel-entrapment of perfluorocarbons: a fluorine-19 NMR spectroscopic method for monitoring oxygen concentration in cell perfusion systems.* Magn Reson Med, 1993. 29(2): p. 196-204.
359. Pilatus, U., et al., *Imaging prostate cancer invasion with multi-nuclear magnetic resonance methods: the Metabolic Boyden Chamber.* Neoplasia, 2000. 2(3): p. 273-9.
360. Shah, T., et al., *Noninvasive imaging identifies new roles for cyclooxygenase-2 in*

choline and lipid metabolism of human breast cancer cells. NMR in biomedicine, 2012. 25(5): p. 746-754.
361. Hetherington, H.P., M.J. Avison, and R.G. Shulman, *1H homonuclear editing of rat brain using semiselective pulses.* Proceedings of the National Academy of Sciences of the United States of America, 1985. 82(10): p. 3115-3118.
362. Shah, T., et al., *Noninvasive imaging identifies new roles for cyclooxygenase-2 in choline and lipid metabolism of human breast cancer cells.* NMR Biomed, 2012. 25(5): p. 746-54.
363. Shen, W., et al., *Measurement of intramyocellular lipid levels with 2-D magnetic resonance spectroscopic imaging at 1.5 T.* Acta diabetologica, 2003. 40 Suppl 1(Suppl 1): p. S51-S54.
364. Uhlen, M., et al., *A pathology atlas of the human cancer transcriptome.* Science, 2017. 357(6352).
365. Dalton, D.K., et al., *Multiple defects of immune cell function in mice with disrupted interferon-gamma genes.* Science, 1993. 259(5102): p. 1739-42.
366. Proulx, S.T., et al., *Use of a PEG-conjugated bright near-infrared dye for functional imaging of rerouting of tumor lymphatic drainage after sentinel lymph node metastasis.* Biomaterials, 2013. 34(21): p. 5128-37.
367. *National Center for Biotechnology Information. PubChem Database. Patent Blue V sodium, CID=9916325*. [cited 2020 July 8]; Available from: https://pubchem.ncbi.nlm.nih.gov/compound/Patent-Blue-V-sodium.
368. *LI-COR, IRDye® 800CW PEG Fluorescent Contrast Agent* [cited 2020 July, 8]; Available from: https://www.licor.com/bio/reagents/irdye-800cw-peg-fluorescent-contrast-agent.
369. Weiler, M. and J.B. Dixon, *Differential transport function of lymphatic vessels in the rat tail model and the long-term effects of Indocyanine Green as assessed with near-infrared imaging.* Front Physiol, 2013. 4: p. 215.
370. Carr, J.A., et al., *Shortwave infrared fluorescence imaging with the clinically approved near-infrared dye indocyanine green.* Proc Natl Acad Sci U S A, 2018. 115(17): p. 4465-4470.
371. Fleiss, A. and K.S. Sarkisyan, *A brief review of bioluminescent systems (2019).* Current Genetics, 2019. 65(4): p. 877-882.
372. Thorek, D.L., et al., *Non-invasive mapping of deep-tissue lymph nodes in live animals using a multimodal PET/MRI nanoparticle.* Nature communications, 2014. 5(1): p. 1-9.
373. *National Center for Biotechnology Information. PubChem Database. [18F]Fluorodeoxyglucose, CID=3232583*. [cited 2020 July 8]; Available from: https://pubchem.ncbi.nlm.nih.gov/compound/18F_Fluorodeoxyglucose.
374. Lockau, H., et al., *Dynamic (18)F-FDG PET Lymphography for In Vivo Identification of Lymph Node Metastases in Murine Melanoma.* J Nucl Med, 2018. 59(2): p. 210-215.
375. Chen, L.Q., et al., *Evaluations of extracellular pH within in vivo tumors using acidoCEST MRI.* Magn Reson Med, 2014. 72(5): p. 1408-17.
376. Jones, K.M., et al., *Respiration gating and Bloch fitting improve pH measurements with acidoCEST MRI in an ovarian orthotopic tumor model.* Proc SPIE Int Soc Opt Eng, 2016. 9788.
377. Longo, D.L., et al., *Iopamidol as a responsive MRI-chemical exchange saturation transfer contrast agent for pH mapping of kidneys: In vivo studies in mice at 7 T.* Magn Reson Med, 2011. 65(1): p. 202-11.
378. Lindeman, L.R., et al., *Differentiating lung cancer and infection based on measurements of extracellular pH with acidoCEST MRI.* Sci Rep, 2019. 9(1): p.

13002.
379. Fischer, A.H., et al., *Hematoxylin and eosin staining of tissue and cell sections.* CSH Protoc, 2008. 2008: p. pdb.prot4986.
380. Garon, E.B., et al., *Pembrolizumab for the Treatment of Non–Small-Cell Lung Cancer.* New England Journal of Medicine, 2015. 372(21): p. 2018-2028.
381. Loughlin, P.M., et al., *Quantifying tumour-infiltrating lymphocyte subsets: a practical immuno-histochemical method.* J Immunol Methods, 2007. 321(1-2): p. 32-40.
382. Kunder, S., et al., *A comprehensive antibody panel for immunohistochemical analysis of formalin-fixed, paraffin-embedded hematopoietic neoplasms of mice: analysis of mouse specific and human antibodies cross-reactive with murine tissue.* Toxicologic pathology, 2007. 35(3): p. 366-375.
383. Chong, J., et al., *MetaboAnalyst 4.0: towards more transparent and integrative metabolomics analysis.* Nucleic Acids Research, 2018. 46(W1): p. W486-W494.
384. Iglewicz, B. and D.C. Hoaglin, *How to Detect and Handle Outliers*. 1993: ASQC Quality Press.
385. Barnett, V. and T. Lewis, *Outliers in statistical data.* osd, 1984.
386. Michl, J., K.C. Park, and P. Swietach, *Evidence-based guidelines for controlling pH in mammalian live-cell culture systems.* Commun Biol, 2019. 2: p. 144.
387. Kondo, A. and T. Osawa, *Establishment of an Extracellular Acidic pH Culture System.* J Vis Exp, 2017(129).
388. Gerweck, L.E. and K. Seetharaman, *Cellular pH gradient in tumor versus normal tissue: potential exploitation for the treatment of cancer.* Cancer research, 1996. 56(6): p. 1194-1198.
389. Kondo, A., et al., *Extracellular Acidic pH Activates the Sterol Regulatory Element-Binding Protein 2 to Promote Tumor Progression.* Cell Rep, 2017. 18(9): p. 2228-2242.
390. Rofstad, E.K., et al., *Acidic extracellular pH promotes experimental metastasis of human melanoma cells in athymic nude mice.* Cancer Res, 2006. 66(13): p. 6699-707.
391. Chen, S., et al., *Mechanisms regulating PD-L1 expression on tumor and immune cells.* J Immunother Cancer, 2019. 7(1): p. 305.
392. Pan, L., et al., *Rocaglamide, silvestrol and structurally related bioactive compounds from Aglaia species.* Nat Prod Rep, 2014. 31(7): p. 924-39.
393. Sadlish, H., et al., *Evidence for a functionally relevant rocaglamide binding site on the eIF4A-RNA complex.* ACS Chem Biol, 2013. 8(7): p. 1519-27.
394. Chu, J., et al., *CRISPR-Mediated Drug-Target Validation Reveals Selective Pharmacological Inhibition of the RNA Helicase, eIF4A.* Cell Rep, 2016. 15(11): p. 2340-7.
395. Basmadjian, C., et al., *Flavaglines: potent anticancer drugs that target prohibitins and the helicase eIF4A.* Future Med Chem, 2013. 5(18): p. 2185-97.
396. Wolfe, A.L., et al., *RNA G-quadruplexes cause eIF4A-dependent oncogene translation in cancer.* Nature, 2014. 513(7516): p. 65-70.
397. Yan, R. and R.E. Rhoads, *Human protein synthesis initiation factor eIF-4 gamma is encoded by a single gene (EIF4G) that maps to chromosome 3q27-qter.* Genomics, 1995. 26(2): p. 394-8.
398. Yan, R., et al., *Amino acid sequence of the human protein synthesis initiation factor eIF-4 gamma.* J Biol Chem, 1992. 267(32): p. 23226-31.
399. Etchison, D. and J.R. Etchison, *Monoclonal antibody-aided characterization of cellular p220 in uninfected and poliovirus-infected HeLa cells: subcellular distribution and identification of conformers.* J Virol, 1987. 61(9): p. 2702-10.

400. Platanias, L.C., *Mechanisms of type-I- and type-II-interferon-mediated signalling.* Nat Rev Immunol, 2005. 5(5): p. 375-86.
401. Mesev, E.V., R.A. LeDesma, and A. Ploss, *Decoding type I and III interferon signalling during viral infection.* Nat Microbiol, 2019. 4(6): p. 914-924.
402. Grasselly, C., et al., *The Antitumor Activity of Combinations of Cytotoxic Chemotherapy and Immune Checkpoint Inhibitors Is Model-Dependent.* Front Immunol, 2018. 9: p. 2100.
403. Kleffel, S., et al., *Melanoma Cell-Intrinsic PD-1 Receptor Functions Promote Tumor Growth.* Cell, 2015. 162(6): p. 1242-56.
404. Peng, W., et al., *PD-1 blockade enhances T-cell migration to tumors by elevating IFN-gamma inducible chemokines.* Cancer Res, 2012. 72(20): p. 5209-18.
405. Duan, Q., et al., *Turning Cold into Hot: Firing up the Tumor Microenvironment.* Trends Cancer, 2020. 6(7): p. 605-618.
406. Galon, J. and D. Bruni, *Approaches to treat immune hot, altered and cold tumours with combination immunotherapies.* Nature Reviews Drug Discovery, 2019. 18(3): p. 197-218.
407. Dominguez-Soto, A., et al., *Intravenous immunoglobulin promotes antitumor responses by modulating macrophage polarization.* J Immunol, 2014. 193(10): p. 5181-9.
408. Cianciaruso, C., et al., *Molecular Profiling and Functional Analysis of Macrophage-Derived Tumor Extracellular Vesicles.* Cell Rep, 2019. 27(10): p. 3062-3080.e11.
409. Baer, C., et al., *Suppression of microRNA activity amplifies IFN-gamma-induced macrophage activation and promotes anti-tumour immunity.* Nat Cell Biol, 2016. 18(7): p. 790-802.
410. Hoves, S., et al., *Rapid activation of tumor-associated macrophages boosts preexisting tumor immunity.* J Exp Med, 2018. 215(3): p. 859-876.
411. Ries, C.H., et al., *Targeting tumor-associated macrophages with anti-CSF-1R antibody reveals a strategy for cancer therapy.* Cancer Cell, 2014. 25(6): p. 846-59.
412. Ohsawa, K., et al., *Microglia/macrophage-specific protein Iba1 binds to fimbrin and enhances its actin-bundling activity.* J Neurochem, 2004. 88(4): p. 844-56.
413. Imai, Y., et al., *A novel gene iba1 in the major histocompatibility complex class III region encoding an EF hand protein expressed in a monocytic lineage.* Biochem Biophys Res Commun, 1996. 224(3): p. 855-62.
414. Mall, C., et al., *Repeated PD-1/PD-L1 monoclonal antibody administration induces fatal xenogeneic hypersensitivity reactions in a murine model of breast cancer.* Oncoimmunology, 2016. 5(2): p. e1075114.
415. Ding, X.-c., et al., *The relationship between expression of PD-L1 and HIF-1α in glioma cells under hypoxia.* Journal of Hematology & Oncology, 2021. 14(1): p. 92.
416. Koh, W.J., et al., *Imaging of hypoxia in human tumors with [F-18]fluoromisonidazole.* Int J Radiat Oncol Biol Phys, 1992. 22(1): p. 199-212.
417. Sachpekidis, C., et al., *Combined use of (18)F-FDG and (18)F-FMISO in unresectable non-small cell lung cancer patients planned for radiotherapy: a dynamic PET/CT study.* Am J Nucl Med Mol Imaging, 2015. 5(2): p. 127-42.
418. Mahling, M., et al., *A Comparative pO2 Probe and [18F]-Fluoro-Azomycinarabino-Furanoside ([18F]FAZA) PET Study Reveals Anesthesia-Induced Impairment of Oxygenation and Perfusion in Tumor and Muscle.* PLoS One, 2015. 10(4): p. e0124665.
419. Maier, F.C., et al., *Significant impact of different oxygen breathing conditions on noninvasive in vivo tumor-hypoxia imaging using [(1)(8)F]-fluoro-azomycinarabino-furanoside ([(1)(8)F]FAZA).* Radiat Oncol, 2011. 6: p. 165.

420. Mortensen, L.S., et al., *FAZA PET/CT hypoxia imaging in patients with squamous cell carcinoma of the head and neck treated with radiotherapy: results from the DAHANCA 24 trial.* Radiother Oncol, 2012. 105(1): p. 14-20.
421. Schweifer, A., et al., *[(18)F]Fluoro-azomycin-2 -deoxy-beta-d-ribofuranoside - A new imaging agent for tumor hypoxia in comparison with [(18)F]FAZA.* Nucl Med Biol, 2016. 43(12): p. 759-769.
422. Riley, P.A., *Melanin.* Int J Biochem Cell Biol, 1997. 29(11): p. 1235-9.
423. Tiffen, J.C., et al., *Luciferase expression and bioluminescence does not affect tumor cell growth in vitro or in vivo.* Molecular cancer, 2010. 9: p. 299-299.
424. Piret, J.P., et al., *CoCl2, a chemical inducer of hypoxia-inducible factor-1, and hypoxia reduce apoptotic cell death in hepatoma cell line HepG2.* Ann N Y Acad Sci, 2002. 973: p. 443-7.
425. Kim, K.S., et al., *A novel role of hypoxia-inducible factor in cobalt chloride- and hypoxia-mediated expression of IL-8 chemokine in human endothelial cells.* J Immunol, 2006. 177(10): p. 7211-24.
426. Metzen, E., et al., *Nitric oxide impairs normoxic degradation of HIF-1α by inhibition of prolyl hydroxylases.* Molecular biology of the cell, 2003. 14(8): p. 3470-3481.
427. Kaczmarek, M., et al., *Metal ions-stimulated iron oxidation in hydroxylases facilitates stabilization of HIF-1 alpha protein.* Toxicol Sci, 2009. 107(2): p. 394-403.
428. Noman, M.Z., et al., *Improving Cancer Immunotherapy by Targeting the Hypoxic Tumor Microenvironment: New Opportunities and Challenges.* Cells, 2019. 8(9).
429. Rotman, J., et al., *Unlocking the therapeutic potential of primary tumor-draining lymph nodes.* Cancer Immunol Immunother, 2019. 68(10): p. 1681-1688.
430. Hoshida, T., et al., *Imaging steps of lymphatic metastasis reveals that vascular endothelial growth factor-C increases metastasis by increasing delivery of cancer cells to lymph nodes: therapeutic implications.* Cancer Res, 2006. 66(16): p. 8065-75.
431. Commerford, C.D., et al., *Mechanisms of Tumor-Induced Lymphovascular Niche Formation in Draining Lymph Nodes.* Cell Rep, 2018. 25(13): p. 3554-3563.e4.
432. Zhang, F., et al., *Preclinical lymphatic imaging.* Mol Imaging Biol, 2011. 13(4): p. 599-612.
433. Johnson, S., S. Arora, and E. Babu, *Injecting patent blue dye V for sentinel lymph node biopsy without skin staining.* Ann R Coll Surg Engl, 2012. 94(4): p. 277-8.
434. Paulinelli, R.R., et al., *A prospective randomized trial comparing patent blue and methylene blue for the detection of the sentinel lymph node in breast cancer patients.* Rev Assoc Med Bras (1992), 2017. 63(2): p. 118-123.
435. Tsopelas, C. and R. Sutton, *Why certain dyes are useful for localizing the sentinel lymph node.* J Nucl Med, 2002. 43(10): p. 1377-82.
436. Van den Broeck, W., A. Derore, and P. Simoens, *Anatomy and nomenclature of murine lymph nodes: Descriptive study and nomenclatory standardization in BALB/cAnNCrl mice.* J Immunol Methods, 2006. 312(1-2): p. 12-9.
437. Bavik, C., et al., *The gene expression program of prostate fibroblast senescence modulates neoplastic epithelial cell proliferation through paracrine mechanisms.* Cancer Res, 2006. 66(2): p. 794-802.
438. Krtolica, A., et al., *Senescent fibroblasts promote epithelial cell growth and tumorigenesis: a link between cancer and aging.* Proc Natl Acad Sci U S A, 2001. 98(21): p. 12072-7.
439. Coppé, J.P., et al., *Secretion of vascular endothelial growth factor by primary human fibroblasts at senescence.* J Biol Chem, 2006. 281(40): p. 29568-74.
440. Valenzuela, C.A., et al., *SASP-Dependent Interactions between Senescent Cells and Platelets Modulate Migration and Invasion of Cancer Cells.* Int J Mol Sci, 2019.

20(21).
441. Koguchi, T., et al., *Regulation of myo-inositol biosynthesis by p53-ISYNA1 pathway.* Int J Oncol, 2016. 48(6): p. 2415-24.
442. Vaddepally, R.K., et al., *Review of Indications of FDA-Approved Immune Checkpoint Inhibitors per NCCN Guidelines with the Level of Evidence.* Cancers, 2020. 12(3): p. 738.
443. Qian, J., et al., *The IFN-γ/PD-L1 axis between T cells and tumor microenvironment: hints for glioma anti-PD-1/PD-L1 therapy.* Journal of Neuroinflammation, 2018. 15(1): p. 290.
444. Karachaliou, N., et al., *Interferon gamma, an important marker of response to immune checkpoint blockade in non-small cell lung cancer and melanoma patients.* Ther Adv Med Oncol, 2018. 10: p. 1758834017749748.
445. Chen, H., et al., *Anti-CTLA-4 therapy results in higher CD4+ICOShi T cell frequency and IFN-gamma levels in both nonmalignant and malignant prostate tissues.* Proc Natl Acad Sci U S A, 2009. 106(8): p. 2729-34.
446. Nakayama, Y., et al., *PhosphoSTAT1 expression as a potential biomarker for antiPD1/antiPDL1 immunotherapy for breast cancer.* Int J Oncol, 2019. 54(6): p. 2030-2038.
447. Sadzak, I., et al., *Recruitment of Stat1 to chromatin is required for interferon-induced serine phosphorylation of Stat1 transactivation domain.* Proceedings of the National Academy of Sciences, 2008. 105(26): p. 8944-8949.
448. Meissl, K., et al., *The good and the bad faces of STAT1 in solid tumours.* Cytokine, 2017. 89: p. 12-20.
449. Decker, T. and P. Kovarik, *Serine phosphorylation of STATs.* Oncogene, 2000. 19(21): p. 2628-2637.
450. Kovarik, P., et al., *Stress-induced phosphorylation of STAT1 at Ser727 requires p38 mitogen-activated protein kinase whereas IFN-γ uses a different signaling pathway.* Proceedings of the National Academy of Sciences, 1999. 96(24): p. 13956-13961.
451. Riemann, A., et al., *Acidic environment activates inflammatory programs in fibroblasts via a cAMP-MAPK pathway.* Biochim Biophys Acta, 2015. 1853(2): p. 299-307.
452. Riemann, A., et al., *Acidic priming enhances metastatic potential of cancer cells.* Pflügers Archiv - European Journal of Physiology, 2014. 466(11): p. 2127-2138.
453. Hornbeck, P.V., et al., *PhosphoSite: A bioinformatics resource dedicated to physiological protein phosphorylation.* Proteomics, 2004. 4(6): p. 1551-1561.
454. Diella, F., et al., *Phospho. ELM: a database of experimentally verified phosphorylation sites in eukaryotic proteins.* BMC bioinformatics, 2004. 5(1): p. 1-5.
455. Yu, H., et al., *Correlation of PD-L1 Expression with Tumor Mutation Burden and Gene Signatures for Prognosis in Early-Stage Squamous Cell Lung Carcinoma.* J Thorac Oncol, 2019. 14(1): p. 25-36.
456. Bullock, B.L., et al., *Tumor-intrinsic response to IFNγ shapes the tumor microenvironment and anti–PD-1 response in NSCLC.* Life Science Alliance, 2019. 2(3): p. e201900328.
457. Kleinovink, J.W., et al., *PD-L1 immune suppression in cancer: Tumor cells or host cells?* Oncoimmunology, 2017. 6(7): p. e1325982.
458. Noguchi, T., et al., *Temporally Distinct PD-L1 Expression by Tumor and Host Cells Contributes to Immune Escape.* Cancer Immunol Res, 2017. 5(2): p. 106-117.
459. Warburg, O., *On respiratory impairment in cancer cells.* Science, 1956. 124(3215): p. 269-70.

460. Supuran, C.T., *Carbonic anhydrases: novel therapeutic applications for inhibitors and activators.* Nat Rev Drug Discov, 2008. 7(2): p. 168-81.
461. Castro, F., et al., *Interferon-Gamma at the Crossroads of Tumor Immune Surveillance or Evasion.* Front Immunol, 2018. 9: p. 847.
462. Seth, P., et al., *Deletion of Lactate Dehydrogenase-A in Myeloid Cells Triggers Antitumor Immunity.* Cancer Res, 2017. 77(13): p. 3632-3643.
463. Iwai, Y., et al., *Involvement of PD-L1 on tumor cells in the escape from host immune system and tumor immunotherapy by PD-L1 blockade.* Proceedings of the National Academy of Sciences, 2002. 99(19): p. 12293-12297.
464. Liakou, C.I., et al., *CTLA-4 blockade increases IFNγ-producing CD4⁺ICOS^{hi} cells to shift the ratio of effector to regulatory T cells in cancer patients.* Proceedings of the National Academy of Sciences, 2008. 105(39): p. 14987-14992.
465. Peng, W., et al., *PD-1 blockade enhances T-cell migration to tumors by elevating IFN-γ inducible chemokines.* Cancer Res, 2012. 72(20): p. 5209-18.
466. Tumeh, P.C., et al., *PD-1 blockade induces responses by inhibiting adaptive immune resistance.* Nature, 2014. 515(7528): p. 568-71.
467. Manguso, R.T., et al., *In vivo CRISPR screening identifies Ptpn2 as a cancer immunotherapy target.* Nature, 2017. 547(7664): p. 413-418.
468. Scharping, N.E., et al., *Efficacy of PD-1 Blockade Is Potentiated by Metformin-Induced Reduction of Tumor Hypoxia.* Cancer Immunol Res, 2017. 5(1): p. 9-16.
469. Muz, B., et al., *The role of hypoxia in cancer progression, angiogenesis, metastasis, and resistance to therapy.* Hypoxia (Auckl), 2015. 3: p. 83-92.
470. Petrova, V., et al., *The hypoxic tumour microenvironment.* Oncogenesis, 2018. 7(1): p. 10.
471. Bharti, S.K., et al., *Hypoxia Patterns in Primary and Metastatic Prostate Cancer Environments.* Neoplasia, 2019. 21(2): p. 239-246.
472. Jayaprakash, P., et al., *Targeted hypoxia reduction restores T cell infiltration and sensitizes prostate cancer to immunotherapy.* J Clin Invest, 2018. 128(11): p. 5137-5149.
473. Schwenck, J., et al., *Cancer immunotherapy is accompanied by distinct metabolic patterns in primary and secondary lymphoid organs observed by non-invasive in vivo (18)F-FDG-PET.* Theranostics, 2020. 10(2): p. 925-937.
474. Wu, H., et al., *T-cells produce acidic niches in lymph nodes to suppress their own effector functions.* Nat Commun, 2020. 11(1): p. 4113.
475. Hoogendam, J.P., et al., *99mTc SPECT/CT Versus Planar Lymphoscintigraphy for Preoperative Sentinel Lymph Node Detection in Cervical Cancer: A Systematic Review and Metaanalysis.* J Nucl Med, 2015. 56(5): p. 675-80.
476. Taupitz, M., *Imaging of lymph nodes—MRI and CT*, in *MRI and CT of the Female Pelvis*. 2007, Springer. p. 321-329.
477. *National Center for Biotechnology Information. PubChem Database. CID=19190*. [cited 2020 July, 9]; Available from: https://pubchem.ncbi.nlm.nih.gov/compound/Indocyanine-green.
478. Hackethal, A., et al., *Role of Indocyanine Green in Fluorescence Imaging with Near-Infrared Light to Identify Sentinel Lymph Nodes, Lymphatic Vessels and Pathways Prior to Surgery - A Critical Evaluation of Options.* Geburtshilfe Frauenheilkd, 2018. 78(1): p. 54-62.
479. Knackstedt, R., et al., *Indocyanine Green Fluorescence Imaging with Lymphoscintigraphy for Sentinel Node Biopsy in Melanoma: Increasing the Sentinel Lymph Node-Positive Rate.* Annals of Surgical Oncology, 2019. 26(11): p. 3550-3560.

480. Kwon, S. and E.M. Sevick-Muraca, *Noninvasive quantitative imaging of lymph function in mice.* Lymphat Res Biol, 2007. 5(4): p. 219-31.
481. Sharma, R., et al., *Quantitative imaging of lymph function.* Am J Physiol Heart Circ Physiol, 2007. 292(6): p. H3109-18.
482. Griessinger, C.M., et al., *In vivo tracking of Th1 cells by PET reveals quantitative and temporal distribution and specific homing in lymphatic tissue.* J Nucl Med, 2014. 55(2): p. 301-7.
483. Calcinotto, A., et al., *Cellular Senescence: Aging, Cancer, and Injury.* Physiol Rev, 2019. 99(2): p. 1047-1078.
484. Yin, Q., et al., *Comparison of senescence-related changes between three- and two-dimensional cultured adipose-derived mesenchymal stem cells.* Stem Cell Research & Therapy, 2020. 11(1): p. 226.
485. Zwerschke, W., et al., *Metabolic analysis of senescent human fibroblasts reveals a role for AMP in cellular senescence.* Biochem J, 2003. 376(Pt 2): p. 403-11.
486. Venable, M.E., G.C. Blobe, and L.M. Obeid, *Identification of a defect in the phospholipase D/diacylglycerol pathway in cellular senescence.* Journal of Biological Chemistry, 1994. 269(42): p. 26040-26044.
487. Augert, A., et al., *The M-type receptor PLA2R regulates senescence through the p53 pathway.* EMBO Rep, 2009. 10(3): p. 271-7.
488. Griveau, A., et al., *Targeting the phospholipase A2 receptor ameliorates premature aging phenotypes.* Aging Cell, 2018. 17(6): p. e12835.
489. Yeo, E.-J., et al., *Agonist-specific differential changes of cellular signal transduction pathways in senescent human diploid fibroblasts.* Experimental gerontology, 2002. 37(7): p. 871-883.
490. Webb, L.M., A.T. Arnholt, and M.E. Venable, *Phospholipase D modulation by ceramide in senescence.* Molecular and Cellular Biochemistry, 2010. 337(1): p. 153-158.
491. James, E.L., et al., *Replicatively senescent human fibroblasts reveal a distinct intracellular metabolic profile with alterations in NAD+ and nicotinamide metabolism.* Sci Rep, 2016. 6: p. 38489.
492. Mijit, M., et al., *Role of p53 in the Regulation of Cellular Senescence.* Biomolecules, 2020. 10(3): p. 420.
493. Schwartzenberg-Bar-Yoseph, F., M. Armoni, and E. Karnieli, *The tumor suppressor p53 down-regulates glucose transporters GLUT1 and GLUT4 gene expression.* Cancer Res, 2004. 64(7): p. 2627-33.
494. Wiley, C.D. and J. Campisi, *From Ancient Pathways to Aging Cells-Connecting Metabolism and Cellular Senescence.* Cell metabolism, 2016. 23(6): p. 1013-1021.
495. Chauvin, T.R. and M.D. Griswold, *Characterization of the expression and regulation of genes necessary for myo-inositol biosynthesis and transport in the seminiferous epithelium.* Biol Reprod, 2004. 70(3): p. 744-51.
496. Guan, G., P. Dai, and I. Shechter, *cDNA cloning and gene expression analysis of human myo-inositol 1-phosphate synthase.* Arch Biochem Biophys, 2003. 417(2): p. 251-9.
497. Ju, S., et al., *Human 1-D-myo-inositol-3-phosphate synthase is functional in yeast.* J Biol Chem, 2004. 279(21): p. 21759-65.